Current and rotation driven instabilities in Couette flows

Adam Child

Submitted in accordance with the requirements for the degree of

Doctor of Philosophy

The University of Leeds

School of Mathematics

August 2017

The candidate confirms that the work submitted is his own, except where work has formed part of jointly authored publications has been included. The contribution of the candidate and the other authors to this work has been explicitly indicated below. The candidate confirms that appropriate credit has been given within the thesis where reference has been made to the work of others.

The work in Chapter 3 of the thesis has appeared in publication as follows:

Child, A., Kersalé, E. and Hollerbach, R. (2015). Nonaxisymmetric linear instability of cylindrical magnetohydrodynamic Taylor-Couette flow. *Phys. Rev. E*, **92** (3), 033011.

The work in Chapter 4 of the thesis has appeared in publication as follows:

Child, A., Hollerbach, R., Marston, B. and Tobias, S. (2016). Generalised quasilinear approximation of the helical magnetorotational instability. *J. Plasma Phys.* **82** (3), 905820302–18.

The work in Chapter 5 of the thesis has appeared in publication as follows:

Child, A., Hollerbach, R. and Kersalé, E. (2017). Axisymmetric pulse train solutions in narrow-gap spherical Couette flow. *Physica D*, **348**, 54–59.

In each publication, the candidate was responsible for carrying out the mathematical research and obtaining all results, as well as composing the first drafts. The co-authors provided ideas and guidance, and collaborated in writing the final publications.

Acknowledgements

I would like to thank my supervisors, Prof. Rainer Hollerbach and Dr. Evy Kersalé, for their guidance throughout my PhD studies, which has proved invaluable. I am also grateful to Prof. Steven Tobias for introducing me to a topic that constitutes a large part of this work, as well as for his insight and collaboration, and to Prof. Brad Marston for his input on the resulting publication.

On a personal note, I thank my parents, Susan and Ian, who have provided a great deal of support over the last four years.

Finally, I am grateful to the STFC, who have provided the funding for this work.

Abstract

Couette flows are an invaluable tool in understanding some of the most important processes in astrophysical and geophysical fluid dynamics. When driven by rotation or electric currents, instability in such flows can be a key ingredient in a number of fundamental processes. For example, Taylor-Couette flow can give rise to the magnetorotational instabilities widely thought to be responsible for angular momentum transport in astrophysical disks.

In this thesis, we add to the understanding of instabilities in Couette flows by focussing on two specific applications; inductionless magnetorotational instability in Taylor-Couette flow, and narrow-gap spherical Couette flows.

After providing an overview of the numerical methods utilised throughout, we perform a linear stability analysis on inductionless magnetorotational instability, allowing for a fully generalised set-up which allows for every possible combination of imposed currents. A full exploration of the relevant parameter space is given. We then introduce the generalised quasilinear approximation, which serves to restrict nonlinear interaction between modes. In doing so, we are able to ascertain which modal interactions are essential to the key flow dynamics. More importantly, this is formally equivalent to the cumulant expansions utilised in the growing field of direct statistical simulation. Therefore, we are able to posit the future usefulness of statistical simulations to general wall-bounded flows.

Finally, we utilise direct numerical simulation to probe the existence of axisymmetric pulse train solutions in narrow-gap spherical Couette flow, in which computations have been, until now, unable to utilise sufficiently

narrow gap widths. As such, the only detailed prior solutions consist of asymptotic studies. We numerically confirm the existence of these pulse trains, and chart their initial bifurcations from the steady state solution. We also examine their magnetohydrodynamic equivalents, which have so far not been considered.

Abbreviations

MRI	Magnetorotational instability
AMRI	Azimuthal magnetorotational instability
HMRI	Helical magnetorotational instability
SMRI	Standard magnetorotational instability
TI	Tayler instability
LLL and ULL	Lower and upper Liu limits, respectively
DNS	Direct numerical simulation
NL DNS	Fully nonlinear direct numerical simulation
DSS	Direct statistical simulation
QL	Quasilinear approximation
GQL	Generalised quasilinear approximation
FFT	Fast Fourier transform
Re	Reynolds number
Rm	Magnetic Reynolds number
Pm	Magnetic Prandtl number
Ha	Hartmann number
S	Lundquist number
Ro	Rossby number
Rb	Magnetic Rossby number
Ta	Taylor number

Contents

List of Figures

Chapter 1

Introduction

1.1 Taylor-Couette flow

Taylor-Couette flow describes the motion of fluid contained in the annulus between two coaxially rotating cylinders. It has a rich history, though was first investigated thoroughly by Couette (1890) and Mallock (1888), who performed separate experiments on the set-up and prompted the great interest in Taylor-Couette flow that persists today. The two used opposite rotational profiles and found the resulting flows to be fundamentally different; Mallock, who rotated only the inner cylinder, found the flow to be unstable to Taylor vortices – rings of oppositely rotating fluid stacked between the cylinders – whilst Couette rotated only the outer cylinder, resulting in perfectly stable flow. Clearly the simple geometry allows for more than simple dynamics, given the right conditions.

The Taylor-Couette geometry consists of two cylinders located at radii $r_{i,o}$, each rotated with angular velocity $\Omega_{i,o}$, for the inner and outer cylinders respectively, as in figure 1.1. For theoretical applications, these cylinders are often assumed to be infinitely long, such that axial boundary conditions do not pose a problem. The Navier-Stokes equations permit the basic state flow $u_\phi = a_\Omega r + b_\Omega / r$, with a_Ω and b_Ω depending on the quantities r_o/r_i and Ω_o/Ω_i.

Rayleigh's inviscid analysis (Rayleigh, 1917) generated a simple yet powerful result

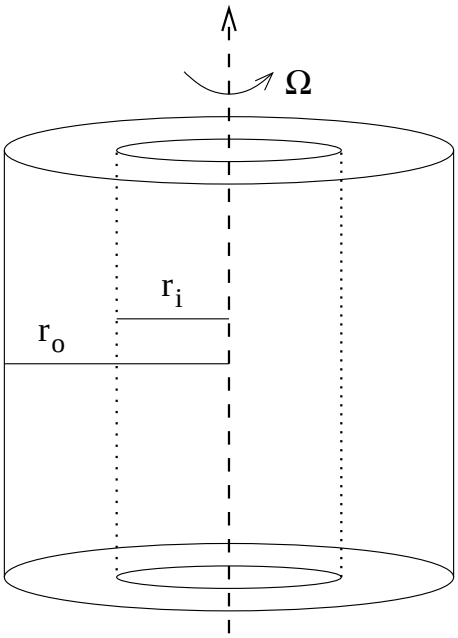

Figure 1.1: A schematic diagram of Taylor-Couette flow.

to explain the discrepancy between both experiments. By considering the stability of two rings of fluid as their positions are exchanged, he found that a necessary condition for instability is for angular momentum to increase toward the inner cylinder; that is,

$$r_i^2 \Omega_i > r_o^2 \Omega_o. \tag{1.1}$$

This explains why Couette's and Mallock's experiments yielded such different outcomes; Mallock's experimental set-up satisfied Rayleigh's instability criterion, whilst Couette's did not. Though certainly useful in predicting regions of instability, Rayleigh's criterion is not applicable in all cases – it is strictly only applicable to axisymmetric and inviscid fluid, and it makes no predictions about the angular velocity required to induce instability. A full mathematical investigation on the conditions for instability was performed by Taylor (1923), pioneering the use of linear stability analysis. Via examining perturbations about the basic flow, Taylor derived a critical parameter for instability, $\mathrm{Ta}_c = 4\mathrm{Re}^2((1-\Omega_o/\Omega_i)/(r_o/r_i)^2)[(1-r_o/r_i)/(1+r_o/r_i)]$. Indeed, the stability diagram given by Andereck *et al.* (1986) shows the wide array of possible unstable solutions that may occur in Taylor-Couette flow, each depending on the rotation speeds of the two cylinders, as well as their radii.

Though our discussion so far has been focused on the theoretical aspects of Taylor-Couette flow, it is important to note that such flows have applications in many astrophysical and geophysical flows, as well as in industrial applications. One major astrophysical application is that of accretion disks.

1.1.1 Accretion disks

Accretion disks are ubiquitous in our universe, and are found as an essential component in the process of star and planetary formation, as well as around black holes, for example. They are flat, rotating disks of matter that accrete onto some central body. Importantly, the particles in the disk may be modelled as a fluid, allowing for a fluid dynamical approach to accretion. Taylor-Couette flows provide a natural geometry with which to explore the disks, though there are some fundamental differences, namely the boundary conditions and flattened structure. Like many astrophysical objects, the disks possess a Keplerian rotation profile, and so their angular velocity scales as $\Omega(r) = r^{-3/2}$ (which is easily derived via balancing centripetal and gravitational forces, $(r\Omega)^2/r = GM/r^2$). For an in-depth review of the disk properties, we refer to (Pringle, 1981).

The key property, indeed the key purpose of accretion disks, is that their matter spirals into the central point. Therefore, in order for angular momentum to be conserved in the disk, there must exist some mechanism for its outward transport. Due to the time scales on which accretion occurs, it is known that this must result from a turbulent process; laminar viscous effects do not adequately explain the rate of this angular momentum transport. Indeed, if laminar viscosity *was* the cause of the angular momentum transport, the rate of accretion would be so slow that stars would not yet have formed. See (Balbus, 2003) for a review of the problems and solutions to the angular momentum transport problem.

It is clear then that this phenomena cannot be explained using purely hydrodynamic theory. Indeed, Rayleigh's criterion explicitly states that flows with outwardly increasing angular momentum are inherently stable. The review of Andereck *et al.*

(1986) confirms that, though hydrodynamic Taylor-Couette flow plays host to numerous instabilities, none take hold for Keplerian rotation profiles. So, the cause of turbulence in disks must be due to some other, more complex, phenomena.

1.1.2 Magnetorotational instability

Balbus & Hawley (1991) proposed that the key to turbulence in Keplerian profiles is the addition of a magnetic field, allowing for the excitation of the magnetorotational instability (MRI). In contrast to pure Taylor-Couette flow, this instability is driven by the combination of large-scale rotation and mean magnetic fields. Originally discovered by Velikhov (1959), the magnetorotational instability relies upon the addition of a weak axial magnetic field, $B_z = B_0$, to allow for instability without being bound by the Rayleigh criterion. This was particularly counter-intuitive, as magnetic fields are usually a largely stabilising influence on fluid systems, as found in experiments performed by Donnelly & Ozima (1962). The frozen-in-flux theorem would imply that magnetic fields act to resist fluid motion. Magnetohydrodynamic Taylor-Couette flow was developed further by Chandrasekhar (1960, 1961), though the MRI received little additional attention in the following decades as it was perceived to be a purely theoretical instability, with little real work use. After being rehabilitated for use in the accretion problem, the MRI is now a vibrant area of research, subjected to continual study; see the review of Julien & Knobloch (2010) for some of the more recent developments in the field. The original MRI with an imposed axial magnetic field, as described by Balbus and Hawley, is now often referred to as the standard MRI (SMRI).

The physical mechanism of the MRI can be understood best by using a simple analogy. Recall that, in a perfectly conducting fluid, each fluid element is linked by magnetic field lines. Moreover, electrically conducting fluid that moves through field lines generates a Lorentz force, composed of magnetic pressure and magnetic tension. The magnetic tension can be thought of as acting like a spring connecting two fluid elements. Let us consider two such fluid elements orbiting a central body, as would be the case in a disk, with some imposed axial magnetic field connecting

the two (see figure 1.2). If one element is perturbed to orbit at a slightly smaller radius than the other, it will as a consequence possess greater angular velocity, and therefore travel faster relative to the other element. However, the magnetic tension in the spring acts to keep the two elements together, and so acts to decelerate the inner element whilst accelerating the outer element. This causes the inner element to move to a closer orbit, whilst moving the outer element to an orbit even further away. The angular momentum has decreased for the inner element and increased for the outer element, and has been transported outwards via the spring. Note that the two elements have orbits that are further apart than the original perturbed state, and so the process repeats with greater effect due to the larger magnetic tension. Hence, the process is unstable.

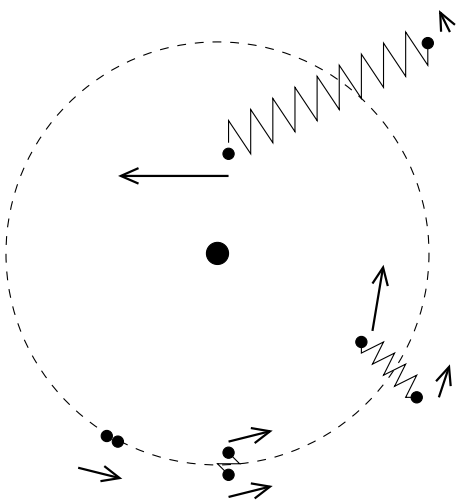

Figure 1.2: A simplified spring mechanism for the MRI. If the two fluid elements are slightly perturbed, the magnetic spring holding them together exerts a torque leading to the elements transferring angular momentum and taking higher and lower orbits. This only exaggerates the original perturbation, and so the process is unstable.

Despite the continued attention the MRI has received, numerical simulations are limited in that they cannot be performed in the relevant parameter regime for disks (Bai & Stone, 2014; Gressel & Pessah, 2015; Meheut *et al.*, 2015; Suzuki & Inutsuka, 2014). As such, alternative methods are often utilised to investigate the instability.

1.1.3 Experimental work

One such option is the use of smaller scale experiments to reproduce the instability. Independently, Rüdiger & Zhang (2001) and Ji *et al.* (2001) first proposed a series of experiments that involved imposing an axial field over a liquid metal Taylor-Couette set-up. It is known that, for instability, a magnetic Reynolds number $\mathrm{Rm} = \Omega_i r_i^2/\eta \geq \mathcal{O}(10)$ is required, which coupled with the magnetic Prandtl number of liquid metals, $\mathrm{Pm} = \nu/\eta = \mathcal{O}(10^{-6})$, results in a necessary Reynolds number $\mathrm{Re} = \mathrm{Rm}/\mathrm{Pm} = \mathcal{O}(10^7)$. Here, Rm is a measure of angular velocity compared to magnetic dissipation, Re is a measure of angular velocity compared to viscous dissipation, and Pm is a measure of viscous dissipation compared to magnetic dissipation. The parameter ν is the kinematic viscosity, and η is magnetic diffusivity. However, this extremely large Reynolds number causes critical difficulties in performing such experiments (Schartman *et al.*, 2009), primarily due to the effect of the Taylor-Proudman theorem.

The Taylor-Proudman theorem (as first derived by Hough (1897)) states that, when a system undergoes strong enough rotation, fluid velocity becomes independent of the axis of rotation. That is, in Taylor-Couette flow, fluid velocity becomes independent along the z axis. For a derivation of Taylor-Proudman theorem in Taylor-Couette flow, see appendix A.2.

Of course, any physical experiment requires that the cylinders have end-caps. Due to the Taylor-Proudman theorem, as well as Ekman pumping (a consequence of the rotation at the axial boundary, whereby fluid is pumped perpendicularly from the Ekman layer away from the boundary), the conditions at these end-caps will overcome the bulk of the flow (Avila, 2012; Gissinger *et al.*, 2012; Hollerbach & Fournier, 2004). As such, the MRI has yet to be seen in the laboratory - though experiments at Princeton have generated other worthwhile fluid dynamical results (Nornberg *et al.*, 2010; Roach *et al.*, 2012). Recently, Flanagan *et al.* (2015) has proposed that the difficulty here might be overcome by performing the experiments with plasma, instead of liquid metal, so as to lower the critical Reynolds number.

1.1.4 Inductionless MRI

Motivated by the desire to obtain magnetorotational instability in the laboratory, Hollerbach & Rüdiger (2005) proposed that an azimuthal magnetic field $B_\phi = r^{-1}$ be added to the set-up, such that the total magnetic field is then helical. This is achieved via running a current through the central core of the Taylor-Couette device. It transpires that this allows for the excitation of a different kind of axisymmetric magnetorotational instability, now coined helical MRI (or HMRI). For the HMRI, the parameters governing instability are no longer the magnetic Reynolds and Lundquist numbers, Rm and $\mathrm{S} = B_0 r_i/\eta\sqrt{\mu_0\rho}$, but rather the Reynolds and Hartmann numbers, $\mathrm{Re} = \Omega_i r_i^2/\nu$ and $\mathrm{Ha} = B_0 r_i/\sqrt{\mu_0\rho\nu\eta}$, where μ_0 the permeability of free space and ρ is density. Here, the Lundquist number measures the ratio of the Alfvén crossing and resistive diffusion time scales, and the Hartmann number measures the ratio of magnetic versus viscous forces. Importantly, this decoupling from Rm allows for instability at finite $\mathrm{Re} \sim \mathcal{O}(10^3)$, even when $\mathrm{Pm} \approx 0$, and so is able to avoid the destructive effects of the Taylor-Proudman theorem. The HMRI is closely connected to the SMRI (via a spectral exceptional point), as shown by Kirillov & Stefani (2010), though there are some fundamental differences; it manifests as a weakly destabilised inertial oscillation, for example, whereas the SMRI is a slow magnetocoriolis wave Liu *et al.* (2006).

The HMRI has proven to be relatively straightforward to reproduce in the laboratory via the PROMISE experiments of Stefani *et al.* (2006, 2007, 2008, 2009). The PROMISE experiment consists of a copper Taylor-Couette cell, with inner and outer radii of 4cm and 8cm, respectively, and has a height of 40cm. This is filled with the alloy GaInSn (Gallium-Indium-Tin), which is fluid at room temperature and has an effective $\mathrm{Pm} = 1.4 \times 10^{-6}$. Typically, the inner cylinder is rotated with frequencies $\mathcal{O}(0.1\mathrm{Hz})$, whilst axial magnetic fields of $\mathcal{O}(10\mathrm{mT})$ are generated by up to 200A currents in an external coil. Currents of up to 8000A are then run up the core to generate the azimuthal magnetic field.

Initial evidence for the instability showed travelling wave solutions exist within a predicted Hartmann number interval, with good qualitative agreement to linear

numerics (Stefani *et al.*, 2006). Further comparisons to numerical results were given by Rüdiger *et al.* (2006), showing good agreement in wave speed, but not wavelength, presumably due to end effects. The experiment was not without its shortcomings, with the existence of a radial jet at the midpoint, generated by a mixture of Ekman pumping at the end-caps and Hartmann currents, introducing noise into the flow and restricting the extent of the travelling waves Stefani *et al.* (2008). This was remedied by the development of more sophisticated, multi-component end-caps, eventually giving results that show good agreement with both theory and numerics (Stefani *et al.*, 2009). Though initially debated (Liu, 2009), the instability has been shown to be self-sustaining, and not convective (Priede & Gerbeth, 2009). There is still considerable research interest into the HMRI (Priede, 2011, 2015), and its regions of instability.

There is, however, one major drawback to the HMRI. It was shown by Liu *et al.* (2006) that the instability occurs only for a certain range of rotational profiles $\Omega(r)$, now known as the Liu limits. Unfortunately, these do not include Keplerian rotation, seemingly ruling out the possibility of HMRI in any astrophysical application. This is particularly disappointing as it precludes any meaningful conclusion on accretion disks from the experiments involving inductionless MRI. There have been some suggestions as to how this may be overcome, for example Kirillov & Stefani (2012) posit that there may exist certain layers in accretion disks that have rotation profiles that allow for local HMRI. It is not clear whether this is a realistic possibility though, and the HMRI certainly cannot account for the large-scale turbulent momentum transport throughout the whole disk.

Of course, if a helical magnetic field can give rise to inductionless variants of MRI, it is only natural to consider the possibility of MRI for purely azimuthal magnetic fields, with $B_\phi \sim 1/r$. Though it is known that there can be no axisymmetric modes of instability when the background magnetic field is purely azimuthal, (Herron & Soliman, 2006), there exists a nonaxisymmetric variant of MRI, called the azimuthal MRI (AMRI), first theorised by Ogilvie & Pringle (1996). The AMRI has also since been evidenced in the laboratory (Seilmayer *et al.*, 2014). The azimuthal field

can also be generated by running a current through the fluid itself, leading to the case $B_\phi \sim r$. Work involving more generalised fields, as well as nonaxisymmetric instabilities, is further discussed in chapter 3.

1.1.5 Tayler instability

Of course, running a current through electrically conducting fluid can also allow for current driven instabilities, such as the Tayler instability (TI, or sometimes the Tayler-Vandakurov instability). Originally studied in the context of stellar cores (Tayler, 1973; Vandakurov, 1972), the Tayler instability is a nonaxisymmetric, 'kink-type' instability, which may be excited even in the absence of differential rotation. In contrast to the MRI's reliance upon magnetic tension, the Tayler instability utilises the magnetic pressure component of the Lorentz force, exerted perpendicular to the magnetic field. As such, energy is received from the current, and not differential rotation. To elucidate upon the mechanism for the Tayler instability, we refer to a simple example whereby an azimuthal magnetic field is applied to the Taylor-Couette system. In the case of compressible fluids, the magnetic pressure is directed entirely along the magnetic field axis. With a large enough magnitude, this magnetic pressure can cause instability in the vicinity of the magnetic axis, forcing the magnetic field lines away from the axis in an unstable manner (see figure 1.3). Of course, for incompressible flows, pressure doesn't provide energy to the system. Instead, the kink type instability is excited via perturbations in the current, though the result is essentially the same.

The TI can occur in a number of astrophysical contexts. As previously, mentioned, the instability was initially investigated within the field of stably-stratified stars, whereby weak toroidal fields are wound up by differential rotation. The instability is found to occur in radiative stellar cores, causing instability in the absence of differential rotation, and is essential to the Tayler-Spruit dynamo, where it provides the α effect (Spruit, 2002). It has also been investigated more generally as a potential source of helicity (Gellert *et al.*, 2011). Perhaps most importantly from a practical standpoint, the instability is of importance in the field of liquid metal batteries,

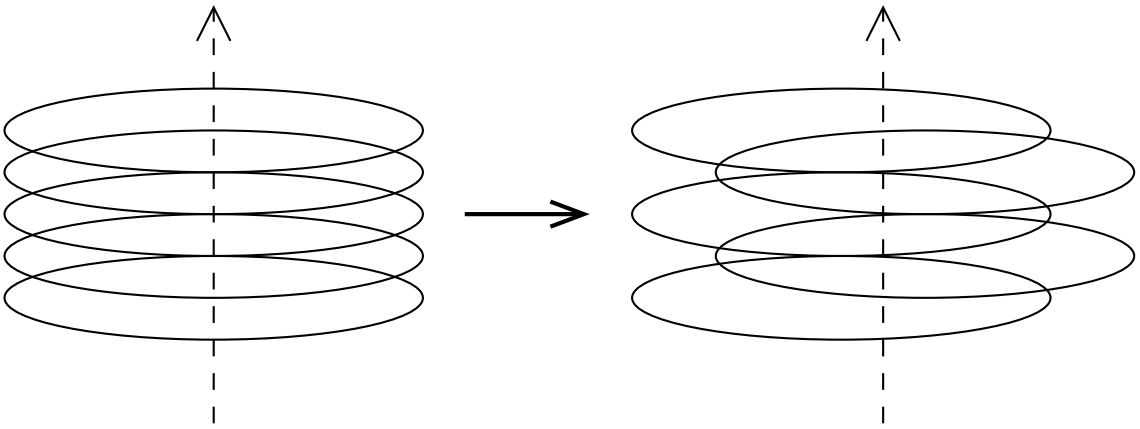

Figure 1.3: A simple diagram showing the mechanism for the Tayler instability in astrophysical applications. Magnetic pressure due to the aligned toroidal fields forces the magnetic field axis to undergo a kink instability.

which can be treated as non-rotating Taylor-Couette flow without an inner core. The batteries consist of two layers of metal and alloy that are separated by an electrolyte layer, which must stay intact for the battery to operate. Whilst small batteries have been produced without major issue, large batteries are inherently susceptible to current driven instabilities. As such, a knowledge of which parameter regimes at which the Tayler instability is (or is not) excited, is essential. Numerous suggestions have been given for how to circumvent the destructive effect of the Tayler instability (Stefani *et al.*, 2011; Weber *et al.*, 2014). Reassuringly, a recent study however, showed that the Tayler instability may not actually be strong enough to disrupt the electrolyte layer (Herreman *et al.*, 2015).

The instability has been observed experimentally (Seilmayer *et al.*, 2012), though rather complicated behaviour was observed due to the role of ohmic heating. Further numerical simulations have also been carried out (Weber *et al.*, 2013). Recent work has focused on the possibility of the Tayler instability under super-rotation (Rüdiger *et al.*, 2016b), where it was shown that flows can be subcritical under extremely steep positive shear.

1.2 Spherical Couette flow

The second type of Couette flow geometry discussed in this thesis is that of Spherical Couette flow, whereby fluid is driven between two coaxially rotating spheres. It has countless applications to geophysical, astrophysical and theoretical flows. Developing the understanding of spherical Couette flow has thus been of great importance, and the topic has enjoyed continual study over the years, benefiting from the ideal combination of experimental, numerical and analytical research. Indeed, the stability of spherical Couette flow has been of interest since the work of Khlebutin (1968), where it was established that, depending on gap width, the flow may either undergo instability yielding vortices, or remain stable in its transition to turbulence.

The spherical geometry consists of two spheres, located at $r_{i,o}$, each rotating with angular velocity $\Omega_{i,o}$, for the inner and outer spheres, respectively, as in figure 1.4. Due to the boundary curvature, the basic state flow is not trivial as in cylindrical Taylor-Couette flow. In this work we are only concerned with axisymmetric solutions of the flow, for which the Navier-Stokes equations permit the basic state solution $u_\phi = (a_\Omega r + b_\Omega / r^2) \sin\theta$ where a_Ω and b_Ω depend on the quantities r_o/r_i and Ω_o/Ω_i. Note that this is valid only for $\mathrm{Re} \to 0$, where there are no nonlinear effects.

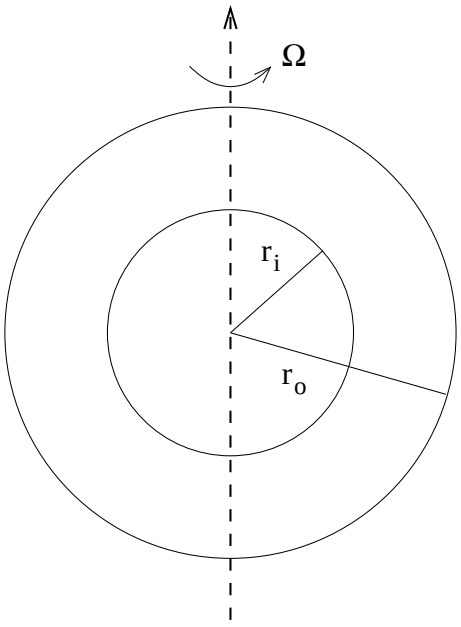

Figure 1.4: A schematic diagram of spherical Couette flow.

It is well known that the dynamics of spherical Couette flow are governed by the aspect ratio, $\epsilon = (r_i - r_o)/r_i$ (where r_i and r_o are the radii of the inner and outer shells, respectively), with three distinct flow regimes: Wide-gap $\epsilon > 0.24$ (see for example (Egbers & Rath, 1995; Hollerbach *et al.*, 2006; Munson & Menguturk, 1975)), medium-gap $0.12 < \epsilon < 0.24$ (Bühler, 1990; Mamun & Tuckerman, 1995; Nakabayashi *et al.*, 2005), and narrow-gap $\epsilon < 0.12$ (Nakabayashi *et al.*, 2002; Wimmer, 1976, 1981). As the scale separation between instabilities (which have length scale corresponding to the gap width $r_i - r_o$) and background flow (which depends mainly on r_i) increases, complicated and interesting dynamics can arise. In this thesis we focus purely on the narrow-gap regime, though do give comparisons to the aforementioned medium gap solutions. Of course, such narrow-gap solutions are not only interesting in the frame of spherical Couette flow; the existence of small scale patterns in large scale background flow is a common theme in the area of pattern formation [see for example (Cross & Greenside, 2009; Cross & Hohenberg, 1993; Hoyle, 2006)], which has a wide variety of applications. Previous work in the narrow gap is discussed in greater detail in chapter 5.

1.3 Thesis structure

The work in this thesis shall be organised as follows. In chapter 2, the numerical methods utilised in later chapters are discussed. We introduce the spectral collocation method that is used to solve the eigenvalue problem in chapter 3, as well as pseudo-spectral time-stepping techniques for both MHD Taylor-Couette flow and spherical Couette flow. Then in chapter 3 we explore the linear stability of nonaxisymmetric instabilities in MHD Taylor-Couette flow near the inductionless limit, as would be the case for liquid metal experiments. This work expands upon the numerics performed by Hollerbach and Rüdiger, and touches upon some of the asymptotic predictions given by Kirillov and collaborators in their various publications. By allowing for a more generalised azimuthal magnetic field than has been used previously, we fully explore the parameter regime. We exclusively make use of the aspect ratio of the PROMISE experiment, allowing for ease of reproduction experimen-

tally. In chapter 4, we present a generalised quasilinear approximation of the HMRI in comparison with the full solution. This approximation allows us to test for the accuracy of direct statistical simulation, to which it is essentially equivalent, which may offer a further avenue for study into the HMRI alongside other flows. Finally, we build upon this by considering GQL for non-inductionless MRI, and examine the effect that the balance between the Reynolds and magnetic Reynolds number driven nonlinear terms. Then, in chapter 5, we consider the stability of narrow gap spherical Couette flow, and investigate the existence of axisymmetric pulse train solutions. Previous work, though containing many interesting results, has been severely limited in terms of numerical simulation due to the resolution required versus computational efficiency. We make use of an efficient associated Legendre transform routine in order to provide simulations at previously unexplored gap widths. We search for the pulse-train solutions identified by Soward, Bassom and colleagues' asymptotic analysis (Bassom & Soward, 2004; Blockley *et al.*, 2007; Harris *et al.*, 2000), as well as evidence of other, previously asymptotic only, results. Furthermore, we consider the equivalent magnetohydrodynamic problem – previously unexplored in the narrow gap regime – for a number of different boundary conditions and magnetic field geometries. Finally, in chapter 6 a summary of the key results is given as a brief overview of this thesis, and a number of avenues for further work are discussed.

Chapter 2

Numerical Methods

In order to explore the stability of Couette flows, we shall need a set of robust numerical methods to solve for the flow in both cylindrical and spherical geometries. We begin by recapping the Navier-Stokes and induction equations, then derive an inductionless approximation of them for use with liquid metals. We then detail the spectral methods that are utilised throughout this thesis, starting with collocation. The spectral expansion functions for both periodic and aperiodic domains are discussed and then put to use in pseudo-spectral time-stepping schemes, which are used in chapters 4 and 5 to evolve the flow forward in time. This is achieved via a Crank-Nicolson scheme in both cases. We then describe the pseudo-spectral method for both cylindrical and spherical geometries, detailing the procedure for evaluating nonlinearities in the governing equations, and the transforms that are used therein. Finally, an alternate cosine transform method is described for the case of spherical Couette flow.

The standard Navier-Stokes and induction equations governing the evolution of the velocity and magnetic fields are

$$\frac{\partial \mathbf{U}}{\partial t} + \mathbf{U}\cdot\nabla\mathbf{U} = -\frac{\nabla p}{\rho} + \nu\nabla^2\mathbf{U} + \frac{1}{\mu_0\rho}(\nabla\times\mathbf{B})\times\mathbf{B}, \tag{2.1}$$

$$\frac{\partial \mathbf{B}}{\partial t} = \eta\nabla^2\mathbf{B} + \nabla\times\mathbf{U}\times\mathbf{B}. \tag{2.2}$$

Here the velocity field is denoted $\mathbf{U}$, the magnetic field $\mathbf{B}$, and the pressure is given by p. In the following chapters we suitably nondimensionalise the equations; however, as this is not done uniformly the precise details are left to each chapter. Throughout this work we take the fluid to be incompressible, and magnetic field to be solenoidal; that is

$$\nabla\cdot\mathbf{U} = 0, \tag{2.3}$$

$$\nabla\cdot\mathbf{B} = 0. \tag{2.4}$$

In order to fulfil these conditions automatically, we make use of the toroidal-poloidal decomposition for field and flow variables. For example, in 2D and 3D flows respectively, the velocity field can be expressed as

$$\mathbf{U} = v\,\mathbf{e}_\phi + \nabla\times(\psi\,\mathbf{e}_\phi), \tag{2.5}$$

$$\mathbf{U} = \nabla\times(e\,\mathbf{e}_\phi) + \nabla\times\nabla\times(f\,\mathbf{e}_\phi). \tag{2.6}$$

It is easily verified that this satisfies the two incompressibility conditions in all cases. By this definition, the decomposed variables are orthogonal.

2.1 Quasi-static approximation

In laboratory fluids, the magnetic Prandtl number Pm is extremely small ($\mathcal{O}(10^{-6})$), due to the diminished role viscous dissipation has when compared to magnetic dissipation. As a consequence, the magnetic Reynolds number $\mathrm{Rm} \ll 1$ in most experiments (though not all; the Princeton MRI apparatus can in theory reach $\mathrm{Rm} = 10$ – for $\mathrm{Re} = 10^7$ – with recent simulations reaching values up to $\mathrm{Rm} = 20$ (Wei *et al.*, 2016)). In this case, we can significantly simplify the Navier-Stokes and induction equations, in the form of the low Rm – or quasi-static – approximation.

We split the magnetic field into its two constitutive components, the imposed ($\mathbf{B}_0$) and induced ($\mathbf{b}$) magnetic fields, which allows us to compare the relative sizes of each. So, if we let

$$\mathbf{B} = \mathbf{B}_0 + \mathbf{b}, \tag{2.7}$$

then the induction equation becomes

$$\frac{\partial(\mathbf{B}_0 + \mathbf{b})}{\partial t} = \nabla \times (\mathbf{U} \times (\mathbf{B}_0 + \mathbf{b})) + \eta \nabla^2 (\mathbf{B}_0 + \mathbf{b}). \tag{2.8}$$

As $\mathbf{B}_0$ is time independent, this of course yields

$$\frac{\partial \mathbf{b}}{\partial t} + (\mathbf{U} \cdot \nabla)\mathbf{b} - (\mathbf{b} \cdot \nabla)\mathbf{U} = (\mathbf{B}_0 \cdot \nabla)\mathbf{U} - (\mathbf{U} \cdot \nabla)\mathbf{B}_0 + \eta \nabla^2 \mathbf{b} + \eta \nabla^2 \mathbf{B}_0, \tag{2.9}$$

Let us nondimensionalise as follows: $\mathbf{b} = b\hat{\mathbf{b}}$, $\mathbf{B}_0 = B_0 \hat{\mathbf{B}}_0$, $\mathbf{U} = r_i \Omega_i \hat{\mathbf{U}}$ and $t = \Omega^{-1} \hat{t}$. This yields

$$b\Omega \left(\frac{\partial \hat{\mathbf{b}}}{\partial \hat{t}} + \left(\hat{\mathbf{U}} \cdot \nabla \right) \hat{\mathbf{b}} - \left(\hat{\mathbf{b}} \cdot \nabla \right) \hat{\mathbf{U}} \right) = B_0 \Omega \left(\left(\hat{\mathbf{B}}_0 \cdot \nabla \right) \hat{\mathbf{U}} - \left(\hat{\mathbf{U}} \cdot \nabla \right) \hat{\mathbf{B}}_0 \right) + \frac{\eta b}{r^2} \nabla^2 \hat{\mathbf{b}} + \frac{\eta B_0}{r^2} \nabla^2 \hat{\mathbf{B}}_0. \tag{2.10}$$

We seek a dominant balance in the terms, given that we know $B_0 \gg b$. As a consequence, it is clear that the only possible option is to let

$$B_0 \Omega \sim \frac{\eta b}{r^2}, \tag{2.11}$$

from which we may ascertain that

$$b \sim \frac{\Omega r^2}{\eta} B_0 = \mathrm{Rm} B_0. \tag{2.12}$$

This tells us that the magnetic field induced by the flow scales with Rm, which will allow for some simplification in the Navier-Stokes and Induction equations. Indeed, utilising our split $\mathbf{B}$ and the resulting scaling gives

$$\mathrm{Re} \frac{\partial \mathbf{U}}{\partial t} + \mathbf{U} \cdot \nabla \mathbf{U} = -\frac{\nabla p}{\rho} + \nu \nabla^2 \mathbf{U} + \frac{1}{\mu_0 \rho} [\nabla \times (\mathbf{B}_0 + \mathrm{Rm}\mathbf{b}) \times (\mathbf{B}_0 + \mathrm{Rm}\mathbf{b})], \tag{2.13}$$

$$\frac{\partial (\mathbf{B}_0 + \mathrm{Rm}\mathbf{b})}{\partial t} = \eta \nabla^2 (\mathbf{B}_0 + \mathrm{Rm}\mathbf{b}) + \nabla \times [\mathbf{U} \times (\mathbf{B}_0 + \mathrm{Rm}\mathbf{b})], \tag{2.14}$$

In order to yield the inductionless equations, we will take the limit $\mathrm{Rm} \to 0$. However, we must first nondimensionalise. Using our previously defined dimensions, this yields

$$\frac{\partial \mathbf{B}_0 + \mathrm{Rm}\mathbf{b}}{\partial t} = \frac{1}{\mathrm{Rm}}\nabla^2(\mathbf{B}_0 + \mathrm{Rm}\mathbf{b}) + \nabla \times [\mathbf{U} \times (\mathbf{B}_0 + \mathrm{Rm}\mathbf{b})]. \tag{2.15}$$

The factor of $1/\mathrm{Rm}$ is clearly important here, as it cancels on the $\mathbf{b}$ term. Now, taking $\mathrm{Rm} \to 0$ yields the appropriate set of (dimensionless) inductionless equations (assuming that the mean flow $\mathbf{B}_0$ is time-independent, $\partial \mathbf{B}_0/\partial t = 0$, and also that the Laplacian $\nabla^2 \mathbf{B}_0 = 0$)

$$\begin{aligned} \mathrm{Re}\frac{\partial \mathbf{U}}{\partial t} + \mathrm{Re}\mathbf{U} \cdot \nabla \mathbf{U} &= -\frac{\nabla p}{\rho} + \nabla^2 \mathbf{U} + \mathrm{Ha}^2[(\nabla \times \mathbf{b}) \times \mathbf{B}_0], & (2.16) \\ 0 &= \nabla^2 \mathbf{b} + \nabla \times [\mathbf{U} \times \mathbf{B}_0]. & (2.17) \end{aligned}$$

2.2 Spectral methods

In order to solve the Navier-Stokes equations in our flow geometries, we employ a series of spectral methods, developed for popular use (but not incepted) by Orszag (1969). Spectral methods solve the series of differential equations via expressing variables in terms of an expansion on some set of orthogonal basis functions; that is, a given function $f(x)$ defined on the interval (a,b) is expanded as

$$f(x) = \sum_{n=1}^{\infty} a_n \phi_n(x), \tag{2.18}$$

where, given some specific weighting function $w(x)$, the inner product $\langle \phi_n, \phi_m \rangle$ satisfies

$$\int_a^b w(x)\phi_n(x)\phi_m(x)\mathrm{d}x = \delta_{nm}. \tag{2.19}$$

Solving differential equations under these expansions presents many advantages when compared to traditional finite-difference schemes, chiefly that they enable the commutative treatment of derivatives, and that they offer a global solution to the problem, resulting in spectral (exponential) error convergence instead of algebraic error convergence. Of the many spectral implementations, we utilise the collocation method throughout this thesis, as it is both simple to implement and unparalleled if implemented correctly.

2.3 Collocation

The crux of the collocation method is to solve a given set of differential equations at specific collocation points in the domain of the spectral basis functions. The solution at the nodes is then interpolated to be representative of the full domain. One key advantage that collocation presents is that by choosing the correct basis function and collocation points we are able to focus nodes in areas where the solution is the most complicated, whilst providing fewer nodes in areas with more easily resolvable flows. This is beneficial when dealing with complicated boundary flows and conditions. In order to collocate Taylor-Couette and spherical Couette flows we require a series of basis functions for both periodic and aperiodic boundary conditions, which are suited to cylindrical and spherical geometries. Furthermore, we require a series of collocation points that are suitable for each of these choices of basis.

2.3.1 Spectral expansion functions for periodic domains

Fourier expansions

The obvious choice for the spectral representation of periodic functions is in the form of a Fourier series, where the functions are expanded in terms of trigonometric functions as

$$f(x) = \frac{1}{2}a_0 + \sum_{k=1}^{\infty} a_k \cos\left(\frac{2\pi kx}{L}\right) + \sum_{k=1}^{\infty} b_k \sin\left(\frac{2\pi kx}{L}\right). \tag{2.20}$$

Here a_k and b_k are constant coefficients, and L is the periodic lengthscale. Equivalently, and more conveniently, this can be expressed in terms of exponentials as

$$f(x) = a_k \sum_{k=0}^{\infty} e^{2\pi ikx/L}. \tag{2.21}$$

Throughout this thesis, we use the exponential notation for its simplicity, though in practice it is often better to expand on the sinusoidal basis. Of course, the advantage of such basis functions is the ease of differentiation, whereby given some function v, $\partial v/\partial x = (2\pi ik/L)v$.

It should be noted that these expansions are suitable only for periodic domains. Due to the oscillatory nature of the sinusoidal functions, aperiodic features lead to the Gibbs phenomenon, whereby increasing errors are manifested in the immediate vicinity of discontinuities or boundaries. This is a well known limitation of Fourier series expansions, caused by the lack of absolute convergence at the boundaries.

In chapter 4, we typically expand variables with up to $K = 600$ Fourier modes.

2.3.2 Spectral expansion functions for aperiodic domains

Chebyshev polynomials

The Chebyshev polynomials of the first kind – hereby referred to as only Chebyshev polynomials – are defined primarily by the recurrence relationship

$$\begin{aligned} T_0(x) &= 1, \\ T_1(x) &= x, \\ T_{n+1}(x) &= 2xT_n(x) - T_{n-1}(x). \end{aligned}$$

They may be equivalently described via the trigonometric equation

$$T_n(x) = \cos\left(n\cos^{-1}(x)\right), \tag{2.22}$$

and so it is clear that

$$T_n(\cos(\theta)) = \cos(n\theta). \tag{2.23}$$

They are of particular use when approximating functions, due to their clustering of nodes near the radial boundaries, and are valuable in overcoming the Runge phenomena in non-periodic domains. The Runge phenomenon occurs for equispaced grid points and results from high order polynomials producing increasingly large errors near the boundary, similar to the Gibbs phenomenon. Chebyshev polynomial expansions and their appropriate choice of nodes guarantee that solutions are absolutely convergent. Indeed, it can be found that expansion via Chebyshev polynomials can lead to a near minimax approximation (maximum error is minimised).

In spectral methods it is common to collocate with nodes located at either the zeros of the polynomials (Gauss-Chebyshev points) or their extrema (Gauss-Lobatto points), given respectively via

$$x = \cos\left(\frac{(2k-1)\pi}{2n}\right) \text{ for } k = 1, \ldots, n,$$
$$x = \cos\left(\frac{k\pi}{n}\right) \text{ for } k = 0, \ldots, n.$$

Note that the Gauss-Lobatto points naturally contain the boundary values, whilst the Gauss-Chebyshev points do not. If we plot the roots and extrema, it is obvious as to why the Chebyshev polynomials are of particular use for boundary layer problems. Taking $n = 20$ In figure 2.1, the roots and extrema are found to be at the equidistantly spaced angles θ of the unit semi-circle. As a consequence of the curvature of the semi-circle, projecting these onto the domain $x \in [-1, 1]$ clearly shows that the nodes are unevenly distributed towards the boundaries of the domain. As the polynomials are only defined over $x \in [-1, 1]$, in order to expand functions with a Chebyshev basis, an affine transformation of variables onto that range is required.

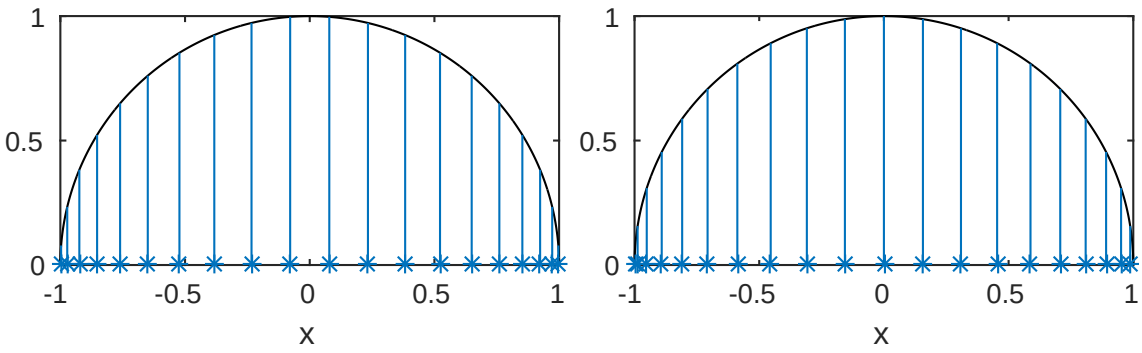

Figure 2.1: Sample plots of the Chebyshev roots and extrema, respectively.

The derivatives of Chebyshev polynomials $\partial T_n(x)/\partial x$, may be obtained in a variety of ways. It is simplest to obtain an expression for the integral of a Chebyshev sum, and then differentiate this. For further details, we refer to the procedure given in the text (Mason & Handscomb, 2002).

Typical Chebyshev expansions in chapters 3, 4 and 5 consist of $N = 30, 50$, and 20 polynomials, respectively.

Associated Legendre polynomials

In order to utilise spectral methods in spherical geometry we require a set of orthogonal basis functions in which to expand. Of course, the obvious choice in spherical coordinates are the spherical harmonics, a series of associated Legendre polynomials that are the eigenfunction of the Laplacian operator. Indeed, these may be derived by using separation of variables to solve Laplace's equation on the surface of a sphere. Laplace's equation states that

$$\nabla^2 f = \frac{1}{r^2}\frac{\partial}{\partial r}\left(r^2\frac{\partial f}{\partial r}\right) + \frac{1}{r^2\sin\theta}\frac{\partial}{\partial\theta}\left(\sin\theta\frac{\partial f}{\partial\theta}\right) + \frac{1}{r^2\sin^2\theta}\frac{\partial^2 f}{\partial\phi^2}. \tag{2.24}$$

Now let us apply separation of variables so that $f = R(r)Y(\theta,\phi)$. We may rearrange to obtain

$$\frac{1}{R}\frac{\partial}{\partial r}\left(r^2\frac{\partial R}{\partial r}\right) = -\frac{1}{Y}\left(\frac{1}{\sin\theta}\frac{\partial}{\partial\theta}\left(\sin\theta\frac{\partial Y}{\partial\theta}\right) + \frac{1}{\sin^2\theta}\frac{\partial^2 Y}{\partial\phi^2}\right). \tag{2.25}$$

On the left hand side there is no Y dependence whilst on the right hand side there is no R dependence, therefore we may let both equal some constant, λ, say. In constructing spherical harmonics we are concerned only with the angular part of this equation, and so neglect the radial solution from herein. Thus, we have

$$\frac{1}{Y\sin\theta}\frac{\partial}{\partial\theta}\left(\sin\theta\frac{\partial Y}{\partial\theta}\right) + \frac{1}{Y\sin^2\theta}\frac{\partial^2 Y}{\partial\phi^2} = -\lambda. \tag{2.26}$$

Once more separating into the angular variables, $Y = \Theta(\theta)\Phi(\phi)$, we may rearrange to give

$$\frac{\sin\theta}{\Theta}\frac{\partial}{\partial\theta}\left(\sin\theta\frac{\partial\Theta}{\partial\theta}\right) + \lambda\sin^2\theta = -\frac{1}{\Phi}\frac{\partial^2\Phi}{\partial\phi^2}, \tag{2.27}$$

for which we can see that, in general, $\frac{1}{\Phi}\frac{\partial^2\Phi}{\partial\phi^2} = -m^2$, another constant. However, as we are interested only in axisymmetric solutions, we can go further in stating that m=0.

Finally, we let $\lambda = l(l+1)$ in order to satisfy regularity conditions at the poles and ensure 2π periodicity in ϕ (Courant & Hilbert, 2008), and expand, and so are left with

$$\frac{\partial^2\Theta}{\partial\theta^2} + \cot\theta\frac{\partial\Theta}{\partial\theta} + \left(l(l+1) - \frac{m^2}{\sin^2\theta}\right) = 0. \tag{2.28}$$

The solutions to this equation are the associated Legendre polynomials,

$$P_l^m(\cos\theta) = (\sin\theta)^m \frac{\mathrm{d}^m}{\mathrm{d}(\cos\theta)^m} P_l(\cos\theta) \tag{2.29}$$

Here we have omitted the Condon-Shortley phase, $(-1)^m$, as it has no impact on the orthogonality of the polynomials and therefore serves only to further complicate the equations. The polynomials are eigenfunctions of the axisymmetric Laplacian operator, $\nabla^2 P_l^m = l(l+1)P_l^m$.

In chapter 5, variables are typically expanded in terms of $L = 1000$ associated Legendre polynomials.

Orthonormalised associated Legendre polynomials

A problem that occurs when expanding in standard associated Legendre polynomials is that they involve increasingly large multiplicative factors. Indeed, at even moderate resolutions ($l \approx 250$) we find that the magnitude of the coefficients is large enough to compromise computational accuracy. We therefore employ a suitable orthonormalisation of the associated Legendre polynomials to bypass this. I.e., we expand in terms of associated Legendre polynomials of the form

$$Y_l^m = Q_l^m P_l^m, \tag{2.30}$$

with some orthonormalisation factor Q_l^m. As we are only interested in axisymmetric spherical geometry, instead of the full spherical harmonics normalisation it is natural to make use of the so-called '4π' normalisation,

$$Q_l^m = \sqrt{2l+1}\frac{\sqrt{(l-m)!}}{\sqrt{(l+m)!}}, \tag{2.31}$$

as we have not introduced the factor 2π in integrating over the azimuthal direction. Of course, the choice of normalisation factor does not affect the orthogonality of the polynomials, and they are an equally valid choice of basis.

The various Y_l^m are now defined as

$$Y_1^0 = \sqrt{3}\cos\theta \tag{2.32}$$

$$Y_2^1 = 3\sqrt{\frac{5}{6}}\cos\theta\sin\theta \qquad \text{etc.} \tag{2.33}$$

2.4 Time-stepping

In chapters 4 and 5, in order to analyse the behaviour of Taylor-Couette and spherical Couette flows, respectively, we require a method of advancing the fully nonlinear Navier-Stokes and induction equations forward in time. This is achieved via a Crank-Nicolson time-stepping scheme, based upon that used by Hollerbach (2000b).

As the flows in both of chapters 4 and 5 are axisymmetric, we use the previously discussed toroidal-poloidal expansion to express our velocity and magnetic fields as

$$\mathbf{U} = v\,\mathbf{e}_\phi + \nabla \times (\psi\,\mathbf{e}_\phi) \qquad\qquad \mathbf{B} = b\,\mathbf{e}_\phi + \nabla \times (a\,\mathbf{e}_\phi).$$

So, as we have four variables for which to solve, in both chapters we choose to solve the following four equations: the ϕ component of the Navier-Stokes equation and its curl, as well as the ϕ component of the induction equation and its vector potential. Three of these equations can be restated simply in the form

$$\left(A\frac{\partial}{\partial t} - D^2\right) = [\text{nonlinear terms}]_\phi,$$

with $A = 1$ for the Navier-Stokes equations and $A = 0$ for the induction equations. We use the notation D^2 for the ϕ component of the Laplacian operator, such that

$$D^2 = \frac{\partial^2}{\partial r^2} + \frac{1}{r}\frac{\partial}{\partial r} - \frac{1}{r^2} + \frac{\partial^2}{\partial z^2}, \tag{2.34}$$

in cylindrical geometry, or

$$D^2 = \frac{\partial^2}{\partial r^2} + \frac{2}{r}\frac{\partial}{\partial r} - \frac{l(l+1)}{r^2}, \tag{2.35}$$

in spherical geometry. However, more thought has to be given to the curl of the Navier-Stokes equation. We have that

$$\left[\frac{\partial(\nabla \times \mathbf{U})}{\partial t} - \nabla \times \nabla^2\mathbf{U}\right]_\phi = [\nabla \times [\text{nonlinear terms}]]_\phi.$$

Here,

$$\begin{aligned}
[\nabla \times \mathbf{U}]_\phi &= [\nabla \times (v\,\mathbf{e}_\phi + \nabla \times (\psi\,\mathbf{e}_\phi))]_\phi, \\
&= \nabla \times (\nabla \times (\psi\,\mathbf{e}_\phi)), \\
&= \nabla(\nabla \cdot (\psi\,\mathbf{e}_\phi) - \nabla^2(\psi\,\mathbf{e}_\phi), \\
&= -D^2\psi,
\end{aligned} \tag{2.36}$$

from the definition of the vector Laplacian. Also

$$\begin{aligned}
\nabla \times (\nabla^2(v\,\mathbf{e}_\phi + \nabla \times (\psi\,\mathbf{e}_\phi))) &= [\nabla \times \nabla(\nabla \cdot (v\,\mathbf{e}_\phi + \nabla \times (\psi\,\mathbf{e}_\phi))), \\
&\quad -\nabla \times \nabla \times \nabla \times (v\,\mathbf{e}_\phi + \nabla \times (\psi\,\mathbf{e}_\phi))]_\phi, \\
&= -\nabla \times \nabla \times \nabla^2(\psi\,\mathbf{e}_\phi), \\
&= -\nabla(\nabla \times \nabla^2(\psi\,\mathbf{e}_\phi)) - \nabla^2(-\nabla^2(\psi\,\mathbf{e}_\phi)). \\
&= D^4\psi. \qquad (2.37)
\end{aligned}$$

Hence, our four governing equations can be written concisely in the form

$$\left(\frac{\partial}{\partial t} - D^2\right) v = \mathbf{e}_\phi \cdot \mathbf{F} \qquad (2.38)$$

$$-\left(\frac{\partial}{\partial t} - D^2\right) D^2\psi = \mathbf{e}_\phi \cdot \nabla \times \mathbf{F} \qquad (2.39)$$

$$-D^2 a = \mathbf{e}_\phi \cdot \mathbf{F}' \qquad (2.40)$$

$$-D^2 b = \mathbf{e}_\phi \cdot \nabla \times \mathbf{F}', \qquad (2.41)$$

Here $\mathbf{F}$ and $\mathbf{F}'$ are arrays containing the respective nonlinear terms from the Navier-Stokes and induction equations,

$$\mathbf{F} = -\mathbf{U} \cdot \nabla\mathbf{U} + (\nabla \times \mathbf{B}) \times \mathbf{B}_0 \qquad (2.42)$$

$$\mathbf{F}' = \mathbf{U} \times \mathbf{B}_0. \qquad (2.43)$$

for inductionless fluid, or

$$\mathbf{F} = -\mathbf{U} \cdot \nabla\mathbf{U} + (\nabla \times \mathbf{B}) \times \mathbf{B}_0 + (\nabla \times \mathbf{B}) \times \mathbf{B} \qquad (2.44)$$

$$\mathbf{F}' = \mathbf{U} \times \mathbf{B}_0 + \mathbf{U} \times \mathbf{B}. \qquad (2.45)$$

otherwise.

2.4.1 Crank-Nicolson scheme

To evolve the equations forward in time, we use a second order Runge-Kutta method; a modified semi-implicit Crank-Nicolson predictor-corrector scheme. When considering the low Rm limit, as in chapters 4 and 5, the induction equation is time-independent so we need only time-step the Navier-Stokes equations. The magnetic

field variables are instead evolved by solving the induction equation. If the full Navier-Stokes equations are used, as in section (4.4), we must time-step both the velocity and magnetic fields. The method proceeds in two steps: an initial guess for the nonlinear forcing terms is computed using the flow coefficients at a given time, then the equations are time-stepped. The nonlinear forcing terms are then recomputed using the new flow variables, and the equations are solved once more to refine the time-stepped variables. The flow variables at the new time-step are then taken to be an average of the predictor and corrector steps.

Standard finite difference methods, such as the basic forward difference scheme, are generally explicit. Whilst we could solve them in a fairly straightforward manner, the problem is that the ratio of the size of the chosen time-step to the square of the step size must be small to ensure stability. This is unsuitable if one wants to take moderate time-steps. The Crank-Nicolson scheme, centred about $t + \Delta t/2$, instead evaluates variables semi-implicitly as an average between time-steps; i.e., for the variable v we have

$$v = \frac{v^{m+1} + v^m}{2}. \tag{2.46}$$

So, this allows us to obtain the benefits to stability that are possessed by implicit schemes, without sacrificing the accuracy of the explicit scheme. Based on the observations of Hollerbach (2000b) that this weighting between explicit and implicit can in fact be unstable for the HMRI, in chapter 4 we use the modified scheme

$$v = 0.6v^{m+1} + 0.4v^m \tag{2.47}$$

instead, which is entirely stable. Derivatives are still handled by forward differences in the standard fashion;

$$\frac{\partial v}{\partial t} = \frac{v^{m+1} - v^m}{\Delta t}. \tag{2.48}$$

Thus, our governing equations are discretised to

$$\mathrm{Re}\frac{v^{m+1} - v^m}{\Delta t} - D^2\left(0.6v^{m+1} + 0.4v^m\right) = DV, \tag{2.49}$$

(with DV the spectral coefficients of the nonlinear forcing terms $\mathbf{F}$), which we can rearrange to yield

$$\left(\mathrm{Re} - 0.6\Delta t\right) v^{m+1} = \left(\mathrm{Re} + 0.4\Delta t\right) v^m + \Delta t DV. \tag{2.50}$$

We solve this alongside the two equations for the boundary conditions, then, given our estimate for v^{n+1}, we recalculate the spectral coefficients of the forcing, say as DV', and take an average in the corrector step,

$$(\mathrm{Re} - 0.6\Delta t)\, v^{m+1} = (\mathrm{Re} + 0.4\Delta t)\, v^m + \Delta t \frac{(DV + DV')}{2}. \tag{2.51}$$

Matrix-vector notation

Considering how the collocation method is implemented in these equations, it is beneficial to reformulate them in terms of matrix-vector notation, corresponding in practice to various numerical arrays. The detail is similar for each variable, so we choose only to discuss the scheme for v. So, we have

$$\mathbf{X}_v \mathbf{v}^{m+1} = \mathbf{Y}_v \mathbf{v}^m + \Delta t \mathbf{DV} \tag{2.52}$$

$$\mathbf{X}_v \mathbf{v}^{m+1} = \mathbf{Y}_v \mathbf{v}^m + \Delta t \frac{\mathbf{(DV+DV')}}{2} \tag{2.53}$$

where $\mathbf{X}_v$ and $\mathbf{Y}_v$ are $(N+2)\times(N+2)$ arrays containing the operations on $\mathbf{v}^{m+1}$ and $\mathbf{v}^m$ respectively, with the last two rows of $\mathbf{X}_v$ implementing the boundary conditions. Thus, for the first N rows

$$X_{v,jn} = \left(Re - 0.6\Delta t D^2\right) T_{n-1}(x_j), \tag{2.54}$$

$$Y_{v,jn} = \left(Re + 0.4\Delta t D^2\right) T_{n-1}(x_j), \tag{2.55}$$

in addition to

$$\mathbf{X}_{v,N+1\,n} = (-1)^n, \tag{2.56}$$

$$\mathbf{X}_{v,N+2\,n} = 1, \tag{2.57}$$

$$\mathbf{Y}_{v,N+1\,n} = \mathbf{Y}_{v,N+2\,n} = 0. \tag{2.58}$$

Here, $\mathbf{v}^m$ is the vector of the spectral coefficients of v at time-step m,

$$\mathbf{v} = \left[v_1^m, v_2^m, \ \ldots\ , v_{N+2}^m\right], \tag{2.59}$$

and **DV** and **DV'** are the spectral coefficients of the nonlinear forcing terms, also implementing the right hand sides of the boundary conditions (here identically zero), given by,

$$\mathbf{DV} = [DV_1, DV_2, \ \ldots\ , DV_N, 0, 0], \tag{2.60}$$

and similarly for **DV'**.

Note that, whilst it is possible to compute the equations in this way, we can further increase the efficiency of the code by pre-multiplying by $\mathbf{X}_v^{-1}$ to yield

$$\mathbf{v}^{m+1} = \mathbf{X}_v^{-1}\mathbf{Y}_v\mathbf{v}^m + \Delta t\mathbf{X}_v^{-1}\mathbf{DV}, \tag{2.61}$$

$$\mathbf{v}^{m+1} = \mathbf{X}_v^{-1}\mathbf{Y}_v\mathbf{v}^m + \Delta t\mathbf{X}_v^{-1}\frac{\mathbf{(DV+DV')}}{2}. \tag{2.62}$$

As the matrices $\mathbf{X}_v$ and $\mathbf{Y}_v$ are invariant over time, we can pre-compute the matrices $\mathbf{X}_v^{-1}\mathbf{Y}_v$ and $\Delta t\mathbf{X}_v^{-1}$, such that the only matrix operations that are computed on the fly at each time-step are of those applied to $\mathbf{v}^m$ and $\mathbf{DV}$. We calculate $\mathbf{X}_v^{-1}$ via solving the linear system of equations $\mathbf{X}_v\mathbf{X}_v^{-1} = \mathbf{I}$ using NAG routine F04AEF, which utilises a LU decomposition method. Taking an LU decomposition is more efficient than explicitly finding the inverse.

So, put simply, our method requires the calculation of the matrices $\mathbf{X}_v^{-1}\mathbf{Y}_v$ and $\Delta t\mathbf{X}_v^{-1}$ only, to be applied to the spectral coefficients $\mathbf{v}$ and nonlinear coefficients at each time-step as in the predictor corrector scheme.

2.5 Pseudo-spectral method

An integral part of the time-stepping procedure is the twice-per-step evaluation of nonlinear terms. This presents a problem though, as our spectral method does not allow for the simple treatment of vector algebra; though the collocation method and its utilisation of spectral expansions have so far provided a more effective way to treat our numerics, the operations involved in the nonlinear terms can more easily be performed in real space. Thus, in order to time-step the Navier-Stokes and induction equations efficiently we utilise a pseudo-spectral method. Pseudo-spectral methods are not strictly confined to spectral space, and take advantage of relatively cheap transformations to swap between spectral and real-space representations depending on which is most efficient. As such, our standard pseudo-spectral method involves transforming to real space to perform the vector algebra involved in the nonlinear terms, before re-expanding in terms of the spectral basis functions in order to

time-step the variables. Throughout this thesis we use variations on this pseudo-spectral method depending on which geometry the equations are being solved for. As such, the details of the nonlinear terms, and the various transforms, are described separately. The Chebyshev transforms are employed in both sections.

2.5.1 Chebyshev transforms

In our Taylor-Couette and spherical Couette applications it turns out that the structures produced in the radial direction are relatively uncomplicated compared to the z (Taylor-Couette) or θ (spherical Couette) directions. Thus, when expanding in terms of Chebyshev polynomials, we do not require excessive resolution. As a consequence, we are able to transform between configuration and spectral space representations via matrix multiplication, even though such operations scale as $\mathcal{O}(N^3)$.

Recall that we have expansions of the form $v_j = \sum_{n=1}^{N} v_n T_{n-1}(x_j)$, at the j_{th} collocation point. Transforming the spectral coefficients to the real space variable is achieved by performing the matrix multiplication

$$\mathbf{v}_j = \mathbf{T}\mathbf{v}_n, \tag{2.63}$$

with the matrix $T_{jn} = T_{n-1}(x_j)$. Similarly, any differentiation, or multiplications involving the radius, can be applied at this stage, i.e.

$$\frac{1}{r}\frac{\partial \mathbf{v}_j}{\partial r} = \left(\frac{1}{r}\frac{\partial}{\partial r}\mathbf{T}\right)\mathbf{v}_n. \tag{2.64}$$

Re-expanding in terms of spectral coefficients is then just a matter of inverting the Chebyshev operator,

$$\mathbf{v}_n = \mathbf{T}^{-1}\mathbf{v}_j, \tag{2.65}$$

where $\mathbf{T}^{-1}$ is time independent and is trivially applied.

Transforming via matrix multiplication allows for greater efficiency in some of the operations in spectral space. If, for example, one is required to differentiate immediately *after* transforming from real to spectral space, the standard procedure would be to take

$$v_n = \mathbf{T}^{-1}(\mathbf{T}'(\mathbf{T}^{-1}v_j)). \tag{2.66}$$

However, it is clear that the matrices can be simplified to a single multiplication of $\mathbf{T}_1 = \mathbf{T}^{-1}\mathbf{T}'\mathbf{T}^{-1}$, which performs the differentiation for free during the transform.

2.5.2 Cylindrical coordinates

In cylindrical geometry, we expand our variables in space via a Fourier-Chebyshev expansion scheme based upon that detailed in Hollerbach (2008), and use the relevant methods and transforms detailed in Boyd (2001); Canuto *et al.* (2007); Hollerbach (2000b) to deal with the nonlinear terms in the Navier-Stokes and induction equations.

We first express the flow and magnetic field variables in terms of our spectral expansion functions. Radially, we expand in terms of Chebyshev polynomials, which eliminate the Gibbs and Runge phenomena for the aperiodic boundaries, and weight the nodes about the inner and outer cylinder walls to ensure satisfactory resolution of complicated boundary structure. For the axial expansion, recall that we have assumed that the cylinders are of infinite height. Therefore, it follows that over some length-scale significantly longer than the wavelength of the instability, the axial structure of the variables is periodic. The scale here is arbitrary, so we choose $z_0 = 40$, much larger than a single wavelength of the HMRI. For periodic boundary conditions we have no Gibbs phenomena to contend with, nor do we need to focus nodes at irregular points, so we take a Fourier expansion using uniformly spaced nodes. Therefore, expanding up to K modes in z and $N+2$ radial modes ($N+4$ for ψ to incorporate the additional two boundary conditions), we may write

$$v = \sum_{n=1}^{N+2}\sum_{k=0}^{K} v_{kn} e^{i\kappa z} T_{n-1}(x), \qquad \psi = \sum_{n=1}^{N+4}\sum_{k=0}^{K} \psi_{kn} e^{i\kappa z} T_{n-1}(x), \tag{2.67}$$

$$a = \sum_{n=1}^{N+2}\sum_{k=0}^{K} a_{kn} e^{i\kappa z} T_{n-1}(x), \qquad b = \sum_{n=1}^{N+2}\sum_{k=0}^{K} b_{kn} e^{i\kappa z} T_{n-1}(x), \tag{2.68}$$

where $\kappa = 2\pi k/z_0$ and $x = 2r/(r_o - r_i) - (r_o + r_i)/(r_o - r_i)$. Practically, we express the Fourier series in terms of sines and cosines, as this is more efficient when performing the Fourier transform (see section 2.5.2).

Using the spectral expansion functions, the no-slip boundary conditions become,

$$v_0 = r_i\Omega_i, \quad v_1 = v_2 = ... = 0, \quad \psi_k = 0, \quad \frac{\partial \psi_k}{\partial r} = 0 \tag{2.69}$$

$$v_0 = r_o\Omega_o, \quad v_1 = v_2 = ... = 0, \quad \psi_k = 0, \quad \frac{\partial \psi_k}{\partial r} = 0 \tag{2.70}$$

at the $r = r_i$ and $r = r_o$ boundaries respectively. Furthermore, the perfectly conducting boundary conditions become

$$a_k = 0, \quad \frac{b_0}{r_i} = 0, \quad \frac{b_{k\neq 0}}{r_i} + \frac{\partial b_{k\neq 0}}{\partial r} = 0 \tag{2.71}$$

$$a_k = 0, \quad \frac{b_k}{r_o} + \frac{\partial b_k}{\partial r} = 0 \tag{2.72}$$

at $r = r_i$ and $r = r_o$ respectively.

Fast Fourier transform

In order to transform between Fourier coefficients and real space values, we employ the Fourier transform. More precisely, in order to be maximally efficient, we use the fast Fourier transform (FFT). Before we detail the nonlinear terms then, we briefly introduce the FFT as well as the concept of aliasing.

We consider a periodic function F, expanded into K modes and sampled at K points, each with value F_n. The Fourier transform allows us to obtain values of F_n given the spectral coefficients f_k,

$$F_n = \sum_{k=0}^{K} f_k e^{\frac{-2i\pi kn}{K+1}}. \tag{2.73}$$

The inverse transform, which yields the coefficients f_k given data at the sampling points F_k, is

$$f_k = \frac{1}{K+1} \sum_{k=0}^{K} F_n e^{\frac{2i\pi kn}{K+1}}. \tag{2.74}$$

This may be derived by approximating the standard integral for finding Fourier coefficients with a trapezoidal quadrature (which is exact for trapezoidal functions). Here, instead of an infinite Fourier series we have necessarily truncated our expansions at some finite number of modes; in practice it is important to choose a resolution such that the flow is sufficiently resolved.

If we were to naively apply the Fourier transform as is, we would find that the effort taken scales as $\mathcal{O}(K^2)$, due to the various matrix multiplications involved. This, however, is prohibitive for suitably large spectral truncations, though in practice is negated by the existence of the fast Fourier transform. Based on an algorithm known as long ago as Gauss (Heideman *et al.*, 1985), the FFT algorithm – developed for modern use by Cooley & Tukey (1965) – reduces the computational scaling to $\mathcal{O}(K \log_2(K))$, giving a marked numerical advantage. There are numerous commercially available FFT packages (FFTW, NAG etc.), of which we use FFTPACK (Swarztrauber, 1982), an efficient FFT routine for Fortran that expresses the Fourier series in terms of sines and cosines (via Euler's formula).

Aliasing

Before we apply the FFT, we must account for any possible aliasing that may occur. Aliasing errors result from sinusoidal functions, such as our Fourier basis, when they are sampled on a finite grid; a higher order harmonic could be observed as a lower order harmonic if sampled at an insufficient number of grid points.

Take for example the functions $\sin(x)$ and $\sin(15x)$ in figure 2.2, each sampled over eight points in the interval $[0, \pi]$. It can clearly be seen that the sampling points

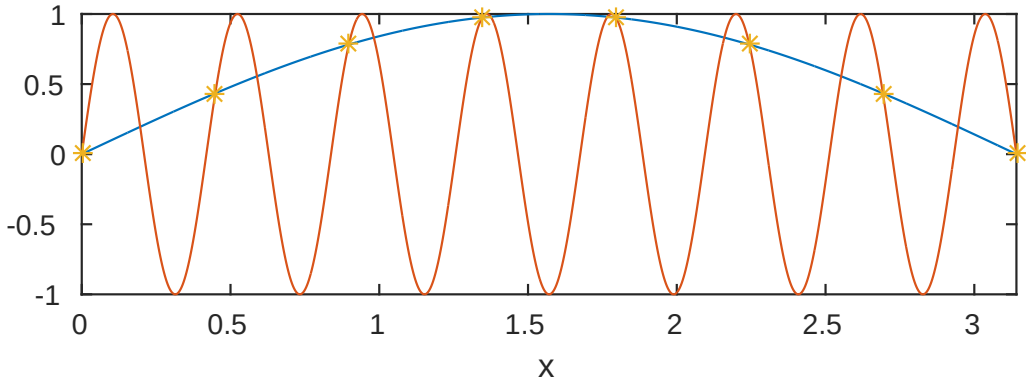

Figure 2.2: Aliasing as observed between $\sin(x)$ and $\sin(15x)$. At the sampled grid points the two harmonics are indistinguishable.

are in fact the same for both functions, and therefore both functions would have equivalent spectral coefficients. In our equations, the nonlinear terms may produce

a Fourier mode higher than accounted for in our expansion. This would then be aliased onto a lower mode inside our basis, causing spurious values. There are a number of ways in which one can solve the problem of aliasing, discussed in Boyd (2001), originating with the method of Phillips (1959) whereby a larger than required spectral expansion is utilised, and the upper half of the spectra is filtered out before the Fourier transform, i.e. the upper half of the spectral coefficients are set to equal zero. Orszag (1971) showed this to be inefficient, with his two-thirds rule – now the de-facto anti-aliasing solution – requiring only the upper third of modes to be filtered. As we wish to keep our modes unfiltered, this is essentially equivalent to (and often expressed as) the three-halves rule, whereby instead $(3/2)K$ sample points are used, necessitating a padding of the spectral coefficients with zeros (up to $K/2$ modes).

Nonlinear terms

For inductionless fluids under the quasi-static approximation, the calculation of nonlinear terms is achieved in two distinct steps: first, magnetic field variables are updated to the current time step via solving the induction equation, then these updated variables are used to calculate the nonlinear terms in the Navier-Stokes equations. This is necessary as our induction equations do not have explicit time dependence with which to evolve the magnetic field. If the fluid was not inductionless, and the full Navier-Stokes and induction equations were used, all nonlinear terms would be evaluated concurrently.

To update b and a, we rearrange equations 2.40 and 2.41 and solve

$$-D^2 a = \mathbf{U} \times \mathbf{B}_0, \tag{2.75}$$

$$-D^2 b = \nabla \times (\mathbf{U} \times \mathbf{B}_0)\,. \tag{2.76}$$

To do so, we require arrays of the various components of $\mathbf{U} \times \mathbf{B}_0$ and $\nabla \times (\mathbf{U} \times \mathbf{B}_0)$ evaluated at the collocation points. Recall that,

$$\mathbf{U} = \left(-\frac{\partial \psi}{\partial z}, v, \frac{\partial \psi}{\partial r}\right) \qquad \mathbf{B} = \left(-\frac{\partial a}{\partial z}, b, \frac{\partial a}{\partial r}\right) \tag{2.77}$$

Here derivatives are trivially obtained, acting either upon $e^{i\kappa z}$ or the Chebyshev polynomials. As such radial derivatives are best performed during the transformations to and from real space. It should be noted that all FFTs are performed whilst variables are still expanded in terms of Chebyshev polynomials, as there are far fewer spectral modes than radial grid points. This minimises the computational effort on what is the most expensive operation in our routine.

So, if we denote the FFT as $\mathcal{F}\{\}$ and let the index i denote axial grid points; we obtain in real space

$$[U_r]_{ji} = \sum_{n=1}^{N+4} \mathcal{F}\left\{-i\kappa\psi_{nk}\right\} T_{n-1}(x_j), \tag{2.78}$$

$$[U_\phi]_{ji} = \sum_{n=1}^{N+4} \mathcal{F}\left\{\psi_{nk}\right\} T_{n-1}(x_j), \tag{2.79}$$

$$[U_z]_{ji} = \sum_{n=1}^{N+4} \mathcal{F}\left\{\psi_{nk}\right\} T'_{n-1}(x_j). \tag{2.80}$$

Then, we have that

$$[(\mathbf{U}\times\mathbf{B}_0)_r]_{ji} = [U_\phi]_{ji}\cdot[B_{0\,z}]_j - [U_z]_{ji}\cdot[B_{0\,\phi}]_j, \tag{2.81}$$

$$[(\mathbf{U}\times\mathbf{B}_0)_\phi]_{ji} = -[U_r]_{ji}\cdot[B_{0\,z}]_j, \tag{2.82}$$

$$[(\mathbf{U}\times\mathbf{B}_0)_z]_{ji} = [U_r]_{ji}\cdot[B_{0\,\phi}]_j. \tag{2.83}$$

If we collocate at I axial grid points, for example, then transforming these quantities back into spectral space yields the coefficients of $[\mathbf{U}\times\mathbf{B}_0]_\phi$,

$$[(\mathbf{U}\times\mathbf{B}_0)_\phi]_{nk} = \mathcal{F}^{-1}\left\{\sum_{i=1}^{I}[(\mathbf{U}\times\mathbf{B}_0)_\phi]_{ji}\mathbf{T}^{-1}\right\}. \tag{2.84}$$

We further need $\nabla\times(\mathbf{U}\times\mathbf{B}_0) = \partial/\partial z[\mathbf{U}\times\mathbf{B}_0]_r - \partial/\partial r[\mathbf{U}\times\mathbf{B}_0]_z$, so require expressions for the spectral coefficients

$$[(\mathbf{U}\times\mathbf{B}_0)_r]_{nk} = \mathcal{F}^{-1}\left\{\sum_{i=1}^{I}[(\mathbf{U}\times\mathbf{B}_0]_r)_{ji}\mathbf{T}^{-1}\right\}, \tag{2.85}$$

$$\frac{\partial}{\partial r}[(\mathbf{U}\times\mathbf{B}_0)_z]_{nk} = \mathcal{F}^{-1}\left\{\sum_{i=1}^{I}[(\mathbf{U}\times\mathbf{B}_0]_z)_{ji}\mathbf{T}_1^{-1}\right\}. \tag{2.86}$$

Note again that we perform the FFT in Chebyshev space to minimise the computational effort, and that we express $\mathbf{T}_1^{-1} = \mathbf{T}^{-1}\mathbf{T}'\mathbf{T}^{-1}$. Hence, we find the spectral

coefficients,

$$DA_{nk} = [(\mathbf{U} \times \mathbf{B}_0)_\phi]_{nk}, \tag{2.87}$$

$$DB_{nk} = i\kappa[(\mathbf{U} \times \mathbf{B}_0)_r]_{nk} - \frac{\partial}{\partial r}[(\mathbf{U} \times \mathbf{B}_0)_z]_{nk} \tag{2.88}$$

The variables a and b are updated to the current time-step using analogues of the precomputed arrays discussed previously:

$$\mathbf{a}^m = \mathbf{X}_a^{-1}\mathbf{DA}, \tag{2.89}$$

$$\mathbf{b}^m = \mathbf{X}_b^{-1}\mathbf{DB}. \tag{2.90}$$

With these new coefficients for a and b, we then calculate the nonlinearities in the Navier-Stokes equation. Recall that we require spectral coefficients for $[F_\phi]$ and $[\nabla \times \mathbf{F}]_\phi$, where

$$\mathbf{F} = \mathrm{Re}[\mathbf{U} \times \nabla \times \mathbf{U}] + \mathrm{Ha}^2[(\nabla \times \mathbf{B}) \times \mathbf{B}_0] \tag{2.91}$$

Real space arrays for the components of $\nabla \times \mathbf{U}$ may be obtained by using the various transforms in a similar fashion as before.

$$[(\nabla \times \mathbf{U})_r]_{ji} = \sum_{n=1}^{N+4} \mathcal{F}\left\{-i\kappa v_{nk}\right\} T_{n-1}(x_j), \tag{2.92}$$

$$[(\nabla \times \mathbf{U})_\phi]_{ji} = \sum_{n=1}^{N+4} \left(\mathcal{F}\left\{-\psi_{nk}\right\} T''_{n-1}(x_j) + \mathcal{F}\left\{-\kappa^2\psi_{nk}\right\} T_{n-1}(x_j)\right), \tag{2.93}$$

$$[(\nabla \times \mathbf{U})_z]_{ji} = \sum_{n=1}^{N+4} \mathcal{F}\left\{v_{nk}\right\} T'_{n-1}(x_j). \tag{2.94}$$

Clearly, $\nabla \times \mathbf{B}$ is the same, with v and ψ replaced with the magnetic field variables b and a, respectively. The real-space nonlinear terms are thus

$$\begin{aligned}[F_r]_{ji} = \mathrm{Re}\,&([U_\phi]_{ji} \cdot [(\nabla \times \mathbf{U})_z]_{ji} - [U_z]_{ji} \cdot [(\nabla \times \mathbf{U})_\phi]_{ji}) \\ &+ \mathrm{Ha}^2\left(([\nabla \times \mathbf{B})_\phi]_{ji} \cdot [B_{0\,z}]_j - [(\nabla \times \mathbf{B})_z]_{ji} \cdot [B_{0\,\phi}]_j\right),\end{aligned} \tag{2.95}$$

$$\begin{aligned}[F_\phi]_{ji} = \mathrm{Re}\,&([U_z]_{ji} \cdot [(\nabla \times \mathbf{U})_r]_{ji} - [U_r]_{ji} \cdot [(\nabla \times \mathbf{U})_z]_{ji}) \\ &+ \mathrm{Ha}^2\left(-[(\nabla \times \mathbf{B})_r]_{ji} \cdot [B_{0\,z}]_j\right),\end{aligned} \tag{2.96}$$

$$\begin{aligned}[F_z]_{ji} = \mathrm{Re}\,&([U_r]_{ji} \cdot [(\nabla \times \mathbf{U})_\phi]_{ji} - [U_\phi]_{ji} \cdot [(\nabla \times \mathbf{U})_r]_{ji}) \\ &+ \mathrm{Ha}^2\left(([\nabla \times \mathbf{B})_r]_{ji} \cdot [B_{0\,\phi}]_j\right).\end{aligned} \tag{2.97}$$

To transform the ϕ component of $\mathbf{F}$ back to spectral space, we have the coefficients

$$[F_\phi]_{nk} = \mathcal{F}^{-1}\left\{\sum_{i=1}^{I}[F_\phi]_{ji}\mathbf{T}^{-1}\right\}. \tag{2.98}$$

Exactly as in equations (2.85) and (2.86), we may evaluate the spectral coefficients of $[\nabla \times \mathbf{F}]_\phi$, eventually leading to the result

$$DV_{nk} = [F_\phi]_{nk}, \tag{2.99}$$

$$DP_{nk} = i\kappa[F_r]_{nk} - \frac{\partial}{\partial z}[F_z]_{nk}. \tag{2.100}$$

These spectral coefficients can then be then utilised in the time-stepping algorithm given in section 2.4.1.

2.5.3 Spherical coordinates

In spherical geometry, we expand our variables in a Legendre-Chebyshev scheme. We proceed using exactly the same method as in the previous sections, though the boundary curvature and spherical co-ordinates add additional complications.

We expand our variables in terms of L normalised associated Legendre polynomials,

$$v = \sum_{l=1}^{\infty} v_l(r)Y_l^1(\cos\theta), \qquad \psi = \sum_{l=1}^{\infty} \psi_l(r)Y_l^1(\cos\theta). \tag{2.101}$$

We further expand in the radial direction in $N+4$ Chebyshev polynomials, but for the time being do not explicitly express this, in order to simplify notation. Here, as we are concerned only with narrow-gap solutions, $N \ll L$. Note that any $'$ notation refers to differentiation in the radial direction with respect to r.

In terms of these spectral expansion functions, the no-slip boundary conditions, $\mathbf{U} = \Omega_{i,o} r_{i,o} \sin\theta\, \mathbf{e}_\theta$ are

$$v_1 = \sqrt{\frac{2}{3}}\Omega_i r_i \qquad v_1 = \sqrt{\frac{2}{3}}\Omega_o r_o, \tag{2.102}$$

at the inner and outer boundaries, respectively.

Legendre transforms

When our variables are expanded in terms of associated Legendre polynomials, it is natural to transform between real and spectral space via the finite Legendre transform. Formally, the transform consists of the synthesis step

$$f(\theta) = \sum_{l=1}^{\infty} f_l P_l^1(\cos\theta), \tag{2.103}$$

and the analysis step

$$f_l = \int_0^{\pi} f(\theta) P_l^1(\cos\theta) \sin\theta \, \mathrm{d}\theta, \tag{2.104}$$

or equivalently via Gauss-Legendre quadrature (with nodes θ_j and weights w_j)

$$f_l = \sum_j f(\theta) P_l^1(\cos\theta_j) w_j. \tag{2.105}$$

Most simply, the direct transform is achieved via matrix operations, where we transform to real space via multiplication with the matrix $P_{jl} = P_l^1(\cos\theta_j)$. Then direct transforms from real space to spectral space involve multiplication by the matrix $(P_l^1(\cos\theta_j))^{-1}$. However, dense matrix inversion requires operations that scale $\mathcal{O}(L^3)$, for some resolution L. Unlike for Chebyshev polynomials though, large θ resolutions are required to properly resolve small scale flow.

In order to perform the associated Legendre transform at high resolution then a faster, more efficient method is required. There are a number of fast Legendre transforms in the literature, yielding a computational scaling of the order $\mathcal{O}(L(\log(L))^2)$ (Driscoll & Healy (1994); Healy Jr *et al.* (2004); Mohlenkamp (1999); Suda & Takami (2002) for example), however many of the methods presented are problematic in practical situations – they may be unstable, or require too much RAM at high resolutions. We make use of the SHTNS routines developed by Schaeffer (2013), which are built upon the Gauss-Legendre algorithm. Though this also scales as $\mathcal{O}(L^3)$, a number of computational optimisations are employed that result in faster, more efficient computation than technically fast algorithms. Indeed, even at high resolution $L \approx 4000$ the routine is markedly more efficient than those based upon Healy et al.'s algorithm.

Alternatively, we could have made use of the relation between P_l^1 and P_l^0 to reformulate the expansions in terms of a cosine series, enabling use of the fast Fourier transform. For a brief discussion on how this would affect the time-stepping scheme, see section 2.6.

Nonlinear terms

The nonlinear terms for which we need to compute the spectral coefficients are in this case

$$\mathbf{F} = [\mathbf{U} \times \nabla \times \mathbf{U}] \cdot \mathbf{e}_\phi \text{ and } \nabla \times \mathbf{F} = \nabla \times [\mathbf{U} \times \nabla \times \mathbf{U}] \cdot \mathbf{e}_\phi, \tag{2.106}$$

In order to perform the vector algebra, we must transform our variables into real space representations. However, first we require expressions for each spectral component of $\mathbf{U}$ and $\nabla \times \mathbf{U}$. We know that

$$\begin{aligned}[U_r]_l &= \frac{1}{r\sin\theta}\left(\frac{\partial}{\partial\theta}(\sin\theta\psi_l Y_l^1)\right) \\ &= \frac{1}{r}\left(\cot\theta\psi_l Y_l^1 + \psi_l\frac{\partial Y_l^1}{\partial\theta}\right).\end{aligned} \tag{2.107}$$

By utilising the various recurrence relations given for the associated Legendre polynomials in Abramowitz & Stegun (1964), we may express the derivative terms of higher order associated Legendre polynomials. For regular polynomials

$$\frac{\partial P_l^1}{\partial\theta} = \cot\theta P_l^1 - P_l^2, \tag{2.108}$$

so in terms our orthonormalised polynomials,

$$\begin{aligned}\frac{\partial Y_l^1}{\partial\theta} = Q_l^1\frac{\partial P_l^1}{\partial\theta} &= \cot\theta Q_l^1 P_l^1 - \frac{Q_l^1}{Q_l^2}Q_l^2 P_l^2, \\ &= \cot\theta Y_l^1 - \sqrt{(L+2)(l-1)}Y_l^2.\end{aligned} \tag{2.109}$$

This then yields the result

$$[U_r]_l = \frac{1}{r}\left(2\cot\theta\psi_l Y_l^1 - \sqrt{(L+2)(l-1)}\psi_l Y_l^2\right). \tag{2.110}$$

In comparison, it is rather straightforward to show that

$$[U_\theta]_l = -\left(\frac{\psi_l}{r} + \psi_l'\right)Y_l^1, \tag{2.111}$$

$$[U_\phi]_l = v_l Y_l^1. \tag{2.112}$$

Thanks to our toroidal-poloidal decomposition, the r and θ components of $\nabla \times \mathbf{U}$ are found to be virtually identical to $\mathbf{U}$,

$$[(\nabla \times \mathbf{U})_r]_l = \frac{1}{r}\left(2\cot\theta v_l Y_l^1 - \sqrt{(L+2)(l-1)}v_l Y_l^2\right), \tag{2.113}$$

$$[(\nabla \times \mathbf{U})_\theta]_l = -\left(\frac{v_l}{r} + v_l'\right) Y_l^1. \tag{2.114}$$

The ϕ component requires more thought, as it yields

$$[(\nabla \times \mathbf{U})_\phi]_l = \frac{1}{r}\left[\frac{\partial}{\partial r}(-\psi_l - r\psi_l') - \frac{\partial}{\partial \theta}\left(\frac{1}{r}\left(\cot\theta\psi_l Y_l^1 + \psi_l \frac{\partial Y_l^1}{\partial \theta}\right)\right)\right], \tag{2.115}$$

which – via Sturm-Liouville theory – reduces to

$$[(\nabla \times \mathbf{U})_\phi]_l = \left(-\frac{2}{r}\psi_l' - \psi_l'' + \frac{l(l+1)}{r^2}\psi_l\right) Y_l^1. \tag{2.116}$$

In order to perform the cross product in F we must transform these quantities to real space, where we may perform vector calculus at the collocation points. We note that because of the effort required in computing Legendre transforms, it is important to make sure that repeated the fewest time possible. As such, all Legendre transforms are performed whilst still in Chebyshev space, as there are far fewer Chebyshev polynomials than radial collocation points. Let us denote the order m Legendre transform as $\mathcal{L}_m$, and assign the index i to the latitudinal grid points. At the collocation points we have the expressions

$$[U_r]_{ji} = \sum_{n=1}^{N+4}\left(2\cot\theta_i \mathcal{L}_1\left\{\psi_{nl}Y_l^1\right\} - \mathcal{L}_2\left\{\sqrt{(l+2)(l-1)}\psi_{nl}Y_l^1\right\}\right)\frac{1}{r_j}T_{n-1}(x_j),$$

$$[U_\theta]_{ji} = \sum_{n=1}^{N+4} -\mathcal{L}_1\left\{\psi_{nl}Y_l^1\right\}\left(T_{n-1}'(x_j) + \frac{1}{r_j}T_{n-1}(x_j)\right),$$

$$[U_\phi]_{ji} = \sum_{n=1}^{N+4} \mathcal{L}_1\left\{v_{nl}Y_l^1\right\}T_{n-1}(x_j),$$

$$[(\nabla \times \mathbf{U})_r]_{ji} = \sum_{n=1}^{N+4}\left(2\cot\theta_i \mathcal{L}_1\left\{v_{nl}Y_l^1\right\} - \mathcal{L}_2\left\{\sqrt{(l+2)(l-1)}v_{nl}Y_l^1\right\}\right)\frac{1}{r_j}T_{n-1}(x_j),$$

$$[(\nabla \times \mathbf{U})_\theta]_{ji} = \sum_{n=1}^{N+4} -\mathcal{L}_1\left\{v_{nl}Y_l^1\right\}\left(T_{n-1}'(x_j) + \frac{1}{r_j}T_{n-1}(x_j)\right),$$

$$[(\nabla \times \mathbf{U})_\phi]_{ji} = \sum_{n=1}^{N+4} -\mathcal{L}_1\left\{v_{nl}Y_l^1\right\}\left(\frac{2}{r_j}T_{n-1}'(x_j) + T_{n-1}''(x_j)\right)$$
$$+ \sum_{n=1}^{N+4}\mathcal{L}_1\left\{l(l+1)Y_l^1\right\}\frac{1}{r_j}T_{n-1}(x_j).$$

Here the θ_i denotes the i^{th} Gauss-Legendre node. Keeping the number of total Legendre transforms in check is of prime importance in making high resolution computation viable. Though there are nine distinct Legendre transforms in these expressions, only five are unique, keeping the computational requirements reasonable.

Each of the components of the cross product can then be evaluated at the grid points with relative ease. However, re-expanding this back in terms of our associated Legendre basis functions is not so simple. Unlike for the Fourier transformations, where the re-expansion functions were the same as the original expansion functions, we know from equations (2.107) (2.111) and (2.112) that we must now let

$$F_r = \sum_{l=1}^{L}\sum_{n=1}^{N+4} a_{nl} T_{n-1}(x) \frac{Y_l^1}{\sin\theta}, \tag{2.117}$$

$$F_\theta = \sum_{l=1}^{L}\sum_{n=1}^{N+4} b_{nl} T_{n-1}(x) Y_l^1, \tag{2.118}$$

$$F_\phi = \sum_{l=1}^{L}\sum_{n=1}^{N+4} c_{nl} T_{n-1}(x) Y_l^1. \tag{2.119}$$

Note that here we have made use of a P_l^1 recurrence formula in equation (2.117), and not the higher order expression given in equation (2.109). In addition, we make use of the fact that $P_l^1 = \sin\theta(\sum_l \cos^{l-1}\theta)$, such that $a_{nl}Y_l^1/\sin\theta = d_{nl}Y_{l-1}^0$. Thus, we can simplify

$$F_r = d_{nl} T_{n-1}(x) Y_l^0. \tag{2.120}$$

The spectral coefficients of F_ϕ can be found via inverse Legendre and Chebyshev transforms,

$$[F_\phi]_{nl} = \mathcal{L}_1^{-1}\left\{\sum_{I=1}^{i} [f_\phi]_{ji}\mathbf{T}^{-1}\right\}. \tag{2.121}$$

The spectral coefficients of $\nabla \times \mathbf{F}$ require more thought however, as the natural expansion for F_r has a Y_l^0 basis. Clearly, we can only use spectral methods to solve the Navier-Stokes equations if all of our terms have a common Y_l^1 basis. We have

that

$$[\nabla \times \mathbf{F}]_\phi = \frac{1}{r}\left(F_\theta + r\frac{\partial F_\theta}{\partial r} - \frac{\partial F_r}{\partial \theta}\right). \\ = \frac{1}{r}\left(\left(b_{nl} + rb'_{nl}\right) Y_l^1 - \frac{\partial (d_{nl} Y_l^0)}{\partial \theta}\right). \tag{2.122}$$

However, by the associated Legendre recurrence formulae we know that

$$\frac{\partial P_l^m}{\partial \theta} = -\frac{1}{2}\left[(l+m)(l-m+1)P_l^{m-1}(\cos\theta) - P_l^{m+1}(\cos\theta)\right], \tag{2.123}$$

and so, by letting $m = 0$, may say that

$$\frac{\partial P_l^0}{\partial \theta} = -\frac{1}{2}\left[l(l+1)P_l^{-1} - P_l^1\right]. \tag{2.124}$$

In order to deal with the negative order polynomial, we recall Rodrigues' formula, which states

$$P_l^m = \frac{(-1)^m}{2^l l!}\sin^m\theta \frac{\partial^{l+m}}{\partial(\cos\theta)^{l+m}}(-\sin\theta)^l. \tag{2.125}$$

By searching for some constant A such that $P_l^{-m} = AP_l^m$, it can be shown that

$$P_l^{-m} = (-1)^m \frac{(l-m)!}{(l+m)} P_l^m. \tag{2.126}$$

Therefore,

$$\frac{\partial P_l^0}{\partial \theta} = -\frac{1}{2}\left[\frac{-l(l+1)(l-1)!}{(l+1)!} - 1\right] P_l^1, \tag{2.127}$$

$$= P_l^1. \tag{2.128}$$

So, we can express our expansions in the form

$$[\nabla \times F]_\phi = \frac{1}{r}\left(\left(b_{nl} + rb'_{nl}\right) Y_l^1 - d_{nl} Q_l^0 \frac{\partial P_l^0}{\partial \theta}\right), \\ = \frac{1}{r}\left(\left(b_{nl} + rb'_{nl}\right) Y_l^1 - d_{nl}\frac{Q_l^0}{Q_l^1} Q_l^1 P_l^1\right), \\ = \frac{1}{r}\left(\left(b_{nl} + rb'_{nl}\right) Y_l^1 - \sqrt{l(l+1)}\, d_{nl} Y_l^1\right). \tag{2.129}$$

Thus, in order to obtain the spectral coefficients on a wholly Y_l^1 basis, we must perform an order zero Legendre transform on F_r, discard the resulting $l = 0$ coefficient, and suitably relabel. So, we have that

$$[(\nabla \times \mathbf{F})_\phi]_{nl} = \mathcal{L}_1^{-1}\left\{\sum_{i=1}^{I} [F_\theta]_{ji}\left(\mathbf{T}_2^{-1} + \mathbf{T}_3^{-1}\right)\right\} Y_l^1 \tag{2.130}$$

$$-\sqrt{l(l+1)}\,\mathcal{L}_0^{-1}\left\{\sum_{i=1}^{I} [F_r]_{ji}\mathbf{T}_2^{-1}\right\} Y_l^1. \tag{2.131}$$

where we have the Chebyshev transform matrices $\mathbf{T}_2^{-1}$ and $\mathbf{T}_3^{-1}$ as

$$\mathbf{T}_2^{-1} = \mathbf{T}^{-1}\frac{1}{r}\mathbf{T}\mathbf{T}^{-1}, \tag{2.132}$$

$$\mathbf{T}_3^{-1} = \mathbf{T}^{-1}\mathbf{T}'\mathbf{T}^{-1}. \tag{2.133}$$

Finally then, we have that the spectral coefficients of the nonlinear terms are

$$DV_{nl} = [F_\phi]_{nl}, \tag{2.134}$$

$$DP_{nl} = [(\nabla \times \mathbf{F})_\phi]_{nl}. \tag{2.135}$$

Magnetohydrodynamics

The pseudo-spectral method which we utilise for MHD spherical Couette flow is exceedingly similar to both a) the hydrodynamic spherical Couette method of section (2.5.3), b) the MHD Taylor-Couette method of section (2.5.2). The main differences we focus on in this section are in the application of Legendre transforms to the additional magnetic field terms.

The sequence of the pseudo-spectral method follows exactly that of the Taylor-Couette case; the induction equation is solved via a series of transforms, before the magnetic field variables a and b are used to evaluate the right hand side of the Navier-Stokes equations.

We require the spectral coefficients of $[\mathbf{G}]_\phi = [\mathbf{U}\times\mathbf{B}_0]_\phi$ and $[\nabla\times\mathbf{G}]_\phi = [\nabla\times\mathbf{U}\times\mathbf{B}_0]_\phi$. From the hydrodynamic method, we already have expressions for $\mathbf{U}$ and so can say that

$$\mathbf{U}\times\mathbf{B_0} = [U_\theta B_{0\phi} - U_\phi B_{0\theta}]\cdot\mathbf{e}_r + [-U_r B_{0\phi} + U_\phi B_{0r}]\cdot\mathbf{e}_\theta + [U_r B_{0\theta} - U_\theta B_{0r}]\cdot\mathbf{e}_\phi. \tag{2.136}$$

Much like before, our preferred spectral expansion functions are of the form

$$G_r = \sum_{l=1}^{L}\sum_{n=1}^{N+4}\alpha_{nl}Y_l^0, \tag{2.137}$$

$$G_\theta = \sum_{l=1}^{L}\sum_{n=1}^{N+4}\beta nl Y_l^1, \tag{2.138}$$

$$G_\phi = \sum_{l=1}^{L}\sum_{n=1}^{N+4}\gamma_{nl}Y_l^1. \tag{2.139}$$

So, the spectral expansion of $[\nabla \times \mathbf{G}]_\phi$ can be expressed exactly as in the hydrodynamic case, via changing the Y_l^0 basis to the Y_l^1 basis in

$$[\nabla \times \mathbf{G}]_\phi = \frac{1}{r}\left(\frac{\partial}{\partial r}\left(\beta_{nl} + r\beta'_{nl}\right) Y_l^1 - \sqrt{l(l+1)}\alpha_{nl} Y_l^1\right). \tag{2.140}$$

Our spectral coefficients are then obtained via the series of transforms

$$[G_\phi]_{nl} = \mathcal{L}_1^{-1}\left\{\sum_{i=1}^{I}[G_\phi]_{ji}\mathbf{T}^{-1}\right\}, \tag{2.141}$$

$$[(\nabla \times \mathbf{G})_\phi]_{nl} = \mathcal{L}_1^{-1}\left\{\sum_{i=1}^{I}[G_\theta]_{ji}\left(\mathbf{T}_2^{-1} + \mathbf{T}_2^{-1}\right)\right\} Y_l^1 \tag{2.142}$$

$$-\sqrt{l(l+1)}\mathcal{L}_0^{-1}\left\{\sum_{i=1}^{I}[G_r]_{ji}\mathbf{T}_2^{-1}\right\} Y_l^1. \tag{2.143}$$

The same can be done with the additional Navier-Stokes term. Indeed, we require $[\mathbf{H}]_\phi = [(\nabla \times \mathbf{B}) \times \mathbf{B}]_\phi$ and $[\nabla \times \mathbf{H}]_\phi = [\nabla \times ((\nabla \times \mathbf{B}) \times \mathbf{B})]_\phi$. Here, the various components of $\mathbf{B}$ may be transformed into real space via exactly the same transformations as $\mathbf{U}$, and we note that $\mathbf{H}$ is re-expanded onto exactly the same basis functions as $\mathbf{F}$ and $\mathbf{G}$ before it. That is, we find the spectral coefficients of $\mathbf{H}$ to be

$$[H_\phi]_{nl} = \mathcal{L}_1^{-1}\left\{\sum_{i=1}^{I}[H_\phi]_{ji}\mathbf{T}^{-1}\right\}, \tag{2.144}$$

$$[(\nabla \times \mathbf{H})_\phi]_{nl} = \mathcal{L}_1^{-1}\left\{\sum_{i=1}^{I}[H_\theta]_{ji}\left(\mathbf{T}_2^{-1} + \mathbf{T}_3^{-1}\right)\right\} Y_l^1 \tag{2.145}$$

$$-\sqrt{l(l+1)}\mathcal{L}_0^{-1}\left\{\sum_{i=1}^{I}[H_r]_{ji}\mathbf{T}_2^{-1}\right\} Y_l^1. \tag{2.146}$$

We note that expanding the set of equations to include MHD effects has come at the cost of nine additional required Legendre transformations, effectively scaling the computational effort by a factor of two. As such, the $\epsilon = 0.02$ gap width is the narrowest that we can reasonably explore.

2.6 Cosine method for spherical Couette flow

We have previously seen how the Legendre polynomials allow for the solution of the Navier-Stokes and induction equations in spherical geometry; in order to transform

between real and spectral space we can make use of optimised Legendre transforms, courtesy of the SHTNS routine, to calculate nonlinear terms. However, no matter how optimised, the Legendre transform is technically slow, scaling as $\mathcal{O}(L^3)$ for some numerical resolution L. This poses a problem when coupled with narrow gaps, causing a trade-off between gap width, time-step length, and resolution. The computational effort required impedes efforts into approaching the almost co-rotating limit, for which an extremely small gap width is required. As an alternative approach, in this section we detail a time-stepping scheme that would allow us to instead use fast Fourier transforms to go between real and spectral space, greatly increasing computational efficiency. Indeed, other authors have used similar trigonometric methods (see Mamun & Tuckerman (1995)). Unfortunately, our cosine scheme was found to be unstable no matter how implicit it is made; however the method is interesting enough to discuss briefly.

We make use of the same equations and expansions used in the main body of this chapter,

$$\left(\frac{\partial}{\partial t} - D^2\right) v = [\mathbf{F}] \cdot \mathbf{e}_\phi, \tag{2.147}$$

$$-\left(\frac{\partial}{\partial t} - D^2\right) D^2 \psi = [\nabla \times \mathbf{F}] \cdot \mathbf{e}_\phi, \tag{2.148}$$

and

$$v = \sum_{l=0}^{L} v_l \sin\theta P_l^0(\cos\theta), \tag{2.149}$$

$$\psi = \sum_{l=0}^{L} \psi_l \sin\theta P_l^0(\cos\theta). \tag{2.150}$$

Note that these spectral representations are identical to those used in the previous sections; we have taken advantage of the fact that $P_l^1(\cos\theta) = \sin\theta \left(\sum_{n=0}^{l} a_n \cos n\theta\right)$, and in turn that $\sum_{n=0}^{l} a_n \cos n\theta = P_l^0(\cos\theta)$, for some constant coefficients a_n. So, we have a spectral representation that takes the form of a cosine series, albeit with a multiplying factor of $\sin\theta$.

Now, note that the inclusion of the $\sin\theta$ factor means that neither v or ψ are

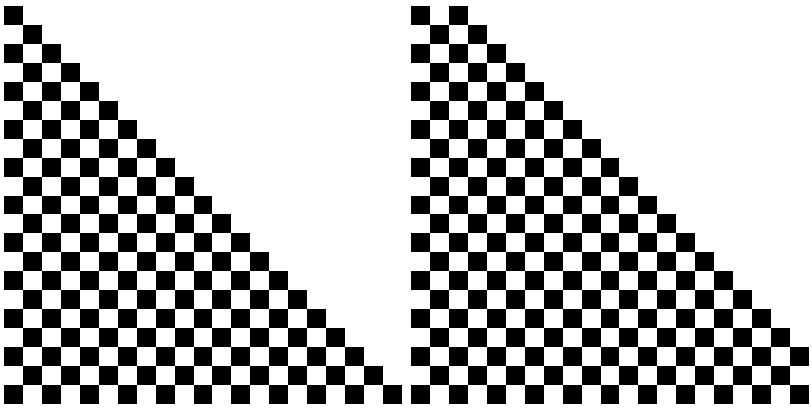

Figure 2.3: Schematic diagrams showing the lower triangular nature of the D^2 and D^4 matrices, respectively. Note that the operators are no longer eigenfunctions.

eigenfunctions of the D^2 or D^4 operators. Indeed, applying the D^2 operator yields

$$D^2 v_0 = a\sin(\theta), \tag{2.151}$$

$$D^2 v_1 = b\sin(\theta)\cos(\theta), \tag{2.152}$$

$$D^2 v_2 = c\sin(\theta) + d\sin(\theta)\cos(2\theta), \qquad \text{etc.} \tag{2.153}$$

for some constants a, b, c, d. Clearly then, matrix inversion on such a dense lower triangular matrix of the kind shown in figure 2.3 would require $\mathcal{O}(L^3)$ operations, completely negating the efficiency afforded by the Fast Fourier transform.

The interesting aspect of our method is therefore how we overcome such dense lower triangular matrices. Instead of dealing with the governing equations as previously defined, we multiply throughout by some trigonometric factor in order to transform the $D^2 v$ and $D^4 v$ matrices into banded forms, for which matrix inversion can be performed efficiently via LU decomposition (Turing, 1948). For the sake of brevity, we shall illustrate this via the $D^2 v$ term in equation 2.147. It can be shown that

$$\sin^2\theta D^2 v = \sum_{n=0}^{\infty} a_n \sin\theta\cos((n-2)\theta) + b_n \sin\theta\cos(n\theta) + c_n \sin\theta\cos((n+2)\theta), \tag{2.154}$$

for

$$a_n = -\frac{1}{4}\left(v_n'' + \frac{2}{r}v_n'\right) + \frac{1}{r^2}\frac{n^2-3n+2}{4}v_n, \tag{2.155}$$

$$b_n = \frac{1}{2}\left(v_n'' + \frac{2}{r}v_n'\right) - \frac{1}{r^2}\frac{n^2+2}{2}v_n, \tag{2.156}$$

$$c_n = -\frac{1}{4}\left(v_n'' + \frac{2}{r}v_n'\right) + \frac{1}{r^2}\frac{n^2+3n+2}{4}v_n. \tag{2.157}$$

It is clear that this can be expressed in terms of a sparse banded penta-diagonal matrix, with non-zero terms in the $(n-2)^{nd}, n^{th}$, and $(n+2)^{nd}$ row entries, as shown in figure 2.4.

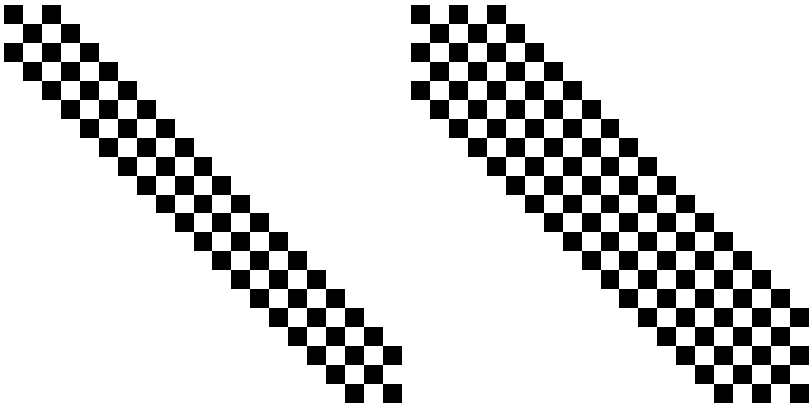

Figure 2.4: Schematic diagrams showing the block penta- and ennea-diagonal nature of $\sin^2\theta D^2 v$ and $\sin^4\theta D^4\psi$ matrices.

In calculating the various entries for our matrix then, it is advantageous to obtain expressions for the coefficients in terms of a single $\cos(n\theta)$. We can suitably transpose the summation to give

$$\sin^2\theta D^2 v = \sum_{n=0}^{\infty}\left[c_{n-2} + b_n + a_{n+2}\right]\sin\theta\cos(n\theta), \tag{2.158}$$

for

$$c_{n-2} = -\frac{1}{4}\left(v_{n-2}'' + \frac{2}{r}v_{n-2}'\right) + \frac{1}{r^2}\frac{n^2-n}{4}v_{n-2}, \tag{2.159}$$

$$b_n = \frac{1}{2}\left(v_n'' + \frac{2}{r}v_n'\right) - \frac{1}{r^2}\frac{n^2+2}{2}v_n, \tag{2.160}$$

$$a_{n+2} = -\frac{1}{4}\left(v_{n+2}'' + \frac{2}{r}v_{n+2}'\right) + \frac{1}{r^2}\frac{n^2+n}{4}v_{n+2}. \tag{2.161}$$

It should be noted that, whilst it is permissible to truncate the $n \to \infty$ terms in our matrices, the $(n-2)$ terms cannot simply be ignored when $n = 0$ and $n = 1$. It is necessary then to rewrite them in terms of the other matrix entries. When $n = 0$, we may replace $a_{-2}\cos(-2\theta) = c_2\cos(2\theta) = c_{n+2}\cos(2\theta)$, and similarly when $n = 1$ we may let $a_1\cos(-\theta) = c_{-1}\cos(\theta) = c_{n-2}\cos(\theta)$. These terms may then be added to the corresponding matrix entries.

It can be shown that similarly multiplying each of the other terms in equations 2.147 and 2.148 by $\sin^2\theta$ and $\sin^4\theta$, we obtain block pentadiagonal and block 9-diagonal matrices, respectively. Our modified time-stepping equations, then, are

$$\sin^2\theta\left(\frac{\partial}{\partial t} - D^2\right)v = [\sin^2\theta\ F]\cdot\mathbf{e}_\phi, \tag{2.162}$$

$$-\sin^4\theta\left(\frac{\partial}{\partial t} - D^2\right)D^2\psi = [\sin^4\theta\ \nabla\times F]\cdot\mathbf{e}_\phi. \tag{2.163}$$

Finally, in order to make the LU decomposition and matrix inversion more efficient, we take advantage of the decoupling between the odd and even $\cos(n\theta)$ components in the matrices, to yield block tri- and penta-diagonal matrices, where each of the central bands has non-zero entries. By evolving the odd and even components separately, we decrease the size of the matrices by a factor of two, a significant improvement given that the inversion step scales as $\mathcal{O}(n^3)$.

This method was benchmarked thoroughly; it was verified that given some initial spectral coefficients, the matrix operations were correct, the time-stepping scheme was accurate, and that the free decay eigenvalues were in agreement with theoretical values. However, no matter how implicit or explicit we made the time-stepping scheme, it could not be made stable at reasonable time-step lengths.

Chapter 3

Linear Stability of Nonaxisymmetric MHD Taylor-Couette flow

In this chapter, we study the linear onset of nonaxisymmetric modes of instability in Taylor-Couette flow with applied helical magnetic fields. We focus on the near inductionless limit (Pm=10^{-6}) and choose geometry that coincides with existing liquid metal experiments, such that any results obtained are experimentally relevant. We allow the azimuthal magnetic field to be generated by a combination of currents both in the inner cylinder and the fluid itself, and introduce a control parameter governing the relative strength of these two currents. This allows for a more general parameter space exploration than those that have been performed previously. A set of eigenvalue equations is derived and then solved numerically using a spectral collocation method with Chebyshev polynomials; the resulting parameter space is then explored in detail. Alongside other results, we find that altering the azimuthal field profile greatly influences the properties of the various instabilities, and gives rise to interesting dynamics, such as different mode types. We also give a comparison to the analytic results given by Kirillov et al. *(2014), in which, via a WKB method, it was predicted that the most unstable modes can be of a wavenumber higher than one if the azimuthal magnetic field profile is suitably shallow.*

3.1 Introduction

One of the current topics of research on inductionless MRI is in nonaxisymmetric modes of instability. As seen in chapter 1, the standard, axisymmetric, HMRI has been studied intensely, with clear experimental evidence and cohesive links to the SMRI. However, nonaxisymmetric modes would afford the opportunity of interaction between rotation and current driven phenomena, which may yield interesting dynamics. Indeed, it can be noted that the various forms of MRI and the TI can be excited for similar overlapping parameter ranges.

It is then of interest to explore the full parameter space of the inductionless MRI and TI, in both linear and asymptotic studies. An initial linear stability analysis of the nonaxisymmetric modes of inductionless HMRI was performed by Hollerbach *et al.* (2010), where it was shown that 3D modes may be produced with the same Re and Ha parameter dependency that was found in 2D, and therefore that these modes may be found in the PROMISE experiment. In particular, this investigation examined the helical field with azimuthal component $b_\phi \sim 1/r$, produced by running a current along the axis of the central cylinder.

In their paper, Rüdiger *et al.* (2010) performed a more general investigation of the nonaxisymmetric modes of AMRI and TI, with the azimuthal magnetic field component taken as $B_\phi = ar + b/r$, produced via running a current in the fluid itself, as well in the inner core. This more general magnetic field profile allowed for further tweaking of the dynamics, and the exploration of new parameter combinations that led to interesting dynamics. However, this work was not without its shortcomings, as the magnetic Prandtl number was taken to be $\mathrm{Pm} = 1$ throughout. This meant that the results were not relevant to any experiment. Further linear analysis has focussed on the astrophysical implications of these results, and did include some low Rm calculations regarding the same results (Rüdiger *et al.*, 2014).

The asymptotic theory of nonaxisymmetric MRI has been provided by the work of Kirillov, Stefani and collaborators, who have utilised various WKB expansions to comprehensively study the possibility of astrophysical rehabilitation for induc-

tionless MRI. Most of this work has been focussed on the previously discussed Liu limits, and if there exists any mathematical argument for overcoming them. In the process of solving a number of paradoxes in the understanding of MRI at different values of Pm, they did indeed find an extension to the Liu limits (Kirillov & Stefani, 2011). Though still not encompassing Keplerian rotation profiles (or more precisely, a local approximation of the Keplerian profile since it does not apply globally to Taylor-Couette flows), this gave traction to the idea that the Liu limits were not insurmountable. In a later work, Kirillov *et al.* (2012) unified each of the inductionless MRI under a single equation for critical Rossby number (defined as $\mathrm{Ro} = r(2\Omega)^{-1}\partial\Omega/\partial r$). The upper and lower Liu limits are then given by $\mathrm{Ro}_{\mathrm{ULL}} = 2(1+\sqrt{2})$ and $\mathrm{Ro}_{\mathrm{LLL}} = 2(1-\sqrt{2})$, respectively. Unfortunately however, this meant that the Liu limits were also unified, with this prohibitive criteria extended from the axisymmetric HMRI to the nonaxisymmetric variants of inductionless MRI, further alienating the possibility of accretion disk application. Furthermore, evidence was given for the existence of higher order azimuthal modes ($m > 1$) in the case where axial magnetic fields were dominant. This required confirmation via a linear stability analysis, which we provide in this chapter.

Perhaps their most important works (Kirillov & Stefani, 2013; Kirillov *et al.*, 2014), however, showed via a WKB expansion that the seemingly strict restrictions posed by the upper and lower Liu limits could be overcome via some clever alternations to the magnetic field geometry. It was found that even Keplerian profiles could be made unstable if the radial profile of the azimuthal magnetic field is modified slightly from the current free profile $B_\phi \sim 1/r$. As we've seen in the work of Rüdiger *et al.*, this can easily be achieved in the linear analysis, and also in experiments, via generating the field from currents in both the fluid and inner core. In deriving a stability criterion involving the Rossby number and magnetic Rossby number ($\mathrm{Rb} = r(2B_\phi r^{-1})\partial(B_\phi r^{-1})/\partial r$), it was shown that the upper and lower Liu limits were not strictly separate quantities, and that they are connected by some stability curve, $\mathrm{Rb} = -(1/8)(\mathrm{Ro}+2)^2/(\mathrm{Ro}+1)$. One of the more interesting results that this predicted was the existence of instability for extremely positive shear; that is, where the angular velocity increases outwards. This has since been confirmed in (Rüdiger

et al., 2016a,b; Stefani & Kirillov, 2015), for both the MRI and TI. We refrain from further exploration of this case as it requires narrower aspect ratios, and is therefore not directly applicable to the PROMISE experiment.

The choice of governing parameters used by Kirillov *et al.* have allowed for particularly generalised magnetic field profiles. However, the use of Ro and Rb does exclude some interesting scenarios, such as if the magnetic field was generated by currents running in opposite directions. In this chapter, we aim to extend the work begun by Rüdiger *et al.* (2010), Hollerbach *et al.* (2010) and Kirillov *et al.* (2014), and provide a linear stability analysis of the full range of parameter space. We focus primarily on the inductionless limit, and choose our set-up in such a way that the azimuthal magnetic field profile is as generalised as possible; we generate it via current in the core and fluid, with particular care taken to allow for each of the currents to be run in opposing directions.

We define a parameter to govern the ratio of current in the core and fluid, and obtain a series of perturbation equations to describe the flow. Via the collocation method discussed in section 2.3, we numerically solve these equations to yield a set of growth rates for instability at any given set of parameters. We use this to investigate the effect that the currents have on instability, the consequences of changing the magnetic field profile, and also the influence of the axial field, from which we find the higher order azimuthal modes. We also briefly mention how our results line up with regards to the Liu limits.

3.2 Equations

We consider cylindrical Taylor-Couette flow, with radii and angular velocity r_i, r_o, Ω_i and Ω_o at the inner and outer boundaries respectively. To allow our results to be examined experimentally, we take the inner and outer radii to coincide with those of the PROMISE experiment, 4cm and 8cm, giving a relative gap width $r_i/r_o = 0.5$. We also denote parameter μ_Ω to be the relative 'steepness' of the rotation profile, given by $\mu_\Omega = \Omega_o/\Omega_i$. Note that the Rayleigh limit in this case, the value of μ_Ω above

which purely hydrodynamic flows are stable, is $\mu_\Omega = 0.25$ (as found by rearranging equation 1.1). We include a basic state helical magnetic field with components in the azimuthal and axial directions, where the axial field is generated by some external magnet and the azimuthal field is generated via a combination of currents running through the inner cylinder (I_{in}) and fluid (I_{fl}). The inherent difficulty in this configuration arises from the sheer number of control parameters that may be varied – the angular velocity at both the inner and outer boundaries, the relative strength of the axial magnetic field, and the relative strength of the currents that produce the azimuthal magnetic field.

The basic state velocity is driven by the differential rotation of the two cylinders, $\mathbf{U_0} = (0, r\Omega e_\phi, 0)$, with the standard Taylor-Couette angular velocity profile

$$\Omega(r) = a_\Omega + \frac{b_\Omega}{r^2}, \tag{3.1}$$

which has

$$a_\Omega = \Omega_i \frac{\mu - (r_i/r_o)^2}{1 - (r_i/r_o)^2} \qquad b_\Omega = \Omega_i r_i^2 \frac{1-\mu}{1-(r_i/r_o)^2}. \tag{3.2}$$

The basic state magnetic field is simply given by $\mathbf{B_0} = (0, B_\phi, B_z)$, with the axial magnetic field B_z and the azimuthal magnetic field

$$B_\phi = \frac{\mu_0}{2\pi}\left[\frac{1}{r}\, I_{in} + \frac{1}{r}\,\frac{r^2 - r_i^2}{r_o^2 - r_i^2}\, I_{fl}\right]. \tag{3.3}$$

as derived in appendix A.3. When examining the linear onset of instability, we are interested in the stability of small perturbations about this basic state. Therefore, if we let $\mathbf{U} = \mathbf{U_0} + \mathbf{u}'$, $\mathbf{B} = \mathbf{B_0} + \mathbf{b}'$ in the governing equations and then linearise, we obtain (after relabelling $\mathbf{u}'$ as $\mathbf{u}$ and $\mathbf{b}'$ as $\mathbf{b}$, for convenience)

$$\begin{aligned} \frac{\partial \mathbf{u}}{\partial t} - \nu\nabla^2\mathbf{u} &= -\nabla p + \Big[\mathbf{U}_0 \times (\nabla \times \mathbf{u}) + \mathbf{u} \times (\nabla \times \mathbf{U}_0)\Big] \\ &\quad + \frac{1}{\mu_0\rho}\Big[(\nabla \times \mathbf{B}_0) \times \mathbf{b} + (\nabla \times \mathbf{b}) \times \mathbf{B}_0\Big], \end{aligned} \tag{3.4}$$

$$\frac{\partial \mathbf{b}}{\partial t} - \eta\nabla^2\mathbf{b} = \nabla \times (\mathbf{u} \times \mathbf{B}_0) + \nabla \times (\mathbf{U}_0 \times \mathbf{b}). \tag{3.5}$$

It is here convenient to nondimensionalise each of the variables. This turns out to be mostly straightforward – we scale lengths with the inner radius r_i, basic state velocity with $\Omega_i r_i$, time on the viscous diffusive time-scale r_i^2/ν and the perturbation

velocity with η/r_i. The choice of normalisation of the magnetic fields is non-trivial – the nondimensionalisation used must be valid for *all* possible combinations of I_{in} and I_{fl}. The cases of zero current in either fluid or core, as well as equal and opposite currents, pose problems. It happens that the best choice for nondimensionalising the magnetic fields is to scale both perturbation and basic state with the RMS mean of B_ϕ, $\bar{B}$. If we define the ratio of the currents $\tau = I_{fl}/I_{in}$ and restrict our attention to $r_i/r_o = 0.5$, as the RMS of B_ϕ is defined to be $(\int B_\phi^2\, r\, dr/\int r\, dr)^{1/2}$, we have that

$$\begin{aligned}\int_{r_1}^{r_0} B_\phi^2 r \, \mathrm{d}r &= \frac{\mu_0^2 I_{in}^2}{4\pi^2}\left(\left(1-\frac{\tau}{3}\right)^2 \ln 2 + \frac{15\tau}{36} + \left(1-\frac{\tau}{3}\right)\tau \right), \\ &= \frac{\mu_0^2 I_{in}^2}{4\pi^2}\left(\left(1-\frac{\tau}{3}\right)^2 \ln 2 + \frac{\tau^2}{12} + \tau \right),\end{aligned} \tag{3.6}$$

and as $\int_{r_i}^{r_o} r \, \mathrm{d}r = \frac{3}{2}$,

$$\bar{B} = \frac{\mu_0}{2\pi} I_{in} \left(\frac{2}{3}\right)^{1/2} \left[\ln 2 \left(1-\frac{1}{3}\tau\right)^2 + \tau + \frac{1}{12}\tau^2 \right]^{1/2}. \tag{3.7}$$

The nondimensionalised equivalent of the azimuthal field profile is then given by

$$\hat{B_\phi}(r) = \left(\frac{3}{2}\right)^{1/2} \left[\frac{1}{r}\left(1-\frac{1}{3}\tau\right) + r\,\frac{1}{3}\tau \right] \Big/ \left[\ln 2 \left(1-\frac{1}{3}\tau\right)^2 + \tau + \frac{1}{12}\tau^2 \right]^{1/2}. \tag{3.8}$$

Note that this profile is well defined for all choices of τ, which would not have been the case for the standard options for nondimensionalisation. Indeed, we are free to take the extreme cases $\tau = 0$, where current is solely in the core and $\tau = \pm\infty$, where current is solely in the fluid, as well as $\tau < 0$, where the currents in the fluid and core are aligned in opposite directions. It is the $\tau < 0$ case that is perhaps the most interesting, with little prior attention in the literature, despite being relatively straightforward to implement experimentally. In particular, the magnetic Reynolds number formulation of Kirillov *et al.* (2014) does not cover these negative τ (as we will see when comparing with their results in section 3.4.1. The nondimensionalised axial magnetic field is governed by the parameter δ, with $B_z = \bar{B}\delta$.

Incorporating these scalings into the Navier-Stokes and induction equations, we thus

have

$$\frac{\partial \mathbf{u}}{\partial t} - \nabla^2 \mathbf{u} = -\nabla p + \mathrm{Re}\Big[\mathbf{U}_0 \times (\nabla \times \mathbf{u}) + \mathbf{u} \times (\nabla \times \mathbf{U}_0)\Big] + \mathrm{Ha}^2\Big[(\nabla \times \mathbf{B}_0) \times \mathbf{b} + (\nabla \times \mathbf{b}) \times \mathbf{B}_0\Big], \tag{3.9}$$

$$\mathrm{Pm}\frac{\partial \mathbf{b}}{\partial t} - \nabla^2 \mathbf{b} = \nabla \times (\mathbf{u} \times \mathbf{B}_0) + \mathrm{Rm}\,\nabla \times (\mathbf{U}_0 \times \mathbf{b}), \tag{3.10}$$

where $\mathrm{Re} = \Omega_i r_i^2/\nu$ is the Reynolds number, $\mathrm{Pm} = \nu/\eta$ is the magnetic Prandtl number, $\mathrm{Rm} = \Omega_i r_i/\eta = \mathrm{PmRe}$ is the magnetic Reynolds number, and $\mathrm{Ha} = \bar{B} r_i/\sqrt{\mu_0 \rho \nu \eta}$ is the Hartmann number.

As we have no desire to prescribe the pressure, it is beneficial to take the curl of the Navier-Stokes equation instead, eliminating the ∇p. Thus, making use of the vector calculus identity $\nabla^2 \mathbf{u} = \nabla(\nabla \cdot \mathbf{u}) - \nabla \times \nabla \times \mathbf{u}$ we yield

$$\frac{\partial (\nabla \times \mathbf{u})}{\partial t} + \nabla \times \nabla \times \nabla \times \mathbf{u} = \mathrm{Re}\nabla \times [\mathbf{u} \times \nabla \times \mathbf{U}_0 + \mathbf{U}_0 \times \nabla \times \mathbf{u}] + \mathrm{Ha}^2 \nabla \times [(\nabla \times \mathbf{B}) \times \mathbf{B}_0 + (\nabla \times \mathbf{B}_0) \times \mathbf{B}] \tag{3.11}$$

To satisfy the $\nabla \cdot \mathbf{u} = \nabla \cdot \mathbf{b} = 0$ conditions by default, we choose to express the field and flow in terms of a toroidal-poloidal decomposition, such that

$$\mathbf{u} = \nabla \times (e\,\mathbf{e_r}) + \nabla \times \nabla \times (f\,\mathbf{e_r}), \tag{3.12}$$

$$\mathbf{b} = \nabla \times (g\,\mathbf{e_r}) + \nabla \times \nabla \times (h\,\mathbf{e_r}), \tag{3.13}$$

As we now have four variables, we take our four governing equations then to be the Navier Stokes equation 3.4, its curl, the Induction equation 3.5, and its vector potential.

3.2.1 Fourier mode expansion

As our domain is essentially periodic (obviously so in the azimuthal direction, and can be taken to be in the axial direction due to the infinite cylinder assumption), it is fair to suppose that solutions will arise in the form of Fourier modes, such that

$$e = e(r)e^{\gamma t + im\phi + ikz} \qquad f = f(r)e^{\gamma t + im\phi + ikz} \tag{3.14}$$

$$g = g(r)e^{\gamma t + im\phi + ikz} \qquad h = h(r)e^{\gamma t + im\phi + ikz}. \tag{3.15}$$

The functions $e(r), f(r), g(r)$ and $h(r)$ describe the radial structure of the various quantities, with the non-periodic nature of the radial domain necessitating a different expansion in this dimension. The scalars m (an integer) and k are the mode numbers in the azimuthal and axial directions respectively. The growth rate γ is complex, though it is $Re\{\gamma\}$ that governs stability – $\gamma < 0$ being stable, $\gamma > 0$ stable, and $\gamma = 0$ signifying marginal stability, such that perturbations neither grow or decay. Any time dependence is controlled by $Im\{\gamma\}$, the frequency. The advantage of using such a decomposition is that non-radial derivatives are now trivially calculated, with $\partial/\partial\theta\, e = ime$, $\partial/\partial z\, e = ike$, etc. allowing for the four governing equations to be expressed as a one dimensional problem. As we are prescribing both m and k, these equations contain only radially dependent variables.

Under this ansatz, in conjunction with the toroidal-poloidal decomposition, the components of the velocity $\mathbf{u}$ may be written as

$$u_r = \left(\frac{m^2}{r^2} + k^2\right) e, \tag{3.16}$$

$$u_\phi = ike + \frac{imf'}{r} - \frac{imf}{r^2}, \tag{3.17}$$

$$u_z = \frac{ikf'}{r} - \frac{ime}{r}, \tag{3.18}$$

with the components of $\mathbf{b}$ taking similar form (with g and h instead of e and f respectively). Applying this to our governing equations we yield (after much algebra),

$$\gamma(C_2 e + C_3 f) + C_4 e + C_5 f = \mathrm{Re}E_1 + \mathrm{Re}F_1 + \mathrm{Ha}^2 G_1 + \mathrm{Ha}^2 H_1, \tag{3.19}$$

$$\gamma(C_3 e + C_4 f) + C_5 e + C_6 f = \mathrm{Re}E_2 + \mathrm{Re}F_2 + \mathrm{Ha}^2 G_2 + \mathrm{Ha}^2 H_2, \tag{3.20}$$

$$\mathrm{Pm}\gamma(C_1 g + C_2 h) + C_3 e + C_4 f = E_3 + F_3 + \mathrm{Rm}G_3 + \mathrm{Rm}H_3, \tag{3.21}$$

$$\mathrm{Pm}\gamma(C_2 g + C_3 h) + C_4 e + C_5 f = E_4 + F_4 + \mathrm{Rm}G_4 + \mathrm{Rm}H_4. \tag{3.22}$$

Here, to simplify the equations we take advantage of the nomenclature

$$C_n p = (\nabla \times)^n (p\, \mathbf{e}_r), \tag{3.23}$$

such that

$$C1 = 0, \tag{3.24}$$

$$C2 = \Delta, \tag{3.25}$$

$$C3 = -2mkr^{-2}, \tag{3.26}$$

$$C4 = -\Delta\partial_r^2 + \left(mr^{-2} - k^2\right)\left(r^{-1}\partial_r - r^{-2}\right) + \Delta^2, \tag{3.27}$$

$$C5 = 4mk\left(r^{-2}\partial_r^2 - r^{-3}\partial_r + (1-m^2)r^{-4} - k^2r^{-2}\right), \tag{3.28}$$

$$\begin{aligned} C6 = {} & \Delta\partial_r^4 - 2\left(m^2r^{-1} - k^2\right)r^{-1}\partial_r^3 + \left(5m^2r^{-4} - 3k^2r^{-2} - 2\Delta^2\right)\partial_r^2 \\ & + \left(3m^2(2m^2-3)r^{-4} + (4m^2+3)k^2r^{-2} - 2k^4\right)r^{-1}\partial_r \\ & + m^2(9-10m^2)r^{-6} - 3k^2r^{-4} + 2k^4r^{-2} + \Delta^3. \end{aligned} \tag{3.29}$$

Now, we have a set of generalised eigenvalue equations for which the existence of a

solution is therefore guaranteed. The various coefficients E1, F1, etc. are given as

$$E1 = -im\Delta\Omega e, \tag{3.30}$$

$$E2 = ik\hat{\Delta}\Omega e, \tag{3.31}$$

$$E3 = 0, \tag{3.32}$$

$$E4 = i\Delta\left(\frac{mB_\phi}{r} + k\delta\right)e, \tag{3.33}$$

$$F1 = ik\left(\hat{\Delta}\Omega + \Delta r\Omega'\right)f, \tag{3.34}$$

$$F2 = -im\Omega\left(C_4 + 4k^2r^{-2}\right)f, \tag{3.35}$$

$$F3 = i\Delta\left(\frac{mB_\phi}{r} + k\delta\right)f, \tag{3.36}$$

$$F4 = ik\left(\Delta B'_\phi - \frac{B_\phi(\hat{\Delta} - \Delta)}{r} - \frac{2km\delta}{r^2}\right)f, \tag{3.37}$$

$$G1 = i\Delta\left(\frac{mB_\phi}{r} + k\delta\right)g, \tag{3.38}$$

$$G2 = -ik\hat{\Delta}\left(\frac{B_\phi}{r} + \frac{km\delta}{r^2}\right)g, \tag{3.39}$$

$$G3 = 0, \tag{3.40}$$

$$G4 = -im\Delta\Omega g, \tag{3.41}$$

$$H1 = -ik\left(\Delta B'_\phi + \frac{B_\phi(\hat{\Delta} - \Delta)}{r} + \frac{2km\delta}{r}\right)h, \tag{3.42}$$

$$H2 = \frac{im\Delta}{r}\left(B''_\phi + \frac{B'_\phi}{r} - \frac{B_\phi}{r^2}\right)h + \frac{4imB_\phi k^2}{r^3}h + i\left(\frac{mB_\phi}{r} + k\delta\right)C_4 h. \tag{3.43}$$

$$H3 = -im\Delta\Omega h, \tag{3.44}$$

$$H4 = ik\left(2m^2r^{-2}\Omega - \Delta r\Omega'\right)h, \tag{3.45}$$

Note that these coefficients are mostly the same as those given by Hollerbach *et al.* (2010), with any differences due to the addition of the nondimensional quantities B_ϕ and δ, which describe the basic state magnetic field.

Here, as in Hollerbach *et al.* (2010), we use the notation $\Delta = m^2/r^2 + k^2$ and $\hat{\Delta} = 4m^2/r^2 + 2k^2$.

3.2.2 Boundary conditions

In order to prescribe the boundary conditions, we use the no–slip condition for the velocity – that is, $\mathbf{u} = 0$ at the boundary – and then take the boundaries to be either perfectly conducting (section 3.3 only) or insulating. Of course, neither is truly representative of an experiment, when the magnetic boundary conditions will be somewhere in between the two cases. For our purposes however, these choices are perfectly acceptable.

First of all, we have from the no–slip condition that

$$e = f = \frac{\partial f}{\partial r} = 0, \tag{3.46}$$

giving us two conditions on e and four on f. Then, considering first the case of insulating boundaries, we note that there must be zero current outside the annulus, i.e. $\mathbf{J} = 0$ for $r < r_i$ and $r > r_o$. Therefore, from Maxwell's equations

$$\mathbf{J} = \nabla \times \mathbf{B} = 0 \Longrightarrow \mathbf{B} = \nabla\Phi \Longrightarrow \nabla^2\Phi = 0 \tag{3.47}$$

outside the cylinders, for some potential field Φ. If we use our Fourier mode ansatz $\Phi = Ae^{im\theta+ikz}F(r)$ in the previous equation, we find that (after cancellations)

$$r^2F''(r) + rF'(r) - \left(m^2 + r^2k^2\right)F(r) = 0, \tag{3.48}$$

which we may recognise immediately to be the modified Bessel's equation. Thus, using the transformation $r \to kr$ we find that

$$F(kr) = \begin{cases} I_m(kr) & \text{if } r < r_i \\ K_m(kr) & \text{if } r > r_o \end{cases}, \tag{3.49}$$

where the modified Bessel's functions of the first and second kind have been appropriately chosen due to their behaviour at small/large values of kr values respectively. Recalling that $\mathbf{B} = \nabla\Phi$, and taking the case $r < r_i$ for convenience, the components of $\mathbf{B}$ are then given as

$$B_r = \frac{\partial\Phi}{\partial r} = kAe^{im\phi+ikz}I'_m(kr_i), \tag{3.50}$$

$$B_\phi = \frac{1}{r}\frac{\partial\Phi}{\partial\phi} = \frac{im}{r}Ae^{im\phi+ikz}I_m(kr_i), \tag{3.51}$$

$$B_z = \frac{\partial\Phi}{\partial z} = ikAe^{im\phi+ikz}I_m(kr_i). \tag{3.52}$$

Note that $B_\phi = \frac{m}{kr} B_z$. Because $\mathbf{B}$ must be continuous at r_i, as there is no surface current, we may yield from our toroidal–poloidal definition of b that

$$\Delta g - \frac{2km}{r_i^2} h = 0. \tag{3.53}$$

Furthermore, to be consistent we must have that

$$\frac{B_r}{B_z} = \frac{\partial \Phi / \partial r}{\partial \Phi / \partial z}, \tag{3.54}$$

i.e. as $\mathbf{B}$ is continuous at the boundary, the ratio between radial and axial components must be the same regardless of which definition of $\mathbf{B}$ is used. Therefore it can be reasoned that

$$\Delta h I_m(kr_i) = \left(-\frac{mg}{r_i} + \frac{kh}{r_i} + kh' \right) I'_m(kr_i).$$

After some simplification, we arrive at the two relevant insulating boundary conditions,

$$\frac{m}{r_i} g = 0, \tag{3.55}$$

$$k \left(h' + \frac{h}{r_i} \right) - \Delta \frac{I_m(kr_i)}{I'_m(kr_i)} h = 0. \tag{3.56}$$

The equivalent boundaries for $r = r_o$ are given by replacing r_i and I_m with r_o and K_m respectively.

For perfectly conducting boundaries the tangential magnetic field and normal magnetic field must vanish at the wall,

$$\begin{aligned} \mathbf{n} \times \mathbf{E} &= 0, \\ \mathbf{n} \cdot \mathbf{B} &= 0. \end{aligned}$$

Therefore, we must have that $B_r = \partial B_\phi / \partial r + B_\phi / r = 0$, leading to the conditions

$$\begin{aligned} h &= 0, \\ ikg' + \frac{ikg}{r} + \frac{imh''}{r^2} - \frac{imh'}{r^2} &= 0. \end{aligned}$$

3.2.3 Numerical method

There are a number of possible methods by which we could solve the one–dimensional eigenvalue problem, each with its own strengths and weaknesses. The simplest of them would be to use a finite difference approximation to the various partial derivatives. However, using a finite difference scheme would yield suboptimal convergence, with errors that scale as $\mathcal{O}((r_{i+1} - r_i)^{-2})$. In addition, the non-periodic nature of the radial domain introduces more complicated flow structure near the boundaries, including boundary layers, for which we require substantially higher resolutions than the main bulk of the fluid. The use of an evenly spaced nodal grid is therefore inefficient, and we would prefer to concentrate our grid points in the vicinity of the boundaries.

We thus choose instead to solve the system of equations numerically using spectral collocation, whereby $e(r), f(r), g(r)$ and $h(r)$ are expanded in terms Chebyshev polynomials. In this chapter, we choose to collocate with the Chebyshev-Gauss-Lobatto nodes as the relevant grid points. The radial coordinates may be transformed onto the universal interval $[-1, 1]$ by letting

$$r = \frac{r_o + r_i}{2} + \frac{r_0 - r_i}{2} x, \tag{3.57}$$

allowing us to take the expansions

$$e(x_j) = \sum_{k=1}^{N+2} e_k T_{k-1}(x_j), \qquad f(x_j) = \sum_{k=1}^{N+4} f_k T_{k-1}(x_j), \tag{3.58}$$

$$g(x_j) = \sum_{k=1}^{N+2} g_k T_{k-1}(x_j), \qquad h(x_j) = \sum_{k=1}^{N+2} h_k T_{k-1}(x_j). \tag{3.59}$$

Note that we have taken expansions up to $N+2$ and $N+4$ polynomials in order to accommodate the number of boundary conditions for each variable. Whilst this is not strictly necessary, it ensures an equal number of equations and coefficients, and so when the generalised eigenvalue problem is expressed in matrix form the various matrices are square. This necessitates that the endpoints are not included in the nodes, as these are treated separately in the boundary conditions.

The Chebyshev expansion allows for the commutative treatment of radial derivatives, i.e

$$\frac{\partial}{\partial r}e(x) = \frac{\partial}{\partial r}\sum_{k=1}^{N+2} e_k T_{k-1}(x_j) \quad = \quad \sum_{k=1}^{N=2} e_k T'_{k-1}(x_j)\frac{\partial x}{\partial r} \tag{3.60}$$

for which we are able to numerically calculate T'_{k-1} at the grid points via the algorithm laid out in Mason & Handscomb (2002).

Thus, we have a generalised eigenvalue problem of the form

$$\gamma A\mathbf{x} = B\mathbf{x} \tag{3.61}$$

with A, B being complex $(4N+10)\times(4N+10)$ matrices. We could solve the system of equations correctly as they are, incorporating the boundary conditions in their current form. However, recall that the boundary conditions are implemented as

$$\gamma\sum_{k=1}^{N+2} e_k T_{k-1}(\pm 1) = 0, \text{ etc.} \tag{3.62}$$

In their current form, any spurious modes would force the solution $\gamma = 0$ in order to satisfy these conditions. Clearly this would pose a problem when searching for marginal instability, and would cast doubt on any result obtained. Thus, we subtly alter the equations for the boundary conditions to

$$(\gamma + 999)\sum_{k=1}^{N+2} e_k T_{k-1}(\pm 1) = 0, \text{ etc.} \tag{3.63}$$

In case of spurious behaviour here, we now find that $(\gamma + 999) = 0$, and hence any spurious modes are fixed with a growth rate $\gamma = -999$, well away from marginal stability. Of course, this change has no bearing on the validity of the boundary conditions, or our solutions.

We solve numerically using the NAG subroutine F02GJF, which makes use of a complex QZ algorithm – we refer to the NAG documentation for further details, and essentially treat this as a black-box routine from herein.

Our code takes the input parameters δ, τ, μ and m, and scans over prescribed ranges for Re and Ha – all the while optimising to find the most unstable axial wavenumber

k (to within 1% accuracy) – such that the most unstable growth rate γ is generated for each point in Re–Ha space. To ensure that the system is sufficiently resolved, we expand with Chebyshev polynomials of degree $N = 30 - 80$. depending on the specific parameter regime.

The code has been benchmarked qualitatively against results from (Rüdiger *et al.*, 2010), and also quantitatively against two additional codes, one of which being that used in (Hollerbach *et al.*, 2010).

3.3 Results – Pm = 1, $\delta = 0$

First of all, we consider the case where Pm=1; coinciding exactly with the work of Rüdiger *et al.* (2010). Though not interesting for experiments, we may use this to reassure ourselves of the validity of our code, as well as further examine some of the results given previously. In the aforementioned paper, perfectly conducting boundary conditions were imposed, as opposed to our insulating boundaries. Thus, in this section we consider both cases. In particular, we focus on the special case where $\mu = 0.5$, with a nearly uniform azimuthal field prescribed by $\tau = 1$. Rüdiger *et al.* showed that – for this Pm – there exists a stable separating region between the AMRI and Tayler instabilities coinciding with Chandrasekhar's equipartition solution. In this stable region the Tayler instability is stabilised by the increasing differential rotation. However, figures included in the paper cover only a limited parameter range; the question is whether this stable region continues as Re and Ha are increased further. It turns out that this is not the case, as seen in figure 3.1. Our plot is clearly equivalent in the parameter range that Rüdiger *et al.* examined, however it can be seen that upon expanding the axis range a relatively weak instability is found in this separating region. This is much more apparent if we switch to insulating boundary conditions, where we find that this weak instability occurs even inside the range that Rüdiger *et al.* examined. If we were to take mixed boundary conditions, it can be shown that it is the condition at the outer boundary that has the most bearing on how readily the separating region can be destabilised, which is

perhaps surprising given that the inner boundary is the main source of energy for the flow. Note also that the growth rate and relative weakness is dependent on the type of magnetic boundary.

It has since been shown via WKB analysis that this weak instability is due to the destabilisation of Chandrasekhar's equipartition solution (Kirillov *et al.*, 2014). As for the nature of the instability, it was shown that it develops into the AMRI as $\mathrm{Rm} \to 0$. We expect then to see little of this destabilisation when looking at $\mathrm{Pm} = 10^{-6}$, appropriate to liquid metals. The results of Rüdiger *et al.* (2015) were published soon after the work in this chapter was carried out, and our plots add nicely to their results given for $\mu_\Omega = 0.25$ and $\mu_\Omega = 0.35$ – the Rayleigh limit and quasi-Keplerian rotation profiles, respectively.

In the preceding paragraphs we have referred a number of times to Chandrasekhar's equipartition solution as a source of the stable separating region. In order to understand this, we consider Chandrasekhar's original work (Chandrasekhar, 1956). Here it was shown that if a flow has kinematic velocity $\mathbf{U}$ that is aligned with a magnetic field of Alfvén velocity $\mathbf{U}_{alf}$,

$$\mathbf{U} = \mathbf{U}_{alf}, \tag{3.64}$$

then the flow is stable. Further work by Tataronis & Mond (1987) illustrated that this equipartition solution could be destabilised if one were to make the addition of scalar factor β, such that

$$\mathbf{U} = \beta \mathbf{U}_{alf}, \tag{3.65}$$

where $\beta \neq 1$. When dissipation is also taken into account, even $\beta = 1$ can be destabilised.

The weak instability that we see in figure 3.1 is then exactly this dissipation induced destabilisation. As β is defined to be the relative strength of kinematic and Alfvén velocities we may express it in our nondimensionalisation via

$$\beta = \frac{\mathrm{Re}\sqrt{\mathrm{Pm}}}{\mathrm{Ha}}. \tag{3.66}$$

Recall that we limited ourselves to the quasi-galactic rotation rate $\mu_\Omega = 0.5$ and the nearly uniform azimuthal field generated by $\tau = 1$. This corresponds to an

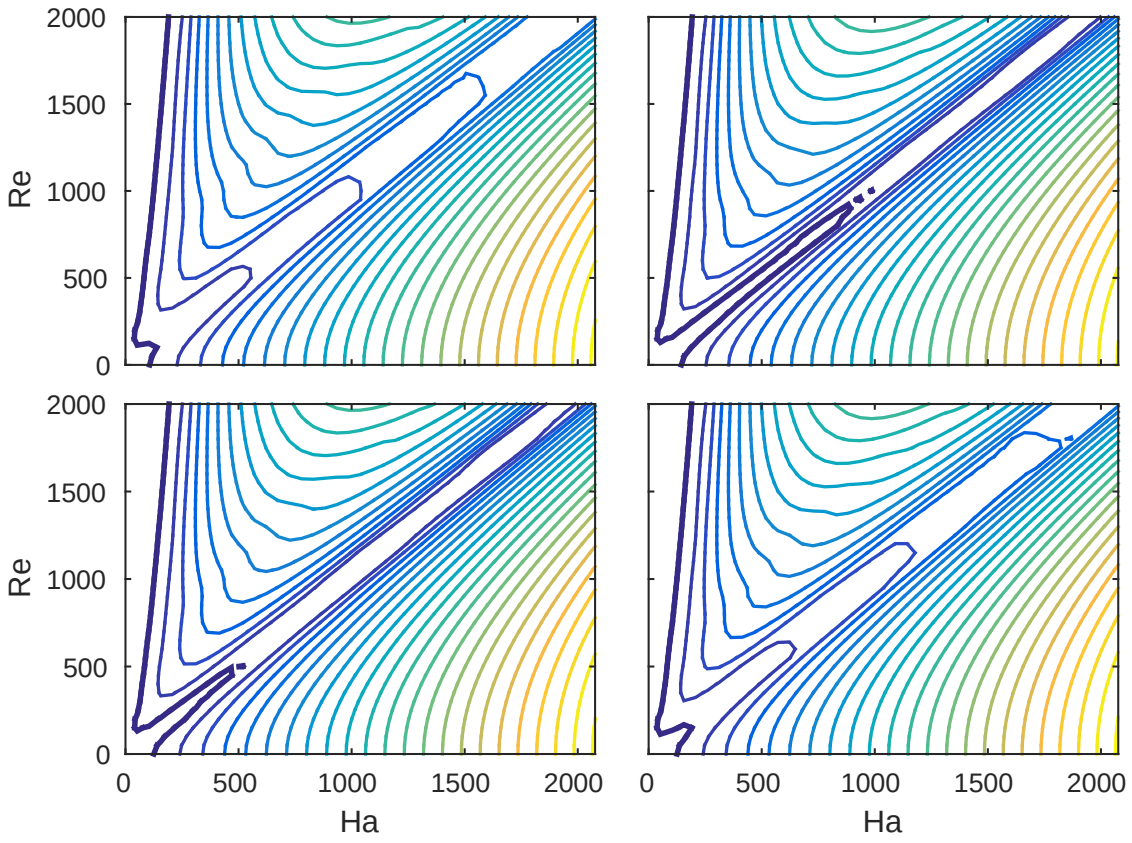

Figure 3.1: Plots showing the weak dissipation-induced instability of Chandrasekhar's equipartition between the AMRI and TI. In each plot the upper left region of instability is the AMRI, whilst the lower right is the TI. Contours are taken of the growth rate γ, for which positive values are plotted. The line of marginal stability is denoted by the thickest line. The various parameters take the values $\mu_\Omega = 0.5$, $\tau = 1$, $m = 1$ and $\delta = 0$, such that the magnetic field is purely azimuthal. Top left: Insulating boundary conditions. Top right: Perfectly conducting boundary conditions. Bottom left: Mixed (IC). Bottom right: Mixed (CI). The perfectly conducting case compares directly with figure 7 in Rüdiger *et al.* (2010), albeit covers a greater range and includes the equipartition instability. In comparison, Rüdiger *et al.* plotted $\mathrm{Re} = [0, 500]$ and $\mathrm{Ha} = [0, 400]$.

azimuthal magnetic field with steepness $\mu_B = B_\phi(r_o)/B_\phi(r_i) = 1$ (where μ_B is defined analogously to μ_Ω), and so we have the Chandrasekhar line $2\mu_\Omega = \mu_B$. It can be seen then that the radial profiles of the kinematic and Alfvén velocities are aligned radially, such that the equipartition $\beta = 1$ corresponds to the stable Re = Ha line seen in figure 3.1.

3.4 $\mathrm{Pm} = 10^{-6}$

3.4.1 Purely azimuthal magnetic fields

For the remainder of this chapter we focus on the specific case $\mathrm{Pm} = 10^{-6}$, the near-inductionless limit, which corresponds to the typical value of liquid metals. We shall examine the effect of each of the parameters in turn, beginning with τ in the purely azimuthal MRI, before looking at the effect of μ_Ω. Then, the axial field is reintroduced through δ, and the simultaneous variation of each parameter is discussed.

Varying the azimuthal field profile

Consider first the parameter τ, which we recall corresponds to the ratio of current running through the fluid versus current running through the inner cylinder. Let us take $\delta = 0$, and so examine purely azimuthal magnetic fields. Note that though all values of τ are valid, we focus mainly on the range $-3 < \tau < 3$, which covers the majority of the interesting dynamics. We use the values $\tau = \pm 100$ as approximations of the $\tau \to \pm\infty$ current solely in fluid cases, as this is suitably close to the limit reached at $\tau = \pm\infty$. For examples of the field profiles for selected τ see figure 3.2.

Whilst this varying magnetic field profile is not in itself a novel idea – Rüdiger *et al.* (2010) and Kirillov *et al.* (2014) have incorporated it in their previous works – a parameter range such as this has never been considered. General currents running in opposite directions, specifically those arising from the values $\tau < -1$, have not been

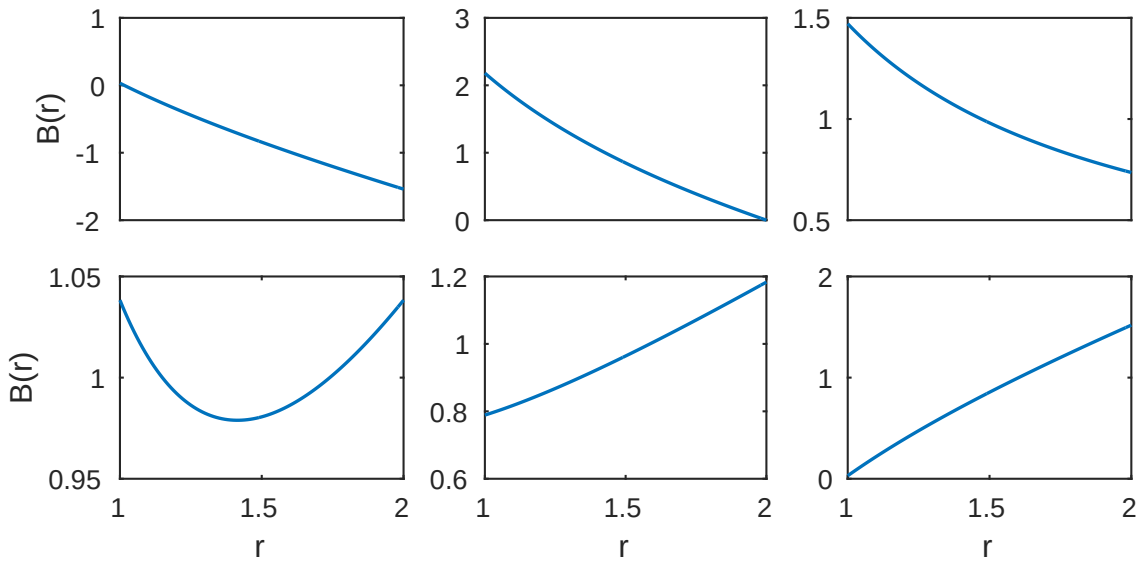

Figure 3.2: The azimuthal field geometry for different τ values. From top-left: $\tau = -100, -1, 0, 1, 2, 100$.

considered when expressing the magnetic field profile in terms of μ_B, and cannot be expressed in terms of a magnetic Rossby number.

First we focus our attention on $\tau > 0$; as seen in figure 3.2, this already encompasses a significant change in the gradient of the azimuthal field profile. It is seen that as one increases τ from zero, steadily increasing the proportion of current in the fluid, the AMRI becomes more readily destabilised in both the Reynolds and Hartmann parameters (figure 3.3). Moreover, as a consequence of the lower marginal Hartmann number, the Tayler instability is also more unstable. This is unsurprising really; we know that the Tayler instability is current driven, and so with more current available in the fluid the instability is more easily attained. Indeed, it has been long known that the Tayler instability is at its most unstable when the magnetic field is produced solely by current in the fluid (Seilmayer *et al.*, 2012; Tayler, 1973). Whilst we have taken $\tau = 100$ as an approximation for this case, it can be seen that $\tau = 5$ already rapidly approaches such a limit.

Now let us consider negative τ; that is again increasing the proportion of current in the fluid, but now in the opposite direction to the current in the core. We see from figure 3.4 that the dynamics are more interesting than the mostly subtle changes

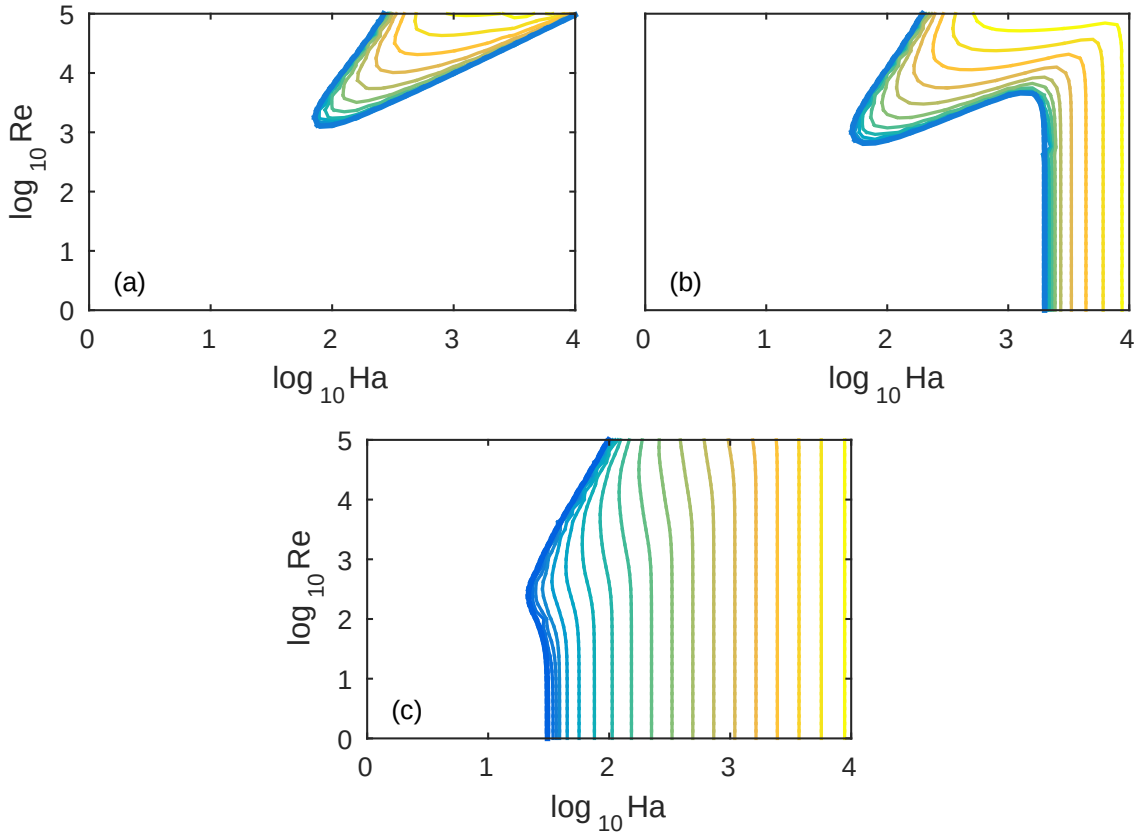

Figure 3.3: Contours of $\log_{10}\gamma$, with the parameters $\mu_\Omega = 0.26, \delta = 0$ and $m = 1$. a) $\tau = 0$, b) $\tau = 0.4$, c) $\tau = 100$. It is clear that increasing τ allows for earlier onset of instability in both the AMRI and Tayler instabilities.

in gradient found in figure 3.2 may have suggested. We now see a stabilisation of the AMRI between the values of $\tau = 0$ and $\tau = -1$. That is, adding current to the fluid here initially has the opposite effect that it had before. Considering that the differences in azimuthal field profiles are minor compared to that of $\tau > 0$, it is not obvious why this should be the case. This stabilisation effect can be amplified via increasing μ_Ω.

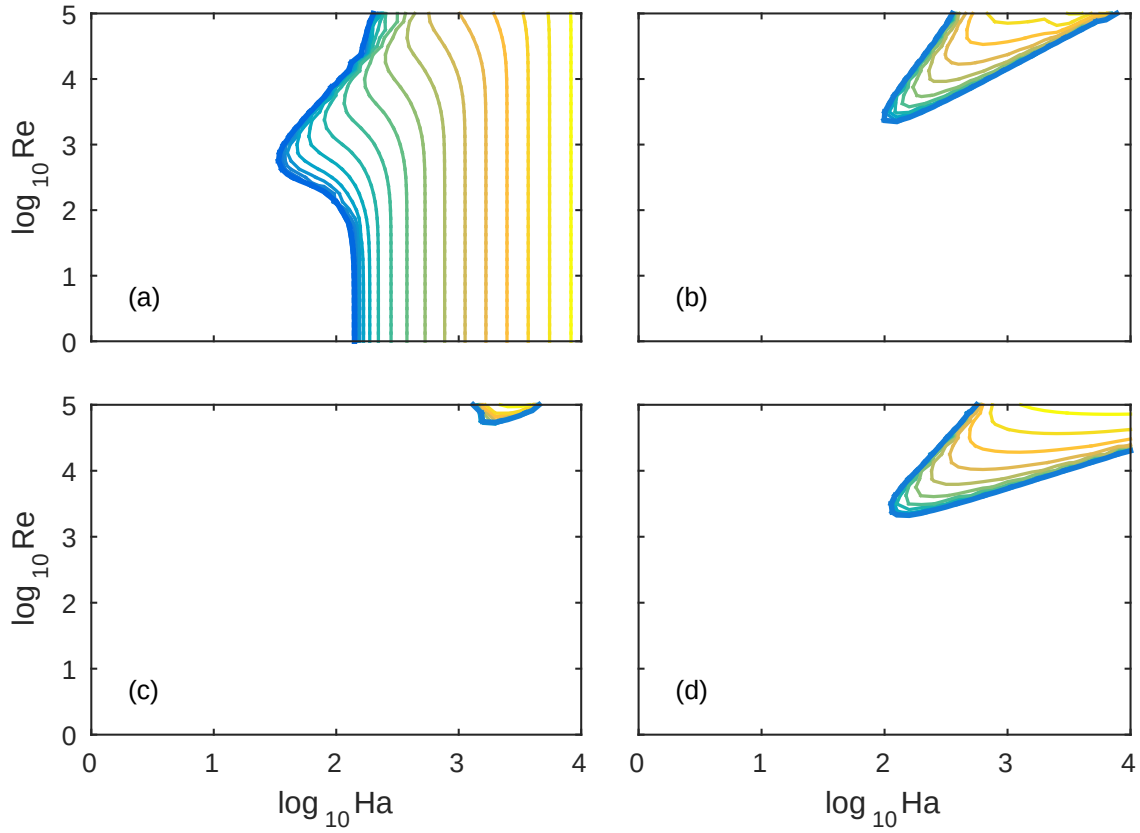

Figure 3.4: Contours of $\log_{10}\gamma$, with the parameters $\mu_\Omega = 0.26, \delta = 0$ and $m = 1$. a) $\tau = -1.4$, b) $\tau = -1$, c) $\tau = -0.6$, d) $\tau = -0.2$. The stabilisation around $\tau = -0.6$ is immediately apparent, whereas upon further decreasing τ the AMRI regains its usually instability for the AMRI and TI. Note that the value of $|\tau|$ is different to that of the positive τ case when comparing the equivalent onset of stability in Ha of the TI.

One immediate question pertains to the nature of these two branches of AMRI, and whether they represent a bifurcation between two distinct modes. Examining the $m = 1$ eigenmodes for both $\tau = -1$ and $\tau = -0.2$ – which straddle either side of the

stabilisation – yields two distinct structures (shown in figure 3.5). One mode has azimuthal flow centred at the midpoint of the annulus, as would be typical for the AMRI, whilst the other is seen to concentrate azimuthal flow at the outer boundary, suggesting some kind of boundary mode. These two modes are more unstable for the different ranges of τ either side of $\tau \approx 0.6$, at which the stabilities exchange. Clearer evidence of this is seen when we also have some imposed axial field (see section 3.4.2).

If we then let τ become more negative, note that current is more predominantly run through in the fluid, we regain the same kinds of dynamics found for large $\tau > 0$. We see that marginal stability tends towards the fully current driven limit, though like-for-like negative τ has a higher critical Hartmann number than positive τ. This acts to inhibit the Tayler instability, and is most likely a consequence of the unfavourable alignment of the flow and magnetic field, as they will act in opposite directions.

Varying μ_Ω

In this section we explore the effect that μ_Ω has on the various instabilities. This parameter, governing the fundamental profile of rotation, has a large influence on the existence of instability on both the Reynolds and Hartmann numbers. Indeed, for the traditionally defined inductionless MRI, where $B_\phi \sim 1/r$ the upper and lower Liu limits that exist on μ_Ω stifle any hope of application to Keplerian profiles. For our generalised azimuthal field profile then, for which the possibility of MRI beyond the Liu limits is realisable (Kirillov *et al.*, 2014), the way in which changing μ_Ω in conjunction with τ affects stability may offer insight into the parameter ranges where Keplerian rotation profiles are unstable.

Rüdiger *et al.* have previously examined the specific cases where there exists a steep rotation profile, $\mu_\Omega = 0$ and that of the quasi-galactic profile $\mu_\Omega = 0.5$ (though for $\mathrm{Pm} = 1$), whereas Hollerbach *et al.* (2010) restricted attention to $\mu_\Omega < 0.35$, showing the increasing critical Reynolds numbers. However, as this only considered the current in core ($\tau = 0$) azimuthal field profile, the Liu limits were in full effect.

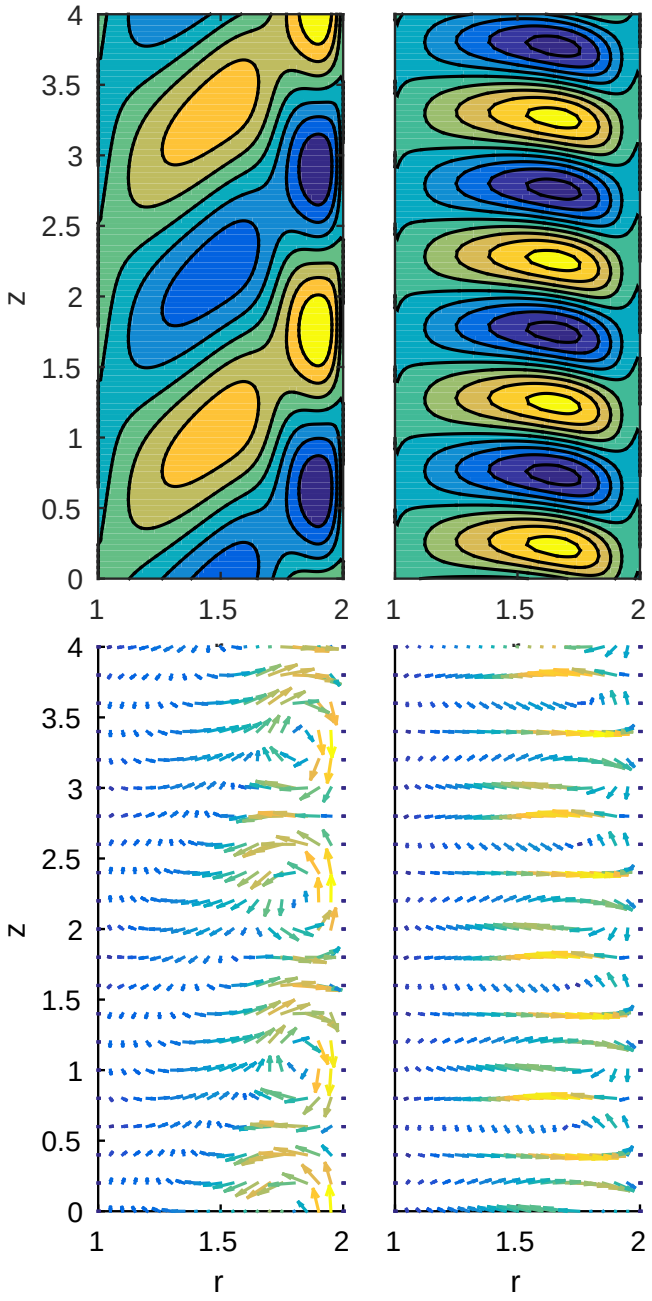

Figure 3.5: Eigenmodes of (3.4b) and (3.4d) taken at Re = 10^4 and Ha = $10^{2.5}$, for which the azimuthal velocity in a meridional cross section of the cylinder is plotted (top) and quiver plots are given for meridional circulation (bottom). Here $\delta = 0$, $m = 1$ and $\mu_\Omega = 0.26$. The different flow structures of the two eigenmodes clearly show there to be two different AMRI modes either side of the stabilisation at $\tau \approx -0.4$.

We consider μ_Ω upwards of the Rayleigh limit for $\tau \neq 0$. We investigate the recent work of Kirillov *et al.* (2014), and confirm in the linear regime that altered azimuthal field profiles allow for MRI at Keplerian values (and beyond). We examine the relationship between μ_Ω and τ, as although we know that the Liu limits can be broken, it is not yet confirmed at what Reynolds and Hartmann numbers; Kirillov *et al.* looked for the existence of *any* such instability via letting $\mathrm{Rm}, \mathrm{Ha} \to \infty$. Furthermore, the dynamics of the Tayler instability in such a regime are of interest.

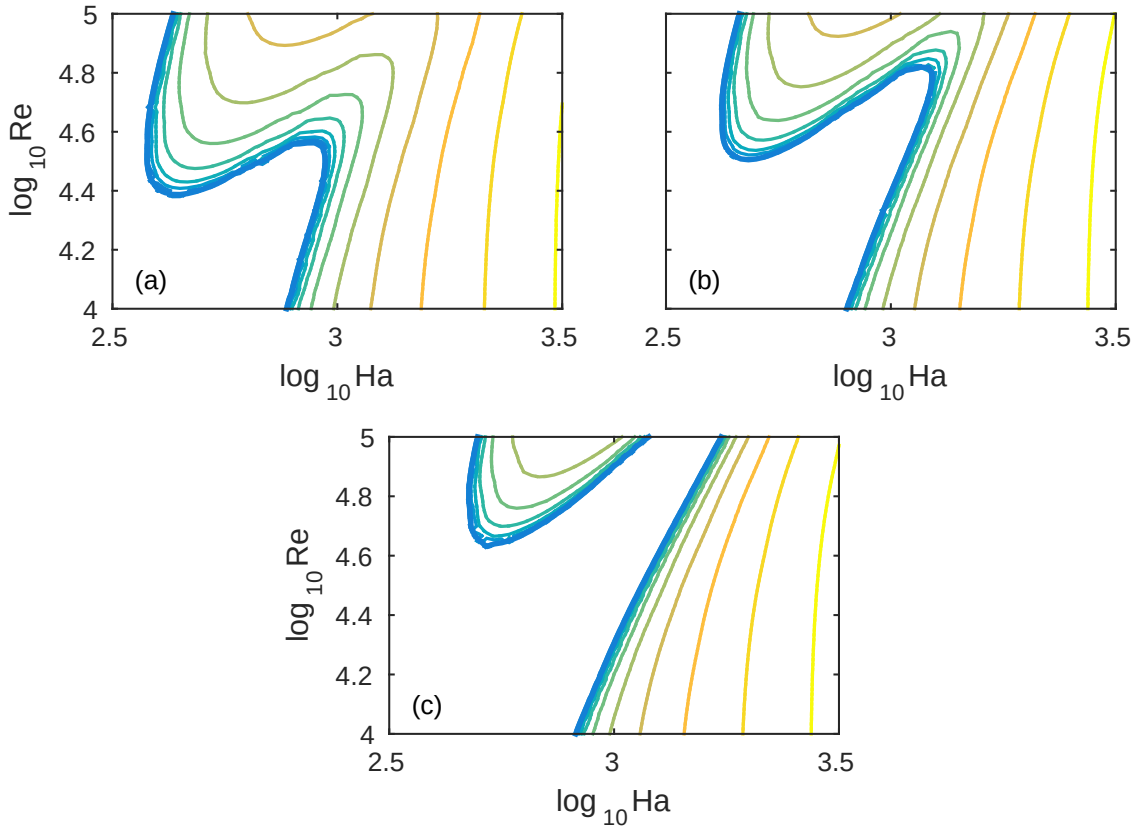

Figure 3.6: Plots of the $\mathrm{Pm} = 10^{-6}$ equivalent of the weak instability found for $\mathrm{Pm} = 1$ showing the dependence on μ_Ω. Here $\tau = 0.5$, $m = 1$ and a) $\mu_\Omega = 0.3975$, b) $\mu_\Omega = 0.4$, c) $\mu_\Omega = 0.4025$. Whilst the AMRI is found in such parameter regimes, it is clear that further increasing μ_Ω, even in small increments, causes the Reynolds threshold to rise markedly. If we were to take μ_Ω approaching that of the connecting curve of Kirillov *et al.* then the AMRI would become completely stable, with Re approaching infinity.

We have previously seen the existence of the dissipation induced weak instability of

Chandrasekhar's equipartition solution for Pm = 1; this should also be obtainable for our resistive, near inductionless fluid. Recall however that β was dependent on Pm – now we will not have the Re = Ha stable line. The combination of μ_Ω and τ will also control the existence and location of such an unstable region.

Indeed, we see that the unstable connection between AMRI and TI exists predominantly when μ_Ω is still relatively low valued. As the rotation is then increased in magnitude, the weak dissipation based instability is stabilised, leading to the familiar stable corridor. In figure 3.6 we consider a set of parameters located near to the Chandrasekhar line that intersects the connecting curve between the two Liu limits. We set the azimuthal magnetic field profile τ to be constant, and increase μ_Ω; this is essentially altering β. As should be the case, as β is decreased, one may note that marginal stability takes a much higher Reynolds number. Note also the size of the increase in this Reynolds number compared to the small increases in μ_Ω. According to the asymptotic theory, as μ_Ω is increased to be closer to the Liu limit curve, the critical Reynolds number should tend to infinity. Our linear numerics confirm this; increasing μ_Ω yet further rapidly yields Reynolds numbers so large that they require prohibitive numerical resolution for adequate convergence.

The question of the linear validity of Kirillov *et al.*'s connecting curve is also interesting. We are able to reproduce, between Ro = -1 and Ro ≈ 1, the stability curve, with strong agreement to the WKB theory. We take a number of $\mu_\Omega > 0.25$ and vary τ, seeing that when τ is close to the magnetic Rossby number Rb given in the connecting curve that both Re and the required resolution tend to infinity. We should note that though it is theoretically possible for instability for very flat profiles near the curve, the Reynolds numbers are completely unrealisable, both in the laboratory and numerics.

Finally, note that for any comparison with Kirillov *et al.*'s work, Ro and Rb may be expressed in terms of μ_Ω and τ as

$$\mu_\Omega = (r_i/r_o)^{-2\mathrm{Ro}}, \qquad \tau = (r_i/r_o)^{-2\mathrm{Rb}-2} - 1. \tag{3.67}$$

For comparison, the Keplerian value of Ro = -0.75 corresponds to $\mu_\Omega \approx 0.354$, and the upper Liu limit requires $\mu_\Omega \approx 800$.

3.4.2 Helical magnetic fields

Having systematically covered the various parameter combinations available when the applied magnetic field is purely azimuthal, we now add in an axial component with strength, relative to the azimuthal field, parametrised by δ. We expect that τ and μ_Ω will have the same effect on stability – and the Liu limit curve – and so do not repeat our previous discussion. However, now that the field is helical it possesses some innate handedness, such that our azimuthal mode numbers $\pm m$ are distinct. The axial field may then have a stabilising or *destabilising* effect, depending on the alignment of the field and flow. Furthermore, Kirillov *et al.*'s analysis identified that the axial field can allow for some resonant appearance of modes that are most unstable for $m \neq 1$, which we aim to evidence in the linear regime.

We should note that, whilst there is no reason we cannot take negative δ in our parameter search, this is physically equivalent to that of positive δ with an oppositely signed m.

Changing δ

The importance of the parameter δ to the properties of the MRI cannot be overstated. It is δ that controls the fundamental nature of the MRI variant after all – from the AMRI when the axial field is weak through to the SMRI when the axial field is dominant. Indeed, with large δ the SMRI is quite stable to differential rotation (more so than any of the inductionless MRI (Hollerbach & Rüdiger, 2005)).

We first restrict attention to the $m = 1$ modes, making note of the effects of transitioning from weak to strongly axial magnetic fields. As is to be expected, in figure 3.7 we note that the Tayler instability – generated via predominantly azimuthal fields – is stabilised at only $\delta = 0.05$. We see that by $\delta = 0.5$, the MRI is almost completely stable (for moderate Re); the axial magnetic field does not need to be particularly large to significantly alter the stability of the system.

Of more interest is what happens when we let $m = -1$. First, if we take some constant $\delta \neq 0$ and vary τ, in figure 3.8 we see an analogous stabilisation effect

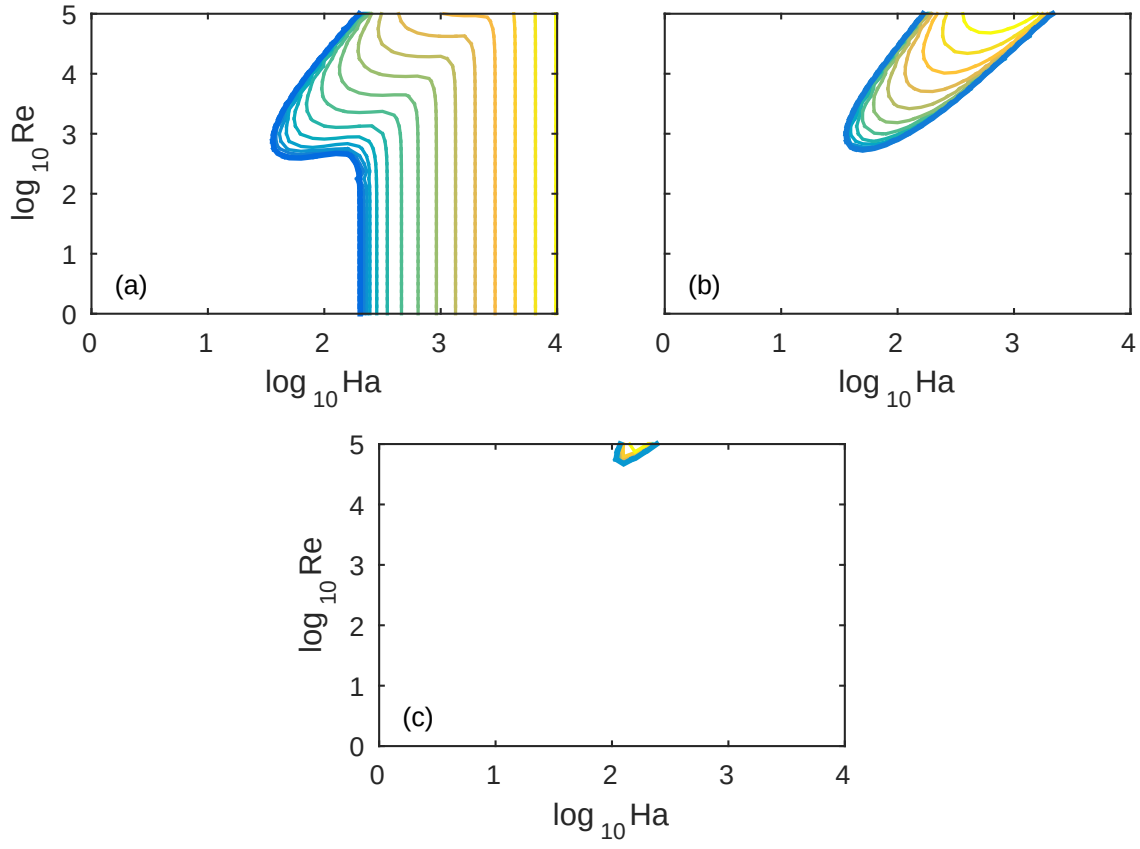

Figure 3.7: Contours of $\log_{10}\gamma$ for the case of helical magnetic fields at Pm = 10^{-6}, with $\mu_\Omega = 0.26$, $\tau = 0.8$ and $m = 1$. The stabilising effect of the helical magnetic field is seen when increasing from a) $\delta = 0.01$ through b) $\delta = 0.05$ and then to c) $\delta = 0.5$. When δ is small there is little difference between the instabilities for helical and azimuthal fields, but as the axial magnetic field component is increased we notice a sharp stabilisation of the Tayler instability, followed by the stabilisation of the nonaxisymmetric helical MRI.

to that seen in section 3.4.1, whereby the instability swaps between two different unstable modes. Taking the same parameter range $-1 < \tau < 0$, we see that as δ is increased from zero, the separation between these modes is made clearer. The exchange between the two is in some ways unsurprising; the transition between AMRI and nonaxisymmetric HMRI is, after all, continuous. These are therefore likely to be the same modes observed in figure 3.4.

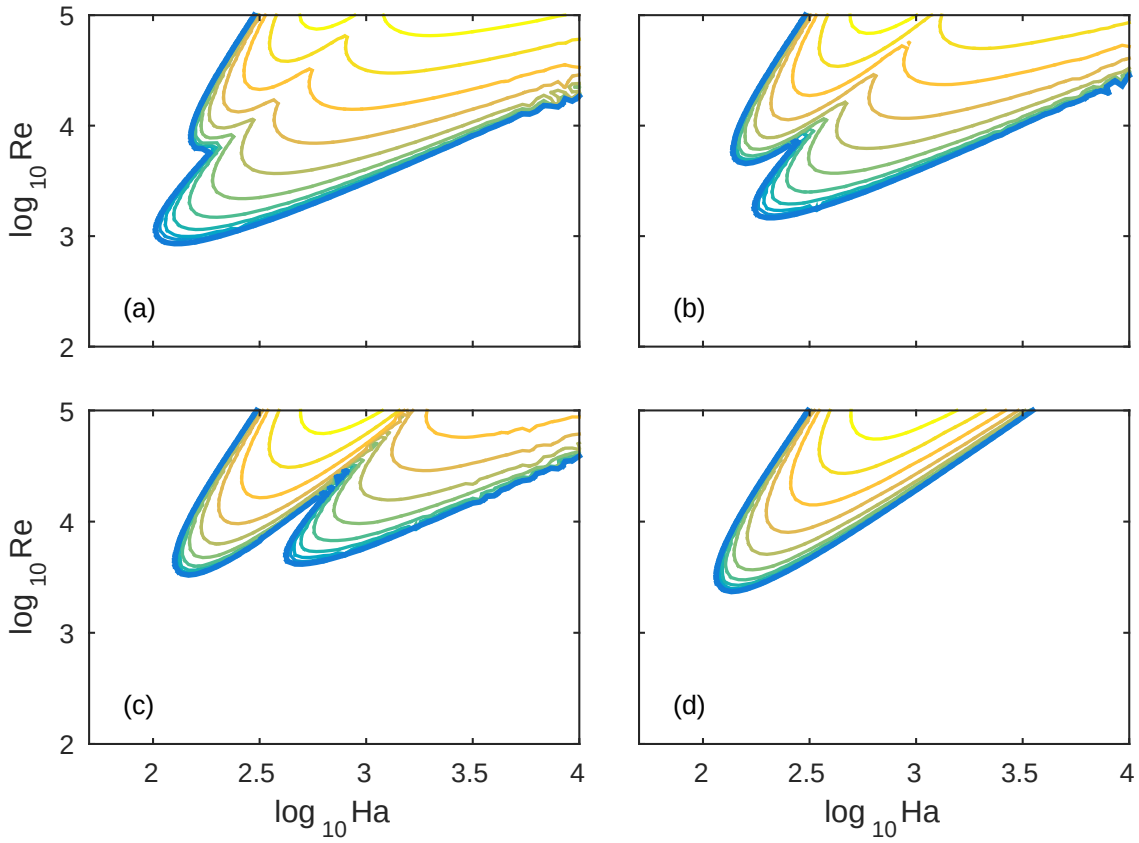

Figure 3.8: Contours of $\log_{10}\gamma$ for the case of helical magnetic fields at $\mathrm{Pm} = 10^{-6}$, with $\mu_\Omega = 0.26$, $\delta = 0.3$ and $m = -1$. Here we examine the effects of changing τ from a) $\tau = -0.75$ to b) $\tau = -0.5$, c) $\tau = -0.25$ and d) $\tau = 0$. There is a clear switching between two separate unstable modes, each dominant for different magnetic field profiles. Importantly, these modes can be seen to have completely different eigenmode structures, reinforcing that they are two distinct mode types.

Indeed, if we plot the eigenmodes (figure 3.9), we see similar – yet not exact – physical structure to that of figure 3.5. Now, however, we have one mode completely localised to the inner boundary with a relatively small axial wavelength, whereas

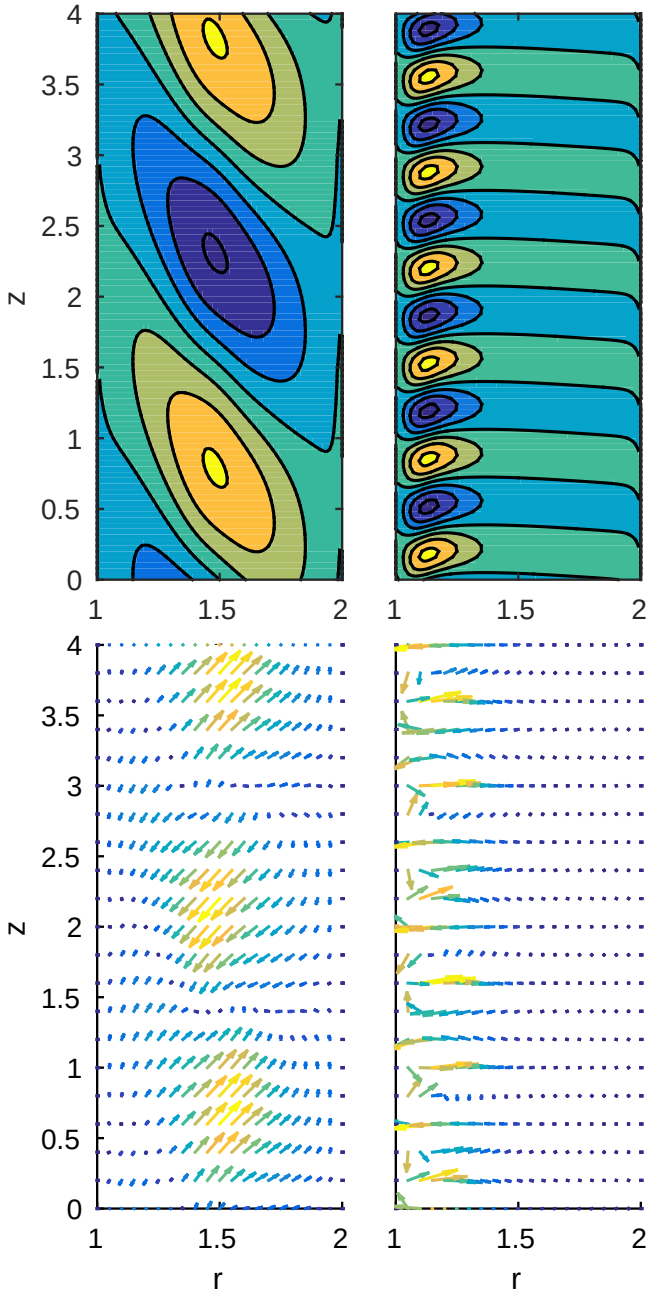

Figure 3.9: Plots of the two different eigenmodes identified in figure 3.8, showing the azimuthal velocity of a meridional cross section (top) and meridional circulation (bottom). Re = 10^4 and (left) Ha = 10^3, (right) Ha = $10^{2.3}$.

the other mode affects the full gap width and has a relatively large axial wavelength. These correspond to boundary and global modes respectively.

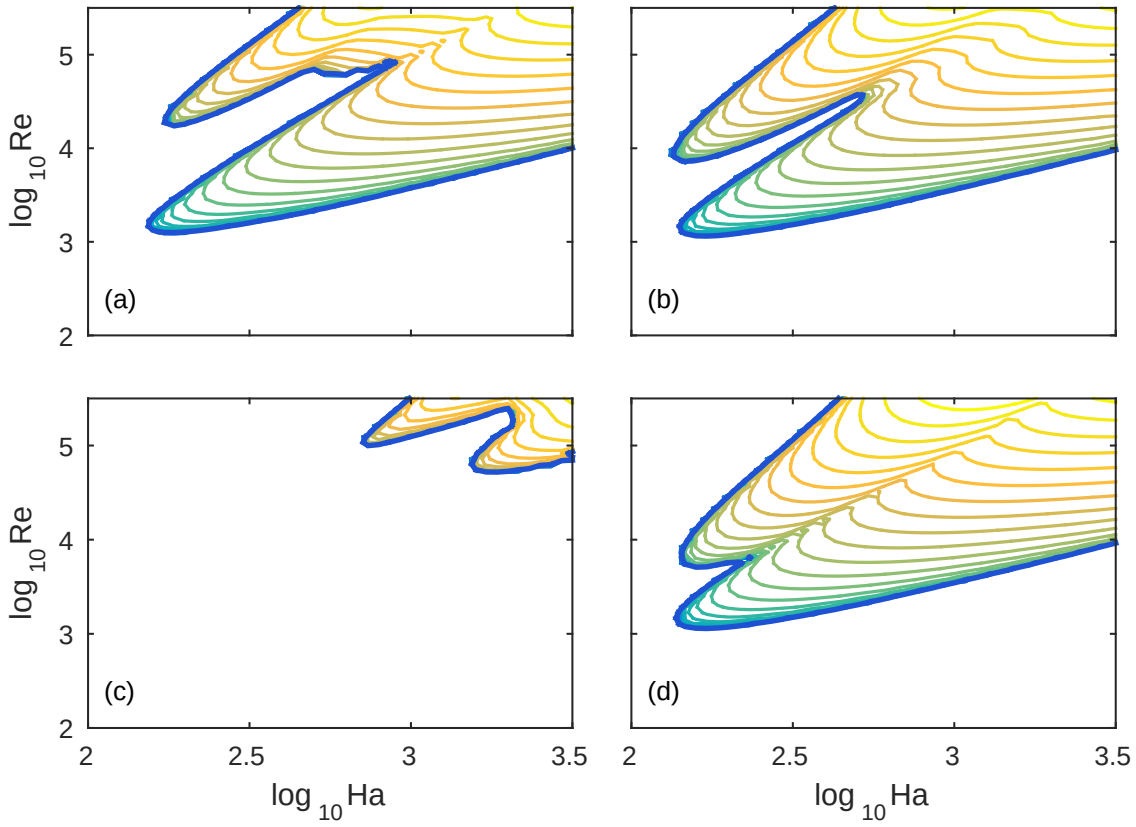

Figure 3.10: Contour plots of $\log_{10}\gamma$ at $\mathrm{Pm} = 10^{-6}$ that show the inherent destabilisation caused by the axial magnetic field. We have that $\tau = -0.6$, $m = 1$ and $\mu_\Omega = 0.26$, and also that a) $\delta = 0$, b) $\delta = 0.3$, c) $\delta = 0.4$, d) $\delta = 0.5$. We see that for $m = -1$ increasing δ can destabilise the system, with the parameter space separation between the two instabilities present governed by the magnitude of δ. Plot a) corresponds to that shown in figure 3.4c), and shows the existence of the two modes types that were briefly mentioned.

If we now fix τ at some constant value and vary δ for $m = -1$, we see immediate differences in the dynamics compared to $m = +1$. It is seen clearly in figure 3.10 that increasing δ causes the flow to become *more* unstable. It is only when moderately high values of δ are attained that the stabilisation process occurs. We see that the lowest critical Reynolds and Hartmann numbers occur for $\delta \approx 0.3$, for which the axial field is not strictly weak. Even the Tayler instability is still present for such

parameters, even though it is generally defined to be an instability occurring in only dominantly azimuthal fields. The symmetry breaking effect of non-zero δ can be seen clearly in figure 3.11.

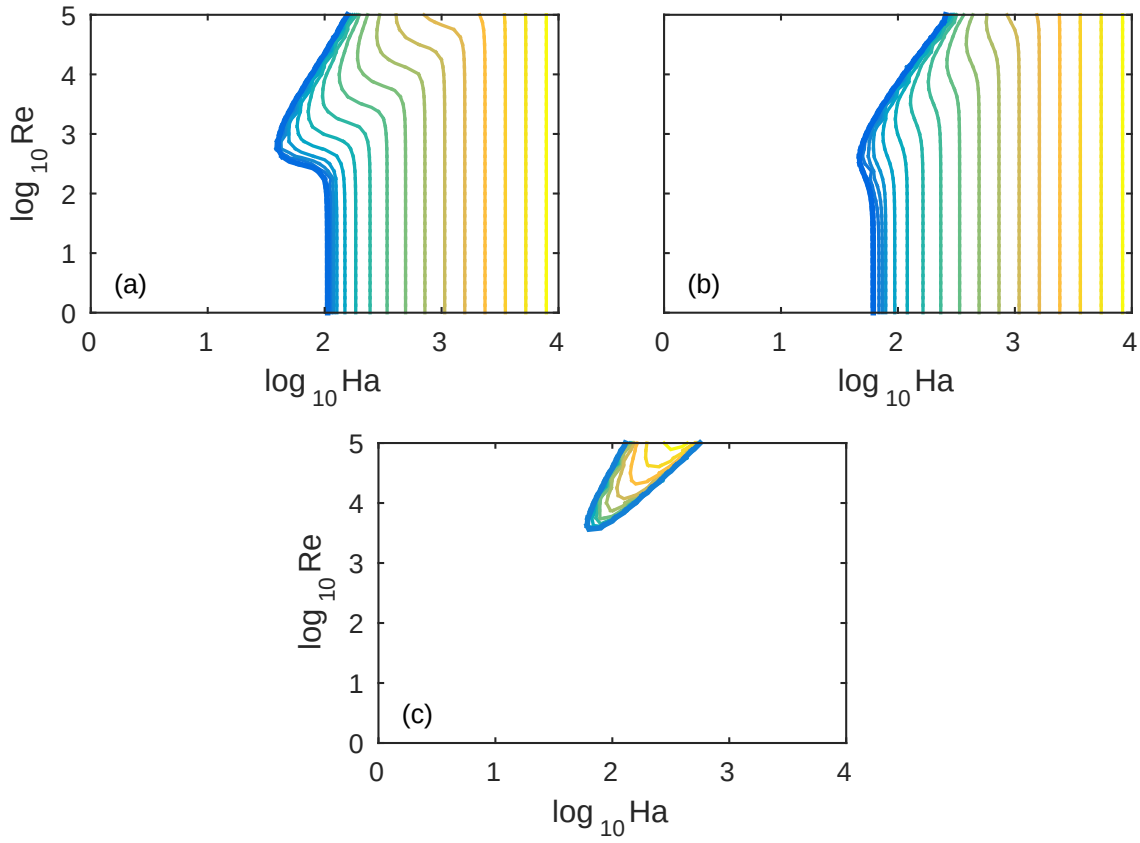

Figure 3.11: Contour plots of $\log_{10}\gamma$ at Pm = 10^{-6} that show the symmetry breaking of $m = \pm 1$ modes as δ is increased. Here we have that $\mu_\Omega = 0.26$, $\tau = 1$, and a) $\delta = 0$, b) $\delta = 0.3$ and $m = -1$, c) $\delta = 0.3$ and $m = +1$. Whilst the $m = +1$ mode is stabilised, the $m = -1$ mode becomes more unstable as δ is increased from zero.

It is more convenient to visualise the destabilising effect of the axial magnetic field by plotting the critical values of either Re or Ha against δ. This has the added advantage of enabling the marginal stability for a number of azimuthal wavenumbers to be plotted on the same figure, and for direct comparisons between them. Motivated by the results of Kirillov *et al.*, whereby unstable non unitary m were found, we look for evidence of their banded nature. We do note, however, that it is impossible for us to give direct comparison to the literature, as a consequence of the radial wavenumber that was introduced in Kirillov *et al.*'s WKB methodology.

The WKB analysis shows that when m is positive then $m = 1$ is always the most unstable mode; as such, we focus attention only on the negative m. We also need to be careful in choosing the values of Re and Ha to keep constant. Indeed, to encompass both MRI and TI, we set Re$= 10^0$ and Re$= 10^4$ when varying Ha, and Ha$= 10^{2.4}$ when varying Re. We further examine the range $-100 < \tau < 100$ for fixed Re, and limit ourselves to $-1 < \tau < 1$ for fixed Ha in order to avoid a situation where the Tayler instability exists for all points.

First let us consider the case when $Re = 10^4$. From figure 3.12, it is clear that, for certain values of τ, $m = -2$ and $m = -3$ are the most unstable modes. In particular, for $0.1 < \delta < 1$ on the upper and lower branches respectively, $m = -2$ and $m = -3$ have critical Ha that extend beyond that of $m = -1$. As τ (positive) is increased we find that such areas of parameter space only encompass that of large δ, as found by Kirillov *et al.* This behaviour can be justified by considering that these modes exist in a banded structure, with band widths dependent on the magnetic Rossby number Rb, here essentially measured by τ. Thus changing τ directly corresponds to changing the width of each of the bands. For the negative values of τ we may see the banded structure appear in the form of an $m = -1, 0, -2, -1...$ pattern (though missing the $m = 0$ in our purely nonaxisymmetric analysis). This also holds for the Tayler instability. If we were to instead fix Ha and vary Re we see that, aside from a specific parameter range about $\tau = 1$, the $m = -1$ mode is the most unstable for all δ.

These two results imply that, whilst resonant higher m modes *can* appear for large δ, they are excited via increasing magnetic field strength, and not increasing angular velocity. This suggests that the magnetic field drives higher modes relatively more than was the case for the $m = 1$ mode, whereas the rotation excites instability with no particular emphasis on the mode.

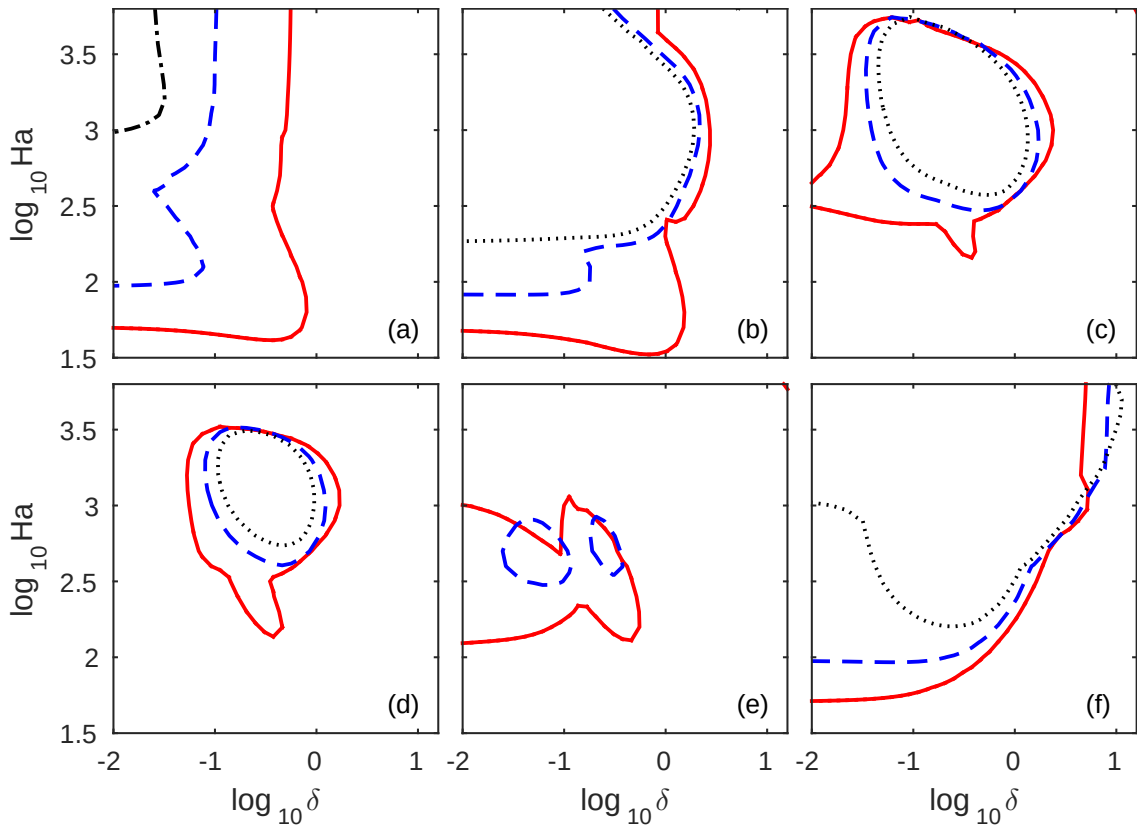

Figure 3.12: Plots of marginal stability for Pm $= 10^{-6}$ and Re $= 10^4$. We have that: a) $\tau = -100$, b) $\tau = -3$, c) $\tau = -0.75$, d) $\tau = -0.5$, e) $\tau = 0$, and f) $\tau = 100$. Plain curves correspond to $m = -1$ modes, dashed correspond to $m = -2$, and dot-dashed correspond to $m = -3$ modes. These graphs are informative of the effect τ has on higher modes, such that for $-3 < \tau < 0$ there exists a more unstable $m = -2$ mode located at modest values of δ. On the upper instability branch we may even note that the $m = -3$ mode is most unstable for a small range of δ. For negative values of τ, increasing towards zero allows for these higher m modes to be found at smaller values of δ. For positive values of τ, we see that the higher m modes are more stable than the $m = \pm 1$ modes for all but the very large values of δ, at large τ.

Chapter 4

Generalised quasi-linear approximation of the HMRI

In the previous chapter we explored the linear stability of nonaxisymmetric inductionless MRI, which is of use to the MRI laboratory experiments. However, such experiments are not the only way to probe the dynamics of the MRI. Direct statistical simulation (DSS) has received much attention recently as an alternative approach to investigating astrophysical flows. Since DSS is still in its infancy however, the conditions under which it is accurate are still being determined. To that end, in this chapter we perform direct numerical simulations (DNS) on the axisymmetric HMRI under the generalised quasilinear approximation (GQL), which is essentially equivalent to DSS. We ask whether GQL, which includes the self-consistent interaction of large-scale modes, can more accurately describe the low-order statistics of the HMRI than standard quasilinear (QL) theory, which only includes self-consistent interaction of the mean flow. Via a comparison of the various statistics, we find that only relatively few large-scale modes are required to accurately reproduce the statistics of the HMRI, providing motivation for future DSS implementations to be based upon GQL, and not QL. Moreover, this implies that to accurately realise the HMRI, one only requires the full nonlinear interactions of a few large-scale modes, and the other nonlinear modal interactions are relatively unimportant.

4.1 Introduction

4.1.1 Direct statistical simulation

In chapter 1, when introducing the MRI it was noted that direct numerical simulations can often be difficult to perform for parameters pertinent to astrophysical disks. Indeed, in general it is difficult to perform DNS for many astrophysical phenomena, due to the large range of scales (in both space and time) that are usually involved. For DNS, one must make sure that such flows are adequately resolved – often the smaller scales feed back onto the larger scales and are therefore integral to the dynamics – which is a tall order for even the most powerful parallelised arrays. This was precisely the reason that focus shifted to laboratory experiments, eventually leading to the discovery and exploration of the various forms of inductionless MRI. Whilst this has led to a number of fruitful avenues of research, the experiments are unfortunately unable to produce the SMRI, and therefore have limited applicability to the angular momentum transport in actual disks. There are many examples of other such flows for which it is difficult to perform DNS or laboratory experiments, motivating the development of a new technique for their study – direct statistical simulation (DSS) for astrophysical flows (Tobias *et al.*, 2011). In DSS, the statistics of the flow are obtained via solving some hierarchy of cumulant equations and applying a closure, rather than via an averaging as one would do in DNS.

Direct statistical simulation provides an attractive alternative to DNS due to the numerous computational advantages it possesses. It takes advantage of the fact that statistics tend to vary slowly with regards to time, and are smooth in space, enabling the use of lower modal resolutions. Though a fairly recent development, there have been a number of papers demonstrating its usefulness. Most relevant to our topic, Squire & Bhattacharjee (2015) utilised DSS to probe the scaling laws governing the MRI dynamo process in a shearing box set-up, which would not have been possible under normal DNS. Furthermore, Tobias *et al.* (2011) examined DSS for jets on a rotating spherical surface, which they then benchmarked against the DNS. They showed that jets were formed under DSS, even though the statistical simulation

utilised doesn't allow for cascades or inverse cascades. This highlights another key advantage of DSS – being able to remove complicated nonlinear behaviour whilst keeping important physical processes may go a long way towards illuminating the underlying physics at play.

The aforementioned works performed DSS using the CE2 cumulant expansion scheme, which is essentially equivalent to the quasilinear (QL) approximation. This is formally equivalent to stochastic structural stability theory (S3T) developed by Constantinou *et al.* (2013); Farrell & Ioannou (2007); Farrell & Ioannou (2008). This scheme has been shown to be viable for systems near equilibrium by Bouchet *et al.* (2013). Recently, S3T has been used by Fitzgerald & Farrell (2016) to provide a theory for jets in stratified turbulence, and allowed for the explanation of the mechanism by which the jets are formed, as well for a number of their other properties.

Though shown to be extremely promising in these papers, it should be noted that the CE2 scheme is not without its shortcomings. Indeed, one could not expect a quasilinear formalism to be universally accurate with regards to fully nonlinear DNS (NL DNS). For example, Tobias & Marston (2013) examined a series of jets both in and out-of-equilibrium. Whilst it was found that near equilibrium CE2 produces accurate results, when the jets were out-of-equilibrium CE2 was found to fail in accurately reproducing the number and strength of jets. Srinivasan & Young (2012) found similar inconsistencies, with CE2 proving unable to accurately describe the onset of zonostrophic instability. Finally, Ait-Chaalal *et al.* (2016) showed that whilst CE2 properly captures the dynamics of waves in atmospheric flows in some circumstances (i.e weaker waves), better closure schemes are required for more general climate modelling. Clearly this is an undesirable scenario; to overcome it, alternative DSS schemes are sought. There are currently two options for rectifying the problem: including the nonlinear eddy interactions in the statistical formalism (CE2.5), or generalising the quasilinear approximation. The first, whilst having been shown to improve the accuracy of DSS far from equilibrium (Marston *et al.*, 2014), does so at a significant computational cost. We instead focus on the generalised quasilinear approximation. This approximation has so far been applied to two-dimensional turbulence on a spherical surface and β plane (Marston *et al.*,

2016), where it was shown to produce more accurate solutions than QL theory. It has also been applied to 3D rotating plane Couette flow, where again very promising results were found compared to QL (Tobias & Marston, 2017).

Much like how CE2 is the statistical representation of QL theory, a statistical formalism GCE2 can be constructed for the GQL theory. However, a corresponding statistical implementation does not yet exist. Indeed, as such a topic is still in its infancy, it is not yet clear whether GCE2 would offer substantive improvement in accuracy, or whether it would even be a worthwhile endeavour. In order to establish the potential of GCE2, similar investigations to that of Marston *et al.* (2016) and Tobias & Marston (2017) must be performed for a variety of different flow regimes. To this end, in this chapter we apply the GQL approximation to the HMRI to gauge the potential viability of GCE2. Through this, we can ascertain the efficacy of GCE2 when applied to wall bounded, rotationally driven electrically conducting flows. Because the HMRI exhibits turbulence even it its axisymmetric state, we are able to obtain statistics at numerically feasible DNS resolution. This enables us to take parameters far from equilibrium, where QL theory encounters problems (as is to be expected for highly nonlinear regimes). The numerical method we use to calculate fully nonlinear DNS is discussed in sections 2.4 and 2.5.2. In this chapter, we first introduce QL and GQL theory, before briefly discussing suitable alterations to the numerics. We then establish a set of DNS solutions and use a series of key diagnostics (energy spectra and cumulants, for example) to benchmark varying degrees of GQL.

4.1.2 Generalised quasilinear approximation

Here we give a brief overview of the quasilinear approximation, and discuss the generalised quasilinear approximation, as introduced by Marston *et al.* (2016). For brevity, we define the approximations using the azimuthal velocity v, though the same expansions hold for our other variables.

Quasilinear theory involves splitting the flow into mean and eddy (fluctuation) com-

ponents, via a Reynolds decomposition. For our azimuthal velocity, this would set

$$v = \bar{v} + v', \tag{4.1}$$

where the overbar represents an averaging, and the prime denotes the fluctuations from the mean. As the HMRI is axisymmetric, the natural average to take here is the $k = 0$ mode, the axial mean. The quasilinear approximation then involves linearising all equations but that involving the mean; i.e. we incorporate mean/eddy $\rightarrow$ eddy and eddy/eddy $\rightarrow$ mean nonlinearities but discard eddy/eddy $\rightarrow$ eddy interactions.

Standard QL theory has many shortcomings however – the nonlinear interactions that distribute energy to higher modes have been discarded, and so there can be no energy scattering off of the mean. This impedes the generation of cascades or inverse cascades (Tobias *et al.*, 2011). To rectify this, let us generalise our mean and fluctuations to large- and small-scale flow components, where we define what constitutes large and small scale via some (arbitrary) wavenumber Λ. This can be achieved via the application of some spectral filter,

$$v = \sum_{k=0}^{\Lambda} v_{lk} e^{ik\kappa z} + \sum_{k=\Lambda+1}^{\infty} v_{hk} e^{ik\kappa z}, \tag{4.2}$$

where v_l and v_h denote the large and small scales respectively (referred to as l for 'low' modes and h for 'high' modes). As noted by Marston *et al.* (2016), setting $\Lambda = 0$ in our GQL formulation is equivalent to the standard QL approximation. It can be seen that taking $\Lambda \rightarrow \infty$ and defining every mode to be large scale then involves solving the full set of nonlinear equations, and is equivalent to NL DNS.

Much like for QL, performing GQL involves retaining only *some* of the nonlinear interactions, and linearising the rest. Though it is more generalised due to the increased number of large scale modes, these interactions are similar to those described previously. We
retain:

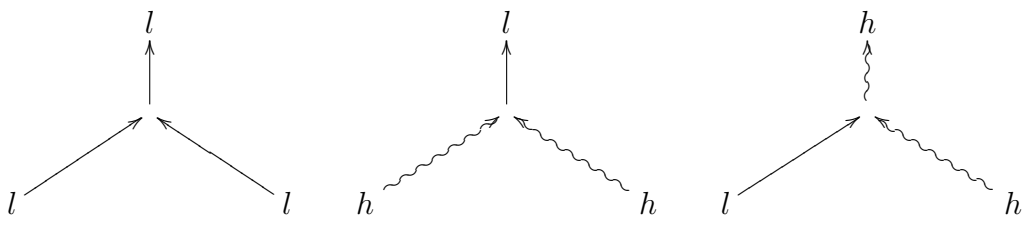

dispose:

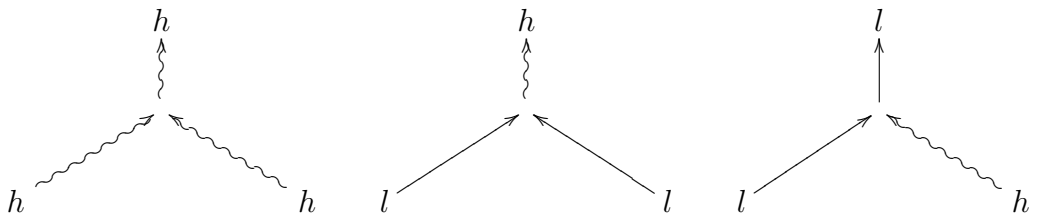

Here the low/high → high interaction is responsible for transferring energy between different high modes, and is referred to as scattering off of the mean. The low/low → low and high/high → low triad interactions are essential in keeping the approximation nonlinear in the large scales, whilst discarding the high/high → high interactions ensures that the approximation is formally linear in the fluctuations. Finally, the low/low → high and low/high → low triad interactions are discarded in order to conserve energy and enstrophy and enable closure (Marston *et al.*, 2016).

In performing GQL we may trivially alter the cut-off scale defining large and small scale modes. However, this is not trivial when considering the application to DSS; each Λ requires a bespoke formalism. Due to this, and the desire to utilise the lowest possible Λ to retain the computational advantages inherent to DSS, we aim to find the optimal Λ such that the key properties of the HMRI are accurately produced by GQL. If this can be done for relatively small Λ, the prospect of utilising similar formalisms for DSS is clearly very appealing.

4.2 Mathematics

Our general set-up is the same as in chapter 2, but since now we are solely interested in the HMRI, the imposed axial magnetic field in the system is generated solely by running current in the inner core. The flow is therefore axisymmetric. As before, we denote the inner and outer radii and angular velocities as r_i, r_o, Ω_i and Ω_o, respectively, and set the aspect ratio to $r_i/r_o = 0.5$ to coincide with that of the PROMISE experiment. The basic state magnetic field takes the form $\mathbf{B}_0 = B_z(0, \beta/r, 1)$ – note that β is not the same quantity as that used in chapter 3. Though the discussion in this chapter will not relate directly to possible experiments, this choice of aspect

ratio is particularly well explored in the literature, and so finding previously calculated critical parameters for the onset of instability is straightforward. We again assume our cylinders to be infinite.

The governing equations given in the previous chapter, which are restated for convenience, again apply. Therefore, we have the Navier-Stokes and induction equations (after some rearranging and the use of vector identities) alongside the incompressibility conditions,

$$\mathrm{Re}\ \frac{\partial \mathbf{U}}{\partial t} - \nabla^2 \mathbf{U} = \mathrm{Re}\ (\mathbf{U}\cdot\nabla)\mathbf{U} + \mathrm{Ha}^2\mathrm{Rm}^{-1}\ (\nabla\times\mathbf{B})\times\mathbf{B} \tag{4.3}$$

$$\frac{\partial \mathbf{B}}{\partial t} - \mathrm{Rm}^{-1}\ \nabla^2\mathbf{B} = \nabla\times(\mathbf{U}\times\mathbf{B}) \tag{4.4}$$

$$\nabla\cdot\mathbf{U} = 0 \tag{4.5}$$

$$\nabla\cdot\mathbf{B} = 0 \tag{4.6}$$

We have nondimensionalised by scaling lengths with the gap width, $r = (r_o - r_i)\,\hat{r}$, time on the rotational time-scale, $t = \Omega^{-1}\,\hat{t}$, velocity as $\mathbf{U} = (r_o - r_i)\Omega\,\hat{\mathbf{U}}$, and the magnetic field with the strength of the axial magnetic field, $\mathbf{B} = B_z\,\hat{\mathbf{B}}$. In the interest of readability, $\hat{}$ notation is subsequently ignored.

As we are only interested in fluids with $\mathrm{Pm} \approx 0$, as well as axisymmetric flows, there are a couple of simplifications that can be made to the governing equations. First of all, we may automatically satisfy the incompressibility conditions via decomposing $\mathbf{U}$ and $\mathbf{B}$ into toroidal and poloidal components, now written as

$$\mathbf{U} = v\,\mathbf{e}_\phi + \nabla\times(\psi\,\mathbf{e}_\phi), \tag{4.7}$$

$$\mathbf{B} = b\,\mathbf{e}_\phi + \nabla\times(a\,\mathbf{e}_\phi), \tag{4.8}$$

due to the axisymmetry. Secondly, that our Pm is small allows for the use of the low-Rm inductionless approximation, as derived in section 2.1,

$$\mathrm{Re}\frac{\partial \mathbf{U}}{\partial t} - \nabla^2\mathbf{U} = -\nabla p - \mathrm{Re}(\mathbf{U}\cdot\nabla)\mathbf{U} + \mathrm{Ha}^2(\nabla\times\mathbf{b})\times\mathbf{B}_0, \tag{4.9}$$

$$0 = \nabla^2\mathbf{b} + \nabla\times(\mathbf{U}\times\mathbf{B}_0). \tag{4.10}$$

These equations show that the magnetic field does not have to be evolved in time concurrently with the velocity field as the time derivative plays no part in the low

Rm induction equation. This simplifies our numerics somewhat, as we are then able to calculate **b** at each time-step via linear operations with **U**.

Finally, we require boundary conditions for both the velocity and magnetic field. For velocity, this is immediate, for it is clear that this set-up demands no-slip conditions at the cylinder walls,

$$v = r_{i,o}\Omega_{i,o} \quad \text{at } r = r_i \text{ and } r = r_o, \tag{4.11}$$

$$\psi = \psi' = 0 \quad \text{at } r = r_i \text{ and } r = r_o. \tag{4.12}$$

For the magnetic field, we have a choice as to whether to specify an insulating or conducting cylinder. In order to allow the use of results obtained for the PROMISE experiment (Rüdiger *et al.*, 2006), it is prudent to make the boundaries perfectly conducting, as the experiment itself uses copper; certainly not an insulating material. Thus, we have that the tangential electric field and normal magnetic field vanish at the boundary, from which it is straightforward to find that the boundary conditions on b and a must be,

$$\frac{\partial b}{\partial r} + \frac{b}{r} = 0, \tag{4.13}$$

$$a = 0. \tag{4.14}$$

To solve the equations, along with their boundary conditions, we employ the method discussed in sections 2.4 and 2.5. That is, we discretise in time via a Crank-Nicolson scheme and in space via a Fourier-Chebyshev pseudo-spectral method.

4.2.1 Generalised quasilinear terms

It is convenient that the generalised quasilinear approximation only really affects the nonlinear section of our numerical method. Here we give a brief description of the alterations required in the procedure, and refer back to section 2.5.2 for the technical details.

The crux of the approximation lies in the retention and deletion of certain nonlinear triad interactions, depending on the combination of large- or small-scale modes

that are involved. The separation of our variables into the two scales is easily accomplished in the spectral expansion; we split our variables into two Fourier series expansions, each containing what we define to be the low and high modes via the spectral filter Λ. So,

$$v_{nk} = [v_{nk}]_{low} + [v_{nk}]_{high} = \sum_{n=1}^{N+2} \sum_{k=0}^{\Lambda} v_{nk} e^{i\kappa z} T_{n-1}(x) + \sum_{n=1}^{N+2} \sum_{k=\Lambda+1}^{K} v_{nk} e^{i\kappa z} T_{n-1}(x) \quad (4.15)$$

Then we are able to perform the spectral transforms separately on the low and high variables.

Of course, this greatly increases computational effort; as all transforms must be performed twice. As such, the generalised quasilinear approximation is not an approximation one would take to save time. The evaluation of the nonlinear terms proceeds as in the previous section, with low and high components obtained for $\mathbf{U}$ and $\nabla \times \mathbf{U}$. $\mathbf{U} \times \mathbf{B}_0$ is then taken as the sum of the low and high components as it is linear. However, when calculating the nonlinear $\mathbf{F}$ terms we must now take care to include only the triad interactions permitted in the approximation. That is,

$$\begin{aligned} [\mathbf{F}]_{low} &= \mathrm{Re}\left([\mathbf{U}]_{low} \times [\nabla \times \mathbf{U}]_{low} + [\mathbf{U}]_{high} \times [\nabla \times \mathbf{U}]_{high}\right) \\ &\quad + \mathrm{Ha}^2 [\nabla \times \mathbf{B}]_{low} \times [\mathbf{B}_0], \quad (4.16) \\ [\mathbf{F}]_{high} &= \mathrm{Re}\left([\mathbf{U}]_{low} \times [\nabla \times \mathbf{U}]_{high} + [\mathbf{U}]_{high} \times [\nabla \times \mathbf{U}]_{low}\right) \\ &\quad + \mathrm{Ha}^2 [\nabla \times \mathbf{B}]_{high} \times [\mathbf{B}_0]. \quad (4.17) \end{aligned}$$

The transform back to spectral space is handled as previously described, but now we evaluate the nonlinear forcing for the low and high modes separately, $\mathbf{DV}_{low}, \mathbf{DV}_{high}$ etc. The full spectral arrays are then recombined as

$$\mathbf{DV} = \sum_{k=0}^{\Lambda} \mathbf{DV}_{low} + \sum_{k=\Lambda+1}^{K} \mathbf{DV}_{high}. \quad (4.18)$$

Our code has been benchmarked against the full DNS via setting $\Lambda = K$, for which all modes are classed as large-scale and thus all nonlinear interactions are retained. The output variables show excellent agreement to the NL DNS.

4.3 Results

4.3.1 Means of comparison

We claim that our GQL approximation has bearing on the accuracy of DSS, a statistical theory. Therefore, it is only logical to use the statistics of the HMRI as our primary method of comparison between the NL DNS and GQL results. Indeed, Marston *et al.* (2016) evaluated both statistics and dynamics when considering zonal jets. We choose to focus on three main statistics: the average vertical energy spectra of the velocity and magnetic fields, as well as the first and second cumulants. The cumulants are of particular importance seeing as the CE2 and GCE2 DSS schemes are based upon cumulant expansions.

Energy spectra

As one of our diagnostics we compare the energy spectra of the GQL results to that of the NL DNS. Of course, it is well known that kinetic and magnetic energies are obtained via

$$\mathbf{E}_k = \int_{r_i}^{r_o} \mathbf{U}^2 \; r \, \mathrm{d}r \, \mathrm{d}\phi \, \mathrm{d}z, \qquad \mathbf{E}_m = \int_{r_i}^{r_o} \mathbf{B}^2 \; r \, \mathrm{d}r \, \mathrm{d}\phi \, \mathrm{d}z. \tag{4.19}$$

Given that our variables are expanded in spectral space in terms of Fourier modes, we choose to calculate the energy for each mode separately, via the following procedure: we first transform radially back into configuration space, then numerically integrate over the full gap width, before calculating the toroidal and poloidal components of the velocity and magnetic field.

The radial integration can be performed accurately via a composite Simpson's rule, which evaluates the integral of some general function $f(x)$ as

$$\int_{r_i}^{r_o} f(x) \; \mathrm{d}x = \frac{h}{3} \left(f(x_0) + 2 \sum_{j=1}^{n/2-1} f(x_{2j}) + 4 \sum_{j=1}^{n/2} f(x_{2j-1}) + f(x_n) \right) \tag{4.20}$$

where h is some integration step length, $h = (r_o - r_i)/n$. Thus, we have that

$$\int_{r_i}^{r_o} \mathbf{U}^2 r \, \mathrm{d}r \, \mathrm{d}\phi \, \mathrm{d}z = \frac{h}{3} \left(\mathbf{U}^2(x_0) + 2 \sum_{j=1}^{n/2-1} \mathbf{U}^2(x_{2j}) + 4 \sum_{j=1}^{n/2} \mathbf{U}^2(x_{2j-1}) + \mathbf{U}^2(x_n) \right) \tag{4.21}$$

where $x = 0 \,..\, \pi z_0$, in increments of $h = (r_o - r_i)/n = 1/n$, with $n = 8 \times N$ giving sufficient accuracy. Integrating the energy in the ϕ and z is simple due to the spectral expansion, multiplying by πz_0 when κ=0, and $\pi z_0/2$ otherwise. The poloidal and toroidal components of the kinetic and magnetic energy are then given by,

$$\mathrm{Pol}_{\mathbf{U}} = (k^2 U_r^2 + U_z^2), \qquad \mathrm{Tor}_{\mathbf{U}} = U_\phi^2 \tag{4.22}$$

$$\mathrm{Pol}_{\mathbf{B}} = (k^2 B_r^2 + B_z^2), \qquad \mathrm{Tor}_{\mathbf{B}} = B_\phi^2 \tag{4.23}$$

4.3.2 Cumulants

The first cumulant is the mean azimuthal velocity (over both z and time, denoted by angled brackets) as a function of r, and is defined to be

$$c_v(r) = \langle v(r, z, t) \rangle. \tag{4.24}$$

The second cumulants are defined as

$$c_{vv}(r_1, r_2, \xi) = \langle v'(r_1, z_1, t) v'(r_2, z_2, t) \rangle, \tag{4.25}$$

$$c_{v\psi}(r_1, r_2, \xi) = \langle v'(r_1, z_1, t) \psi'(r_2, z_2, t) \rangle, \tag{4.26}$$

$$c_{\psi\psi}(r_1, r_2, \xi) = \langle \psi'(r_1, z_1, t) \psi'(r_2, z_2, t) \rangle, \tag{4.27}$$

where the displacement $\xi = z_2 - z_1$. These provide information on the non-local fluctuation/fluctuation nonlinear interactions, and are otherwise known as two-point correlation functions. To simplify matters, for all calculations in this chapter we set $r_1 = 0.5$, which has little bearing on the structure of the cumulants obtained. The cumulants can then be more conveniently expressed as

$$c_{vv}(r_1, r_2, \xi) = \int \int v'(r_1, z_1) v'(r_2, z_1 + \xi) \, \mathrm{d}z_1 \, \mathrm{d}t. \tag{4.28}$$

Numerically, this is performed as a triple summation over r_2, z_1, and ξ.

4.3.3 Parameters and initialisation

In order to initialise our GQL simulations, we first evolve a turbulent NL DNS solution at the relevant parameter set until a statistically steady state is achieved. We then use this state as our initial conditions for each of the GQL runs. It should be noted that the same results are obtained if each GQL simulation is started from a small perturbation about the basic state, though these take much longer to reach equilibrium. At each parameter set we examine $\Lambda = 0$ (the standard QL approximation), as well as $\Lambda = 1, 2, 3, 6$ and $\Lambda = 20$. The equations are evolved with a time-step $dt = 5 \times 10^{-3}$ for at least 8×10^5 times steps (and possibly longer) to ensure a statistically steady solution.

Furthermore, due to the large degree of choice in choosing our three main parameters β, Re and Ha, we also briefly note the reasoning behind our choices. Firstly, we must ensure that Re is sufficiently above the critical value Re_c. One would suspect that the degree of supercriticality $(\mathrm{Re} - \mathrm{Re}_c)$ will be an important factor in the effectiveness of the GQL approximation (recall that previous studies showed QL to be sufficient when near equilibrium). We thus choose our parameter sets to encompass a number of degrees of supercriticality. Based on figure 2 of Rüdiger *et al.* (2006), where Re_c was mapped on a Ha, β axis, we focus on three specific parameter sets; $\beta = 5, \mathrm{Ha} = 16$, $\beta = 2.5$, $\mathrm{Ha} = 16$, and $\beta = 10$, $\mathrm{Ha} = 8$, each for $\mathrm{Re} = 5000$, 7000 and 10000. Each of these generate turbulent solutions. For a given Re, the set $\beta = 5, \mathrm{Ha} = 16$ is the most supercritical, with $\mathrm{Re}_c \approx 1000$. Then at $\beta = 2.5$, $\mathrm{Ha} = 16$ has $\mathrm{Re}_c \approx 1500$, so comparison between the two should elucidate how the strength of turbulence affects GQL. The set $\beta = 10$, $\mathrm{Ha} = 8$ is more interesting in that the value of Re_c is not solely representative of marginal stability. On the figure of Rüdiger *et al.* the contours of Re_c are closely bunched, and so are close to marginal stability in terms of the magnetic field parameters. This parameter set may then be only weakly nonlinear, for which we expect that even $\Lambda = 0$ QL approximations will give accurate statistics.

We claim that these parameter sets capture all properties of the GQL approximation, and account for all types of variation. All simulations that were run at other

parameter values were qualitatively similar.

4.3.4 NL DNS

In order to ascertain whether GQL yields accurate results, we first require a series of accurate NL DNS to compare them against. Thus, in this section we describe the NL DNS behaviour of the HMRI. Figure 4.1 contains contours of mean azimuthal velocity, Hovmöller diagrams and mean azimuthal flows (first cumulants), whilst figure 4.2 contains plots of the energy spectra and two-point correlation functions (second cumulants), for $\langle v'v' \rangle$ and $\langle v'\psi' \rangle$. For brevity, we set $\mathrm{Re} = 10000$, the highest value taken, for each parameter set.

It can be seen clearly in the topmost row of figure 4.1 that our different parameter sets encompass a number of degrees of turbulence, ranging from strong turbulence at $\beta = 5,\ \mathrm{Ha} = 16$, to weak turbulence at $\beta = 10,\ \mathrm{Ha} = 8$, for which it is believed that the flow is only weakly nonlinear.

It is well known that the HMRI manifests as a travelling wave (at onset); The flow consists of a number of Taylor vortices, drifting axially. As adjacent Taylor vortices have stream functions ψ that are oppositely signed, we can conveniently track their evolution via tracking the sign of ψ over time. We do so via Hovmöller plots of ψ, where the z evolution is plotted over time. These show that vortices propagate axially downward, and highlight the nonlinear dislocations that are present in the flow. These dislocations are an effective measure of turbulence, and are one of the key features unique to the nonlinear regime that we wish GQL to reproduce. In support of our claim that $\beta = 10,\ \mathrm{Ha} = 10$ is only weakly nonlinear, note that the Hovmöller plot for this parameter set contains few such dislocations.

In the third row, the first cumulants (mean azimuthal flows) illustrate the perturbation from the basic state flow. As is standard, here turbulence serves to flatten the profile of the flow, removing the root cause of any instability. This in effect leads to angular momentum being transported outwards, the key role of MRI. We see that the strength of turbulence leads to varying degrees of angular momentum transport,

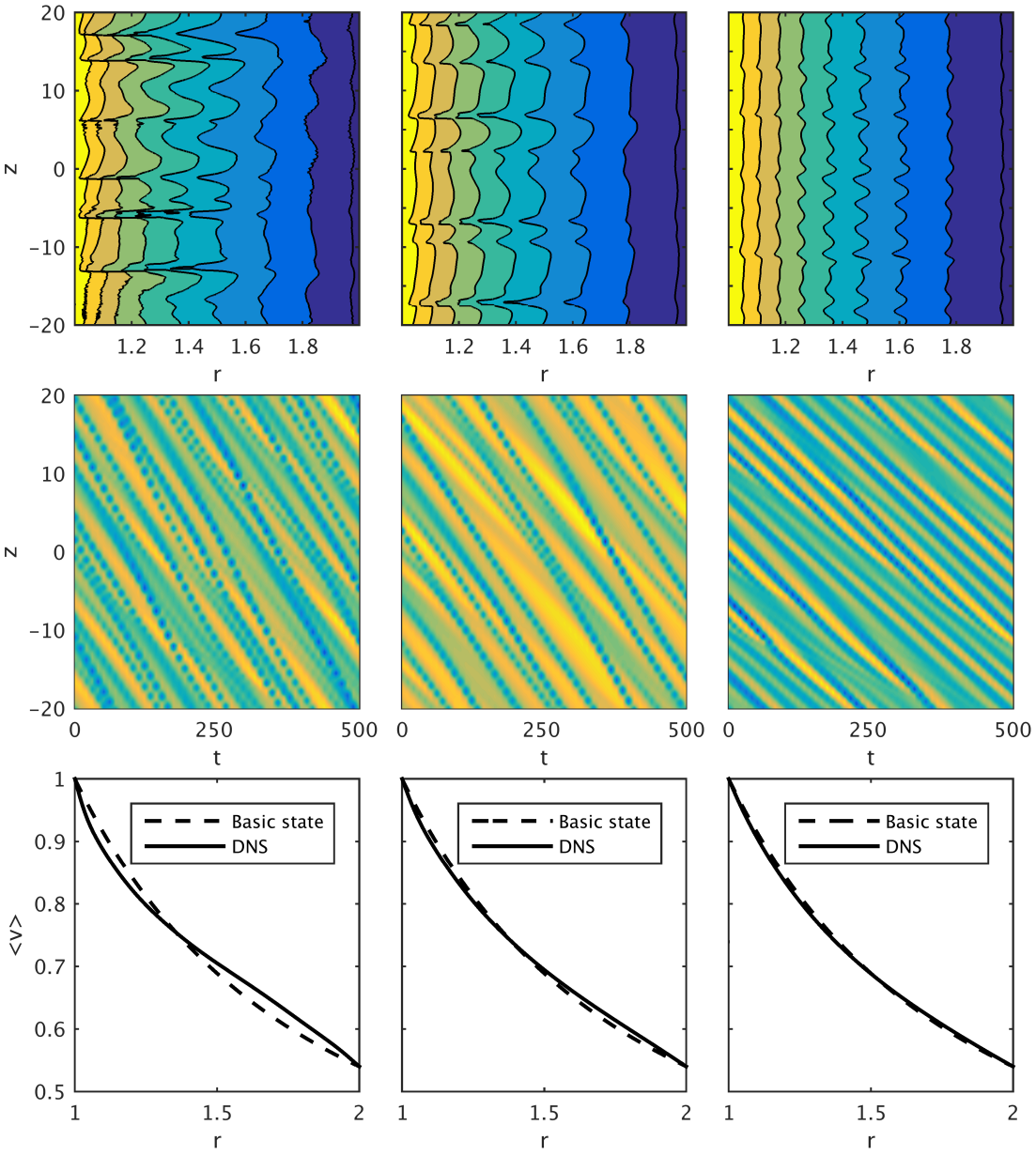

Figure 4.1: Rows showing: contour snapshots of azimuthal velocity; Hovmöller plots of $\psi(r = 1.5, z)$ in terms of z and time; first cumulants $\langle v \rangle$. Shown in the first column is $\beta = 5,\ \mathrm{Ha} = 16$, in the centre column is $\beta = 2.5,\ \mathrm{Ha} = 16$, and in the rightmost column is $\beta = 10,\ \mathrm{Ha} = 8$.

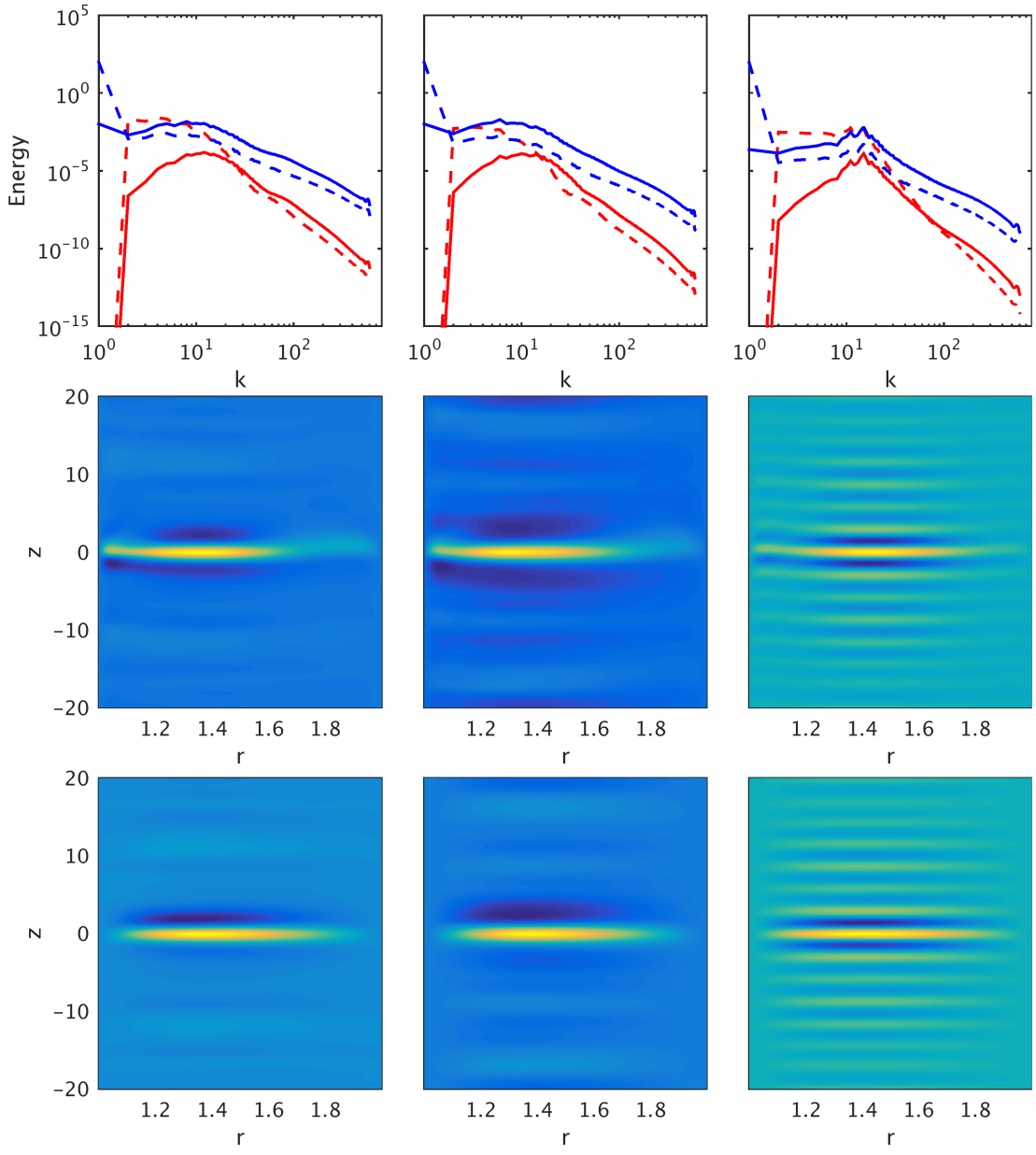

Figure 4.2: Rows showing: vertical energy spectra for the magnetic field (red) and velocity (blue) with poloidal components (solid) and toroidal components (dashed); second cumulants $\langle v'v' \rangle$; second cumulants $\langle v'\psi' \rangle$. Parameter sets taken as in figure 4.1.

as one would expect.

Considering now the energy spectra, both kinetic and magnetic, we note that across each parameter set the profiles are qualitatively similar; though the magnetic energy is of a smaller magnitude than the kinetic energy, they both scale consistently across the three plots. Indeed, there is little difference in the spectra for Re = 7000 and Re = 5000. Note that though the medium and strong turbulent states have relatively flat lower parts of the spectra, the energy in the weakly nonlinear spectra peaks around $\kappa \approx 13$, which coincides with the dominant linear mode of instability.

Finally, the second cumulants $\langle v'v' \rangle$ and $\langle v'\psi' \rangle$ are qualitatively similar, even though here v and ψ are out of phase. Note that both cumulants are strongly localised in the axial direction, a reflection of the flattened spectra for the low modes, which results in a δ–function–like axial correlation. The weakly nonlinear second cumulants, whilst still more strongly correlated in the local axial region, also show a periodic correlation along the axis. This is a direct result of the peak in the spectrum at $k \approx 13$, leading to a $k = 13$ wavenumber in the cumulant. The radial correlation covers much more of the domain, though is strongest at the midpoint. Recall that we chose $r_i = 1.5$ in our calculations for the cumulants; this radial correlation remains largely unchanged if we were to choose a different r_i.

4.3.5 GQL DNS

Strong turbulence - $\beta = 5,\ \mathrm{Ha} = 16$

In plotting the contours of azimuthal velocity and Hovmöller plots for our strongly turbulent flow (figure 4.3), it is immediately clear that $\Lambda = 0$ QL produces visibly different results to NL DNS. We note that QL cannot recreate the nonlinear dislocations that are integral to the strongly turbulent profile. The HMRI manifests as a travelling wave though, with wavelength of acceptable accuracy, so the most fundamental property of the flow is consistent. We notice that by including only two extra large scale modes in the formalism, i.e. taking $\Lambda = 2$, the nonlinear dislocations are properly reproduced. Already, we see that GQL with only the bare minimum of

extra modes can incorporate important flow properties that are overlooked by QL theory.

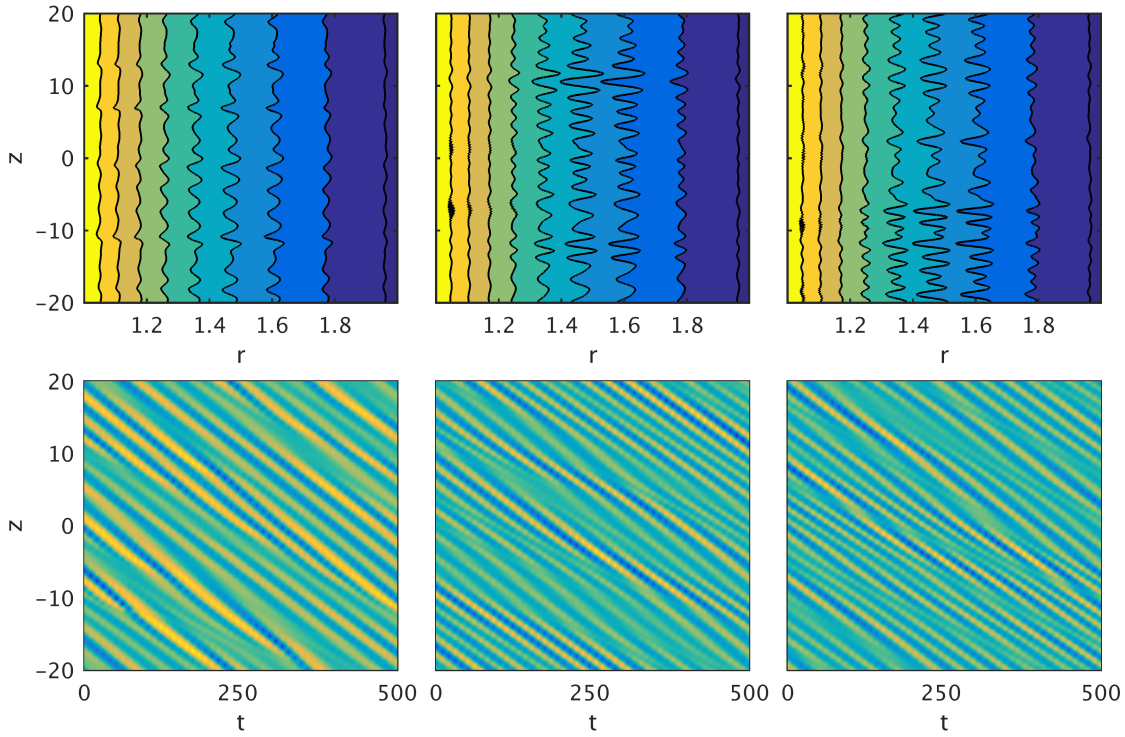

Figure 4.3: Top) Snapshot contour plots of v, and bottom) Hovmöller plots of ψ against z and time. Shown on the left is NL DNS, in the centre is $\Lambda = 0$ and on the right is $\Lambda = 2$.

Next, we compare the various GQL energy spectra to the NL DNS in figure 4.4. It is most important here for our GQL approximations to show good agreement in the lowest, largest scale, modes, as these have the largest influence on the behaviour of the flow. As such, we care little about inaccuracy in the highest modes, which will see energies decay away due to the reduced nonlocal transfer of energy.

Such a decay of energy is immediately apparent in the $\Lambda = 0$ and $\Lambda = 1$ energy spectra, for which the reduced nonlinearity has impeded cascades to the higher modes. Instead, we see a series of peaks, corresponding to a linear instability at $k \approx 40$ – a by-product of our choice of length-scale z_0 earlier – and its harmonics. Of course, one may ask whether this would still be the case if our simulations were initialised from a small random initial condition instead of an already turbulent

state. This is indeed the case; the peaks are truly produced by the linear instability, and are not a remnant of the decayed energy. Note that with the increased energy scattering that results from setting $\Lambda = 1$, we see that the energy does not decay completely, however the linear instability peaks are still the dominant feature in the spectrum.

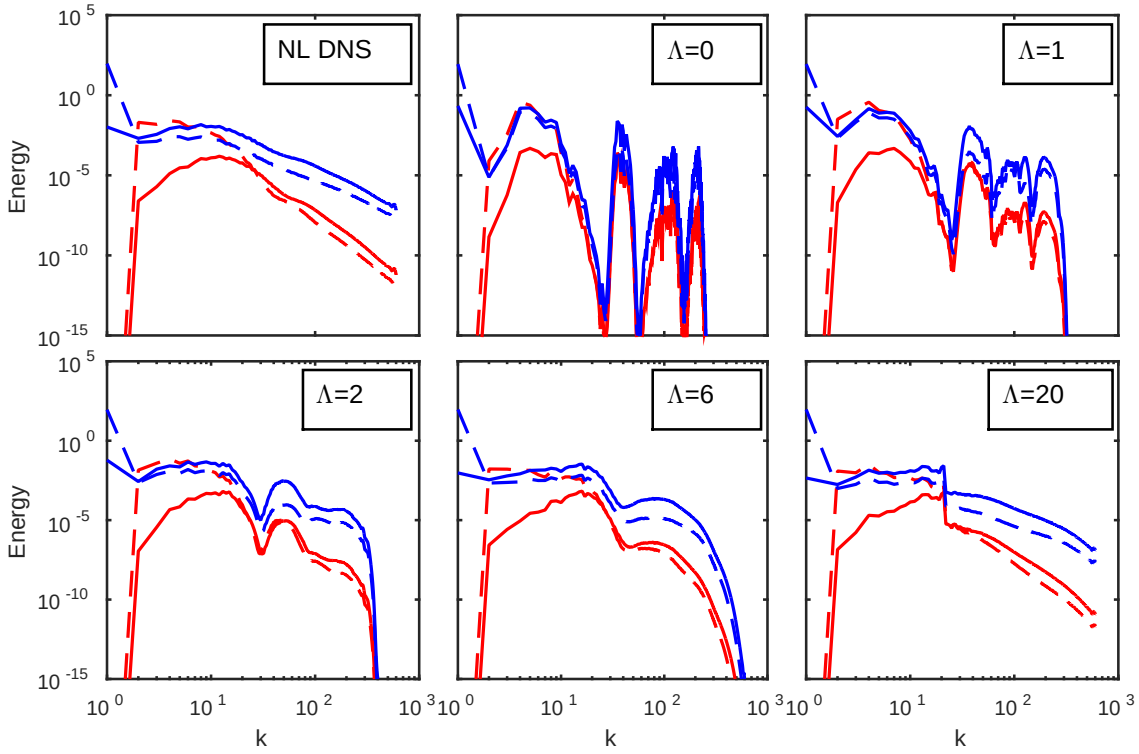

Figure 4.4: Vertical magnetic (red) and kinetic (blue) energy spectra for $\beta = 5$, Ha $= 16$, Re $= 10000$, with separate poloidal components (solid) and toroidal components (dashed).

Adding an additional large scale mode in $\Lambda = 2$ serves to produce a spectrum that more broadly fits the NL DNS profile; it is no longer dominated by linear instability. Indeed, the linear instability only appears as a minor protrusion above a spectrum that adheres more closely to the NL DNS power law scaling (for $k > 200$ at least). The energy decays rapidly above $k \approx 200$, however this is to be expected with our still limited energy scattering. Evidently, GQL with $\Lambda = 2$ is a marked improvement over $\Lambda = 0$ and $\Lambda = 1$. However similarly great improvements are not yielded by increasing to $\Lambda = 3$ and beyond. We find that $\Lambda = 2$ strikes an optimal balance between accuracy and minimising the approximation. Interestingly, the mode at

which energy first decays remains fairly uniform across our various choices of Λ. Increasing to even $\Lambda = 20$, where the remainder of the spectrum is accurate to the NL DNS, we note a sharp transition about the mode $k \approx 20$. It is no coincidence that $k = \Lambda$, as this sharp transition is a direct result of the filtering. It offers a clear view of the gulf between the fully realised modal interactions in the low modes and the linearised high modes and shows plainly the effect of energy scattering.

In order for us to declare $\Lambda = 2$ GQL truly effective, our cumulants have to be accurate, so as to ensure valid DSS. Examining the first cumulants $\langle v \rangle$ in figure 4.5, we see that QL gives a deviation of approximately 10% from the NL DNS. Such a deviation is too large to be considered acceptable for DSS. With GQL however, and in particular between $\Lambda = 1$ and $\Lambda = 2$, we see great improvement in the accuracy of the cumulant, almost halving the error. This relative decrease in error is also seen for lower Re values.

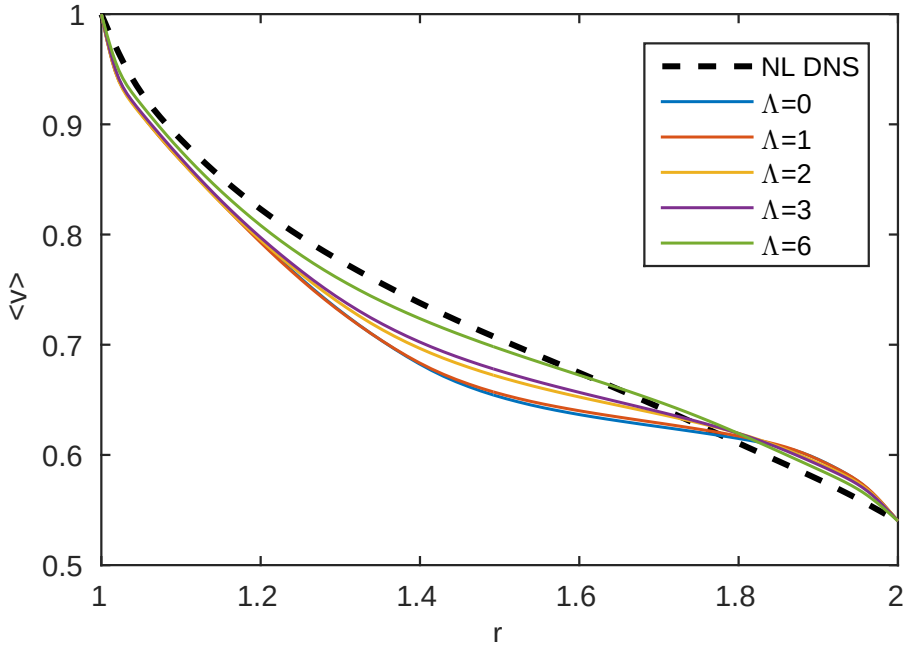

Figure 4.5: First cumulants $\langle v \rangle$ for the parameter set $\beta = 5,\ \mathrm{Ha} = 16,\ \mathrm{Re} = 10000$.

Using $\langle v \rangle$, we can calculate whether our mean azimuthal flow satisfies (or more accurately *doesn't* satisfy) Rayleigh's instability criterion, $\partial/\partial r(r\langle v \rangle) > 0$. Clearly if we have a profile that is Rayleigh stable then the approximation is doing an exceptionally poor job! We see, in figure 4.6 ,that the NL DNS profile should, aside

from adjacent to the boundaries, reside wholly above zero, as expected for a Rayleigh stable flow. For $\Lambda = 0$ and $\Lambda = 1$ GQL however, note that now we see a violation of the Rayleigh criterion near the inner boundary. This could be one of the reasons for which QL theory does such a poor job at recreating our HMRI.

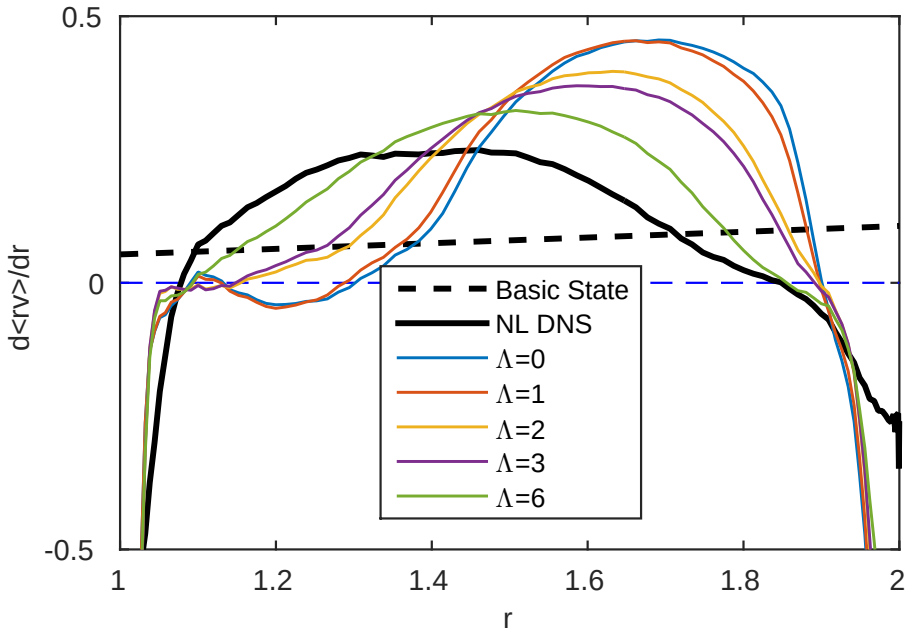

Figure 4.6: $\partial/\partial r(r\langle v\rangle)$ for the parameter set $\beta = 5,\ \mathrm{Ha} = 16,\ \mathrm{Re} = 10000$.

Finally, we examine two of the second cumulants, beginning with $\langle v'v'\rangle$ in figure 4.7. It is important to recall that we chose to cross-correlate with the radial midpoint in order to simplify calculations. This has little bearing on the overall correlation.

It is clear to see that our $\Lambda = 0$ and $\Lambda = 1$ approximations produce inadequate second cumulants; here the inaccuracy is more pronounced than in our previous benchmarks. We see that, whereas the NL DNS is weakly correlated for all but the midpoints due to the flattened lower spectrum, $\Lambda = 0$ and $\Lambda = 1$ show a wave-like overcorrelation, with wavenumber of 5 and 4 corresponding to the small peaks present in the corresponding energy spectra in figure 4.4. We presume that this correlation wavenumber may be related to the axially propagating waves (as also evidenced by Marston *et al.* (2016)). Due to the flattening of the lower part of the spectra that we saw for $\Lambda = 2$, we note that for $\Lambda = 2$ the localised axial correlation of the NL DNS is regained. It should be mentioned that, though these cumulants

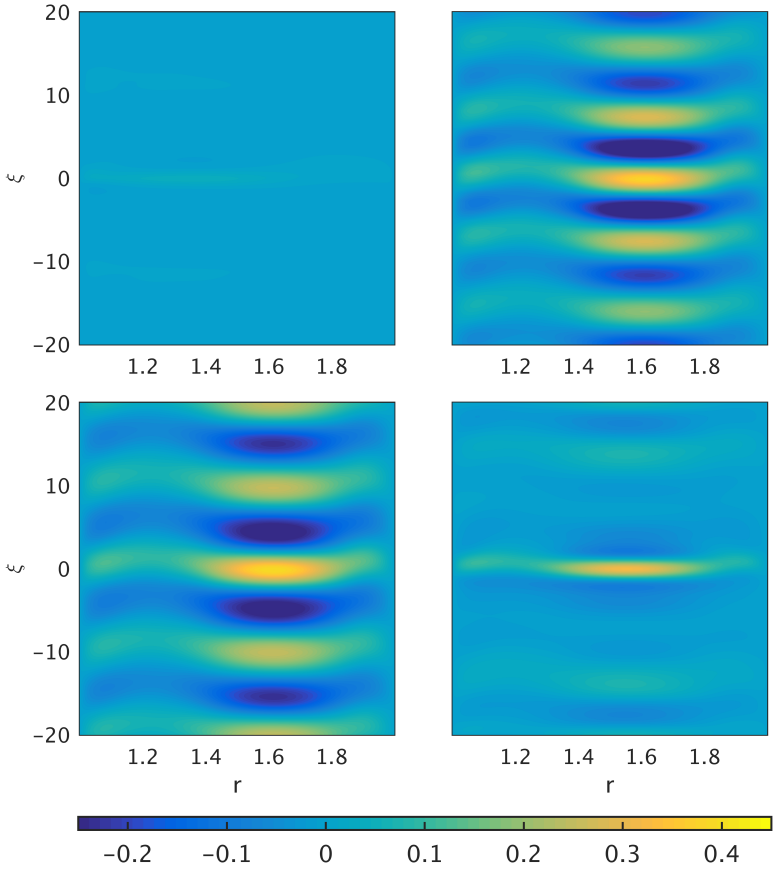

Figure 4.7: Second cumulants $\langle v'v' \rangle$ for the parameter set $\beta = 5$, $\mathrm{Ha} = 16$, $\mathrm{Re} = 7000$. Top to bottom, left to right, we have NL DNS, QL $\Lambda = 0$, and GQL $\Lambda = 1, 2$.

show that $\lambda = 2$ regains the important characteristics of the NL DNS flow, they are by no means perfect. Indeed, to expect that would be foolish given the extreme truncation. However, the magnitude of the background inaccuracy is comparatively small with regards to the main correlation.

This correlation structure is also found in the cross-cumulants $\langle v'\psi' \rangle$ (figure 4.8). We see a similar overcorrelation for $\Lambda = 0$ and $\Lambda = 1$ that is lost at $\Lambda = 2$, where the correlation is then consistent with that of the NL DNS. For the cross-cumulant, we also see a homogeneous radial correlation that is more evenly distributed across the gap width.

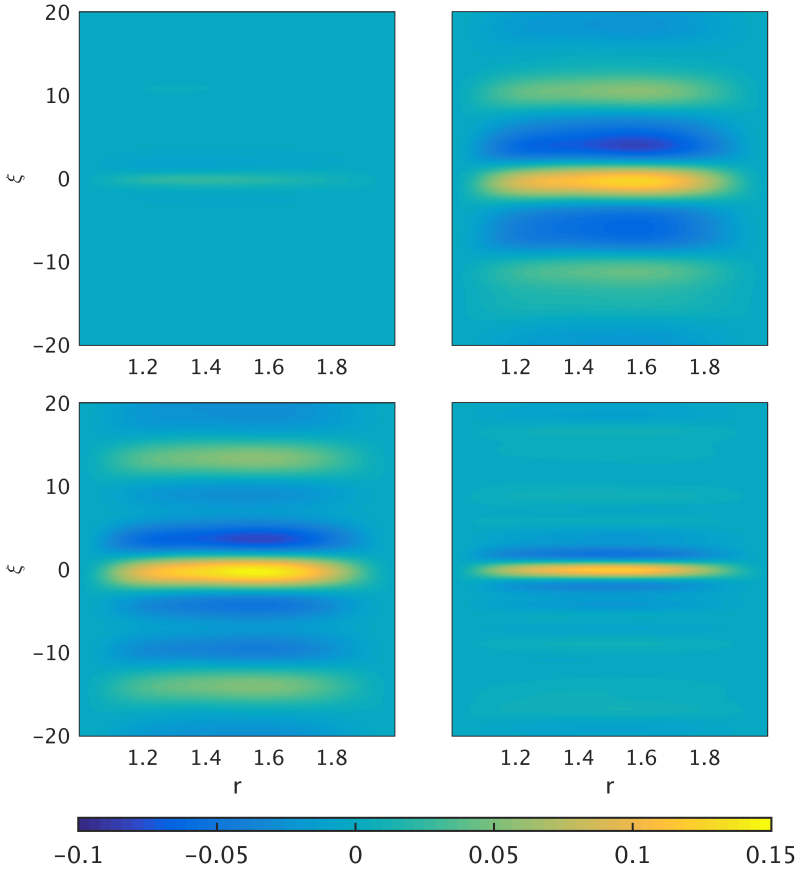

Figure 4.8: Second cumulants $\langle v'\psi' \rangle$ as in figure 4.7.

Moderate turbulence - $\beta = 2.5,\ \mathrm{Ha} = 16$

As seen in figure 4.1, this parameter set is inherently less turbulent than that examined in the previous section, evidenced by having fewer nonlinear dislocations. Thus, it stands to reason that this parameter set may serve to elucidate what effect the degree of supercriticality (in Re) has on GQL.

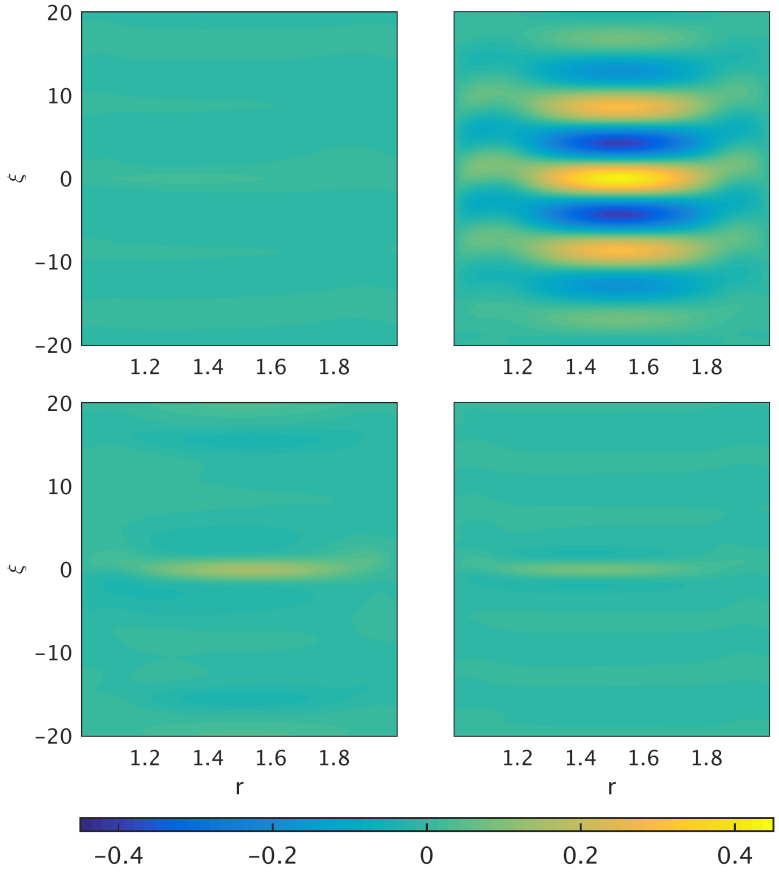

Figure 4.9: Second cumulants $\langle v'v' \rangle$ for the parameter set $\beta = 2.5,\ \mathrm{Ha} = 16,\ \mathrm{Re} = 10000$. Top to bottom, left to right, we have NL DNS, QL $\Lambda = 0$, and GQL $\Lambda = 2, 5$.

It is found that the supercriticality of the flow, though having bearing on the accuracy of some diagnostics, does not affect the relative improvements in reproducing the behaviours of the flow yielded by increasing Λ. Much like in the previous section, it can be seen that for all approximations the HMRI retains its travelling wave nature, though does not produce nonlinear dislocations until $\Lambda = 2$. The first cumulants, though now with smaller deviation from the NL DNS for all approximations,

show similar improvements in accuracy as Λ is increased. The energy spectra and second cumulants likewise adhere to the general behaviour described previously, with GQL yielding a good approximation by $\Lambda = 5$ (see figure 4.9). Thus, we conclude that though GQL may appear less accurate in comparison with the strongly turbulent case, the improvements it presents over standard QL are consistent. Therefore in order to suitably represent the fluctuations, GQL remains essential.

Weak turbulence - $\beta = 10,\ \mathrm{Ha} = 8$

Finally, we examine the efficacy of GQL in comparison with QL for the weakly nonlinear case $\beta = 10,\ \mathrm{Ha} = 8$. Unlike the other parameter sets, it is probable that even QL will have a reasonable degree of success here; it is after all exact in formally weakly nonlinear regimes. The question is then whether GQL can offer any tangible improvements over QL in such cases. Upon comparing Hovmöller diagrams, it is clear that all essential features are reproduced via the $\Lambda = 0$ QL; there are too few nonlinear dislocations to give $\Lambda = 2$ GQL any advantage. Furthermore, the flow is sufficiently laminar that all of the first cumulants are near indistinguishable from the NL DNS profile.

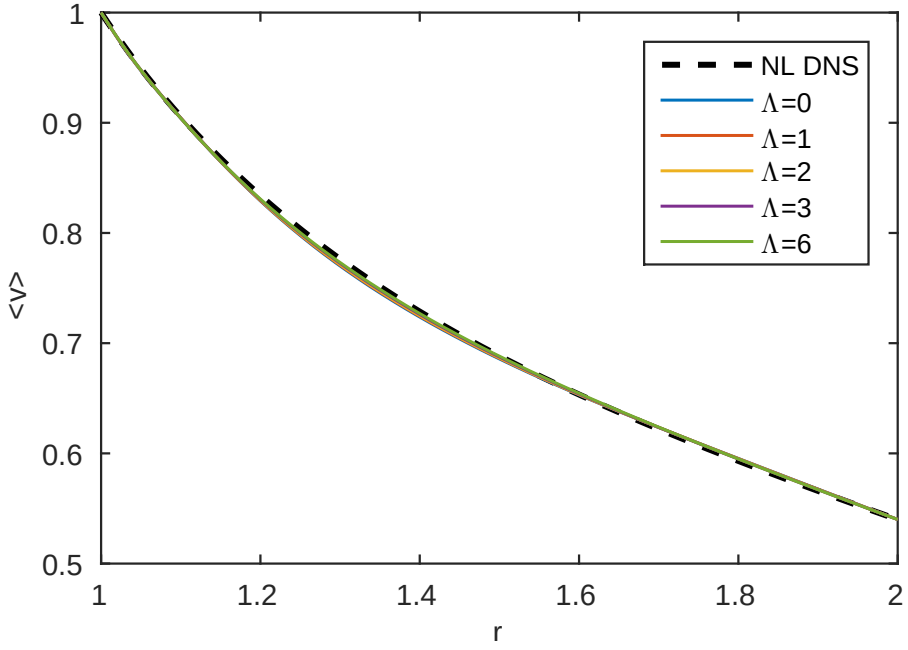

Figure 4.10: First cumulants $\langle v \rangle$ for the parameter set $\beta = 10,\ \mathrm{Ha} = 8,\ \mathrm{Re} = 10000$.

Turning to the second cumulants at Re = 10000, we see that $\Lambda = 0$ reproduces the axial structure of the correlation to a reasonable degree; though the wavelength and magnitudes are not *completely* accurate, the overall result is impressive given the nature of our approximation. Note that the wavenumber is greater than that of the NL DNS for all QL and GQL approximations; this is rectified only when taking much higher Λ. The magnitudes of this spurious periodic correlation does decrease, however, for even $\Lambda = 2$.

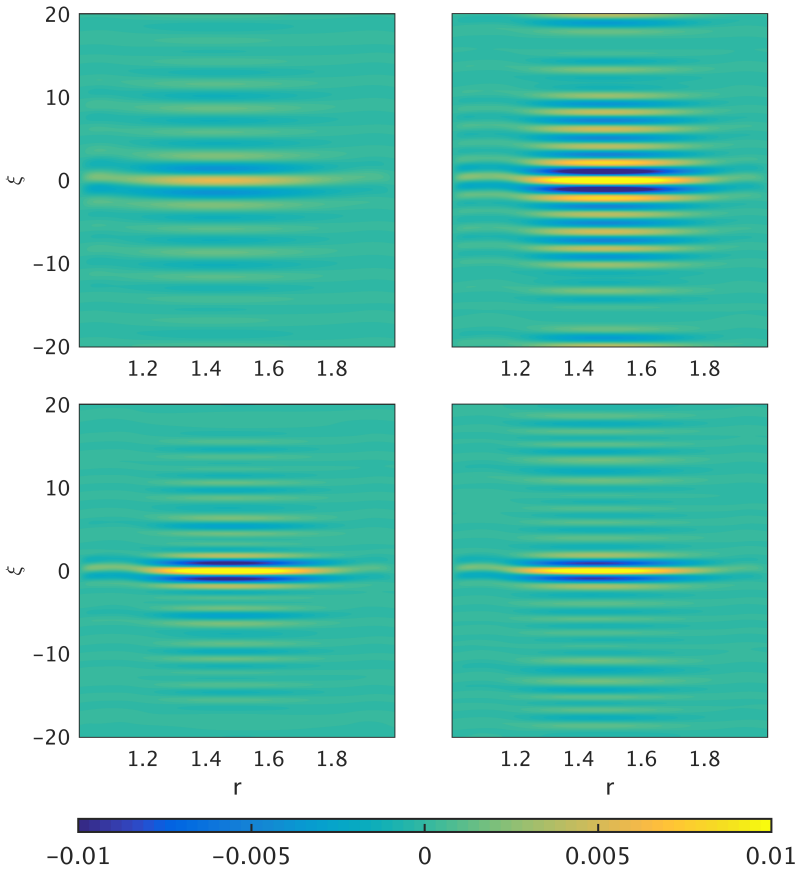

Figure 4.11: Second cumulants $\langle v'v' \rangle$ as a function of r_2 and ξ for the weakly nonlinear $\beta = 10,\ \mathrm{Ha} = 8$. Left to right, top to bottom, we have NL DNS, QL ($\Lambda = 0$) and GQL with $\Lambda = 2, 3$.

That is not to say that our work here has been in vain though; $\Lambda = 0$ does not give universally adequate approximations for weakly nonlinear regimes. Let us consider the case Re = 5000 – which is markedly less supercritical in terms of the rotation parameter – and examine the second cumulants $\langle v'v' \rangle$ (figure 4.12). Here the cu-

mulants are less accurate for the QL case, requiring $\Lambda = 3$ for an axial correlation that is representative of the NL DNS. So, whilst it has been established that QL is, broadly, an adequate approximation to use when dealing with weakly nonlinear flows, we have shown that there exist points whereby QL is not quite good enough, and one requires more of the nonlinearity to be taken into account via GQL. Fortunately, such cases require relatively few large scale modes to adequately incorporate the weak nonlinearity, so a low Λ approximation is sufficient. This is important when considering possible application to DSS.

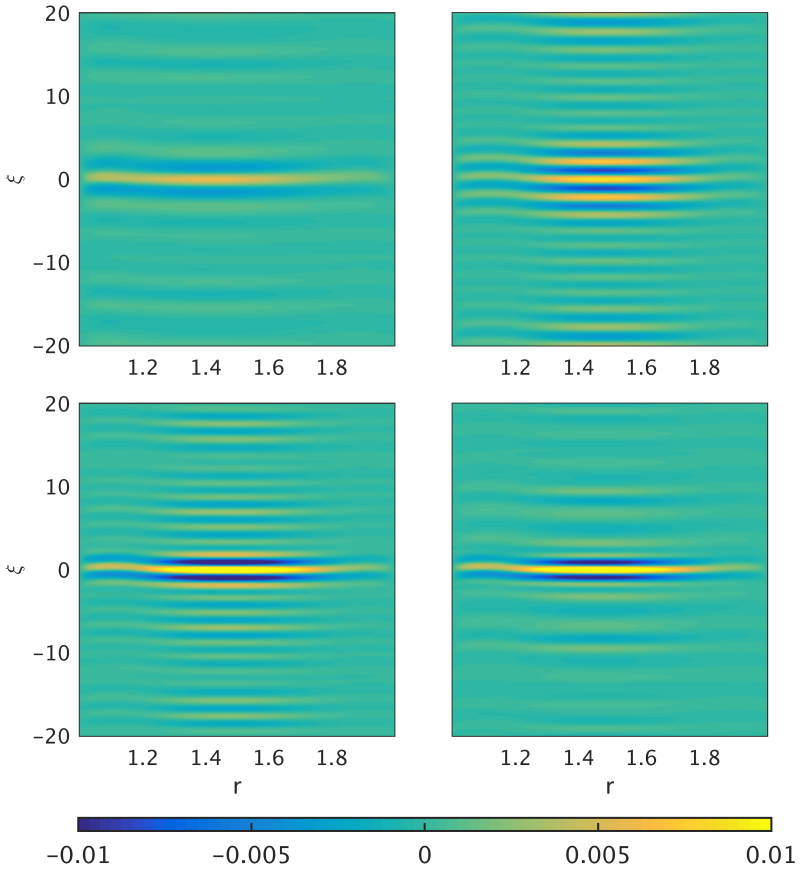

Figure 4.12: Second cumulants $\langle v'v' \rangle$ for $\beta = 10,\ \mathrm{Ha} = 8,\ \mathrm{Re} = 5000$, as in figure 4.11.

4.4 GQL at non–zero Rm

So far in this chapter we have explored the efficacy of the GQL when applied to inductionless HMRI, utilising the inductionless approximation to simplify the Navier-Stokes and induction equations. Our GQL approximation then only had to deal with one nonlinearity, for which it was shown that dynamics and statistics can be accurately reproduced when linearising all but the lowest three modes. However, applying these results to a general magnetohydrodynamical flow is not quite so simple. Indeed, most astrophysical flows are not inductionless – for example, the sun has $\mathrm{Rm} \sim \mathcal{O}(10^6)$ and the Earth has $\mathrm{Rm} \sim \mathcal{O}(10^3)$ – so their governing equations contain two more nonlinear terms. The question, then, is whether these nonlinearities can be approximated with a similar degree of accuracy to the inductionless case for similar choices of spectral filter Λ. There has been no such consideration in any of the prior literature on GQL – though it bears reminding that the approximation has only been introduced in 2016. Other than the inductionless HMRI, the approximation has been investigated for purely hydrodynamic fluids, motivated by applications to atmospheric flows.

In this section, we examine (mainly) the HMRI and (briefly) SMRI when Rm is non-zero, and aim to find out if $\nabla \times (\mathbf{U} \times \mathbf{B})$ and $(\nabla \times \mathbf{B}) \times \mathbf{B}$ can be approximated as successfully as $\mathbf{U} \times \nabla \times \mathbf{U}$. We once more decompose $\mathbf{B}$ into imposed and induced magnetic fields as $\mathbf{B} = \mathbf{B}_0 + \mathrm{Rm}\mathbf{b}$. Recall that the full set of Navier–Stokes and induction equations, taking account that $\nabla \times \mathbf{B}_0 = 0$, are

$$\left(\mathrm{Re}\frac{\partial}{\partial t} - \nabla^2\right)\mathbf{U} = -\nabla p + \mathrm{Re}\mathbf{U} \times (\nabla \times \mathbf{U}) + \mathrm{Ha}^2\left([\nabla \times \mathbf{b}] \times \mathbf{B}_0 + \mathrm{Rm}\,[\nabla \times \mathbf{b}] \times \mathbf{b}\right), \tag{4.29}$$

$$\left(\mathrm{Rm}\frac{\partial}{\partial t} - \nabla^2\right)\mathbf{b} = \nabla \times (\mathbf{U} \times \mathbf{B}_0) + \mathrm{Rm}\nabla \times (\mathbf{U} \times \mathbf{b}). \tag{4.30}$$

So, if we divide through equation (4.29) by Re, we are left with

$$\left(\frac{\partial}{\partial t} - \frac{1}{\mathrm{Re}}\nabla^2\right)\mathbf{U} = \mathbf{U} \times (\nabla \times \mathbf{U}) + \mathrm{Ha}^2\left(\frac{1}{\mathrm{Re}}(\nabla \times \mathbf{b}) \times \mathbf{B}_0 + \mathrm{Pm}(\nabla \times \mathbf{b}) \times \mathbf{b}\right), \tag{4.31}$$

where we note that the relative dominance of the two nonlinear terms in the Navier-Stokes equation is governed by the magnetic Prandtl number, Pm. For $\mathrm{Pm} \ll 1$ we would expect the same inductionless success found previously. The potential success of the cases $0 \ll \mathrm{Pm} < 1$ and $\mathrm{Pm} \gg 1$ is unknown.

4.4.1 Additional mathematics

For our time-stepping scheme we once again choose our governing equations to be the ϕ components of the Navier–Stokes equation, and its curl, as well as the ϕ components of the induction equation and its inverse curl. Unlike for inductionless fluid though, the induced magnetic field now must be time-stepped concurrently with the velocity field.

As we have that $\mathbf{B}_0 = \mathbf{e}_z + \beta/r\,\mathbf{e}_\phi$, it can be shown that $[\nabla^2 \mathbf{B}_0]_\phi = 0$. Similarly, if we take $\nabla \times \mathbf{A}_0 = \mathbf{B}_0$, it can be shown that

$$[\nabla \times \mathbf{A}_0]_z = [\mathbf{B}_0]_z = 1 \qquad \Longrightarrow \qquad \frac{1}{r}\frac{\partial (r\mathbf{A}_0)}{\partial r} = 1 \tag{4.32}$$

Therefore, we find that

$$[\mathbf{A}_0]_\phi = \frac{r}{2} + \frac{c}{r} \qquad \Longrightarrow \qquad [\nabla^2 \mathbf{A}_0]_\phi = 0 \tag{4.33}$$

given some constant, c. So, the governing equations in our time-stepping scheme can be written as

$$\left(\mathrm{Re}\frac{\partial}{\partial t} - D^2\right) v_k = \mathbf{e}_\phi \cdot \mathbf{F}|_k \tag{4.34}$$

$$-\left(\mathrm{Re}\frac{\partial}{\partial t} - D^2\right) D^2 \psi_k = \mathbf{e}_\phi \cdot \nabla \times \mathbf{F}|_k \tag{4.35}$$

$$\left(\mathrm{Rm}\frac{\partial}{\partial t} - D^2\right) a_k = \mathbf{e}_\phi \cdot \mathbf{F}'|_k \tag{4.36}$$

$$\left(\mathrm{Rm}\frac{\partial}{\partial t} - D^2\right) b_k = \mathbf{e}_\phi \cdot \nabla \times \mathbf{F}'|_k \tag{4.37}$$

where $D^2 = \nabla^2 - 1/r^2$ and $\mathbf{F}$, $\mathbf{F}'$ are,

$$\mathbf{F} = -\mathrm{Re}(\mathbf{U} \times \nabla \times \mathbf{U}) + \mathrm{Ha}^2\left([\nabla \times \mathbf{b}] \times \mathbf{B}_0 + \mathrm{Rm}([\nabla \times \mathbf{b}] \times \mathbf{b})\right), \tag{4.38}$$

$$\mathbf{F}' = \nabla \times [\mathbf{U} \times \mathbf{B}_0] + \mathrm{Rm}(\nabla \times [\mathbf{U} \times \mathbf{b}]). \tag{4.39}$$

We note that these may be solved exactly as described in section 2.5, with the majority of the time-stepping routines and nonlinear terms unchanged. We apply the GQL approximation exactly as explained in section 4.2.1, and so split the magnetic field variables into low and high modes via the spectral filter Λ, calculating nonlinear terms as, for example

$$[(\nabla \times \mathbf{b}) \times \mathbf{b}]_{low} = [\nabla \times \mathbf{b}]_{low} \times \mathbf{b}_{low} + [\nabla \times \mathbf{b}]_{high} \times \mathbf{b}_{high}, \tag{4.40}$$

$$[(\nabla \times \mathbf{b}) \times \mathbf{b}]_{high} = [\nabla \times \mathbf{b}]_{low} \times \mathbf{b}_{high} + [\nabla \times \mathbf{b}]_{high} \times \mathbf{b}_{low} \tag{4.41}$$

4.4.2 Results

Parameter choice

With the additional parameter dependencies in the full Navier-Stokes and induction equations, we now have an even more substantial parameter space to explore. Not only do we have Re, β and Ha as before, but we must now factor in Pm, all the while calculating for the full DNS as well as $\Lambda = 0,\ 2,\ \ldots$. On top of this, our calculations have to deal with three times the nonlinearity, so are computationally more expensive to fully equilibrate. As such, we restrict our attention to the parameter set that was – for inductionless HMRI – the most turbulent; $\beta = 5,\ \mathrm{Ha} = 16,\ \mathrm{Re} = 10000$. We then increase Rm from zero, for which the flow is well understood. It should be kept in mind that increasing Rm – and therefore Pm – significantly affects the threshold of linear instability, so we alter Re such that it is consistently ten times greater than the critical value.

NL DNS

In order to judge the efficacy of GQL, we must first adequately understand the corresponding NL DNS solutions at each of our parameter sets.

First of all, if we let Rm be small but non-zero by taking $\mathrm{Rm} = 1$, we note that the time-evolution and cumulants are identical to the inductionless case. This is

reassuring; if the mere presence of the other nonlinearities severely changed the statistics, we would be in trouble.

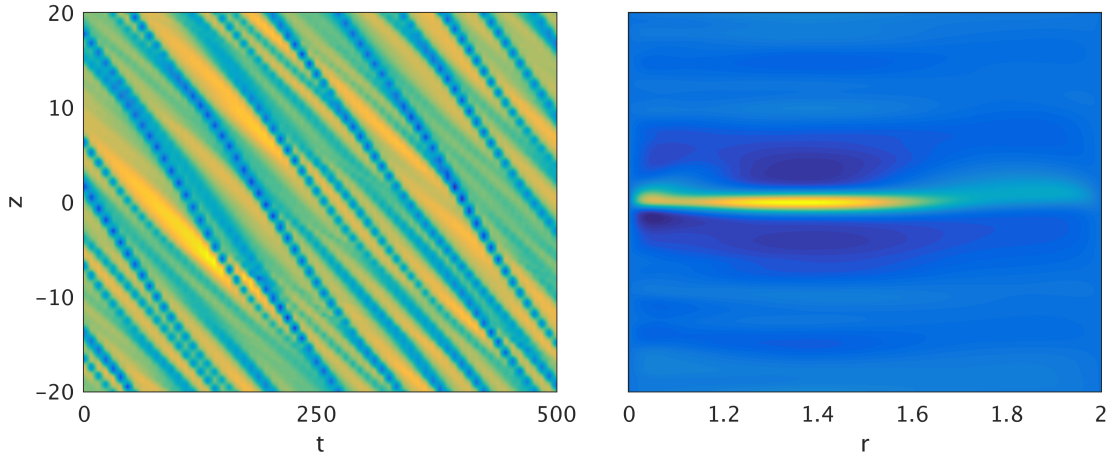

Figure 4.13: Hovmöller plot and second cumulant $\langle v'v' \rangle$ for $\mathrm{Re} = 10000$, $\mathrm{Rm} = 1$.

Increasing to only $\mathrm{Rm} = 100$ though – that is $\mathrm{Pm} = 0.01$ – we note a drastic change in the dynamics and statistics inherent to the flow, even though the Rm dependent nonlinearities are still relatively weak. Note that the critical Reynolds number here $\mathrm{Re}_c \approx 1308$ is not significantly different from the inductionless critical number, so the flow should exhibit the same degree of supercriticality. Looking at the contour plot in figure 4.14, however, it is immediately clear that the flow is much less turbulent – a fact reinforced by the first cumulant $\langle v' \rangle$, which shows that angular momentum transport is less efficient. This parameter set then possesses vastly different dynamics to the well understood inductionless case.

Looking then at the Hovmöller plot, we note that the vortices have banded together to produce a large-scale pattern. These vortex bands propagate comparatively slowly; with a frequency much smaller than the HMRI. Inside the large bands, we note the existence of small-scale drift, of the order of magnitude of the inductionless HMRI vortices. These small-scale flows propagate at a faster speed, comparable to that seen earlier in the chapter. What is interesting is that linear theory predicts that the most unstable mode here will in fact be stationary, so it may be the case that this flow is a combination of HMRI and SMRI (which is also unstable under this parameter set). This could explain the two vortex drift speeds;

slow magnetocoriolis waves vs fast destabilised inertial oscillations.

Of course, the large-scale bands dictate the structure of the second cumulants, seen in figure 4.15, which are in turn made up of two large cells – one strongly correlated and the other strongly anti-correlated. We observe that there is a strong correlation at the inner cylinder about $z = 0$, and anti-correlation as $z \to \pm 40$, while the outer cylinder has correlation in $-z$ and anti-correlation in $+z$. The cross cumulants $\langle v'\psi' \rangle$ offer a simpler picture, with only two large-scale cells. These resemble an exaggerated (and z encompassing) extension of the $\mathrm{Rm} \to 0$ case. These cumulants are governed by the small peak in the $k = 1$ mode in the energy spectrum, and are because the flow is dominated (but not solely consistent of) wavenumber 1.

Next, we take the case $\mathrm{Pm} = 10$ with $\mathrm{Re} = 250$, $\mathrm{Rm} = 2500$. The most striking feature of such $\mathrm{Rm} > 1$ flows is that are very strongly turbulent, a direct consequence of the increasing influence of the induction effects. Clearly, this increasingly strong turbulence does not bode well for the implementation of GQL, as the incredibly fine small scale motion will not be properly captured by any moderate truncation. The energy spectrum is broadly characteristic of generic MHD turbulent flows (see, for example, solar winds (Verma *et al.*, 1996)). Compared to our previous parameter set, the energy is more evenly distributed between the first 600 modes, and whilst it does decay at a sufficient rate to claim that it is adequately resolved, we expect that this will pose significant problems with restricted eddy interactions. The energy peaks at a relatively high $k \approx 10$–20, causing second cumulants to possess a fine axial correlation structure, a direct consequence of small scale wave motion in the flow. The first cumulants reflect the strong turbulence in that they show a particularly efficient outward transfer of angular momentum. In addition, the second cumulants show that correlation only occurs between a point in the flow and itself, which makes a great deal of sense in turbulent flow; we wouldn't expect some cohesive pattern to emerge, after all.

It is unfortunate to note that further increases in Pm only yield increasing levels of turbulence, which gives us great difficulty in resolving the flow at our practical resolutions. Indeed, due to the computational demands of GQL, greatly increasing

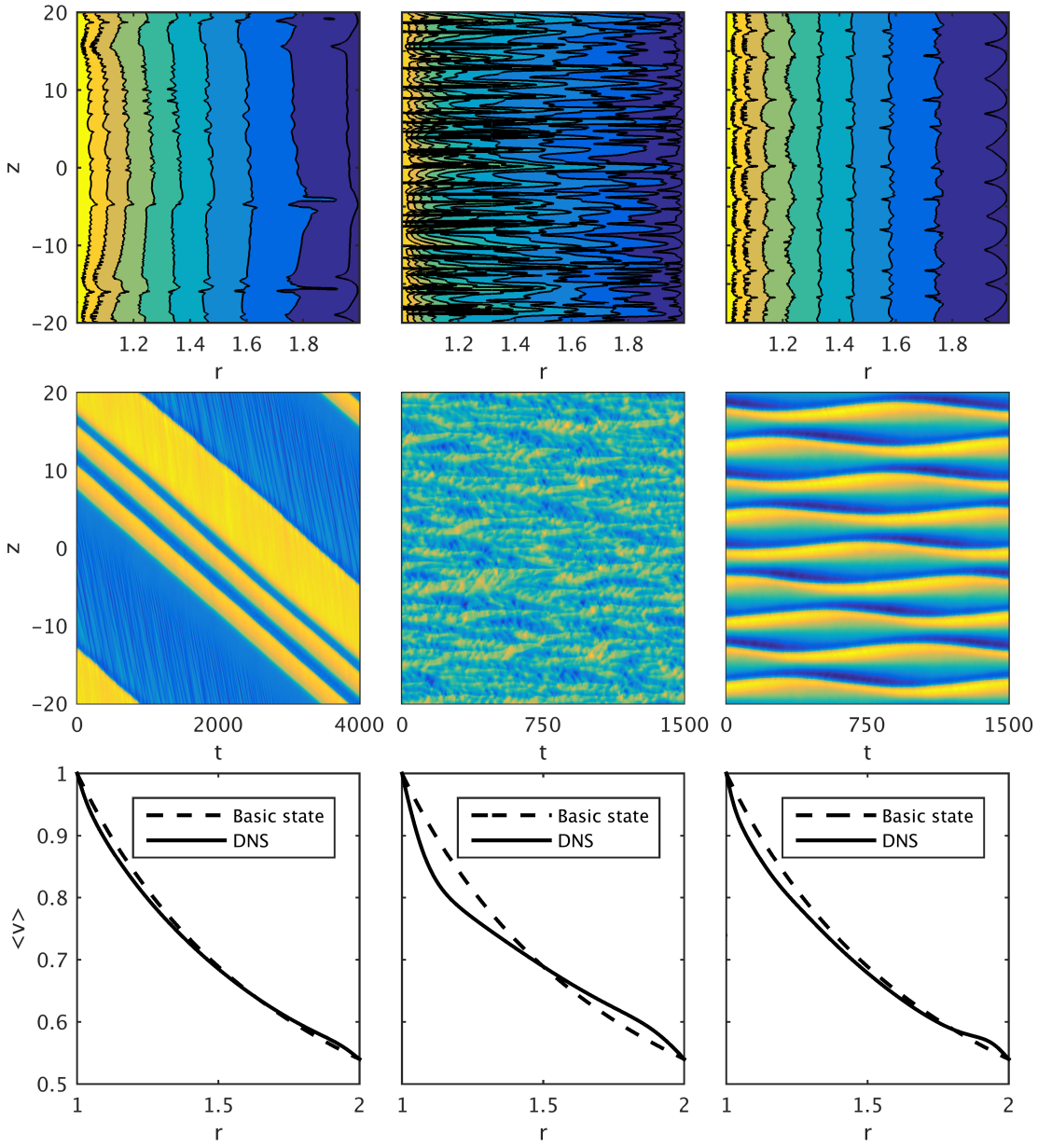

Figure 4.14: Rows showing: contour snapshots of azimuthal velocity; Hovmöller plots of ψ in terms of z and time and first cumulants. Shown in the first column is $\mathrm{Rm} = 100,\ \mathrm{Re} = 10000$, in the centre column is $\mathrm{Rm} = 2500,\ \mathrm{Re} = 250$, and in the rightmost column is the SMRI, $\beta = 0,\ \mathrm{Rm} = 100,\ \mathrm{Re} = 10000$. Comparing with the small Rm cases in figure 4.1, results are strikingly different.

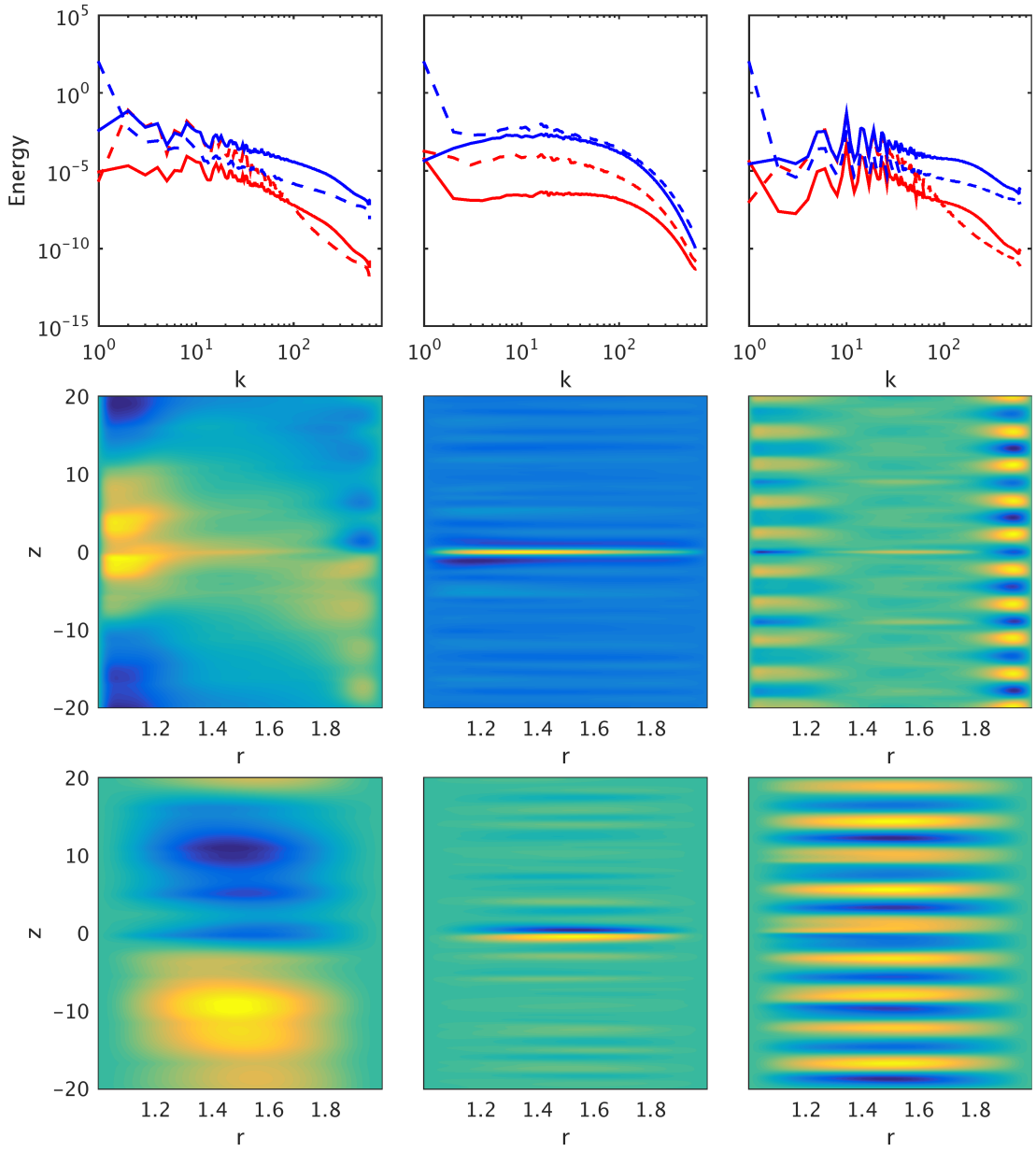

Figure 4.15: Columns as in figure 4.14, with rows showing: vertical energy spectra for the magnetic field (red) and velocity (blue) with poloidal components (solid) and toroidal components (dashed); second cumulants $\langle v'v' \rangle$; second cumulants $\langle v'\psi' \rangle$.

the resolution is not a particularly attractive option. To this end, we claim that the Pm=10 HMRI offers a good representation of the high Pm flows, and extend this work by looking in a different direction.

Let us instead consider the dynamics of the equivalent SMRI flow for Re = 10000, Rm = 100. Note from the contour plot that this shares a consistent degree of turbulence with the equivalent HMRI parameter set. The specific flow however, is vastly different to those seen for the HMRI. For one, we no longer note the characteristic travelling wave, with the solution now consisting of axially oscillating vortices. The wave-pattern has a wavenumber of nine, which is reflected in the dominant energy peak in the spectrum. The first cumulants denote a more efficient momentum transport than the equivalent HMRI; precisely the reason why SMRI is so effective in astrophysical scenarios. The second cumulants are interesting in that they show there to be strong correlations with points at the boundary, yet weak (opposite) or no correlation with the radially central points. Recalling that we are considering correlations of $r_2 = 1.5$, it is peculiar that these central points have almost no correlation with themselves. In addition, note that the cumulants have the same wavenumber nine pattern as found in the Hovmöller plots, and suggested by the small peak in the spectra.

GQL

HMRI – Pm = 0.01**,** Re = 10000**,** Rm = 100

Let us now examine the efficacy of GQL when applied to the low-Pm HMRI. Beginning with QL $\Lambda = 0$, we note in figure 4.16 that the flow shown in the Hovmöller plot gets very little correct in the approximation. Indeed, not only are the number and size of the vortex bands incorrect, but the flow propagates in entirely the wrong direction. We did not expect that QL theory would produce a particularly convincing reproduction of the flow. However, the extent of the inaccuracy extends to the most fundamental of characteristics. It is an understatement to say that $\Lambda = 0$ fails in its approximation. Upon examining the Hovmöller plots for $\Lambda = 2$ and $\Lambda = 6$ – which we recall in inductionless flow proved to be the range of Λ typically required for

accurate flow reproduction – we note that these two approximations offer no great increase in accuracy over $\Lambda = 0$. Whilst they do manage to get the direction of flow correct, they fail in capturing the axial lengthscale of vortices. It is not until Λ is increased much further, say to $\Lambda = 20$, that the Hovmöller plots begin to properly reflect the fully nonlinear flow, though not with 100% accuracy. This is an order of magnitude increase over inductionless flows, and illustrates precisely the additional difficulties that the magnetic nonlinear terms present to the equations. In order to obtain a (nearly) 100% accurate reproduction, one needs to take $30 < \Lambda \leq 50$. Note however, that the flow now has one less vortex pair, presumably a quirk of the initial conditions, so we expect that $\Lambda = 50$ statistics may be more ideal than those of the NL DNS.

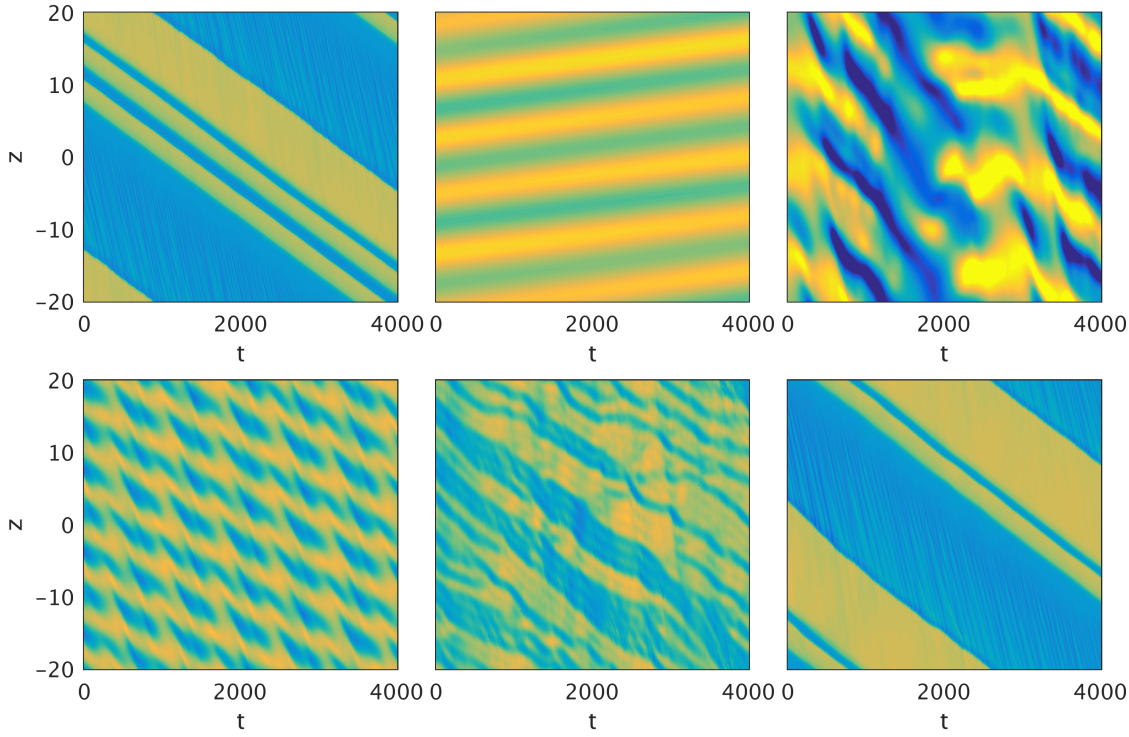

Figure 4.16: Hovmöller plots of ψ against z and time. Shown from left to right are: Top) NL DNS, $\Lambda = 0$, $\Lambda = 2$, bottom) $\Lambda = 6$, $\Lambda = 20$, $\Lambda = 50$.

We now examine the energy spectra of the flow, shown in figure 4.17, in order to gain some insight into why this is the case. On first inspection, these do not look significantly different to the inductionless spectra – the $\Lambda = 0$ case consists of a linear instability mode, and increasing Λ serves to properly distribute energy to

more of the low modes. However, we note that the NL DNS energy is more evenly spread in the lower modes, and now does not diminish until higher k values (even though the magnitudes of energy are comparable at $k = 600$). Because the GQL spectra exhibit a sharp drop at the value of Λ, it is necessary for the spectral filter to be located at higher k, where such a drop does not significantly alter the energy balance.

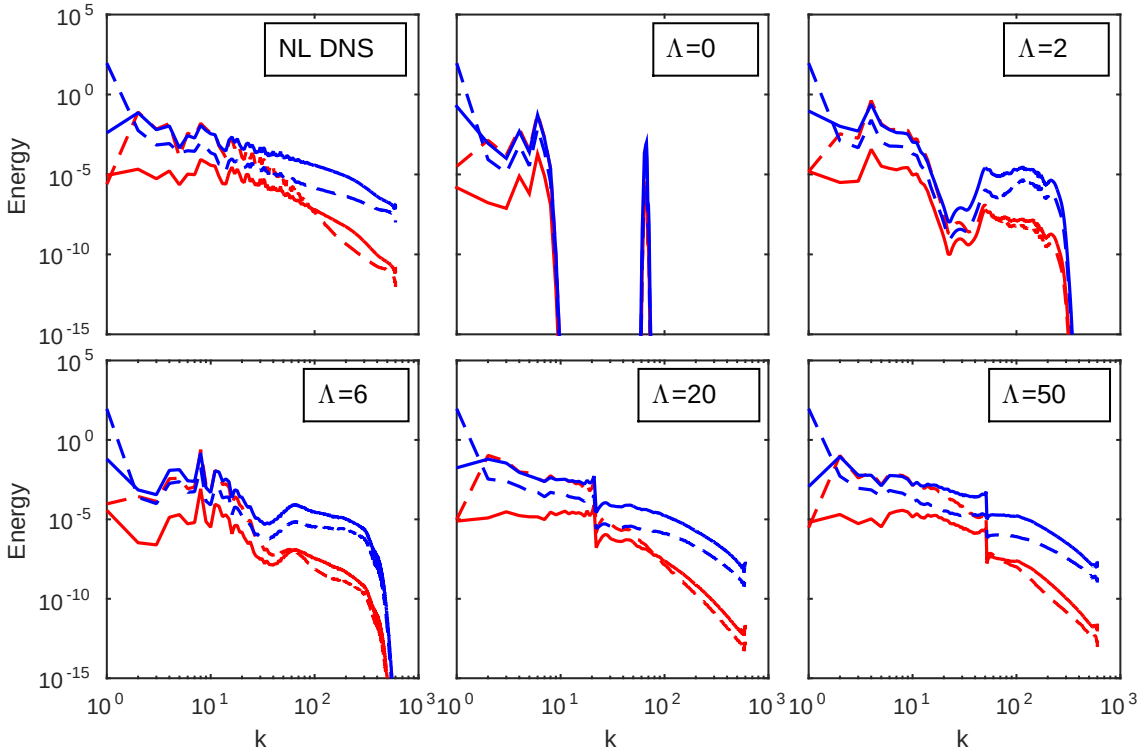

Figure 4.17: Vertical magnetic (red) and kinetic (blue) energy spectra for Rm = 100, Re = 10000, with separate poloidal components (solid) and toroidal components (dashed).

Though results have not been promising for $\Lambda = 2$ so far, we should analyse the accuracy of first and second cumulants before passing judgement – in statistical simulations we wouldn't be too perturbed if the moment-by-moment description of the flow is incorrect if the cumulants were reliable. It turns out that the magnitudes of the first cumulants are not too badly reproduced for any of the flows (figure 4.18), staying within 5% of the NL DNS case at all times; actually better than the respective inductionless flows managed. Indeed, the only Λ that does characteristically worse is the QL $\Lambda = 0$, which has less effective momentum transport (all others are

more effective, with decreasing deviation).

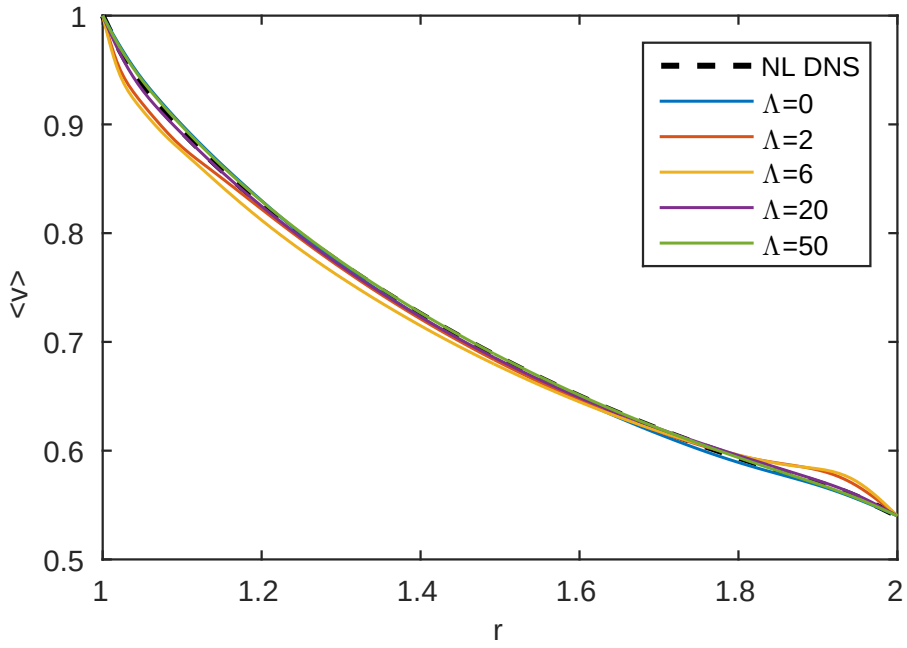

Figure 4.18: First cumulants $\langle v \rangle$ for the parameter set $\mathrm{Rm} = 100,\ \mathrm{Re} = 10000$.

As for the second cumulants, shown in figure 4.19, we find that the lowest truncations have simpler structures due to the dominance of energy in the lowest modes. The relatively strong correlation with the two boundaries is preserved, yet with wavenumbers that do not reflect the complicated NL DNS flow. The complicated structure begins to re-emerge as Λ is increased, and we do indeed find that for $\Lambda = 20$ the overall picture is correct; though it is displaced axially, the correlation structure fits broadly with the NL DNS. However, this does not hold up to close inspection; the modulation at each boundary is not reproduced, and areas of strong correlation do not match. Furthermore, there is a much greater self-correlation than in the full NL DNS system. This is rectified when moving to $\Lambda = 50$, though at the cost of many more nonlinear interactions. It should be noted that the magnitudes of these correlations can be significantly different from the NL DNS, even for higher Λ. Indeed, we observe that the $\Lambda = 50$ magnitudes are approximately a factor a ten lower than their NL DNS counterparts. Whilst this a genuine inaccuracy in the approximation, it is exacerbated by the quadratic nature of the second cumulants.

The cross cumulants (figure 4.20) exhibit the same behaviour; the large scale cor-

relation structure of the NL DNS is only properly reproduced when approaching $\Lambda = 20$, and then with the caveat of some small axial misalignment. It is only when increasing to much higher $\Lambda \approx 50$ that the precise structures match. $\Lambda = 2, 6$ offer a poor representation of the correlations, with a far greater dominant wavenumber. To that end, we reason that $\Lambda = 20$ provides a serviceable approximation, given the extra effort required to make the flow statistics fully accurate.

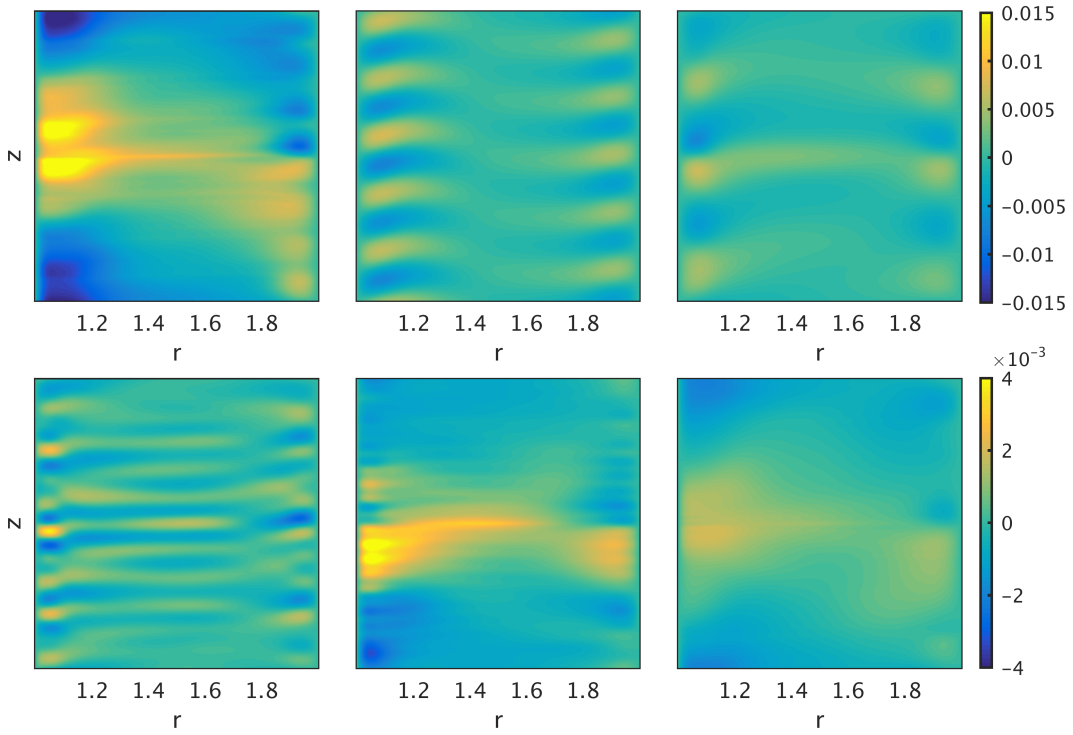

Figure 4.19: Plots of the second cumulant $\langle v'v' \rangle$ for $\mathrm{Rm} = 100$, $\mathrm{Re} = 10000$. Shown from left to right are: Top) NL DNS, $\Lambda = 0$, $\Lambda = 2$, bottom) $\Lambda = 6$, $\Lambda = 30$, $\Lambda = 50$.

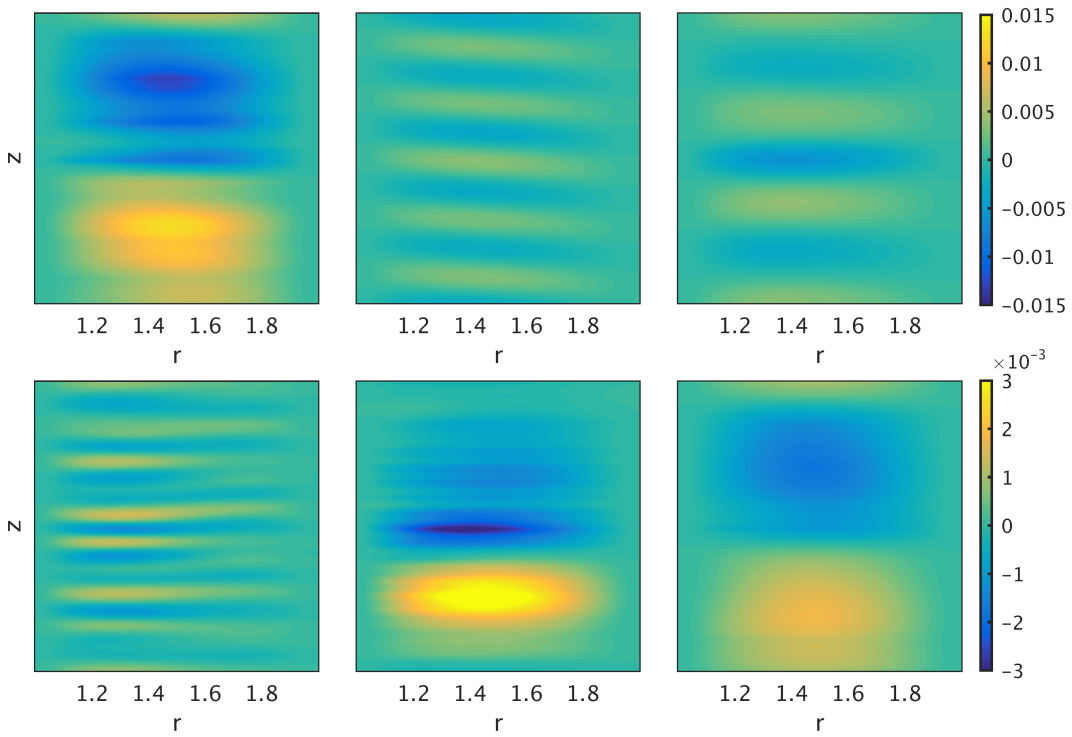

Figure 4.20: Plots of the second cumulant $\langle v'\psi' \rangle$ as in figure 4.19.

HMRI – Pm = 10**,** Re = 250**,** Rm = 2500

As we have seen in the NL DNS, this parameter set leads to a very strongly turbulent flow, with no coherent pattern emerging. It is likely, then, that this will necessitate high modal truncations in order to sufficiently incorporate the intricacies of the small-scale flows. Indeed, this is evident in the Hovmöller plots (figure 4.21), whereby the low mode truncations result in much larger scale patterns, ranging from the dominant linear instability at $\Lambda = 0$ to the large-scale drift at $\Lambda = 6$. Even for $\Lambda = 20$ we observe that the flow organises into large-scale vortex bands, though now not propagating downwards. It is only then once we increase to the much higher values $\Lambda \approx 50$ that a sufficient number of the small-scale modes are incorporated into the flow. Note, though, that even this is not perfect, as the flow here is *too* small scale; though it is suitably turbulent to be deemed a good approximation.

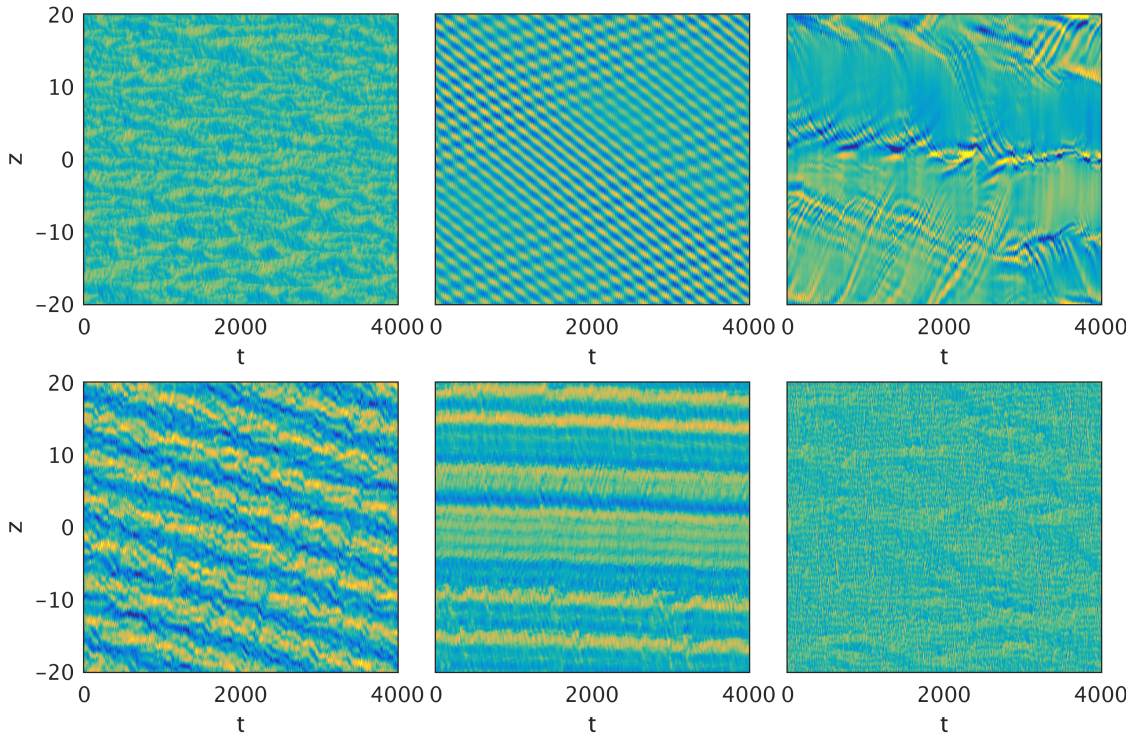

Figure 4.21: Hovmöller plots of ψ against z and time for Rm = 2500, Re = 250. Shown from left to right are: Top) NL DNS, $\Lambda = 0$, $\Lambda = 2$, bottom) $\Lambda = 6$, $\Lambda = 20$, $\Lambda = 50$.

The energy spectrum (figure 4.22) is broadly illustrative of this increase in accuracy.

QL $\Lambda = 0$ produces a linear instability peak, and the energy for $\Lambda = 2$–6 diminishes by the point it has reached $k = 100$; with a small peak at $k = 7$ in the spectra for $\Lambda = 6$. Though the spectrum of $\Lambda = 20$ certainly does a better job, we note that the region about $k = 10$ is not smooth, and it is likely this slight increase in energy that causes the flow to band up. Indeed, it is only moving to $\Lambda = 50$ that we note the energy to be smooth (aside from a small peak at the mode cut-off $k = 50$). Resulting directly from the GQL approximation method, this peak likely causes the smaller-scale flow here; however, to completely eradicate this would necessitate increasing Λ significantly.

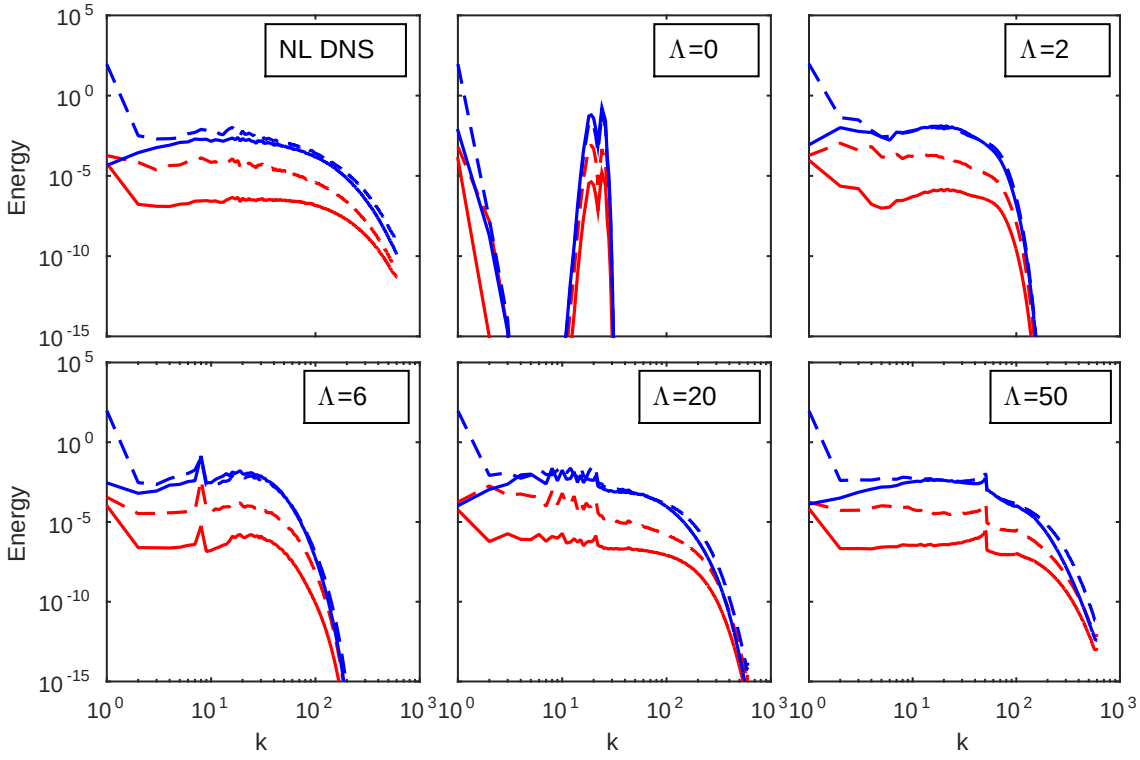

Figure 4.22: Vertical magnetic (red) and kinetic (blue) energy spectra for Rm = 2500, Re = 250, with separate poloidal components (solid) and toroidal components (dashed).

Of particular interest here is the reproduction of the first cumulants, shown in figure 4.23. For the NL DNS case, we previously saw that, as the flow is strongly turbulent, there is a particularly efficient transfer of angular momentum towards the outer boundary;.It is of interest just how GQL fares in such cases. It is immediately clear that there is significant room for improvement in *all* of the values of Λ we have

examined. Immediately one may note that, at some point in the radius, there is a minimum 5% error in each case, and 10% for $\Lambda = 0,\ 2,\ 6$, where we see that the approximation underestimates outwards angular momentum transport. This is unsurprising, as it is the – now missing – turbulence that properly facilitates this process. It is the performance of $\Lambda = 20$ and $\Lambda = 50$ that is most puzzling, however. We note that increasing Λ serves only to increase the accuracy of the graph up to $r = 1.1$, after which the values of $\langle v \rangle$ are higher than expected until around $r = 1.4$. Even doubling the cut-off to $\Lambda = 100$ does not improve this result. This serves to reinforce the difficulty in obtaining accurate statistics for such turbulent systems.

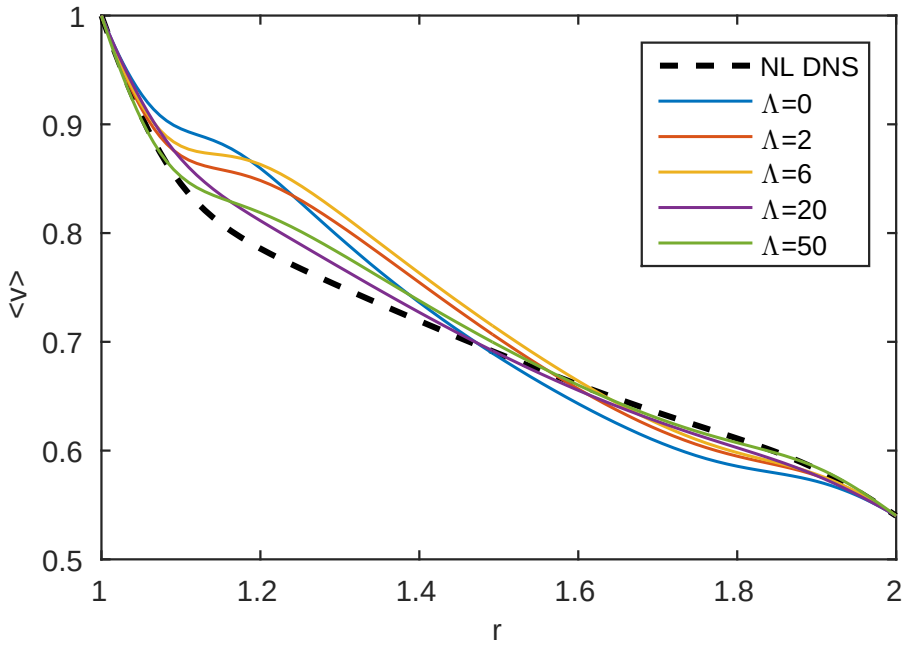

Figure 4.23: First cumulants $\langle v \rangle$ for the parameter set $\mathrm{Rm} = 2500,\ \mathrm{Re} = 250$.

Another point of interest pertains to the Rayleigh criterion, and how well it is adhered to. As we note in figure 4.24, the lowest truncations here present a fundamental violation, in that $\partial/\partial r(r\langle v \rangle)$ crosses the zero line; certainly not a characteristic inherent to HMRI flows!

Finally, in searching for accuracy in the second cumulants, shown in figure 4.25, we aim for a flow that exhibits self-correlation only. Clearly, the lower truncations cannot hope to satisfy this. Indeed, we see that the primarily δ-function-like structure begins to emerge at $\Lambda = 20$, yet it is only when increasing further that all

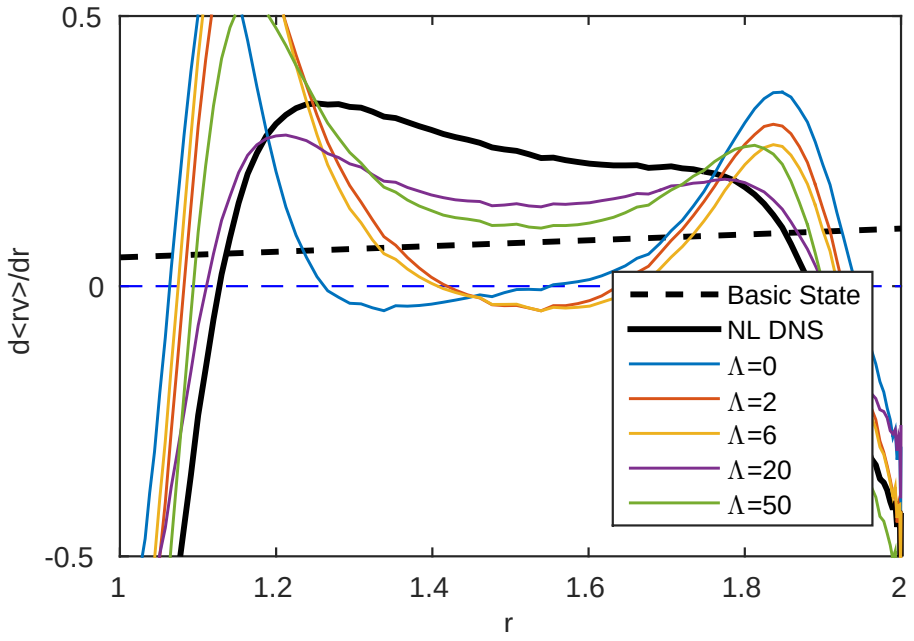

Figure 4.24: $\partial/\partial r(r\langle v\rangle)$ as in figure 4.23

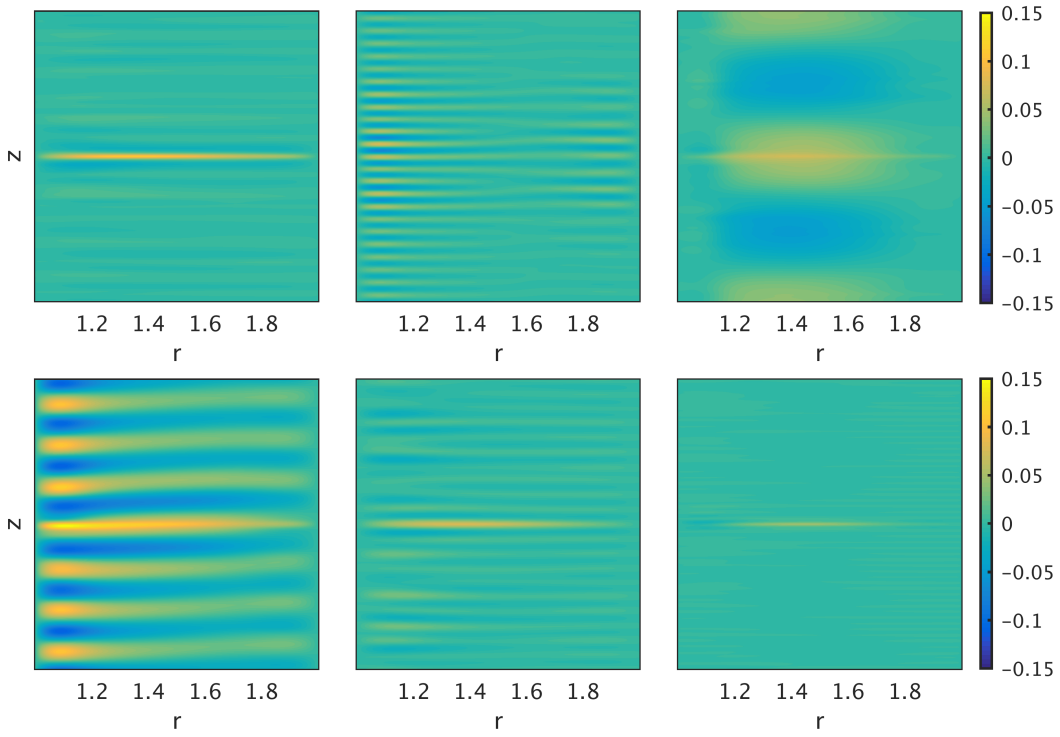

Figure 4.25: Plots of the second cumulant $\langle v'v'\rangle$ for Rm = 2500, Re = 250. Shown from left to right are: Top) NL DNS, $\Lambda = 0$, $\Lambda = 2$, bottom) $\Lambda = 6$, $\Lambda = 10$, $\Lambda = 20$.

other correlations become comparatively weak. Again, this is a key property of the second cumulants at higher spectral filters; as Λ is increased we generally note that the background correlation structure becomes finer (axially), such that it is inconsequential for sufficiently high Λ.

A special case $-$ $\mathrm{Re} = 50$**,** $\mathrm{Rm} = 500$

We have so far claimed that increasing to $\mathrm{Pm} = 10$ leads to strongly turbulent solutions, which are inherently difficult to approximate when limiting the nonlinear interactions. Indeed, we have seen exactly this for $\mathrm{Re} = 250$, and it can also be shown for $\mathrm{Re} = 100$. This leads to a rather pessimistic view of the possibility of GQL in general MRI flows. However, this is not necessarily always the case. Let us take, for example, the case $\mathrm{Re} = 50, \mathrm{Rm} = 500$. Now, $\mathrm{Re} \approx 2\mathrm{Re}_c$, so the flow is still only weakly nonlinear, as is clearly seen in the structure of the energy spectrum. Aside from rapidly decreasing energies in the first few modes, the flow is dominated by the linear instability with mode-number $k \approx 13$, seen also in the structure of the second cumulant. In this case, even $\Lambda = 0$ QL is exactly correct for both the Hovmöller plot and second cumulant correlation. So, though we may conclude that induction effects severely affect the viability of GQL, we may at least be reassured weakly nonlinear flows remain achievable.

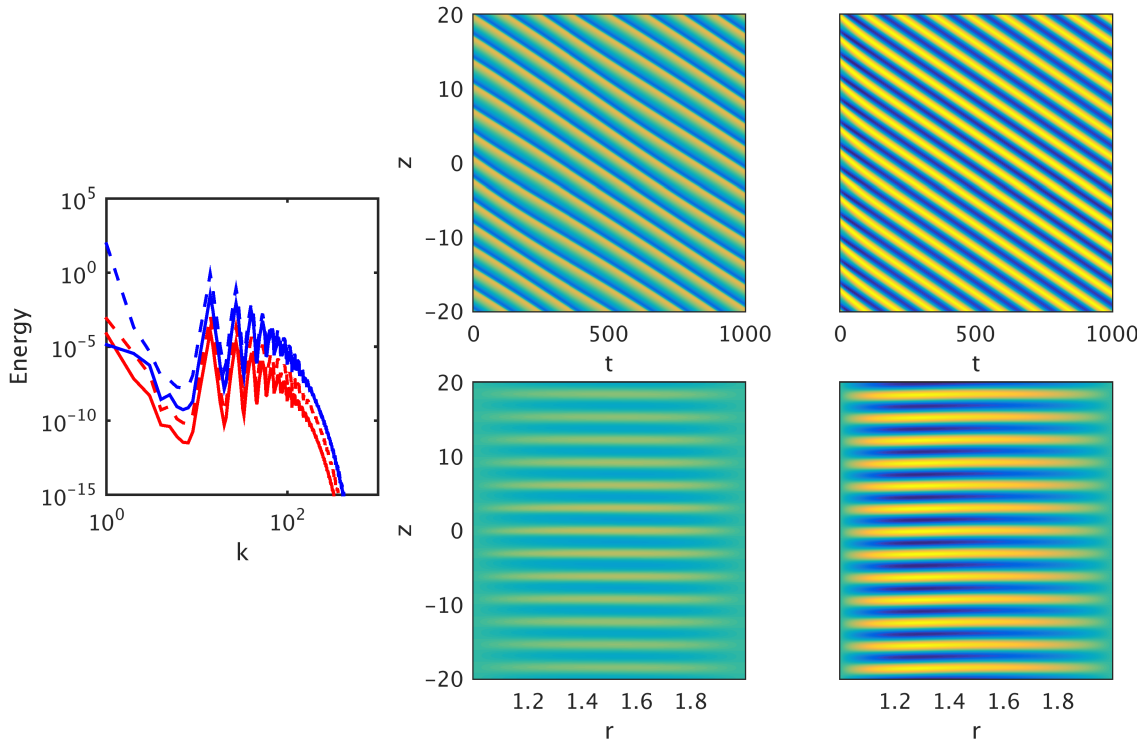

Figure 4.26: Spectra for the weakly nonlinear Rm = 500, Re = 50, alongside Hovmöller plots and second cumulants for the NL DNS and QL $\Lambda = 0$.

SMRI − Pm = 0.01**,** Re = 10000**,** Rm = 100

Let us finally turn to the GQL approximation as implemented on the SMRI. Here, we see a similar situation develop to the HMRI, whereby once again an order of magnitude more large-scale modes are require for accurate solutions. In figure 4.27, we observe that the QL $\Lambda = 0$ produces significant errors in the flow, producing a upwardly travelling wave solution, instead of the oscillating vortices. Indeed, virtually none of the characteristic behaviour of the flow is preserved. Then, as more large-scale modes are included, we see that the flow becomes more complex, consisting of alternating sets of oppositely signed vortices, each propagating in different directions. It is clear that the additional low modes have allowed for a crude incorporation of the axial vortex oscillation found in the NL DNS, yet without properly defined small scale interactions, they struggle to capture anything more than the basic flow characteristics. Indeed, it is not until significantly more large scale modes are considered that these Hovmöller plots gain any kind of accuracy. By $\Lambda = 30$ the vortices regain the same kinds of axial lengthscale, but do not exist in the same coherent manner as the NL DNS. Moreover, it is not until we hit the region $\Lambda \approx 50$ that the vortices begin to persist continually over time. Even so, we still note errors in the Hovmöller plots in this case; an incorrect number of vortices are produced, for example. In fact, we have to increase Λ yet further to receive a plot that closely resembles the NL DNS, at $\Lambda = 100$, say.

We get a hint of precisely why this is the case from the energy spectra in figure 4.28. As is seen, the lowest truncations are unable to properly transport the energy to the higher modes, leading to linear, or more basic, instabilities and flow. When increasing to $\Lambda = 50$ though, this problem is mainly alleviated. However, note that the spectrum is mostly flat in the lowest modes, aside from a small peak at $\Lambda = 8$ coinciding with the wavenumber of the flow. This is significantly simpler than the corresponding NL DNS spectra, whereby there are a number of peaks about this area. The key to the success of $\Lambda = 100$ lies in its ability to reproduce these peaks properly. Quite why such a large number of modes are required to properly reproduce the lowest part of the spectrum is unknown, though it is clear that the feedback from small-scale to large-scale is important here.

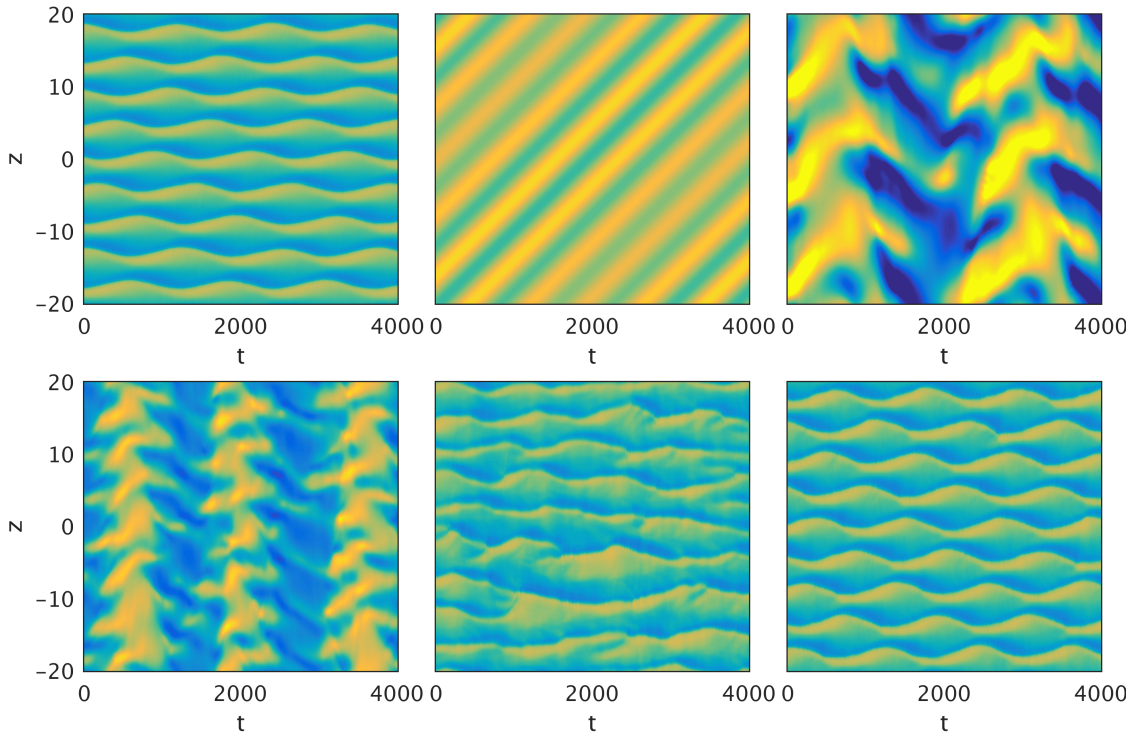

Figure 4.27: Hovmöller plots of ψ against z and time for the SMRI $\beta = 0$, Re $=$ 100, Re $=$ 10000. Shown from left to right are: Top) NL DNS, $\Lambda = 0$, $\Lambda = 2$, bottom) $\Lambda = 6$, $\Lambda = 50$, $\Lambda = 100$.

What is perhaps surprising is how little these various failings seem to affect the first cumulant, shown in figure 4.29, where we see minimal error for all but $\Lambda = 0$. Whilst the approximations do tend to underestimate the efficiency of angular momentum transport, with higher azimuthal velocities at all but the inner boundary, errors are no larger than a couple of percent for even $\Lambda = 2$.

Finally then, we turn to the second cumulants (figure 4.30). The correlations in $\Lambda = 0$ and $\Lambda = 2$ are significant deviations from the NL DNS. Indeed, we see here that the correlations are strongest near the inner boundary, as opposed to the outer boundary, and that, as we had seen in the corresponding Hovmöller plots, the wavenumbers are much less than the full flow. What is interesting is that by $\Lambda = 6$, for which the Hovmöller plot still showed significant errors, we observe that some of the key characteristics of the NL DNS correlations have re-emerged. The correlation structure now once more has three distinct 'sections' across the radius,

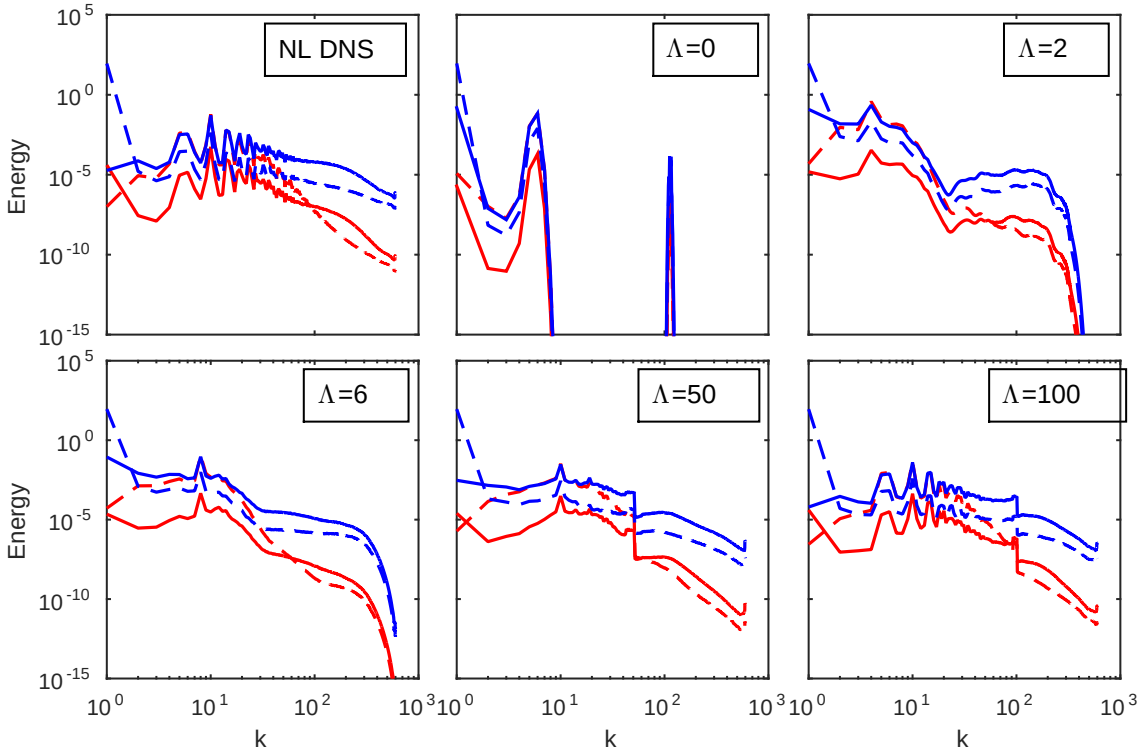

Figure 4.28: Vertical magnetic (red) and kinetic (blue) energy spectra for $\beta = 0$, $\mathrm{Rm} = 100$, $\mathrm{Re} = 10000$, with separate poloidal components (solid) and toroidal components (dashed).

with the correlation at the boundaries and centre being of opposite value. However, the correlations are still in a sense reversed, with the strongest values at the inner boundary. Furthermore, the wavenumber is only seven, and not nine as in the NL DNS. Increasing to $\Lambda = 50$ then, we note that the correlations are once more strongest at the outer boundary, and the self-correlation of any given point is more strongly local. In fact, the wavenumber nine pattern is now present, leading us to believe that $\Lambda = 50$ would be sufficient for GQL. So, we conclude that Λ values $\mathcal{O}(10)$ greater than the inductionless equivalent are required in the approximation, with ~ 50 necessary for accurate low-order statistics and $\sim 100$for proper time-evolution of the flow.

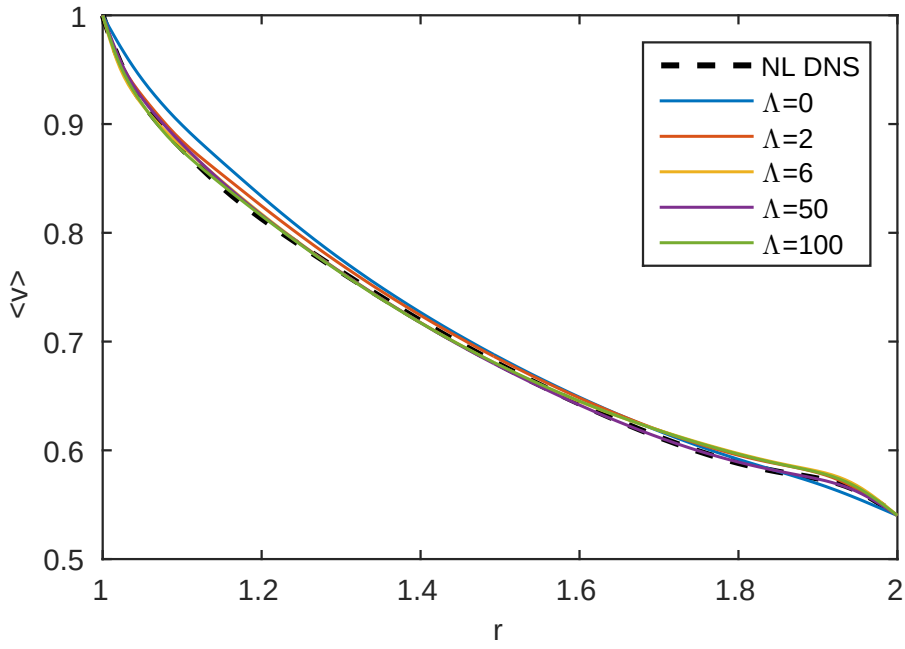

Figure 4.29: First cumulants $\langle v \rangle$ for the SMRI at $\beta = 0,\ \mathrm{Rm} = 100,\ \mathrm{Re} = 10000$.

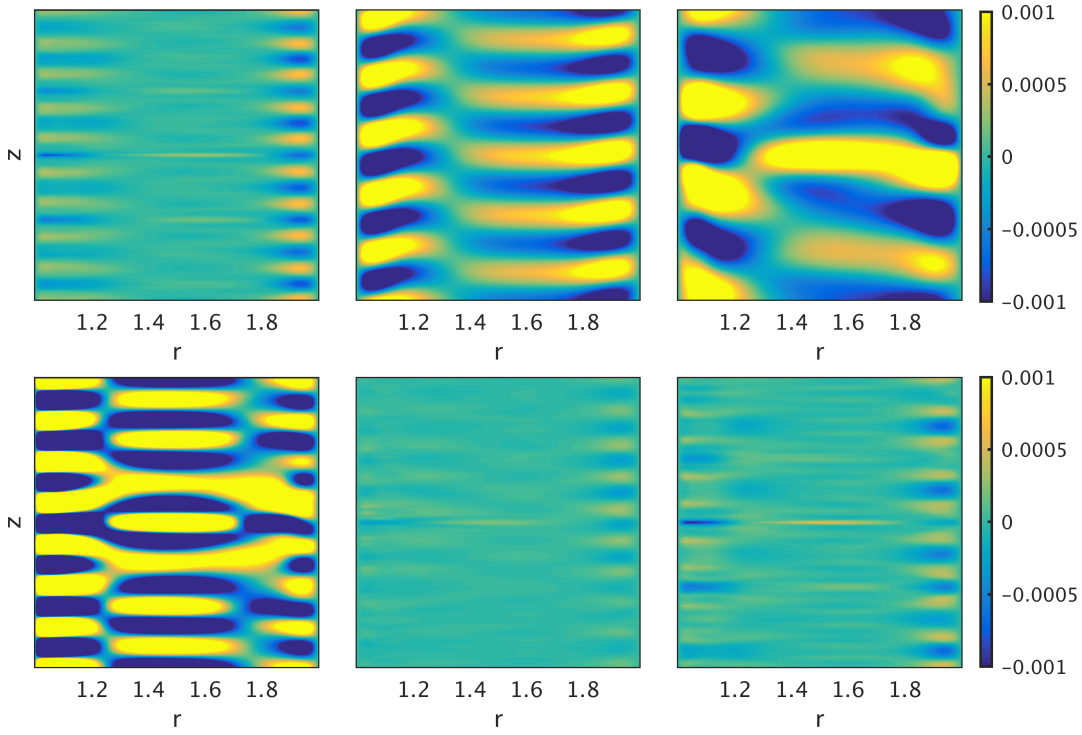

Figure 4.30: Plots of the second cumulant $\langle v'v' \rangle$ for $\beta = 0,\ \mathrm{Rm} = 100,\ \mathrm{Re} = 10000$. Shown from left to right are: Top) NL DNS, $\Lambda = 0$, $\Lambda = 2$, bottom) $\Lambda = 6$, $\Lambda = 50$, $\Lambda = 100$.

Chapter 5

Axisymmetric pulse trains in narrow-gap spherical Couette flow

In this chapter we focus on spherical Couette flow, and in particular the axisymmetric solutions in narrow-gap geometry. Previous works have shown that solutions exist in the form of travelling waves; more specifically as pulse trains of Taylor vortices that propagate equatorward in each hemisphere. Indeed, asymptotic solutions, valid as the aspect ratio $\epsilon \to 0$ *– highlight that pulse trains can have varied and complicated dynamics, with the possibility of a number of different symmetries and periodicities. In this chapter, we give a detailed numerical exploration of the pulse train solutions at finite aspect ratios, and map out the various bifurcations that exist. We find symmetric, asymmetric, periodic and quasi-periodic pulse trains, and show that, based on the bifurcation sequences, a new 'very narrow-gap' classification is warranted, due to differences in the first few bifurcations. Whilst the majority of our results cover the case where only the inner core rotates, then we briefly touch upon the case of co-rotation, before extending our work to include magnetohydrodynamic effects, which have not been examined before for such narrow gaps.*

5.1 Background

We gave a brief introduction to spherical Couette flow in chapter 1, where the more universal properties of its dynamics were discussed. Recall that the flow could be split into three regimes based on the gap width; large gap, medium gap and narrow gap. Whilst much of the previous work on this topic has been concerned with medium or large gaps due to their potential applications, there have been many interesting studies into the dynamics of narrow gap spherical Couette flow. Wimmer (1976, 1981) performed experiments with aspect ratios as narrow as $\epsilon = 0.0063$, finding that instability first manifests in the form of Taylor vortices in the vicinity of the equator, where the centrifugal forces that drive instability are greatest. These vortices are, as expected, of the length-scale ϵ, and of roughly square cross section, filling the whole gap width. Because the vortices are localised to the equator, it was presumed that this region could be approximated by the equivalent Taylor-Couette flow, and that therefore the critical Reynolds number is that of the cylinder, which is well understood.

Asymptotic analysis by Hocking & Skiepko (1981); Walton (1978) did indeed verify that vortices must be localised about the equator, though showed that tangent cylinder approximation to be inaccurate; the onset of instability occurs for Reynolds numbers *higher* than the corresponding critical cylindrical value. The discrepancy can be attributed to the boundary curvature of the spherical geometry and the resulting presence of Ekman cells (where fluid travels toward the equator at the inner sphere, and then returns poleward via the outer sphere). This leads to phase mixing, in which frequencies vary depending on position (see (Heyvaerts & Priest, 1983) for a discussion of phase mixing in an astrophysical context). This phase mixing process shortens length-scales and results in enhanced dissipation, acting as a stabilising influence. The first accurate critical values were given by Soward & Jones (1983), via a WKBJ method.

Pioneering numerical work was carried out by Bartels (1982), whereby axisymmetric solutions were found for ϵ as low as 0.0256. Given the available computational power

in 1982, certain compromises had to be made in achieving such computations; as well as being axisymmetric, the numerics forced symmetry about the equator, and few calculations could be performed for the narrowest of gaps (only one Reynolds number was examined for $\epsilon = 0.0256$, resulting in non-periodic travelling wave solutions). Nonetheless, to have performed these calculations – which must have required high numerical resolution – was impressive, and the complicated travelling wave solutions that were found certainly help to motivate the present work.

Further exploration of the travelling wave solutions was given in a series of asymptotic publications by Soward, Bassom and collaborators. Here we will discuss briefly their findings, but for a more thorough review, see (Soward & Bassom, 2016), which covers all results in detail whilst briefly expanding on the concept of frequency staircases in the flow.

These asymptotic works extended the problem to weakly nonlinear theory, and derived nonlinear equations governing the amplitude of the various Taylor vortices. Harris *et al.* (2000, 2003) looked specifically at the case of almost co-rotation between the two spherical shells, i.e the parameter range $\delta = (\Omega_i - \Omega_o)/\Omega_i \sim \epsilon^{1/2}$, valid in the asymptotic regime $\epsilon \to 0$. The weakly nonlinear formulation allowed for effects such as phase mixing to be properly taken into account, yielding travelling wave solutions. These solutions, much like Bartels', consist of a number of Taylor vortices, each travelling towards the equator. In particular, a number of solutions and symmetry classes are discussed, and some plots of the travelling wave solutions are presented.

Bassom & Soward (2004) then developed a rigorous asymptotic theory, in the $\epsilon \to 0$ limit, for such travelling wave solutions for a wider range of δ, finding travelling wave solutions to exist in the range $\epsilon^{1/2} \leq \delta \leq 1$. This includes not only the aforementioned case of almost co-rotation, but also the experimentally viable $\delta = 1$ case, where only the inner sphere rotates, and the outer sphere is stationary. Furthermore, influenced by Ewen & Soward (1994a,b), they identified that the travelling wave solutions take the form of pulse trains, with Taylor vortex pulses. Hence, for $\epsilon \to 0$, these vortices exist in the vicinity local to the equator, travelling towards it as

pulses, with amplitude modulated under some wave-envelope. It is stated that there is some dislocation halfway between each pulse centre, where the locally dominant pulse changes, and over extremely long time-scales these pulse centres drift poleward. They state that this leads to unstable solutions over such long time-scales, however it is unclear whether this would be the case for small but finite ϵ, as well as precisely how long such time-scales would be.

Blockley *et al.* (2007) significantly expanded upon this work, increasing the number of known symmetry classes for the pulse train solutions. Moreover, solutions are found possessing not only periodic but weakly chaotic dynamics. It was highlighted that in the $\epsilon \to 0$ limit there exists no bifurcation sequence directly to the pulse train solutions, which would certainly not be expected for finite ϵ. Finally, Blockley *et al.* reached the conclusion that the pulse train solutions are qualitatively similar to spiral vortex solutions found in the 3-D spherical Couette problem.

Of course, prior experimental work on narrow-gap spherical Couette flow has all been conducted in 3-D, giving a rich array of results for comparison. Studies such as those of Nakabayashi (1983); Nakabayashi *et al.* (2002) (including ϵ as low as 0.024) have identified many different 3-D solutions that may occur, including toroidal, wavy, and spiral vortices. More recent experiments have examined the transition to turbulence using novel methods, with the same array of complicated 3-D flow identified (Mahloul *et al.*, 2016). Adel & Ahcene (2016) increased the Reynolds number high enough that they observe a reversal in the turbulent solution, with flow spiralling from the equator to the poles. The spiral vortices are perhaps best illustrated numerically in the work of Dumas & Leonard (1994), where the similarities to the axisymmetric pulse trains are clear to see; the azimuthal evolution of the spiral vortex flow corresponds to the time evolution of the axisymmetric pulse trains.

Of most interest in the 3-D solutions are the parameter ranges close to critical; that is, where the flow is only weakly nonlinear and thus axisymmetric solutions prevail. There have been a select number of numerical solutions that have briefly examined this, for example Zikanov (1995, 1996) generated axisymmetric one- and two-vortex states without imposing any kind of symmetry, for the gap width $\epsilon = 0.11$. It is

stated that the bifurcation sequences proceeds as: the fluid undergoes a subcritical pitchfork bifurcation to axisymmetric vortices, before another bifurcation causes azimuthal secondary flows to appear, causing spiral vortices. However, this value of ϵ is borderline medium-gap; it is likely that this does not cover the true extent of the dynamics that can occur when the gap width is very narrow. Yuan (2004) took $\epsilon = 0.06$, now safely in narrow gap territory, yet still not approaching the asymptotic solutions. Here agreement was again found with the initial bifurcation to one- and two-vortex flow, however, it was noted that the subsequent bifurcation results in unsteady axisymmetric travelling wave solutions, which are unstable over long time-scales to 3-D wavy and spiral modes. This travelling wave solution is found to remain stable over increasingly long time-scales as ϵ is decreased, motivating our exploration of the axisymmetric pulse trains in very narrow gaps.

Finally, we shall give a brief overview of the medium gap dynamics, so that we can distinguish any overlap between regimes. Though many of the experimental and analytical works had shown that Taylor vortex solutions exist in the medium gaps, it was Schrauf (1986) that first described the transition from the basic state. It was shown that the first bifurcation is a subcritical pitchfork, causing the basic state to become unstable to asymmetric perturbations and eventually resulting in a one-vortex state. This one vortex branch was shown to possess a slight amount of hysteresis. In addition, Marcus & Tuckerman (1987a,b) examined the steady states and transitions between vortex solutions in greater detail. The authors discuss pinches that may occur in the flow below marginal stability, as well as the bifurcations and symmetries that can occur above it. Bühler (1990) independently investigated the transitions between the different vortex states for the same aspect ratio, and gave comparison to experiments. Finally, Mamun & Tuckerman (1995) produced a full bifurcation schematic detailing the dynamics for $\epsilon = 0.154$ as the Reynolds number is increased. They plotted the stable and unstable branches, showing the range of the zero-, one-, and two-vortex solutions, and also asymmetric solutions.

In this chapter, we aim to bridge the gap between prior 2-D numerical work and the asymptotic pulse train solutions of Soward and collaborators, As such we examine the cases $\epsilon = 0.04$ and 0.02, and map out the bifurcation sequences that occur. In

order to examine such small aspect ratios, we develop an efficient time-stepping code in spherical geometry and probe the various pulse train solutions that appear. We show how the narrow gap bifurcation sequences link to those of the medium gap, and justify why the smallest aspect ratios, $\epsilon \leq 0.023$ should be classified separately as 'very narrow-gap' solutions. Finally, we examine the wave-envelope under which the pulse train solutions develop, and link this to both the bifurcation sequence and the location of any phase-slips that arise.

5.2 Mathematics

We take axisymmetric spherical Couette flow, with radii and angular velocity at the two shells given by r_i, r_o and Ω_i, Ω_o, respectively. Our flow is thus governed by the Navier-Stokes equation, suitably nondimensionalised as

$$\frac{\partial \mathbf{U}}{\partial t} + \mathbf{U} \cdot \nabla \mathbf{U} = -\nabla p + \frac{1}{\mathrm{Re}} \nabla^2 \mathbf{U}, \tag{5.1}$$

with the addition of the incompressibility condition $\nabla \cdot \mathbf{U} = 0$. Here we choose to nondimensionalise length with the inner radius, r_i and time with respect to the rotational period Ω_i^{-1}. In spherical geometry, the boundary conditions are straightforward; we have that $\mathbf{U} = \Omega_{i,o} \sin\theta \, \mathrm{e}_\phi$. As in previous chapters, we take advantage of the toroidal-poloidal expansion to enforce axisymmetry in our solutions whilst also guaranteeing incompressibility. That is, we let

$$\mathbf{U} = v \, \mathrm{e}_\phi + \nabla \times (\psi \, \mathrm{e}_\phi) \, . \tag{5.2}$$

In order to evolve the equations in time, we again use a pseudo-spectral time-stepping method. This is implemented in a similar fashion to the previous chapter, and any intricacies that are unique to the spherical geometry are discussed in section 2.5.3.

5.2.1 Energy spectra

We know from prior asymptotic treatments of narrow-gap spherical Couette flow that the solutions consist of many small-scale Taylor vortices. As such, numerical

resolution is a real concern, as truncating the higher modes too eagerly could result in a loss of important small-scale flow behaviour. It is important that we know the energy spectra then, as to guarantee this is not the case.

The kinetic energy present in the flow is given by an integral over the whole volume,

$$\int_0^{2\pi}\int_0^{\pi}\int_{r_i}^{r_o}\frac{1}{2}|\mathbf{U}|^2 r^2\sin\theta\,\mathrm{d}r\,\mathrm{d}\theta\,\mathrm{d}\phi. \tag{5.3}$$

It has previously been established in section 4.3.1 that radial integration may be performed via the composite Simpson's rule, and it is that ϕ integrals are trivial, resulting in a factor of 2π. In this section, we briefly discuss the θ integration. Let us first express the integral as,

$$\pi\int_{r_i}^{r_o}\left[\int_0^{\pi}\left(U_r^2+U_\theta^2+v^2\right)\sin\theta\;\mathrm{d}\theta\right]r^2\;\mathrm{d}r. \tag{5.4}$$

Turning our attention to the toroidal component, we have that

$$\int_0^{\pi}v^2\sin\theta\;\mathrm{d}\theta=\int_0^{\pi}\sum_{l=1}^{L}\sum_{l'=1}^{L}v_l Y_l^1 v_{l'}Y_{l'}^1\sin\theta\;\mathrm{d}\theta. \tag{5.5}$$

But, by the orthogonality of associated Legendre polynomials,

$$\int_0^{\pi}Y_l^1(\cos\theta)Y_{l'}^1(\cos\theta)\sin\theta\,\mathrm{d}\theta=\int_{-1}^{1}Q_l^1Q_{l'}^1P_l^1(x)P_{l'}^1(x)\,\mathrm{d}x=2\delta_{ll'}, \tag{5.6}$$

so the integral simplifies to

$$\int_0^{\pi}v^2\sin\theta\,\mathrm{d}\theta=\sum_{l=1}^{L}2v_l^2. \tag{5.7}$$

In addition,

$$\int_0^{\pi}u_\theta^2\sin\theta\,\mathrm{d}\theta=\int_0^{\pi}\sum_{l=1}^{L}\sum_{l'=1}^{L}\left(-\frac{\psi_l}{r}-\frac{\partial\psi_l}{\partial r}\right)Y_l^1\left(-\frac{\psi_{l'}}{r}-\frac{\partial psi_l'}{\partial r}\right)Y_{l'}^1, \tag{5.8}$$

for which we apply the same reasoning to show that

$$\int_0^{\pi}u_\theta^2\sin\theta\,\mathrm{d}\theta=2\sum_{l=1}^{L}\left(-\frac{\psi_l}{r}-\frac{\partial\psi_l}{\partial r}\right)^2. \tag{5.9}$$

Finally,

$$\int_0^{\pi}u_r^2\sin\theta\,\mathrm{d}\theta=$$
$$\int_0^{\pi}\sum_{l=1}^{L}\sum_{l'=1}^{L}\left(\frac{1}{r\sin\theta}\frac{\partial}{\partial\theta}\left(Y_l^1\sin\theta\right)\right)\psi_l\left(\frac{1}{r\sin\theta}\frac{\partial}{\partial\theta}\left(Y_{l'}^1\sin\theta\right)\right)\psi_{l'}\,\mathrm{d}\theta. \tag{5.10}$$

Fortunately, it can be found that the two summed quantities are in fact orthogonal (as implied via Sturm–Liouville theory),

$$\int_0^\pi \left(\frac{1}{r\sin\theta}\frac{\partial}{\partial\theta}\left(Y_l^1\sin\theta\right)\right)\left(\frac{1}{r\sin\theta}\frac{\partial}{\partial\theta}\left(Y_{l'}^1\sin\theta\right)\right)\,\mathrm{d}\theta = 2l(l+1)\delta_{ll'}, \tag{5.11}$$

and so

$$\int_0^\pi u_r^2\sin\theta\,\mathrm{d}\theta = \frac{2}{r^2}\sum_{l=1}^{L} l(l+1)\psi_l^2. \tag{5.12}$$

Given these results for θ integration, all that remains is to apply Simpson's rule in r, for which we do not give further detail here.

5.3 Results

To explore the bifurcations that occur, we begin with stationary flow, and gradually increase the Reynolds number until it reaches the critical value. In all aspect ratios discussed the basic state flow is the same so-called zero-vortex state, where the flow takes the form of two Ekman cells, one in each hemisphere. As the flow is stable in this configuration, there are no Taylor vortices.

5.3.1 $\epsilon = 0.04$

We first consider the case where $\epsilon = 0.04$, and plot a schematic bifurcation diagram in figure 5.1. Here we find that the basic state becomes unstable at Re = 5395 via a subcritical pitchfork bifurcation, resulting in a one-vortex solution. We see that the mechanism for this instability involves equatorially asymmetric transients, which eventually decay as the system equilibrates to the symmetric one-vortex state. This one-vortex branch possesses hysteresis, persisting as we decrease to Re = 5391. The branch remains stable as we increase up to $Re \approx 5450$, whereby it loses stability via another subcritical pitchfork, involving similarly asymmetric transients. Indeed, this process involves one of the vortices drifting into the opposing hemisphere, with an additional two being generated in its place, yielding a two-vortex solution. Again, note that the two-vortex branch also has hysteresis, with the state persisting as Re is decreased Re $\approx$ 5435. It can easily be verified (via forcing equatorial symmetry) that the zero- and two-vortex solutions are connected by an asymmetrically unstable state.

To illustrate such solutions, we plot contours of the meridional circulation ψ in figure 5.2; here the vortex structures are clearly defined. It is clear that, because the gap-width is so narrow, the vortices possess only a simple radial structure. It is also beneficial to consider the Taylor vortices in terms of the magnitude of ψ, so we plot a one-dimensional slice of ψ taken at a radius that is nearly the centre of the annulus. Here, the Taylor vortices correspond to any oscillation of ψ that crosses the $\psi = 0$ line. Note that the precise nature of the Ekman cells present in the flow

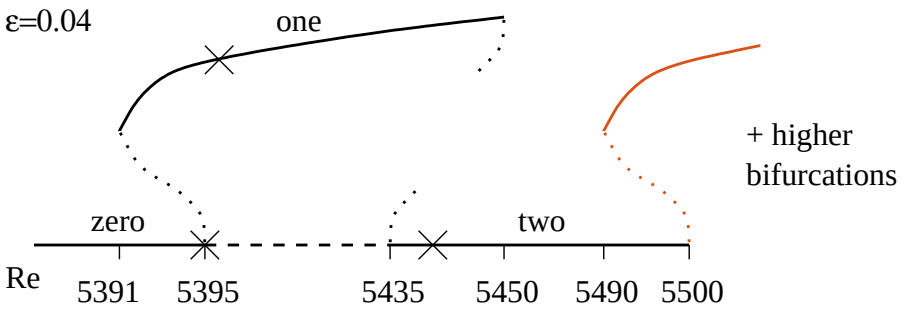

Figure 5.1: Schematic bifurcation diagram for $\epsilon = 0.04$. Solid lines indicate stable solutions, dashed lines indicate verified unstable solutions and dash-dotted lines indicate presumed unstable solutions. Black lines represent symmetric, steady state solutions, whilst red are symmetric and periodic. Crosses denote solutions shown in figure 5.2.

cause a background gradient to appear in this plot. This is difficult to remove, as the unstable flow deviates slightly from the basic state solution, and there are no analytic expressions to account for this.

It turns out that the solutions described thus far are exactly the same as those described by Mamun & Tuckerman (1995) for the medium gap $\epsilon = 0.154$. Indeed, the bifurcation sequence, hysteresis, and instability mechanism is unchanged in our moderately narrow-gap case. It is only when Re is increased even further that any significant variation from the medium-gap case is noticed. Whereas for medium gaps, subsequent solutions are steady state (or steady state asymmetric), in the moderately narrow gap we begin to obtain the time-dependent pulse train solutions described by Bassom, Soward *et al.* However, we choose not to describe them in further detail for $\epsilon = 0.04$, as they are fundamentally similar to the pulse train solutions found for the more interesting $\epsilon = 0.02$.

5.3.2 $\epsilon = 0.02$

In figure 5.3, we plot the bifurcation schematic for $\epsilon = 0.02$, and may note some immediate differences to the bifurcation sequence previous discussed. First, we find that the one-vortex state is no more, and that there is no longer an unstable

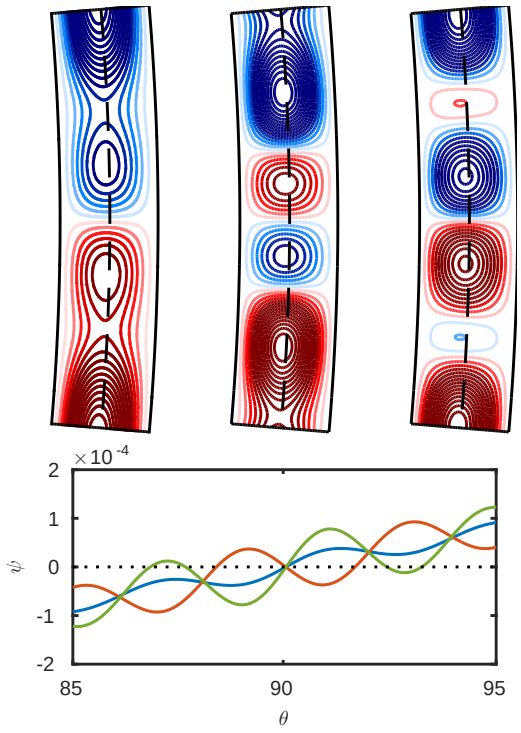

Figure 5.2: In the top row we show contours of the meridional circulation ψ for $\mathrm{Re} = 5395$ (zero-vortex), $\mathrm{Re} = 5400$ (one-vortex), and $\mathrm{Re} = 5440$ (two-vortex). In the bottom row we plot ψ – for some r roughly half way between the shells, given by a dashed line on the above plots – in terms of θ. Here the blue, red and green lines correspond to the zero- one- and two-vortex states, respectively.

region separating the zero- and two-vortex states. It is not certain whether these two changes have a causal relationship – it is more likely that they are separately occurring events as ϵ is decreased. It is interesting that there is no longer an unstable region on the zero- and two-vortex branch; this means that there is no longer a change in stability or symmetry – and hence there is no bifurcation – between the two. This implies that, technically, the two-vortex state now occurs as part of the basic state solution. This is similar in nature to the imperfect bifurcation to normal modes in cylindrical Taylor-Couette flow with end-caps (Cliffe *et al.*, 2012). We may narrow down the region where these two states merge to within $0.22 < \epsilon < 0.23$ via searching for the unstable branch region in each case. However, it should be noted that finding a more precise parameter value for the disappearance of the one-vortex solution is not easy, due to the ϵ dependence on Re as well as the time taken to

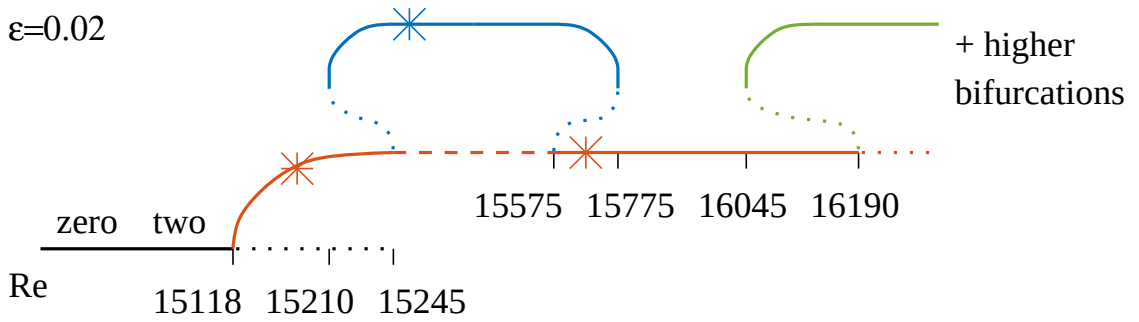

Figure 5.3: Schematic bifurcation diagram for $\epsilon = 0.02$. Solid lines indicate stable solutions, dashed lines indicate verified unstable solutions and dash-dotted lines indicate presumed unstable solutions. Black lines represent symmetric, steady state solutions, red lines are symmetric and periodic, blue lines are asymmetric and periodic, and green lines are asymmetric and quasi-periodic. Asterisks denote solutions shown in figure 5.4.

equilibrate solutions near turning points, exacerbated by the intensive computation already inherent to high resolution computations.

It is not until we increase to $\mathrm{Re} = 15118$ then that the first true bifurcation occurs. This results in periodic travelling pulse solutions, and is thus of the supercritical Hopf type. The solutions here are symmetric about the equator (defined $\psi(\theta, t) = -\psi(\pi - \theta, t)$), and consist of pulse trains of Taylor vortices travelling equatorward as predicted by Harris *et al.* (2000),Bassom & Soward (2004) and Blockley *et al.* (2007). Looking at the work of Blockley *et al.* (2007) in particular, we find that this solution is qualitatively very similar to their figure 3. In order to properly illustrate the travelling wave solutions, we plot the evolution of ψ over time via a Hovmöller plot (see figure 5.4). As in figure 5.2 there is no interesting dynamical variation across the radius – vortices span the entire width – so we concentrate on the point $r = (r_1 + r_2)/2$ half-way between the shells. We note that when the vortices inevitably meet at the equator they annihilate in phase-slip events. Plotting the toroidal and poloidal components of the energy spectra of typical pulse solutions, seen in figure 5.5 for $\mathrm{Re} = 15200$, we see that the energy peaks not only in the lowest (mean flow) modes, but also in the higher modes where the short-scale Taylor vortices reside. The medium lengthscale modes $10 < l < 100$ have

comparatively little influence on the dynamics. The large discrepancy between even and odd modes is here due to the symmetric nature of the flow; energy is $\mathcal{O}(10^{10})$ greater in the even (symmetric) modes than in the odd (asymmetric) modes. There is a clear resonance in the energy spectra, with resonant peaks occurring regularly in the higher modes. By analysing the evolution of the components of the energy, and in particular pinpointing the location of successive minima and maxima, we are also able to confirm that the solutions are indeed truly periodic. Finally, we see that this branch shows *no* hysteresis as Re is decreased, with the transition to the two vortex-state occurring exactly below Re = 15118.

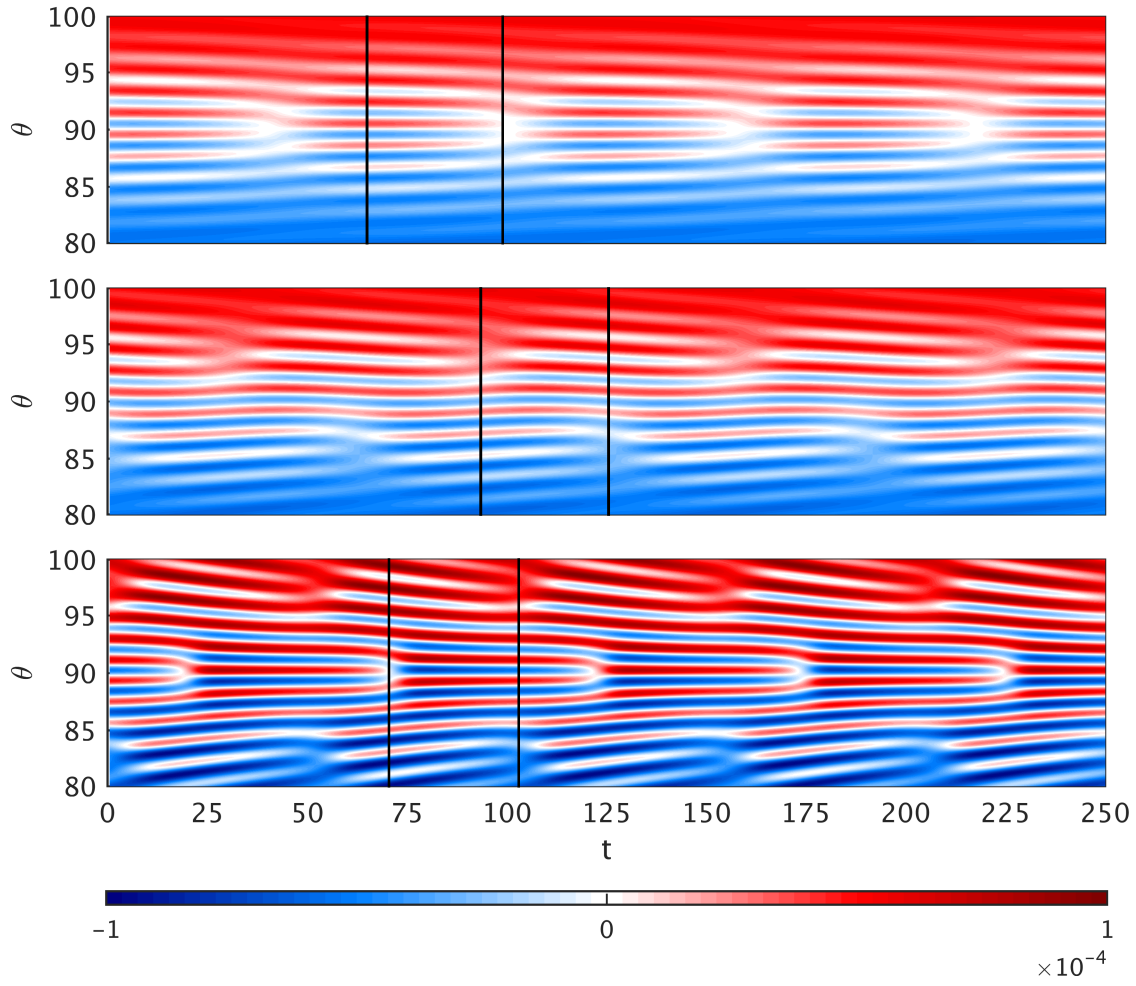

Figure 5.4: Hovmöller plots of ψ for the parameters: Top) Re = 15200, middle) Re = 15250, bottom) Re = 15650. The black lines denote specific times plotted in figure 5.6.

Increasing Re once more, we find a subcritical pitchfork bifurcation at Re = 15245.

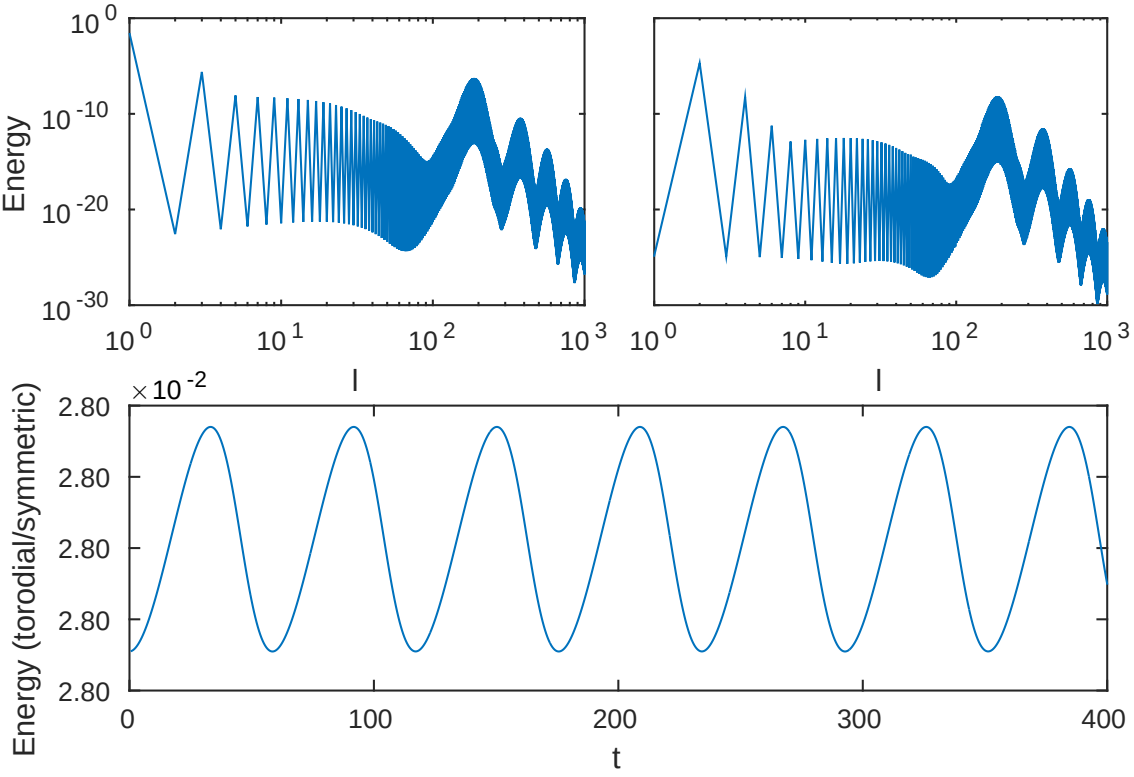

Figure 5.5: Shown are the toroidal and poloidal energy spectra, as well as plots of the energy evolution showing periodicity. Note the resonances in the spectra at multiples of $l = 188$.

Subsequent solutions are then found to be equatorially asymmetric, exhibiting a shift-and-reflect symmetry ($\psi(\theta, t) = -\psi(\pi - \theta, t + T/2)$, with period T). This is seen in the middle row of figure 5.4, which again consists of vortices moving equatorward, though now with markedly different behaviour at the equator. Indeed, we note that the two phase-slips now occur at latitudes a couple of degrees away from the equator, and alternate due to the shifted symmetry. This means that the vortices located at the equator persist ad infinitum, oscillating between the influence of each hemisphere. This solution branch exists in the range $15210 \leq \mathrm{Re} \lesssim 15775$, with some degree of hysteresis observed on the lower bound. It is likely that the bifurcations are turning points, with unstable solutions (not verified) joining to the symmetric pulse branch.

After the solution passes the turning point bifurcation at $\mathrm{Re} \approx 15775$ it becomes symmetric about the equator once again. This branch shows hysteresis as Re is

decreased; unsurprising given the similar nature of the turning point at Re = 15210. The solution is qualitatively similar to the previous symmetric one, though now has additional phase slips that occur approximately 7° above and below the equator (and three in total). In an analogous fashion to the one- and two-vortex solutions at $\epsilon = 0.04$, it can be shown that the two equatorially symmetric branches are in fact connected by solutions unstable to asymmetric perturbations. This can be verified much like before, by suppressing asymmetry in the code.

We may gain a better understanding of the solutions by examining the wave-envelope under which they propagate. As such, in figure 5.6 we plot radial slices of ψ, as in figure 5.2, at some time before, at, and after a phase slip, for each of the three hitherto discussed solution types. The first symmetric solution – taken at Re = 15200 – is seen to consist of only one wave-packet, whose amplitude oscillates. For the most part, the flow has little time dependence and only the vortex amplitude varies. The vortices then evolve quickly when the system undergoes a phase-slip at the equator. On the asymmetric branch, most of the time-dependence is also localised at the phase-slip events. Here, however, after undergoing bifurcation the wave-envelope includes an additional packet. Note that the phase-slip locations are now exactly the centres of each packet, and that the persistent vortices at the equator are those which lie in the region overlapping both packets, and so always have non-zero amplitude. Examining the symmetric branch at Re = 15650 confirms that each subsequent bifurcation serves to add a packet to the wave-envelope of ψ. Of course, this necessitates the alternation between symmetric and asymmetric solutions that we have encountered, and prescribes additional phase slips after each bifurcation, located at each packet centre.

Next, it is found that above Re = 16190 a second Hopf bifurcation occurs, adding an extra time-dependency to the solutions. This additional frequency causes the periodic solutions to become only quasi-periodic. If we consider the wave-packet diagrams of figure 5.6, this essentially causes the frequencies of each packet to decouple from each other, leading to a vast array of possible solutions. The sheer number of possible patterns that may arise pose a problem in fully mapping the bifurcations here; the long time-scales on which quasi-periodic solutions must be

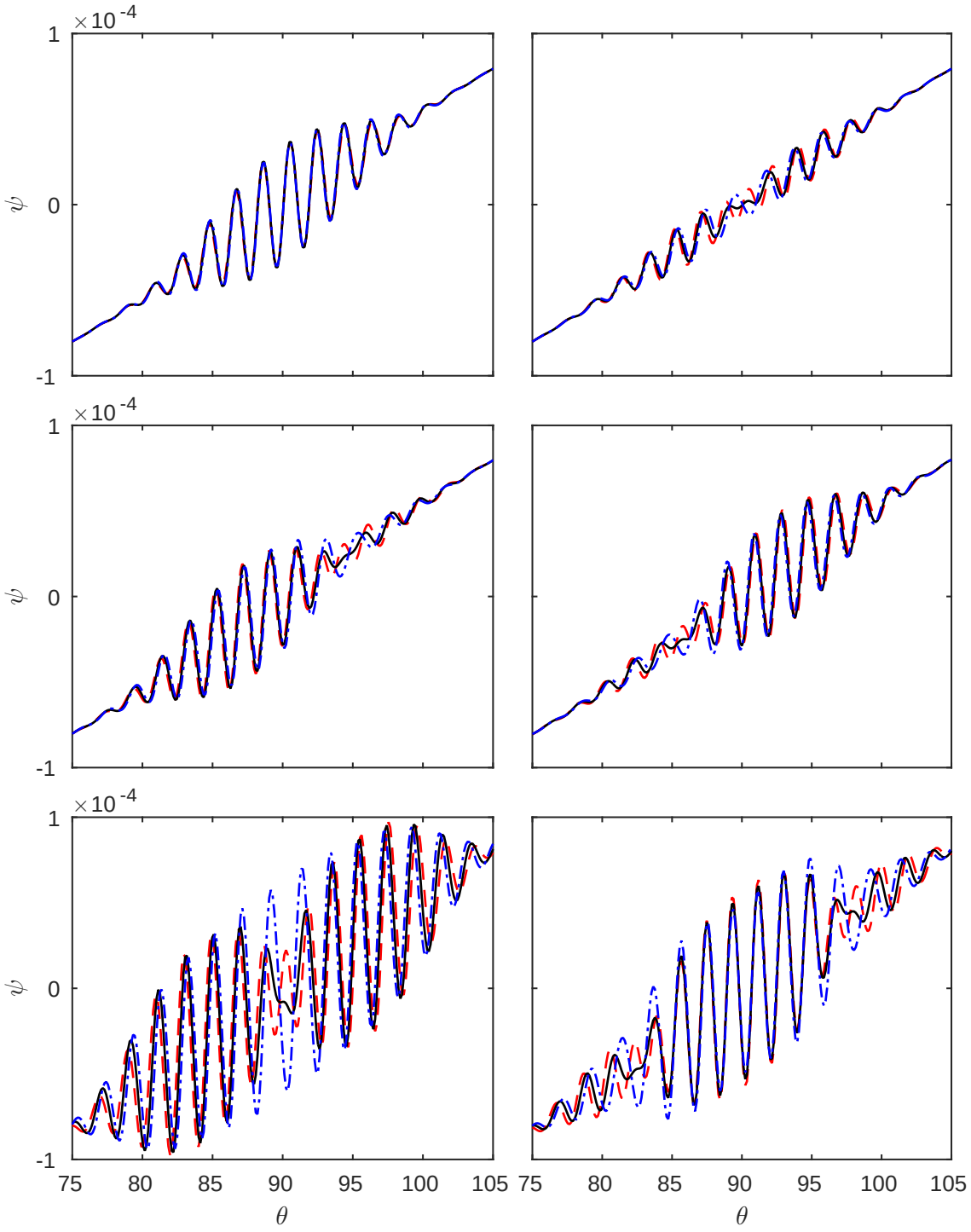

Figure 5.6: Plotted is the evolution of ψ in the vicinity of phase-slips for: Top) Re = 15200, middle) Re = 15250, bottom) Re = 15650. Solid black lines coincide exactly with the times highlighted in figure 5.4, whilst four rotation periods before and after are plotted as red dashed lines and blue dot-dashed lines, respectively.

examined already lead to difficult computations. As such, further bifurcations are not pinpointed explicitly. Here we discuss only the solutions shown in figure 5.7.

First, at Re = 16200, we see pulse trains that behave in a manner consistent with previous results away from the equator. Between the latitudes of 85° and 92° though it can be seen that vortices instead travel unidirectionally. Here the direction is from 'south' to 'north', however there will exist similar 'north' to 'south' patterns (see at Re = 16275 for example). There are now four wave-packets in total, and so phase slips occur away from the equator, where the drifting and standard vortices meet. Further quasi-periodic solutions consist of pulse trains that oscillate between hemispheres, at Re = 16250 and Re = 16400 for example. The quasi-periodic solution branch exhibits hysteresis, and we are able to decrease to Re $\approx$ 16045 before the secondary frequency is lost. It is believed that the bifurcation here is a turning point.

We plot the energy spectrum and evolution for a typical quasi-periodic solution (Re = 16200) in figure 5.8. Note that the spectrum here shows little difference in magnitude between the symmetric and asymmetric modes, due to the quasi-periodicity. The magnitude of energy in the higher modes is much greater in this case, as these higher modes are essential to the quasi-periodic behaviour, which would not have equilibrated correctly with a more aggressive truncation. We also present a snapshot of the evolution of the toroidal energy, from which it is clear that the solutions are not periodic. This has been verified precisely over a much longer time period (seven times greater than that shown). Finally, we find a range about Re = 16120 where solutions also appear to be perfectly periodic, with inherent shift-and-reflect symmetry. Here we believe that the solution has become phase-locked, where the two frequencies are close enough to lock to an equal value. As the solution is asymmetric, we note that the secondary Hopf bifurcation has also caused a change in symmetry.

It should be emphasised that all of these solutions exist within +10% of the critical Reynolds number. As such, we are confident that they are valid, and that the system would not otherwise be dominated by 3-D effects. We choose not to go into great

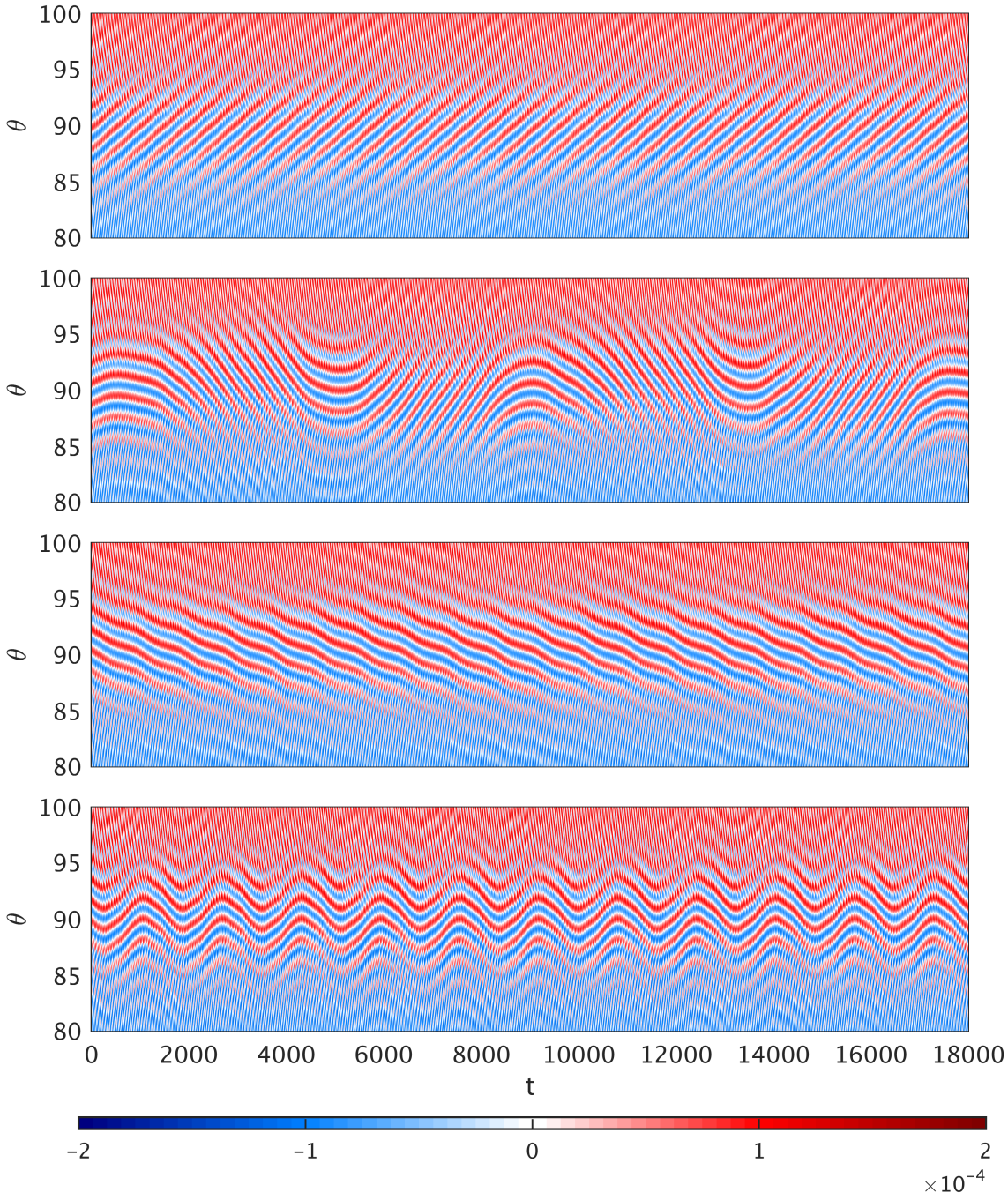

Figure 5.7: Hovmöller plots of ψ for (top to bottom) $\mathrm{Re} = 16200$, $\mathrm{Re} = 16250$, $\mathrm{Re} = 16275$, and $\mathrm{Re} = 16400$. Note that pulses either oscillate about the equator or drift unidirectionally across it.

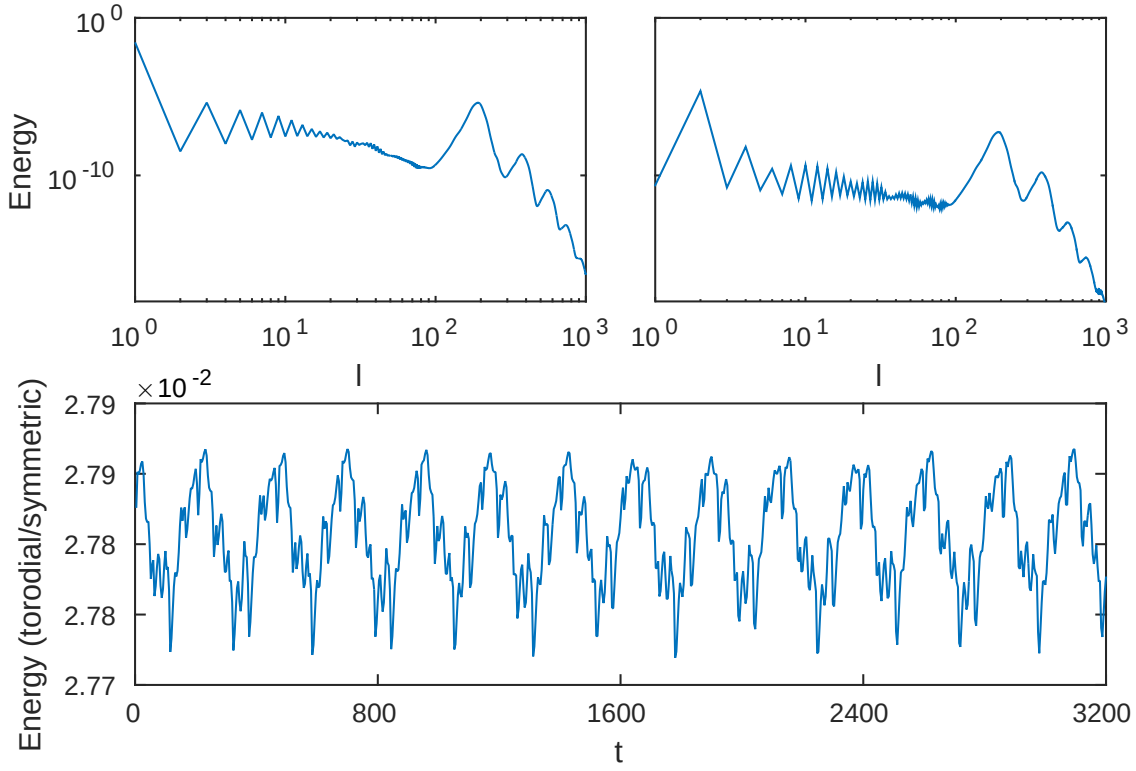

Figure 5.8: Shown are the toroidal and poloidal energy spectra for Re = 16200, as well as plots of the energy evolution showing quasi-periodicity. Note that there is no longer such a large jump between even and odd modes.

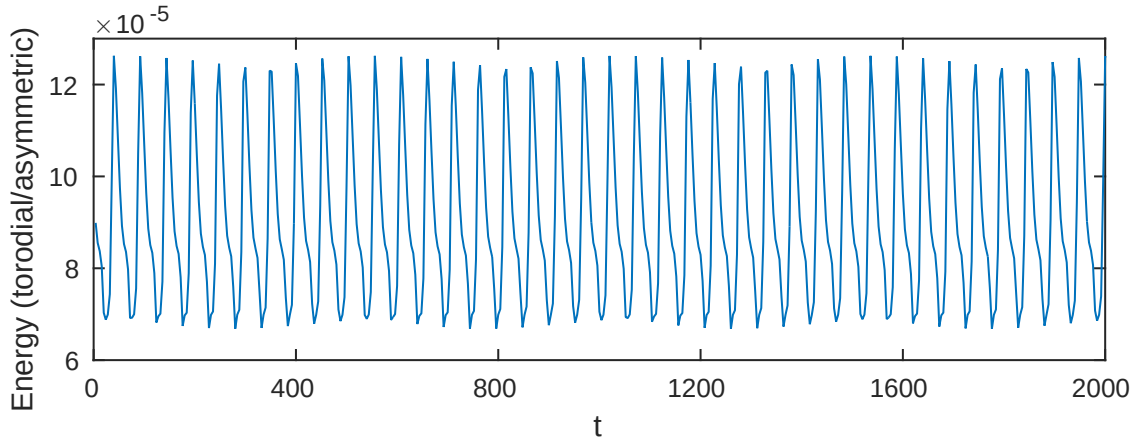

Figure 5.9: Plot of the asymmetric component of the energy over time for Re = 16120. Here the two distinct frequencies have locked together to give periodic solutions.

detail about subsequent bifurcation and solution branches, where this may not be the case.

Instead, we briefly note a mathematically interesting result for Re = 25000, a parameter where the axisymmetric solutions are unlikely to persist in a fully 3-D simulation. Whilst it has been the case that increasing Re has led to a greater number of vortices and phase-slips, and more complicated solutions in general, in the region $1.7\mathrm{Re}_c \leq \mathrm{Re} \leq 2\mathrm{Re}_c$ there becomes fewer pulse trains, each of which travels more slowly. In fact, at Re = 25000 the solution is completely steady, though with many more vortices than are found in previous steady solutions (figure 5.10). Increasing Re further then leads to a pulse reversal, whereby pairs of vortices are spontaneously created at the equator, before travelling poleward and dissipating at the edge of the locally unstable region. Similar reversals can be seen in the 3-D solutions of Adel & Ahcene (2016), and in the context of magnetically modulated Taylor-Couette flow in Hollerbach & Khan (2016).

5.3.3 The case $\delta \neq 1$

An additional area of interest is the case $\delta \neq 1$; that is, when the outer sphere is co-rotating. In fact, the asymptotic work of Bassom and Soward focussed almost exclusively on such solutions. Pulse train solutions can be excited for a whole host of $\epsilon^{1/2} < \delta < 1$, though particular attention was given to the case of almost co-rotation i.e $\delta \sim 0$, or $\mu = \Omega_o/\Omega_i \sim 1$. Whilst we are able to look at certain cases of $\delta < 1$, it is unfortunate that we are constrained by the condition $\epsilon^{1/2} < \delta$, such that the almost co-rotating case $\delta \to 0$ as studied by Bassom and Soward would require exceptionally small gap widths. As a consequence, we were only able to get to *at most* $\mu = 0.7$ whilst still keeping computation viable. It is interesting, however, to probe whether there exist any significant changes from our bifurcation sequence in this case.

Looking first at the case $\mu = 0.5$, we again increase Re until instability sets in. However, we come across the familiar bifurcation sequence of two vortices leading to symmetric and asymmetric pulse train solutions. The pulse trains, whilst covering a

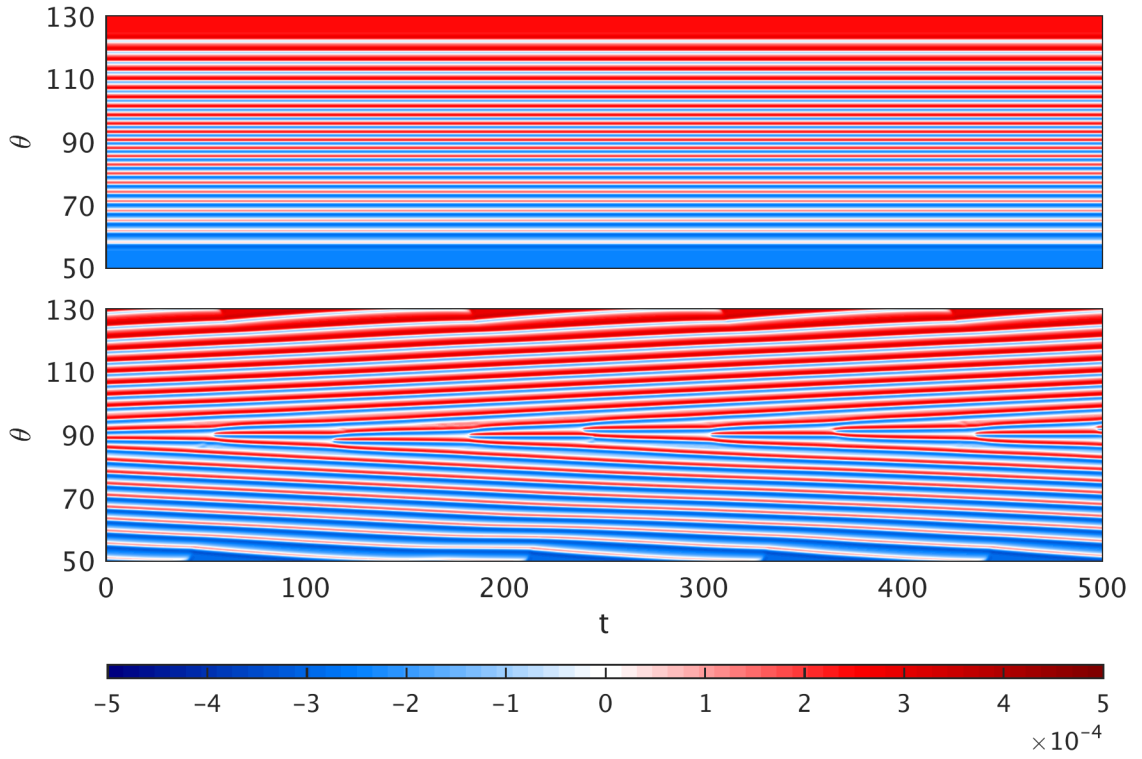

Figure 5.10: Hovmöller plots for Re = 25000 and Re = 30000. We see that increasing the Reynolds number much beyond supercritical can lead to stationary solutions, followed by pulse reversal.

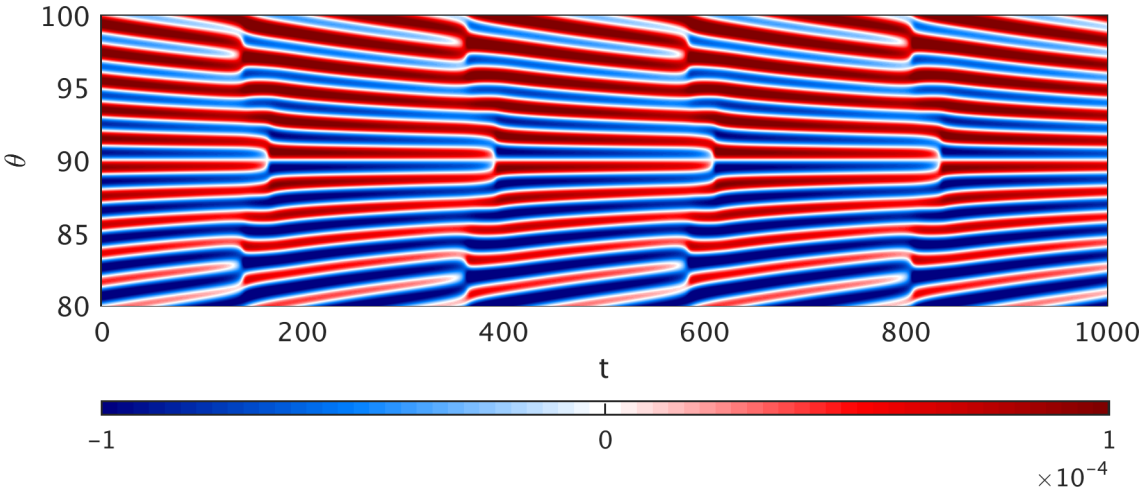

Figure 5.11: A Hovmöller plot of ψ for the case $\mu = 0.5$, Re=20000. Note the familiar pulse train dynamics.

greater latitudinal extent than the stationary $\mu = 0$, possess the same fundamental dynamics; see for example the symmetric solution in figure 5.11 and compare with the bottom row of figure 5.4. Hence, the bifurcation scheme for $\mu = 0.5$ is no different to the well explored very-narrow gap case.

This is the case even at $\mu = 0.7$, shown in figure 5.12. We first see instability in the form of a stationary vortex solution, before symmetric pulses develop. Here we note that these symmetric pulses propagate significantly more slowly than previously due to the smaller difference in rotation speed between the spherical shells. Even though the pulse trains occur over relatively large time periods, we note that the overall rotation speed is significantly higher than in the $\mu = 0$ case. Subsequent bifurcations follow the previous sequence – we find asymmetric 'shift and reflect' symmetries, followed by solutions that are once more symmetric. As such, we conclude that the bifurcation sequence is sufficiently similar to warrant no further in depth exploration, though posit by the changing properties of the solutions that the start of the co-rotating regime is close to this choice of μ.

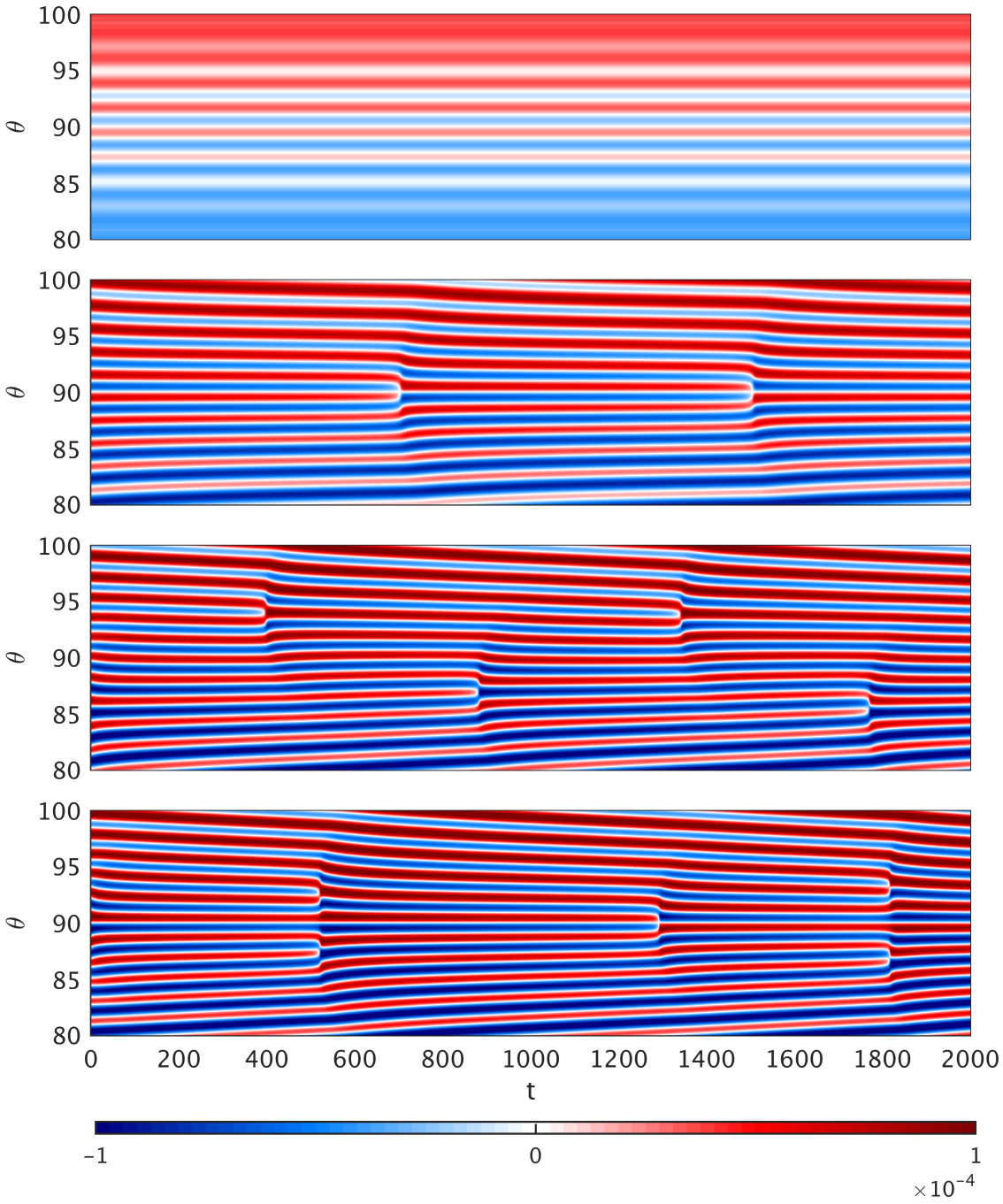

Figure 5.12: Hovmöller plots showing the familiar pulse train solutions at $\mu = 0.7$. Plotted are (top to bottom) $\mathrm{Re} = 22000,\ 24000,\ 25000,\ 26000,\ 27000$ and 28000.

5.4 Magneto-hydrodynamics

Given that we have already described an efficient spherical Couette code, it is only natural to extend the investigation of the narrow gap regime to cover magnetohydrodynamics. We consider only axisymmetric magnetic fields, and let our electrically conducting fluid be some liquid metal, such that the low-Rm approximation of equations 4.9 and 4.10 can be utilised. As such, the magnetic field is split into induced and imposed fields, $\mathbf{B}$ and $\mathbf{B}_0$, and express the induced field in terms of a toroidal-poloidal decomposition $\mathbf{B} = b\,\mathbf{e}_\phi + \nabla \times (a\,\mathbf{e}_\phi)$. Recall that the induction equation is given by

$$-D^2 b = [\mathbf{U} \times \mathbf{B}_0] \cdot \mathbf{e}_\phi \qquad -D^2 a = [\nabla \times [\mathbf{U} \times \mathbf{B}_0]] \cdot \mathbf{e}_\phi. \tag{5.13}$$

The field variables are expressed in terms of Chebyshev and Legendre polynomials

$$b = \sum_{l,k} b_{lk} Y_l^1(\cos\theta) T_k(x), \qquad a = \sum_{l,k} a_{lk} Y_l^1(\cos\theta) T_k(x), \tag{5.14}$$

and are evolved in time and space analogously to v and ψ.

Much of the mathematical detail is either: a) the same as for purely hydrodynamic flow, or b) implemented in the same way as the pseudo-spectral method utilised in the previous chapter. So, we choose to discuss only three aspects of the new MHD formulation in detail: the choice of external magnetic field, appropriate boundary conditions, and additional nonlinear terms.

5.4.1 Background

MHD spherical Couette flow is a relatively recent avenue of research, first examined by Hollerbach (1994) as an extension of classical spherical Couette flow. It is perhaps surprising that this was the case, given that the spherical Couette system is similar to the Earth's core geometry used in dynamo theory. The geometry is entirely the same as defined previously, though now there is some externally imposed magnetic field. The addition of a magnetic field to our narrow gap spherical Couette flow has the potential to yield solutions that possess a wide array of interesting dynamics.

Due to the 'frozen in flux' theorem, the fluid advects magnetic field lines. As the gap between our spherical shells is particularly narrow, there is then a large shearing at each boundary, for which field line stretching occurs, and is resisted via the magnetic tension component of the Lorenz force. The magnetohydrodynamic solutions of narrow-gap spherical Couette flow have so far not been studied, either numerically or asymptotically. Certainly, hydrodynamic asymptotic solutions are sufficiently abstract that adding MHD effects would prove exceedingly difficult.

The initial work of Hollerbach (1994) (and many of subsequent investigations) focuses on the wide gap aspect ratio – with $\epsilon = 1/3$ – and charts the evolution of the flow as dipolar magnetic field strength is increased. The boundary layer structures that exist in the hydrodynamic regime, Ekman layers and Stewartson layers (the tangent cylinder resulting from the application of Taylor-Proudman theory to the spherical shells) evolve into Ekman-Hartmann layers or are suppressed, respectively. The Ekman-Hartmann layer is made stronger at the inner boundary and weaker at the outer boundary as the field strength is increased, in contrast to the standard hydrodynamic layer that is relatively uniform across both. Asymptotic analysis for the Ekman Hartmann layers and Stewartson layer were later published by Kleeorin *et al.* (1997).

Much of the prior work has concentrated on the effects of the electromagnetic boundary conditions, as different combinations of insulating and perfectly conducting boundaries can lead to vastly different flow regimes. The works of Starchenko (1997) and Dormy *et al.* (1998), for example, impose mixed boundary conditions, with perfectly conducting inner spheres and insulating outer spheres. They predominantly consider dipolar magnetic fields, though Starchenko also briefly covers quadrupolar fields too. Surprisingly, it was found that in this case the conducting boundary causes the flow the exhibit super-rotation, where the azimuthal velocity is greatest in the fluid, and not at the boundary. This is presumably due to the feedback effect that exists between the current and boundary, whereby current that builds up in the conducting shell re-enters the fluid. Indeed, it is shown that given two perfectly conducting boundaries, the effect is amplified (and does not saturate) (Hollerbach, 2000a, 2001). Furthermore, it is found that such set-ups can even cause pockets of

counter-rotation in the flow.

In these works, the effects of the boundary conditions were examined systematically for each possible combination under both dipolar and quadrupolar imposed magnetic fields. This concluded with a discussion of the consequences on possible unstable states, and in particular that of the one-vortex solution in wide gaps. It was seen that the dipolar fields suppress the instability, with a greater suppression of the extent of the vortices for conducting boundaries. Quadrupolar magnetic fields however cause a lesser suppression with insulating boundaries, and then destabilise the flow for conducting boundaries, acting to amplify the latitudinal extent of the vortices. This may inform as to possible outcomes for our pulse train solutions, with the equatorially horizontal quadrupolar field being most accommodating of the potentially fragile state of instability.

Various nonaxisymmetric instabilities were examined by Hollerbach & Skinner (2001), and the asymptotic solutions for the super- and counter-rotating solutions was given by Bühler (2009); Soward & Dormy (2010).

There has also been much work completed on the instabilities in the (wide gap) MHD spherical Couette set-up, with varying results depending on the imposed field. For axial fields, for example, axisymmetric solutions are essentially the same as for hydrodynamic flows. The instabilities found are only nonaxisymmetric, and so are of little interest in the present work. (Hollerbach, 2009; Hollerbach & Skinner, 2001; Sisan *et al.*, 2004). More interestingly, under imposed dipolar magnetic fields, it happens that the super-rotation is suppressed considerably by inertia (Hollerbach *et al.*, 2007). However, consequently it is then more localised the the equator, at the inner boundary; precisely the region of flow that drives the pulse train solutions. This is confirmed by the experiments of Nataf *et al.* (2008). So, we suspect that under conducting boundary conditions that this equatorially focused super-rotation could lead to interesting pulse train dynamics.

Finally, axisymmetric solutions of wide-gap flow have been exampled under a linear combination fo axial and dipolar magnetic fields (Wei & Hollerbach, 2010). The instabilities here were found to be stabilised / destabilised by Ha / Re respectively,

however the most interesting aspect of this work is the imposed field itself. The combination of axial and dipolar fields allows for the possibility of an imposed field that does not thread either the inner or outer boundary. Implementing this to simplify the imposed field about the equator may be conducive to generating MHD pulse train solutions.

5.4.2 Imposed magnetic field

The largest influence on the dynamics of our narrow gap spherical Couette flow will be, due to the 'frozen flux theorem', the choice of imposed magnetic field. Indeed, as our gap is so narrow the field lines at the equatorial plane will be subjected to large shears, opposed by the magnetic tension. As such, it is imperative that the field lines near the equator be geometrically simple and that boundary threading is kept to a minimum, otherwise the travelling vortex solution could be lost.

The most commonly imposed magnetic fields in past literature are axial and dipolar (multipolar fields are derived in appendix A.4),

$$\mathbf{B}_a = \cos\theta\,\mathbf{e}_r - \sin\theta\,\mathbf{e}_\theta \qquad \mathbf{B}_d = 2r^{-3}\cos\theta\,\mathbf{e}_r + r^{-3}\sin\theta\,\mathbf{e}_\theta, \tag{5.15}$$

though it should be noted that both of these fields thread both boundaries. As in Wei & Hollerbach (2010), we choose instead to take a combination of axial and dipolar fields, such that there is no threading at the outer boundary (field lines run parallel to it instead). Hence, one option for the imposed magnetic field is

$$\mathbf{B}_0 = 2\mathbf{B}_a - r_0^3\mathbf{B}_d, \tag{5.16}$$

chosen such that $\mathbf{B}_r = 0$ at $r = r_o$.

Furthermore, we also consider the quadrupolar magnetic field,

$$\mathbf{B}_q = r_0^4 r^{-4}(3\cos^2\theta - 1)\,\mathbf{e}_r + 2r_0^4 r^{-4}\cos\theta\sin\theta\,\mathbf{e}_\theta, \tag{5.17}$$

which is constructed such that field lines are uncomplicated at the equator, as well as normalised at the outer boundary.

5.4.3 Boundary conditions

As discussed, the choice of boundary condition may radically alter MHD spherical Couette flow, strengthening Hartmann layers or causing pockets of super–rotation. As such, we examine both insulating and perfectly conducting boundaries.

Insulating boundaries

If the regions external to the shells are insulating, then we may express $\mathbf{B}$ as a potential field,

$$\mathbf{J} = \nabla \times \mathbf{B} = 0 \qquad \Longrightarrow \qquad \mathbf{B} = \nabla\Phi. \tag{5.18}$$

The form of the potential field Φ is then well known; it is a separable solution, consisting of spherical harmonics in θ and a Frobenious type solution, $Cr^l + Dr^{-(l+1)}$, in r. As we wish to have bounded solutions as $r \to \infty$, then it is clear that we must have solutions of the form

$$\Phi_l = r^{-(l+1)} Y_l^0(\cos\theta). \tag{5.19}$$

The components of $\mathbf{b}$ then may be expressed

$$B_r = -(l+1) r^{-(l+2)} Y_l^0(\cos\theta), \tag{5.20}$$

$$B_\theta = r^{-(l+2)} \frac{\mathrm{d}\, Y_l^0(\cos\theta)}{\mathrm{d}\,\theta}, \tag{5.21}$$

$$B_\phi = 0, \tag{5.22}$$

which requires for consistency that

$$B_\theta = -\frac{1}{(l+1)} \frac{\partial B_r}{\partial \theta}. \tag{5.23}$$

The boundary condition on b is trivial. Then, inserting the toroidal–poloidal decomposition of $\mathbf{B}$ we find

$$-\frac{a_l}{r} + a_l' = -\frac{1}{l+1} \frac{\mathrm{d}}{\mathrm{d}\,\theta} \left(\frac{1}{r} \left(\cot\theta Y_l^1 + \frac{\mathrm{d}\, Y_l^1}{\mathrm{d}\,\theta} \right) a \right) \tag{5.24}$$

$$= -\frac{1}{l+1} \frac{1}{r} \left(\frac{\mathrm{d}^2\, Y_l^1}{\mathrm{d}\,\theta^2} + \cot\theta \frac{\mathrm{d}\, Y_l^1}{\mathrm{d}\,\theta} - \frac{1}{\sin^2\theta} Y_l^1 \right) a_l \tag{5.25}$$

$$= \frac{l a_l}{r} \tag{5.26}$$

$$\Longrightarrow \; a_l' + \frac{a_l (l+1)}{r} = 0. \tag{5.27}$$

So, our insulating boundary conditions are

$$b_l = 0 \qquad a_l' + \frac{a_l(l+1)}{r} = 0 \tag{5.28}$$

Perfectly conducting boundaries

For perfectly conducting boundaries, it is known that we must have that

$$\mathbf{n} \cdot \mathbf{B} = 0, \tag{5.29}$$

$$\mathbf{n} \times (\nabla \times \mathbf{B}) = 0, \tag{5.30}$$

at the boundaries. As the normal in our spherical geometry is the radial direction, we then have that

$$\mathbf{e_r} \cdot \mathbf{B} = \frac{1}{r \sin\theta} \frac{\mathrm{d}}{\mathrm{d}\,\theta} (a \sin\theta) = \frac{a_l}{r} \left(\cot\theta Y_l^1 + \frac{\mathrm{d}\, Y_l^1}{\mathrm{d}\,\theta} \right) = 0 \tag{5.31}$$

$$\implies a_l = 0. \tag{5.32}$$

Also,

$$\mathbf{n} \times (\nabla \times \mathbf{B}) = -[\nabla \times \mathbf{B}]_\phi \, \mathbf{e}_\theta + [\nabla \times \mathbf{B}]_\theta \, \mathbf{e}_\phi = 0. \tag{5.33}$$

Taking each vector component separately then, we have

$$-[\nabla \times \mathbf{B}]_\phi = \left(\frac{2}{r} a_l' + a_l'' - \frac{l(l+1)}{r^2} a_l \right) Y_l^1 = 0, \tag{5.34}$$

$$\implies a_l'' + \frac{2}{r} a_l' - \frac{l(l+1)}{r^2} a_l = 0, \tag{5.35}$$

which is satisfied by default for all a_l, and

$$[\nabla \times \mathbf{B}]_\theta = 0, \qquad \implies \qquad b' + \frac{b}{r} = 0. \tag{5.36}$$

Thus, our boundary conditions are

$$b_l' + \frac{b_l}{r} = 0 \qquad a_l = 0. \tag{5.37}$$

5.4.4 Results

As the case $\epsilon = 0.02$ yielded the most interesting dynamics in the purely hydrodynamic set-up, we choose here to focus only on this particular aspect ratio. The

Hartmann number has expanded our parameter space significantly, so our procedure is to take initial conditions from our well-understood hydrodynamic simulation and then ramp up Ha . We can then ascertain what effect the magnetic field has on the stability of the fluid, the pulse train solutions, and on the bifurcation sequence.

Axial and dipolar field

Insulating boundaries: We begin with the periodic symmetric branch of solution, taking Re = 15200 in order to enable comparison with results of figure 5.4. The Hartmann number is increased from zero, with particular focus given to Ha = 10, 25 and Ha = 30. By examining the Hovmöller plots of ψ for each of the Ha values, it is clear that in this case the increasing magnetic field strength serves only to suppress the instability. Increasing Ha effectively acts analogously to decreasing Re in the hydrodynamic case. Instead of allowing for new and interesting dynamics in the pulse trains, we see that the branches of solution and bifurcations therein are exactly the same, albeit shifted in Re. This is seen in the transition between Ha = 10 and Ha = 30 in figure 5.13, where the symmetric pulses are seen to slow before transitioning to the one-vortex basic state. This is interesting, as the one-vortex branch was not found for purely hydrodynamic flows at this aspect ratio.

Setting Re = 15250, we find that increasing Ha leads to the solutions becoming symmetric once more, presumably via the same turning point bifurcation seen in figure 5.3. Indeed, upon first reflection, it appears as though the bifurcation sequence is again just shifted upwards in Re. However, we note that the solution does not transition from the symmetric pulse trains to a two-vortex state – here we find that asymmetry is introduced, with asymmetric periodic solutions followed by an asymmetric one-vortex state. This asymmetric branch is unique to the MHD set-up.

Finally, we note the effect on the flow bifurcation sequence of much larger values of Ha, fixing Ha = 500 and varying Re in figure 5.15. We find again that the increased magnetic field strength suppresses the flow, with the critical Reynolds number now occurring at Re $\approx$ 36000. In disagreement with the non-magnetic flow at $\epsilon = 0.02$,

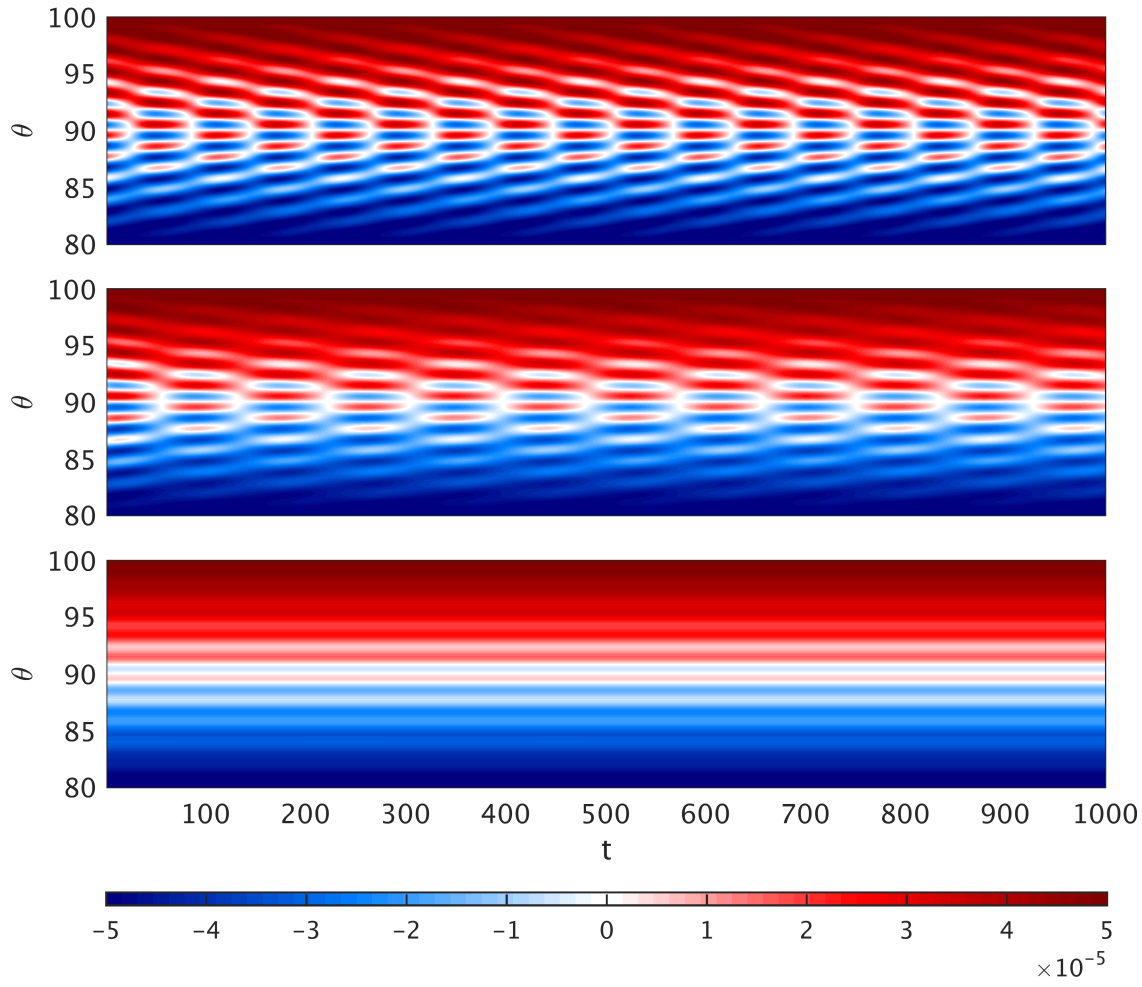

Figure 5.13: Hovmöller plots showing how increasing magnetic field strength under insulating boundary conditions affects the dynamics of the symmetric periodic solution branch at $\mathrm{Re} = 15200$. From top to bottom we have: $\mathrm{Ha} = 10,\ 25,\ 30$.

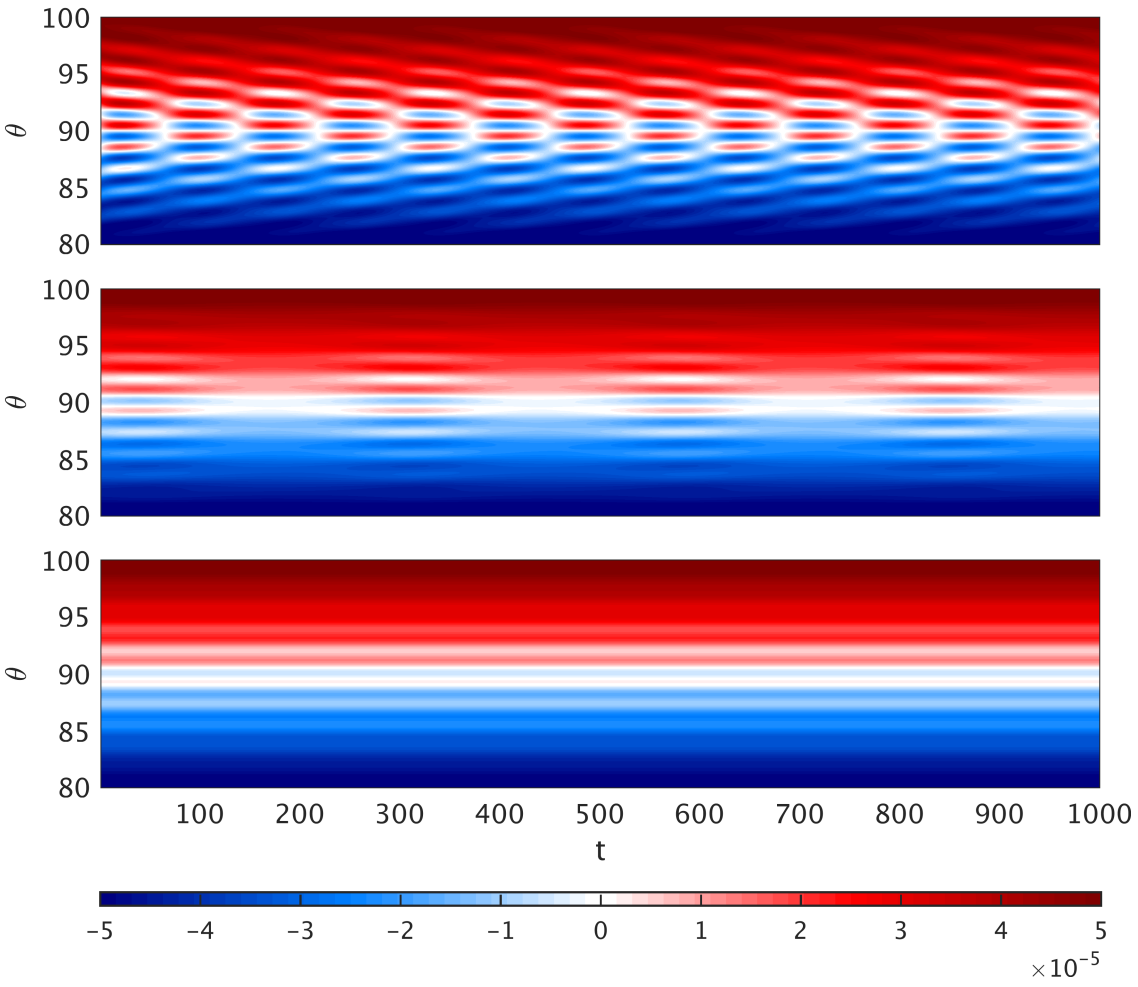

Figure 5.14: Hovmöller plots showing the effect of increasing magnetic field strength on the Re = 15250 asymmetric pulse trains. From top to bottom we have: Ha = 10, 25 and 30.

it is clearly seen that the first bifurcation leads to a one-vortex branch, which we had previously reported as having disappeared. Increasing Re leads to the solution undergoing a bifurcation to a two-vortex, before then transitioning to a series of pulse trains, via a Hopf bifurcation. What is interesting here, however, is the latitudinal length scale of the vortex pulses – we see that these are uncharacteristically large when compared to the non-magnetic flow. Peculiarly, the characteristics of the flow match more closely to that of larger aspect ratios. Indeed, the first bifurcations conform more closely to those of the narrow-gap $\epsilon = 0.04$ instead of the very narrow-gap $\epsilon = 0.02$.

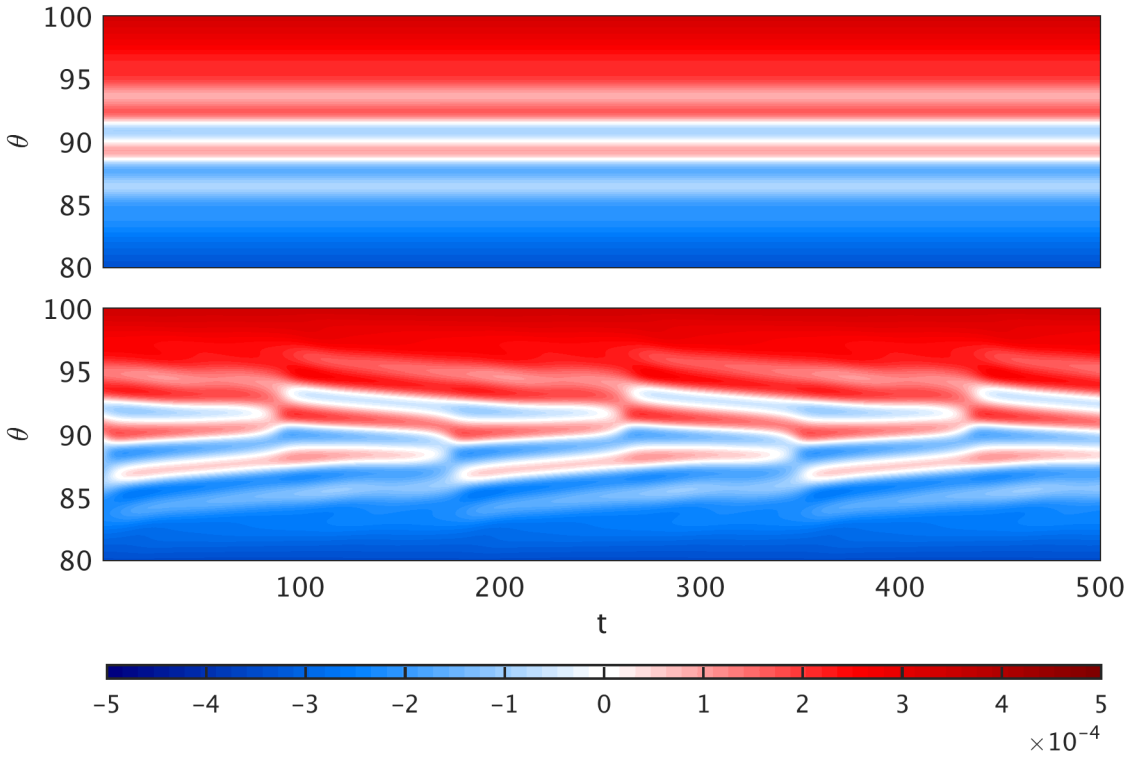

Figure 5.15: Hovmöller plots for perfectly conducting boundaries with Ha = 500 and : top) Re = 36500, bottom) Re = 37000. Here large values of Ha impose characteristics of wider gap flow, including the one-vortex solution and larger pulse length-scales.

Perfectly conducting boundaries: For the case of perfectly conducting boundaries we see the opposite effect; that is, increasing the strength of the magnetic field acts to increase the strength of rotation. This is a by-product of the super-rotation

reported on by Hollerbach for perfectly conducting boundary conditions. Here we suspect that the electric currents that are conducted by the boundaries feed back into the field, increasing the velocity in pockets about the equator – precisely where the pulse trains occur. We can see this when fixing $\mathrm{Re} = 15200$ and steadily increasing Ha, as in figure 5.16. Thus, our axial-dipolar magnetic field is found not to radically change the nature of the pulse train dynamics seen in this system. Indeed, the most important factor here is the nature of the boundary conditions.

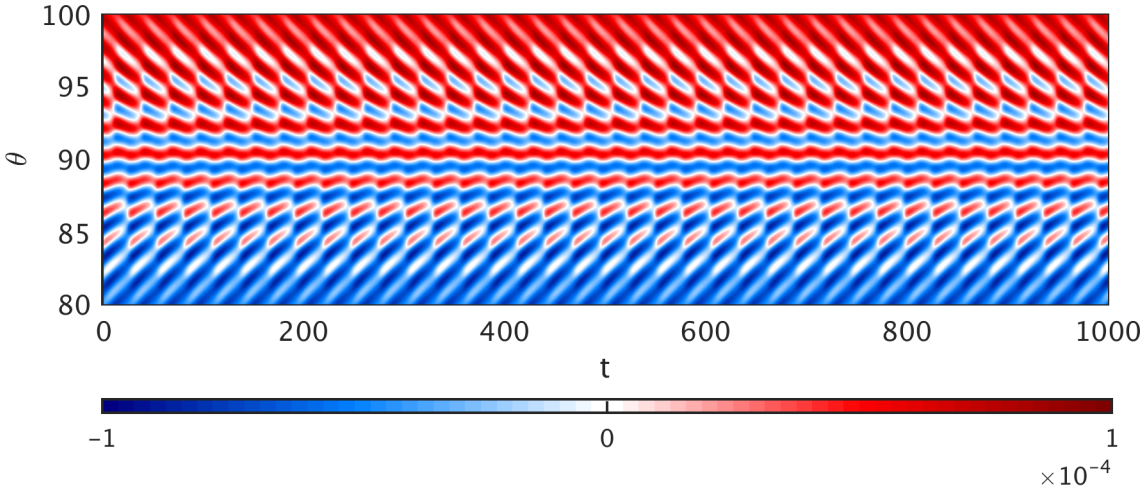

Figure 5.16: Hovmöller plot for $\mathrm{Re} = 15200$ and $\mathrm{Ha} = 30$, with perfectly conducting boundaries. Note how the influence of the magnetic field has forced the previously symmetric solution to undergo bifurcation to an asymmetric state.

Quadrupolar field

Insulating Boundaries: In a similar fashion to the axial/dipolar field, we note that insulating boundaries cause increasing stability with regards to the pulse train solutions. Thus, the overall picture stays the same, yet stronger quadrupolar fields essentially shift the critical Reynolds number upwards. This is achieved at a quicker rate than with the axial/dipolar field - if we compare the Hovmöller plots for Re=15200 at Ha=25 in figure 5.17 to the non-magnetic case, for example, we note that at this point the pulse train solutions still persist, albeit weakly, in the axial-dipole field, yet in the quadrupolar field we have steady vortex solutions. Un-

fortunately, this is the only real difference between the two field geometries - the overriding effect of insulating boundaries always has the same effect as decreasing the rotation speed.

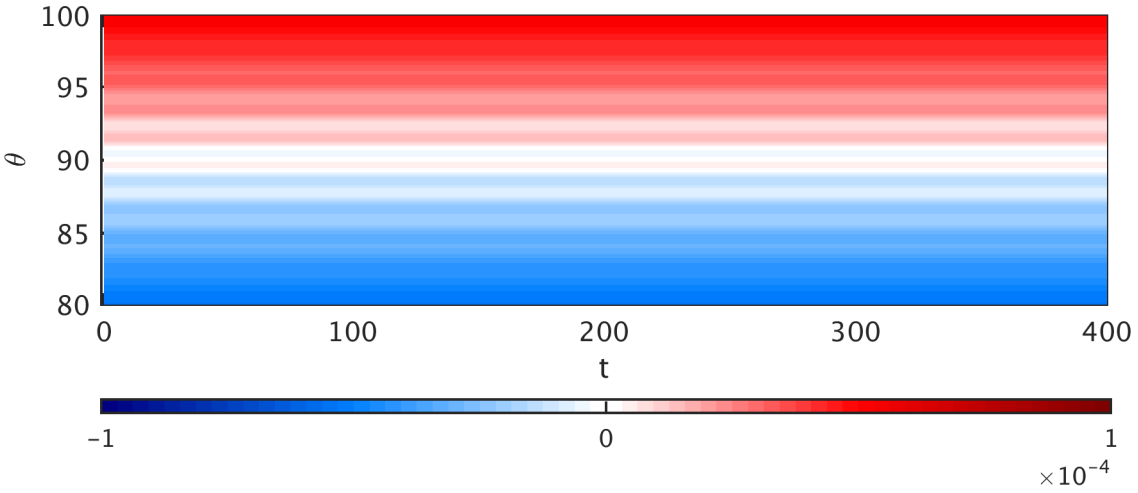

Figure 5.17: Hovmöller plot of ψ for Re = 15200 and Ha = 25, with insulating boundary conditions and an applied quadrupolar magnetic field. Note that there are only stationary solutions here.

Perfectly conducting Boundaries: Though we may expect that the role of the perfectly conducting boundaries would here be the same as in previous sections, it is found that the quadrupolar magnetic field can in fact lead to quite different dynamics. Indeed, we immediately note that weak to moderate strength fields now suppress the instability *entirely*, more so than the corresponding insulating boundary case in fact. Indeed, no matter how we increase the magnetic field strength, instability is always suppressed at the equator. However, beginning around Ha $\approx$ 30, away from the equator we find additional pulse train solutions at latitudes where field lines are concentrated. These pulse trains manifest away from the equator, before propagating poleward, disappearing as they reach the stable latitudes. Note that the stable equatorial region means the solutions no longer undergoes phase slips. These solutions are only quasi-periodic, contrary to the initial unstable states in hydrodynamic flow. After manifesting as the poleward pulses, increasing Re causes the vortices to propagate more slowly, before reaching a value of Re for which the

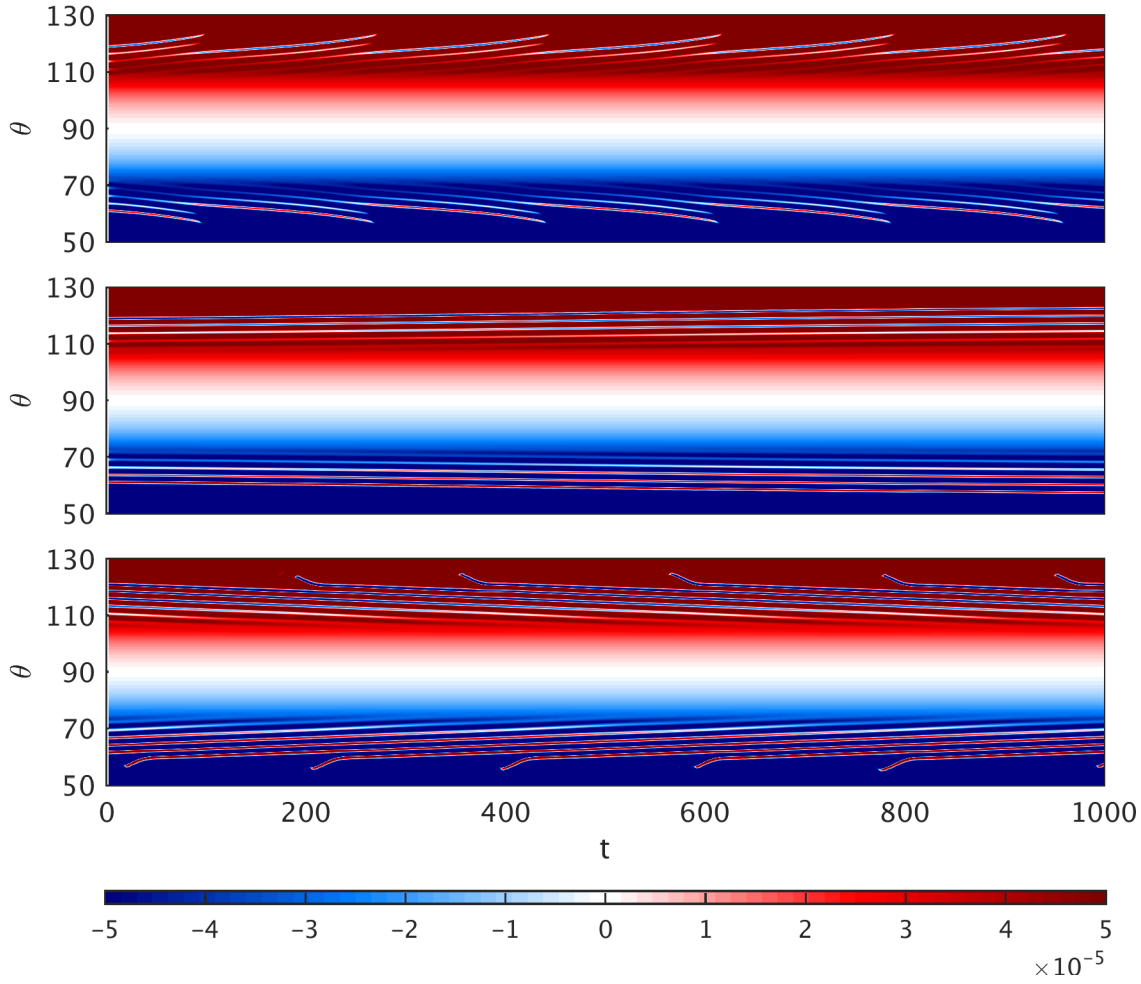

Figure 5.18: Hovmöller plots of ψ for Ha = 30, with perfectly conducting boundary conditions and an imposed quadrupolar magnetic field. Top to bottom, we have Re = 14000, 14500 and 15500. Here the first unstable state consists of quasi-periodic poleward pulses, which do not undergo symmetry changes, and thus further bifurcation.

pulse trains reverse. Importantly however, note that at no point do the solutions undergo a change in symmetry, and hence do not undergo bifurcation.

There are two possible explanations for these kinds of solutions. It may be that there are indeed pulse train solutions unique to this set-up that manifest whilst travelling poleward, completely breaking with the hydrodynamic case. However, it is perhaps more likely that these solutions are actually an analogue of the reversed pulses shown in figure 5.10, brought on by increasingly supercritical flows. Indeed, if the quadrupolar field with insulating boundaries could be more effective at stabilising the flow, it serves to reason that the conducting boundaries may be more effective at destabilising the flow. It is possible that the equatorward pulse solutions occur completely within the confines of the stabilised equatorial region, and these poleward pulses are the first of the solution types to become unstable outside of this. However, this would suggest that such solutions would be unlikely to persist as purely 2-D flows.

Whichever of these explanations may be the case, the fact that these pulse train solutions offer no bifurcation is discouraging, and therefore we give them no further attention.

Chapter 6

Conclusion

6.1 Discussion

In this thesis we have examined the instabilities that can arise in both Taylor-Couette flow and spherical Couette flow, for both hydrodynamic and magnetohydrodynamic flows. As we've seen, these two geometries hold great importance in the field of fluid dynamics, and in examining such instabilities in this work, it is hoped that the understanding of their dynamics is increased.

In chapter 2, we outlined the numerical methods that were utilised throughout this thesis. Beginning with the Navier-Stokes and induction equations, we first described an approximation relevant to inductionless fluids, before giving on overview of how the equations are advanced through time, via a Crank-Nicolson time-stepping scheme. Furthermore, we introduced the area of spectral methods, with particular focus given to collocation. Expansion schemes were introduced that made use of Chebyshev and associated Legendre polynomials as well as Fourier series, and fast transform methods that enable efficient nonlinear term calculation were detailed. In addition to the, so far standard, spectral methods recapped so far, we described a cosine transform scheme for use with spherical co-ordinates. If it could have been sufficiently altered to ensure numerical stability, this would have enabled even more efficient computations. However, the method is interesting enough to have warranted a brief discussion in this work even if it currently unstable. As it is, the methods

described in this chapter provide a general framework for studying the evolution of Couette flows.

In chapter 3, we fully explored the parameter space for nonaxisymmetric instabilities in MHD Taylor-Couette flow. We started from the Navier-Stokes and induction equations, linearised, and yielded an eigenvalue problem for the growth rate that incorporates parameters governing: the magnitude of rotation, relative strength of the azimuthal and axial magnetic fields, the overall strength of the magnetic fields, and the steepness of the azimuthal magnetic field, which we allow to be generated by oppositely signed currents in the fluid and core.

Via solving this eigenvalue problem, we explored the effect of the steepness of the azimuthal magnetic field on the MRI and Tayler instabilities, showing that instabilities are more easily excited when the field is driven by current running through the fluid. Furthermore, we identified the existence of two separate MRI modes governed by the field steepness. In addition, we added to previous research on Chandrasekhar's equipartition solution, for which we see the comparatively weak instability that separates MRI and TI. We also confirmed a number of results from Kirillov *et al.*'s WKB analysis in the linear regime, such as the linear validity of the Liu limit curve, as well as the resonant existence of modes with $m > 1$ for strongly axial magnetic fields. We have also seen evidence of the banded nature of such modes.

In chapter 4 we examined the effectiveness of the GQL approximation in reproducing the statistics of axisymmetric, inductionless HMRI for a number of different parameter sets, varying from weak to strong turbulence. The effectiveness of such an approximation is of key importance when considering the essential nonlinear interaction present in statistical theories, such that low order statistics are accurately produced. That the GQL approximation also establishes which nonlinear modal interactions are integral to a systems dynamics can be enlightening also, though does not have the overarching impact of the statistical association.

In this work, we provided evidence to show that DSS may prove to be an interesting new avenue for probing the HMRI, whose key behaviours, such as the travelling wave nature, are preserved for all choices of spectral filter Λ. Indeed, for weakly nonlinear

flows we have shown that even the QL approximation proves to be accurate, though such special regions are but a small part of the total parameter space. For turbulent flows this is not the case; all key dynamics have been seen to be produced when $\Lambda \geq 2$. At this point, nonlinear dislocations are present in the flow, energy spectra, first and second cumulants are shown to be qualitatively accurate when compared to the full NL DNS. Furthermore, increasing to $\Lambda > 2$, whilst yielding improvements in accuracy over $\Lambda = 2$, does so with rapidly diminishing effect.

We have shown how the parameter regime affects the feasibility of the GQL, with the degree of supercriticality a key factor in determining accuracy. However, the variations in accuracy here are dwarfed by the variations in accuracy relative to Λ, such that $\Lambda = 2$ is always a significant improvement in regaining the dynamics of the HMRI. Thus, we can conclude that for the inductionless HMRI, only the lowest three nonlinear modal interactions are necessary to produce the key flow properties.

More generally, though, the main motivation for testing GQL is in the application of statistical theories to all kinds of rotation driven flows. The work in this chapter has shown that it may prove fruitful to utilise theories other than the standard quasilinear CE2 expansion to conduct any future direct statistical simulation. Previous research has shown that DSS via CE2 (or $\Lambda = 0$), may prove inaccurate for problems far from marginal stability. This work has shown that when the HMRI is far from marginal stability, even the addition of an extra two large-scale modes in our formalism provides significantly more accurate solutions. One may conclude, then, that a similar $\Lambda \geq 2$ cumulant expansion based statistical theory would allow for more accurate DSS in other flows, whilst maintaining the computational advantage inherent to DSS methods. Our results reinforce those of Marston *et al.* (2016), who performed similar GQL calculations on the hydrodynamic problem of jet formation on the β-plane. Though the dynamics are fundamentally different, they saw that a similarly small increase in the number of large scale modes yielded significant improvements in statistical accuracy. We believe that such increases in accuracy are due to this enabling the scattering of energy off of the large scales (which is alternatively referred to as non-local transfer). Indeed, in the standard $\Lambda = 0$ QL approximation, energy is unable to transfer between the smaller scales in

the nonlinear mode interactions; additional non-zero (non-mean flow) large scales modes provide an avenue for energy scattering. It appears that this scattering is crucial in accurately producing statistics, in which energy build up in the lower end of the spectrum can enforce overcorrelations due to travelling waves.

As an extension to this, we then investigated the effect of induction effects. Though taking the inductionless approximation is valid (and sensible) when dealing with the HMRI, it rids the governing equations of two nonlinear terms. The question is, then, how these terms react to GQL; it is conceivable that they could require a significantly higher Λ, stifling the implementation of GCE2 for finite Rm flows. Starting with the inductionless case (Rm = Pm = 0), if we increase to only Pm = 0.01, significant difficulties are introduced in approximating the flow. Indeed, now taking $\Lambda = 2$ proves to be wholly inaccurate. Even with weak induction effects, we instead found it necessary to increase the spectral filter Λ by an order of magnitude. This is problematic enough for our HMRI, but would prove catastrophic for flows with an inductionless regime requiring $\Lambda \gg 2$. Unfortunately, this trend continued throughout the parameter space; taking even higher values of Pm served to make the flow increasingly turbulent, and thus more difficult to approximate with restricted nonlinearity, requiring yet again an order of magnitude increase in spectral filter. In this case, $\Lambda = 2$ was even found to violate the Rayleigh criterion; a serious error capturing key characteristics of the flow. Unfortunately, such levels of turbulence make it increasingly difficult to adequately resolve flows at even higher Pm. Indeed, we can conclude that the lack of coherent patterns in the turbulence leads to second cumulants with only self-correlation, for which GQL necessarily requires large numbers of low modes to reproduce. As such, the prospect of GQL for high Pm flows is unlikely (at least for HMRI). Finally, we examined the SMRI under the same conditions for Pm = 0.01. It was found to have the same limitations as HMRI – a significant number of low modes needed to included for the approximation to be accurate. As such, despite the success of GQL in approximating inductionless MRI, it does not appear to present a promising avenue into finite-Rm MRI research.

Finally, in chapter 5 we extensively examined the axisymmetric pulse train solu-

tions found in spherical Couette flow, originally predicted by the work of Bassom, Soward and collaborators. Focussing primarily on the case where the outer sphere is stationary, we computed the pulse train solutions for two gap-widths, $\epsilon = 0.04$ and $\epsilon = 0.02$, and mapped out the bifurcation sequences in both cases. In taking these two aspect ratios, we found two separate regimes, narrow and very-narrow gap, which differed by the nature of the initial bifurcation from steady state flow; $\epsilon = 0.04$ was found to share the initial one- and two-vortex states of the medium gap flow, whilst $\epsilon = 0.02$ has solutions that switch directly to pulse trains. It is found that the transition between the two regimes occurs around $\epsilon \approx 0.023$, at which point the one-vortex branch becomes disconnected and the zero- and two-vortex solutions are continuously connected on the same branch of solution.

In the very-narrow gap regime we found pulse train solutions that were equatorially asymmetric and symmetric, as well as periodic and quasi-periodic in time. In plotting these solutions, we identified a relationship between the dislocations in the flow (phase-slips) and the wave-envelope of the pulses concluding that each bifurcation results in the addition of a wave-packet, necessarily alternating between equatorially symmetric and 'shift and reflect' symmetry classes. Finally, we explored a variety of quasi-periodic solutions, before noting briefly the solutions that can be obtained when $\mathrm{Re} \gg \mathrm{Re}_c$.

Extending the set-up to include magnetohydrodynamic effects, we then investigated the dynamics of the pulse train solution for electrically conducting fluids for axial-dipolar and quadrupolar magnetic fields, under both insulating and conducting boundary conditions. For the axial-dipolar field we found the boundary conditions to have opposite effects; increasing the magnetic field strength for insulating boundaries acted equivalently to decreasing Re, whilst for conducting boundaries it acted to effectively increase Re, via feedback of the boundary current. This had little effect on the bifurcation sequence though, as we found equivalent bifurcation schemata, only shifted in Re. The same could be said of the quadrupolar magnetic field under insulating boundaries – increasing magnetic field strength served only to shift the value of Re_c upwards. For conducting boundaries, we found that even weak magnetic fields were sufficient to completely stabilise the equatorial region, with

standard Ekman flow for $0 < \mathrm{Ha} < 30$. New dynamics were observed for $\mathrm{Ha} > 30$, whereby pulse trains exist away from the stable equatorial region, initially travelling poleward. Unfortunately, no additional changes in symmetry or bifurcations were observed in these solutions.

6.2 Future work

There are many avenues for future research into each of the three discussed topics.

In the linear theory of MHD Taylor-Couette flow we may ask why, for example, is the value of $\tau = -0.6$ significant in switching between the two distinct MRI modes. It would be interesting to know if it has any physical significance in terms of the magnetic field profile. Indeed, a fully generalised asymptotic analysis that includes all $\tau < 0$ may illuminate any significance that may exist. Secondly, the subject of instability in the vicinity of the upper Liu limit is currently a hot topic of research. A similarly thorough parameter search for this regime would be of interest – though it would be necessary to consider a narrower gap to allow for numerical convergence. Certainly, it is possible that the positive shear environment may yield additional types of instability. On the topic of wide and narrow gap widths, it would also be interesting to perform a detailed parameter search in these regimes. We have seen in the case of spherical Couette flow that sometimes very narrow gaps can yield intriguing results. It would be interesting to utilise our linear instability results in consideration of new experiments in the upcoming DRESDYN experiments. Finally, though the current asymptotic analysis of Kirillov *et al.* is certainly impressive, is is designed mainly for the case in which currents run in the same directions. As our results identify the possibility of interesting dynamics when the magnetic field is generated by oppositely running currents, it would be of great interest to further generalise the analysis to include such cases.

We also note that there are a number of additional considerations one may take into account when considering GQL applied to the MRI. Recall that larger Hartmann numbers may yield the non-axisymmetric AMRI, which would now need to take into

account the separation of scales in both the axial and azimuthal directions. Due to the increased computational requirements of the fully 3-D flow, numerical modelling of this instability is ongoing (see (Guseva *et al.*, 2015)). Such 3-D GQL is a promising future opportunity for research however, as results obtained for hydrodynamic rotating Couette flow show similar improvements in accuracy as Λ is increased (independently) in the stream- and span-wise directions (Tobias & Marston, 2017).

With regards to GQL for finite Rm flows, clearly there is still significant work to be done. Due to the sheer size of the parameter space, we were limited in how many distinct cases could be examined. It remains to be seen whether there exists some special region of parameter space where such effects can be reproduced at only low Λ. In particular, with more computing power, higher values of Pm could be properly resolved. In addition to this, it would be beneficial to examine a number of different kinds of finite-Rm flows under GQL; whilst we have painted a pessimistic picture of GQL in finite Rm wall bounded, electrically conducting, rotating driven flows, this may not be the case otherwise.

In the field of spherical Couette flow, there is also scope for further work on the pulse train solutions. Firstly, the case $\delta \to 0$ remains difficult to probe numerically due to the incredibly narrow gap widths required. It may be possible to overcome this difficulty with the use of more powerful parallel computation. If such computational power were available, taking even narrower gaps may incorporate even more of the asymptotic pulse train behaviour – one may find other subtle variations in the bifurcation scheme as the gap widths narrows. It would also be interesting to be able to further probe the $\Omega_o/\Omega_i \sim 1$ almost co-rotating case, where we have been limited to $\Omega_o/\Omega_i \leq 0.7$. This is the case predominantly featured in the asymptotic literature, so numerics here would be able to better confirm the prior work.

Secondly, the same investigations may be extended to MHD. Though we have not uncovered a swathe of exciting dynamics in this set-up, the co-rotating case may behave differently. Of course, there is also the option of trying ever more intricate imposed magnetic fields. and it might be possible to assemble one in such a way to perfectly compliment the pulse train dynamics.

Finally, it would be of interest to compute nonaxisymmetric analogues of some of our pulse train solutions. Though nonaxisymmetric solutions have been observed experimentally (Nakabayashi, 1983) and numerically (Yuan, 2004) at $\epsilon = 0.08$ and $\epsilon = 0.06$ respectively, computations for our very-narrow gap regime could illuminate whether these pulse train solutions persist over long time-scales. Of course, 3D simulations of these narrow gaps would be computationally intensive.

Appendix A

A.1 Vector calculus identities

Throughout this thesis, we have made use of the following vector calculus identities, in both cylindrical and spherical coordinates. In chapters 4 and 5, these equations have $\partial f/\partial\theta = 0$ and $\partial f/\partial\phi = 0$, respectively.

A.1.1 Cylindrical coordinates

$$\nabla f = \frac{\partial f}{\partial r}\,\mathbf{e}_r + \frac{1}{r}\frac{\partial f}{\partial \theta}\,\mathbf{e}_\theta + \frac{\partial f}{\partial z}\,\mathbf{e}_z, \tag{A.1}$$

$$\begin{aligned}\nabla \times \mathbf{A} = &\left(\frac{1}{r}\frac{\partial A_z}{\partial \theta} - \frac{\partial A_\theta}{\partial z}\right)\mathbf{e}_r + \left(\frac{\partial A_r}{\partial z} - \frac{\partial A_z}{\partial r}\right)\mathbf{e}_\theta \\ &+ \frac{1}{r}\left(\frac{\partial r A_\theta}{\partial r} - \frac{\partial A_r}{\partial \theta}\right)\mathbf{e}_z,\end{aligned} \tag{A.2}$$

$$\nabla^2 f = \frac{1}{r}\frac{\partial}{\partial r}\left(r\frac{\partial f}{\partial r}\right) + \frac{1}{r^2}\frac{\partial^2 f}{\partial \theta^2} + \frac{\partial^2 f}{\partial z^2}, \tag{A.3}$$

$$\begin{aligned}\nabla^2 \mathbf{A} = &\left(\nabla^2 A_r - \frac{A_r}{r^2} - \frac{2}{r}\frac{\partial A_\theta}{\partial \theta}\right)\mathbf{e}_r + \left(\nabla^2 A_\theta - \frac{A_\theta}{r} + \frac{2}{r^2}\frac{\partial A_r}{\partial \theta}\right)\mathbf{e}_\theta \\ &+ \nabla^2 A_z\,\mathbf{e}_z.\end{aligned} \tag{A.4}$$

A.1.2 Spherical coordinates

$$\nabla f = \frac{\partial f}{\partial r}\,\mathbf{e}_r + \frac{1}{r}\frac{\partial f}{\partial \theta}\,\mathbf{e}_\theta + \frac{1}{r\sin\theta}\frac{\partial f}{\partial \phi}\,\mathbf{e}_\phi, \tag{A.5}$$

$$\begin{aligned}\nabla \times \mathbf{A} =& \frac{1}{r\sin\theta}\left(\frac{\partial A_\phi \sin\theta}{\partial \theta} - \frac{\partial A_\theta}{\partial \phi}\right)\mathbf{e}_r + \frac{1}{r}\left(\frac{1}{\sin\theta}\frac{\partial A_r}{\partial \phi} - \frac{\partial r A_\phi}{\partial r}\right)\mathbf{e}_\theta \\ &+ \frac{1}{r}\left(\frac{\partial r A_\theta}{\partial r} - \frac{\partial A_r}{\partial \theta}\right)\mathbf{e}_\phi,\end{aligned} \tag{A.6}$$

$$\nabla^2 f = \frac{1}{r^2}\frac{\partial}{\partial r}\left(r^2\frac{\partial f}{\partial r}\right) + \frac{1}{r^2\sin\theta}\frac{\partial}{\partial \theta}\left(\sin\theta\frac{\partial f}{\partial \theta}\right) + \frac{1}{r^2\sin^2\theta}\frac{\partial^2 f}{\partial \phi^2}, \tag{A.7}$$

$$\begin{aligned}\nabla^2 \mathbf{A} =& \left(\nabla^2 A_r - \frac{2A_r}{r^2} - \frac{2}{r^2\sin\theta}\left(\frac{\partial A_\theta \sin\theta}{\partial \theta} + \frac{\partial A_\phi}{\partial \phi}\right)\right)\mathbf{e}_r \\ &+ \left(\nabla^2 A_\theta + \frac{2}{r^2}\frac{\partial A_r}{\partial \theta} - \frac{2}{r^2\sin^2\theta}\left(A_\theta + \frac{\partial A_\phi}{\partial \phi}\right)\right)\mathbf{e}_\theta \\ &+ \left(\nabla^2 A_\phi - \frac{2}{r^2\sin\theta}\frac{\partial A_r}{\partial \phi} - \frac{1}{r^2\sin^2\theta}\left(A_\phi - 2\cos\theta\frac{\partial A_\theta}{\partial \phi}\right)\right)\mathbf{e}_\phi.\end{aligned} \tag{A.8}$$

A.2 The Taylor-Proudman theorem

Let us consider a flow of constant density in a rotating reference frame, satisfying the momentum equation,

$$\frac{\partial \mathbf{U}}{\partial t} + \mathbf{U}\cdot\nabla\mathbf{U} + 2\boldsymbol{\Omega}\times\mathbf{U} = -\frac{1}{\rho}\nabla p + \nu\nabla^2\mathbf{U}. \tag{A.9}$$

Here, the Coriolis term $2\boldsymbol{\Omega}\times\mathbf{U}$ is a product of the transition to the rotating reference frame and p is the reduced pressure. By considering the dimensions of each of the terms, we note that

$$\frac{\partial \mathbf{U}}{\partial t} \sim \mathbf{U}\cdot\nabla\mathbf{U} \sim \frac{\hat{U}^2}{L}, \tag{A.10}$$

$$\boldsymbol{\Omega}\times\mathbf{U} \sim \hat{\Omega}\hat{U}, \tag{A.11}$$

$$\nu\nabla^2\mathbf{U} \sim \frac{\nu\hat{U}}{L^2}, \tag{A.12}$$

where we scale velocity with $\hat{U}$, length as L, and the angular velocity as $\hat{\Omega}$. When the flow is rotationally dominated, then

$$\mathrm{Ro} = \frac{U}{\Omega L} \ll 1, \tag{A.13}$$

$$\mathrm{Re} = \frac{UL}{\nu} \gg 1, \tag{A.14}$$

so at first order the momentum equation admits the geostrophic balance

$$2\boldsymbol{\Omega} \times \mathbf{U} = -\frac{1}{\rho}\nabla p. \tag{A.15}$$

If we take the curl of the geostrophic balance, we find that

$$\boldsymbol{\Omega} \times \nabla \mathbf{U} = 0, \tag{A.16}$$

which in the case of the rotational axis being aligned with the z direction, $\boldsymbol{\Omega} = \Omega_0\, e_z$, means that we must have

$$\frac{\partial U_z}{\partial z} = 0. \tag{A.17}$$

Expressing equation (A.16) fully, we have the system of equations

$$-2U_\phi\Omega_0 = \frac{\partial p}{\partial x}, \tag{A.18}$$

$$2U_r\Omega_0 = \frac{\partial p}{\partial y}, \tag{A.19}$$

$$0 = \frac{\partial p}{\partial z}. \tag{A.20}$$

So, we may rearrange and differentiate to produce the result

$$\frac{\partial U_\phi}{\partial z} = -\frac{1}{2\Omega_0}\frac{\partial p^2}{\partial x \partial z} = 0, \tag{A.21}$$

$$\frac{\partial U_r}{\partial z} = \frac{1}{2\Omega_0}\frac{\partial p^2}{\partial y \partial z} = 0. \tag{A.22}$$

Hence, we have the main result of the Taylor-Proudman theorem; for rotationally dominated flows, the velocity field becomes independent of the axis of rotation. For our Taylor-Couette set-up, the flow is z independent.

A.3 Azimuthal magnetic fields in Taylor-Couette flow

In chapter 3, we generate an azimuthal magnetic field by applying a combination of axial currents to the Taylor-Couette system, one in the inner core only, and one in the fluid only. These translate to a magnetic field via Ampère's law.

$$\oint \mathbf{B} \cdot \mathbf{dl} = \mu_0 I \tag{A.23}$$

For the current in the core, this reduces simply to

$$\mu_0 I_{in} = \int_0^{2\pi} B_\phi r \, \mathrm{d}\theta, \tag{A.24}$$

giving us

$$B_\phi = \frac{\mu_0 I_{in}}{2\pi r}. \tag{A.25}$$

For fluid running through the current, we must suitably change the expression for the current to reflect that it is located only between the two cylindrical radii. This is achieved via

$$I(r) = I_{fl} \frac{\pi r^2 - \pi r_i^2}{\pi r_o^2 - \pi r_i^2}, \tag{A.26}$$

where we have considered the current as a current density multiplied by total area at a given radius. Hence, Ampère's law gives

$$\mu_0 I_{fl} \frac{r^2 - r_i^2}{r_o^2 - r_i^2} = \int_0^{2\pi} B_\phi r \, \mathrm{d}\theta, \tag{A.27}$$

leading to the azimuthal magnetic field expression

$$B_\phi = \frac{\mu_0 I_{fl}}{2\pi r} \left(\frac{r^2 - r_i^2}{r_o^2 - r_i^2} \right). \tag{A.28}$$

Of course, these two fields can be superimposed, leading to the final expression for an azimuthal magnetic field generated by currents in the core and fluid,

$$B_\phi = \frac{\mu_0}{2\pi} \left[\frac{1}{r} I_{in} + \frac{1}{r} \frac{r^2 - r_i^2}{r_o^2 - r_1^2} I_{fl} \right]. \tag{A.29}$$

A.4 Constructing multipolar magnetic fields

In chapter 5 we impose a number of external magnetic fields onto the spherical Couette geometry, consisting of combinations of axial, dipolar and quadrupolar configurations. Axial fields are trivial to construct, yet dipolar and quadrupolar require a little more effort.

For any magnetic field $\mathbf{B}$, we have some corresponding magnetic scalar potential V, defined via $\mathbf{B} = -\nabla V$. This is not to be confused with the magnetic vector potential, $\mathbf{A}$. For divergence free magnetic fields, we must then have that the scalar

potential satisfies $\nabla \cdot \mathbf{B} = \nabla \cdot \nabla V = \nabla^2 V = 0$. As seen in section 2.3.2, the solutions here take the form of Legendre polynomials. Given that we are only concerned with axisymmetric magnetic fields, the solutions therefore – including the previous discarded r term – are found to take the form

$$V = \sum_{l=1}^{\infty} \frac{1}{r^{l+1}} P_l(\cos\theta). \tag{A.30}$$

That is, the scalar potential is a superposition of many multipole solutions; $l = 1$ being dipolar, $l = 2$ quadrupolar, etc.

Thus, in order to construct a suitable dipolar magnetic field, we take the gradient of the $l = 1$ term,

$$\mathbf{B} = -\nabla \left(\frac{P_1(\cos(\theta)}{r^2} \right), \tag{A.31}$$

which yields

$$\mathbf{B} = 2r^{-3} \cos\theta \, \mathbf{e}_r + r^{-3} \sin\theta \, \mathbf{e}_\theta. \tag{A.32}$$

Similarly, for a quadrupolar field we take the gradient of the $l = 2$ term,

$$\mathbf{B} = -\nabla \left(\frac{P_2(\cos\theta)}{r^3} \right), \tag{A.33}$$

which results in

$$\mathbf{B} = r^{-4}(3\cos^2\theta - 1) \, \mathbf{e}_r + 2r^{-4} \cos\theta \sin\theta \, \mathbf{e}_\theta. \tag{A.34}$$

References

Abramowitz, M. & Stegun, I.A. (1964). *Handbook of mathematical functions: with formulas, graphs, and mathematical tables*, vol. 55. Courier Corporation. 38

Adel, L. & Ahcene, B. (2016). A numerical investigation on the onset of the various flow regimes in a spherical annulus. *J. Fluids Eng.*, **138**, 111201. 136, 152

Ait-Chaalal, F., Schneider, T., Meyer, B. & Marston, J.B. (2016). Cumulant expansions for atmospheric flows. *New J. Phys.*, **18**, 025019. 85

Andereck, C.D., Liu, S.S. & Swinney, H.L. (1986). Flow regimes in a circular Couette system with independently rotating cylinders. *J. Fluid Mech.*, **164**, 155–183. 2, 3

Avila, M. (2012). Stability and angular-momentum transport of fluid flows between corotating cylinders. *Phys. Rev. Lett.*, **108**, 124501. 6

Bai, X.N. & Stone, J.M. (2014). Magnetic flux concentration and zonal flows in magnetorotational instability turbulence. *Astrophys. J.*, **796**, 31. 5

Balbus, S.A. (2003). Enhanced angular momentum transport in accretion disks. *Annu. Rev. Astron. Astrophys.*, **41**, 555–597. 3

Balbus, S.A. & Hawley, J.F. (1991). A powerful local shear instability in weakly magnetized disks. I-Linear analysis. II-Nonlinear evolution. *Astrophys. J.*, **376**, 214–233. 4

Bartels, F. (1982). Taylor vortices between two concentric rotating spheres. *J. Fluid Mech.*, **119**, 1–25. 134

Bassom, A.P. & Soward, A.M. (2004). On finite-amplitude subcritical instability in narrow-gap spherical Couette flow. *J. Fluid Mech.*, **499**, 277–314. 13, 135, 144

Blockley, E.W., Bassom, A.P., Gilbert, A.D. & Soward, A.M. (2007). Pulse-train solutions of a spatially heterogeneous amplitude equation arising in the subcritical instability of narrow gap spherical Couette flow. *Physica D*, **228**, 1–30. 13, 136, 144

Bouchet, F., Nardini, C. & Tangarife, T. (2013). Kinetic theory of jet dynamics in the stochastic barotropic and 2D Navier-Stokes equations. *J. Stat. Phys.*, **153**, 572 – 625. 85

Boyd, J.P. (2001). *Chebyshev and Fourier spectral methods*. Courier Corporation. 30, 33

Bühler, K. (1990). Symmetric and asymmetric Taylor vortex flow in spherical gaps. *Acta Mech.*, **81**, 3–38. 12, 137

Bühler, L. (2009). On the origin of super-rotating layers in magnetohydrodynamic flows. *Theor. Comp. Fluid Dyn.*, **23**, 491–507. 158

Canuto, C., Hussaini, M., Quarteroni, A. & Zang, T. (2007). *Spectral Methods: Fundamentals in Single Domains*. Scientific Computation, Springer Berlin Heidelberg. 30

Chandrasekhar, S. (1956). On the stability of the simplest solution of the equations of hydromagnetics. *Proc. Nat. Acad. Sci.*, **42**, 273. 64

Chandrasekhar, S. (1960). The stability of non-dissipative Couette flow in hydromagnetics. *Proc. Nat. Acad. Sci. USA*, **46**, 253. 4

Chandrasekhar, S. (1961). *Hydrodynamic and Hydromagnetic Stability*. Courier Corporation. 4

Cliffe, K.A., Mullin, T. & Schaeffer, D. (2012). The onset of steady vortices in Taylor-Couette flow: The role of approximate symmetry. *Phys. Fluids*, **24**, 064102. 143

Constantinou, N.C., Farrell, B.F. & Ioannou, P.J. (2013). Emergence and equilibration of jets in beta-plane turbulence: applications of Stochastic Structural Stability Theory. *J. Atmos. Sci.*, **72**, 1689 – 1712. 85

Cooley, J.W. & Tukey, J.W. (1965). An algorithm for the machine calculation of complex Fourier series. *Math. Comput.*, **19**, 297–301. 32

Couette, M. (1890). Etudes sur le frottement des liquides. *Ann. Chem. Phys. Ser. VI*, **21**. 1

Courant, R. & Hilbert, D. (2008). *Methods of Mathematical Physics*. v. 1, Wiley. 22

Cross, M. & Greenside, H. (2009). *Pattern Formation and Dynamics in Nonequilibrium Systems*. Cambridge Univ. Press. 12

Cross, M.C. & Hohenberg, P.C. (1993). Pattern formation outside of equilibrium. *Rev. Mod. Phys.*, **65**, 851–1112. 12

Donnelly, R.J. & Ozima, M. (1962). Experiments on the stability of flow between rotating cylinders in the presence of a magnetic field. *Proc. R. Soc. A*, **266**, 272–286. 4

Dormy, E., Cardin, P. & Jault, D. (1998). MHD flow in a slightly differentially rotating spherical shell, with conducting inner core, in a dipolar magnetic field. *Earth Planet. Sci. Lett.*, **160**, 15–30. 157

Driscoll, J.R. & Healy, D.M. (1994). Computing Fourier transforms and convolutions on the 2-sphere. *Adv. Appl. Math.*, **15**, 202–250. 37

Dumas, G. & Leonard, A. (1994). A divergence-free spectral expansions method for three-dimensional flows in spherical-gap geometries. *J. Comp. Phys.*, **111**, 205–219. 136

Egbers, C. & Rath, H.J. (1995). The existence of Taylor vortices and wide-gap instabilities in spherical Couette flow. *Acta Mech.*, **111**, 125–140. 12

Ewen, S.A. & Soward, A.M. (1994a). Phase mixed rotating magnetoconvection and Taylor's condition II. Travelling pulses. *Geophys. Astrophys. Fluid Dynam.*, **77**, 231–262. 135

Ewen, S.A. & Soward, A.M. (1994b). Phase mixed rotation magnetoconvection and Taylor's condition III. Wave trains. *Geophys. Astrophys. Fluid Dynam.*, **77**, 263–283. 135

Farrell, B.F. & Ioannou, P.J. (2007). Structure and spacing of jets in barotropic turbulence. *J. Atmos. Sci.*, **64**, 3652–3665. 85

Farrell, B.F. & Ioannou, P.J. (2008). Formation of jets by baroclinic turbulence. *J. Atmos. Sci.*, **65**, 3353. 85

Fitzgerald, J.G. & Farrell, B.F. (2016). A theory based on statistical state dynamics for the formation of jets and associated density layers in stratified turbulence. *arXiv preprint arXiv:1612.03243*. 85

Flanagan, K., Clark, M., Collins, C., Cooper, C.M., Khalzov, I.V., Wallace, J. & Forest, C. (2015). Prospects for observing the magnetorotational instability in the plasma Couette experiment. *J. Plasma Phys.*, **81**, 345810401. 6

Gellert, M., Rüdiger, G. & Hollerbach, R. (2011). Helicity and α-effect by current-driven instabilities of helical magnetic fields. *Mon. Not. Roy. Astron. Soc.*, **414**, 2696. 9

Gissinger, C., Goodman, J. & Ji, H. (2012). The role of boundaries in the magnetorotational instability. *Phys. Fluids*, **24**, 074109. 6

Gressel, O. & Pessah, M.E. (2015). Characterizing the mean-field dynamo in turbulent accretion disks. *Astrophys. J.*, **810**, 59. 5

Guseva, A., Willis, A.P., Hollerbach, R. & Avila, M. (2015). Transition to magnetorotational turbulence in Taylor-Couette flow with imposed azimuthal magnetic field. *New J. Phys.*, **17**, 093018. 177

Harris, D., Bassom, A.P. & Soward, A.M. (2000). An inhomogeneous Landau equation with application to spherical Couette flow in the narrow gap limit. *Physica D*, **137**, 260–276. 13, 135, 144

Harris, D., Bassom, A.P. & Soward, A.M. (2003). Global bifurcation to travelling waves with application to narrow gap spherical Couette flow. *Physica D*, **177**, 122–174. 135

Healy Jr, D.M., Kostelec, P.J. & Rockmore, D. (2004). Towards safe and effective high-order Legendre transforms with applications to FFTs for the 2-sphere. *Adv. Comput. Math.*, **21**, 59–105. 37

Heideman, M.T., Johnson, D.H. & Burrus, C.S. (1985). Gauss and the history of the fast Fourier transform. *Arch. Hist. Exact Sci.*, **34**, 265–277. 32

Herreman, W., Nore, C., Cappanera, L. & Guermond, J.L. (2015). Tayler instability in liquid metal columns and liquid metal batteries. *J. Fluid. Mech.*, **771**, 79–114. 10

Herron, I. & Soliman, F. (2006). The stability of Couette flow in a toroidal magnetic field. *Appl. Math. Lett.*, **19**, 1113–1117. 8

Heyvaerts, J. & Priest, E.R.I. (1983). Coronal heating by phase-mixed shear Alfvén waves. *Astron. Astrophys.*, **117**, 220–234. 134

Hocking, L.M. & Skiepko, J. (1981). The instability of flow in the narrow gap between two prolate spheroids. Part I. Small axis ratio. *Q. J. Mech. Appl. Math.*, **34**, 57–68. 134

Hollerbach, R. (1994). Magnetohydrodynamic Ekman and Stewartson layers in a rotating spherical shell. *Proc. R. Soc. A*, **444**, 333–346. 156, 157

Hollerbach, R. (2000a). *Magnetohydrodynamic flows in spherical shells*, vol. 549. Springer. 157

Hollerbach, R. (2000b). A spectral solution of the magneto-convection equations in spherical geometry. *Int. J. Num. Meth. Fluid.*, **32**, 773–797. 24, 26, 30

Hollerbach, R. (2001). Super- and counter-rotating jets and vortices in strongly magnetic spherical Couette flow. In *Dynamo and Dynamics, a Mathematical Challenge*, 189–197, Springer. 157

Hollerbach, R. (2008). Spectral solutions of the MHD equations in cylindrical geometry. *Int. J. Pure Appl. Math.*, **42**, 575. 30

Hollerbach, R. (2009). Non-axisymmetric instabilities in magnetic spherical Couette flow. *Proc. R. Soc. A*, **465**, 2003–2013. 158

Hollerbach, R. & Fournier, A. (2004). *End-effects in rapidly rotating cylindrical Taylor-Couette flow*, vol. 733 of *American Institute of Physics Conference Series*. 6

Hollerbach, R. & Khan, F. (2016). Phase slip solutions in magnetically modulated Taylor–Couette flow. *Acta Mech.*, **227**, 311–319. 152

Hollerbach, R. & Rüdiger, G. (2005). New type of magnetorotational instability in cylindrical Taylor-Couette flow. *Phys. Rev. Lett.*, **95**, 124501. 7, 74

Hollerbach, R. & Skinner, S. (2001). Instabilities of magnetically induced shear layers and jets. *Proc. R. Soc. A*, **457**, 785–802. 158

Hollerbach, R., Junk, M. & Egbers, C. (2006). Non-axisymmetric instabilities in basic state spherical Couette flow. *Fluid Dynam. Res.*, **38**, 257–273. 12

Hollerbach, R., Canet, E. & Fournier, A. (2007). Spherical Couette flow in a dipolar magnetic field. *Eur. J. Mech. B-Fluid*, **26**, 729–737. 158

Hollerbach, R., Teeluck, V. & Rüdiger, G. (2010). Nonaxisymmetric magnetorotational instabilities in cylindrical Taylor-Couette flow. *Phys. Rev. Lett.*, **104**, 044502. 50, 52, 58, 63, 70

Hough, S.S. (1897). On the application of harmonic analysis to the dynamical theory of the tides. Part I. On Laplace's "oscillations of the first species," and on the dynamics of ocean currents. *Phil. Trans. R. Soc. A*, **189**, 201–257. 6

Hoyle, R.B. (2006). *Pattern Formation: An Introduction to Methods*. Cambridge Univ. Press. 12

Ji, H., Goodman, J. & Kageyama, A. (2001). Magnetorotational instability in a rotating liquid metal annulus. *Mon. Not. R. Astron. Soc.*, **325**, L1–L5. 6

Julien, K. & Knobloch, E. (2010). Magnetorotational instability: recent developments. *Phil. Trans. R. Soc. A*, **368**, 1607–1633. 4

Khlebutin, G.N. (1968). Stability of fluid motion between a rotating and a stationary concentric sphere. *Fluid Dyn.*, **3**, 31–32. 11

Kirillov, O. & Stefani, F. (2012). WKB thresholds of standard, helical, and azimuthal magnetorotational instability. *Proc. Int. Astron. U.*, **8**, 233–234. 8

Kirillov, O.N. & Stefani, F. (2010). On the relation of standard and helical magnetorotational instability. *Astrophys. J.*, **712**, 52. 7

Kirillov, O.N. & Stefani, F. (2011). Paradoxes of magnetorotational instability and their geometrical resolution. *Physical Rev. E*, **84**, 036304. 51

Kirillov, O.N. & Stefani, F. (2013). Extending the range of the inductionless magnetorotational instability. *Phys. Rev. Lett.*, **111**, 061103. 51

Kirillov, O.N., Stefani, F. & Fukumoto, Y. (2012). A unifying picture of helical and azimuthal magnetorotational instability, and the universal significance of the Liu limit. *Astrophys. J.*, **756**, 83. 51

Kirillov, O.N., Stefani, F. & Fukumoto, Y. (2014). Local instabilities in magnetized rotational flows: a short-wavelength approach. *J. Fluid Mech.*, **760**, 591–633. 49, 51, 52, 54, 64, 66, 70, 72

Kleeorin, N., Rogachevskii, I., Ruzmaikin, A., Soward, A.M. & Starchenko, S. (1997). Axisymmetric flow between differentially rotating spheres in a dipole magnetic field. *J. Fluid Mech.*, **344**, 213–244. 157

Liu, W. (2009). Noise-sustained convective instability in a magnetized Taylor-Couette flow. *Astrophys. J.*, **692**, 998. 8

Liu, W., Goodman, J., Herron, I. & Ji, H. (2006). Helical magnetorotational instability in magnetized Taylor-Couette flow. *Phys. Rev. E*, **74**, 056302. 7, 8

Mahloul, M., Mahamdia, A. & Kristiawan, M. (2016). The spherical Taylor–Couette flow. *Eur. J. Mech. B-Fluids*, **59**, 1–6. 136

Mallock, A. (1888). Determination of the viscosity of water. *Proc. R. Soc. A*, **45**, 126–132. 1

Mamun, C. & Tuckerman, L. (1995). Asymmetry and Hopf bifurcation in spherical Couette flow. *Phys. Fluids*, **7**, 80–91. 12, 44, 137, 142

Marcus, P.S. & Tuckerman, L.S. (1987a). Simulation of flow between concentric rotating spheres. Part 1. Steady states. *J. Fluid Mech.*, **185**, 1–30. 137

Marcus, P.S. & Tuckerman, L.S. (1987b). Simulation of flow between concentric rotating spheres. Part 2. Transitions. *J. Fluid Mech.*, **185**, 31–65. 137

Marston, J.B., Qi, W. & Tobias, S.M. (2014). Direct statistical simulation of a jet. *arXiv:1412.0381*. 85

Marston, J.B., Chini, G.P. & Tobias, S.M. (2016). Generalized quasilinear approximation: Application to zonal jets. *Phys. Rev. Lett.*, **116**, 214501. 85, 86, 87, 88, 92, 102, 173

Mason, J.C. & Handscomb, D.C. (2002). *Chebyshev Polynomials*. CRC Press. 21, 62

Meheut, H., Fromang, S., Lesur, G., Joos, M. & Longaretti, P.Y. (2015). Angular momentum transport and large eddy simulations in magnetorotational turbulence: The small Pm limit. *Astro. & Astrophys.*, **579**, A117. 5

Mohlenkamp, M.J. (1999). A fast transform for spherical harmonics. *J. Fourier Analy. Appl.*, **5**, 159–184. 37

Munson, B.R. & Menguturk, M. (1975). Viscous incompressible flow between concentric rotating spheres. *J. Fluid Mech.*, **69**, 705–719. 12

Nakabayashi, K. (1983). Transition of Taylor–Görtler vortex flow in spherical Couette flow. *J. Fluid Mech.*, **132**, 209–230. 136, 178

Nakabayashi, K., Tsuchida, Y. & Zheng, Z. (2002). Characteristics of disturbances in the laminar-turbulent transition of spherical Couette flow. 1. Spiral Taylor-Görtler vortices and traveling waves for narrow gaps. *Phys. Fluids*, **14**, 3963–3972. 12, 136

Nakabayashi, K., Sha, W. & Tsuchida, Y. (2005). Relaminarization phenomena and external-disturbance effects in spherical Couette flow. *J. Fluid Mech.*, **534**, 327–350. 12

Nataf, H.C., Alboussiere, T., Brito, D., Cardin, P., Gagniere, N., Jault, D. & Schmitt, D. (2008). Rapidly rotating spherical Couette flow in a dipolar magnetic field: an experimental study of the mean axisymmetric flow. *Phys. Earth Planet. Inter.*, **170**, 60–72. 158

Nornberg, M.D., Ji, H., Schartman, E., Roach, A. & Goodman, J. (2010). Observation of magnetocoriolis waves in a liquid metal Taylor-Couette experiment. *Phys. Rev. Lett.*, **104**, 074501. 6

Ogilvie, G.I. & Pringle, J.E. (1996). The non-axisymmetric instability of a cylindrical shear flow containing an azimuthal magnetic field. *Mon. Not. R. Astron. Soc.*, **279**, 152–164. 8

Orszag, S.A. (1969). Numerical methods for the simulation of turbulence. *Phys. Fluids*, **12**, II–250. 18

Orszag, S.A. (1971). On the elimination of aliasing in finite-difference schemes by filtering high-wavenumber components. *J. Atmos. sci.*, **28**, 1074–1074. 33

Phillips, N.A. (1959). *An example of non-linear computational instability*, vol. 501. Rockefeller Institute Press New York. 33

Priede, J. (2011). Inviscid helical magnetorotational instability in cylindrical Taylor-Couette flow. *Phys. Rev. E*, **84**, 066314. 8

Priede, J. (2015). Metamorphosis of helical magnetorotational instability in the presence of axial electric current. *Phys. Rev. E*, **91**, 033014. 8

Priede, J. & Gerbeth, G. (2009). Absolute versus convective helical magnetorotational instability in a Taylor-Couette flow. *Phys. Rev. E*, **79**, 046310. 8

Pringle, J.E. (1981). Accretion discs in astrophysics. *Annu. Rev. Astron. Astrophys.*, **19**, 137–160. 3

Rayleigh, L. (1917). On the dynamics of revolving fluids. *Phil. Trans. R. Soc. A*, **93**, 148–154. 1

Roach, A.H., Spence, E.J., Gissinger, C., Edlund, E.M., Sloboda, P., Goodman, J. & Ji, H. (2012). Observation of a free-Shercliff-layer instability in cylindrical geometry. *Phys. Rev. Lett.*, **108**, 154502. 6

Rüdiger, G. & Zhang, Y. (2001). MHD instability in differentially-rotating cylindric flows. *Astro. & Astrophys.*, **378**, 302–308. 6

Rüdiger, G., Hollerbach, R., Stefani, F., Gundrum, T., Gerbeth, G. & Rosner, R. (2006). The traveling-wave MRI in cylindrical Taylor-Couette flow: comparing wavelengths and speeds in theory and experiment. *Astrophys. J. Lett.*, **649**, L145. 8, 90, 94

Rüdiger, G., Gellert, M., Schultz, M. & Hollerbach, R. (2010). Dissipative Taylor-Couette flows under the influence of helical magnetic fields. *Phys. Rev. E*, **82**, 016319. xvi, 50, 52, 63, 65, 66

Rüdiger, G., Gellert, M., Schultz, M., Hollerbach, R. & Stefani, F. (2014). Astrophysical and experimental implications from the magnetorotational instability of toroidal fields. *Mon. Not. R. Astron. Soc.*, **438**, 271–277. 50

Rüdiger, G., Schultz, M., Stefani, F. & Mond, M. (2015). Diffusive magnetohydrodynamic instabilities beyond the Chandrasekhar theorem. *Astro. J.*, **811**, 84. 64

Rüdiger, G., Gellert, M., Schultz, M. & Stefani, F. (2016a). Double-diffusive magnetorotational instability of super-rotation under the influence of azimuthal magnetic fields. *arXiv preprint arXiv:1601.01964*. 51

Rüdiger, G., Schultz, M., Gellert, M. & Stefani, F. (2016b). Subcritical excitation of the current-driven Tayler instability by super-rotation. *Phys. Fluids*, **28**. 10, 52

Schaeffer, N. (2013). Efficient spherical harmonic transforms aimed at pseudospectral numerical simulations. *Geochem., Geophys., Geosys.*, **14**, 751–758. 37

Schartman, E., Ji, H. & Burin, M.J. (2009). Development of a Couette-Taylor flow device with active minimization of secondary circulation. *Rev. Sci. Instrum.*, **80**, 024501. 6

Schrauf, G. (1986). The first instability in spherical Taylor-Couette flow. *J. Fluid Mech.*, **166**, 287–303. 137

Seilmayer, M., Stefani, F., Gundrum, T., Weier, T., Gerbeth, G., Gellert, M. & Rüdiger, G. (2012). Experimental evidence for a transient Tayler instability in a cylindrical liquid-metal column. *Phys. Rev. Lett.*, **108**, 244501. 10, 67

Seilmayer, M., Galindo, V., Gerbeth, G., Gundrum, T., Stefani, F., Gellert, M., Rüdiger, G., Schultz, M. & Hollerbach, R. (2014). Experimental evidence for nonaxisymmetric magnetorotational instability in a rotating liquid metal exposed to an azimuthal magnetic field. *Phys. Rev. Lett.*, **113**, 024505. 8

Sisan, D.R., Mujica, N., Tillotson, W.A., Huang, Y., Dorland, W., Hassam, A.B., Antonsen, T.M. & Lathrop, D.P. (2004). Experimental

observation and characterization of the magnetorotational instability. *Phys. Rev. Lett.*, **93**, 114502. 158

Soward, A.M. & Bassom, A.P. (2016). Frequency staircases in narrow-gap spherical Couette flow. *Geophys. Astrophys. Fluid Dynam.*, 1–32. 135

Soward, A.M. & Dormy, E. (2010). Shear-layers in magnetohydrodynamic spherical Couette flow with conducting walls. *J. Fluid Mech.*, **645**, 145–185. 158

Soward, A.M. & Jones, C.A. (1983). The linear stability of the flow in the narrow gap between two concentric rotating spheres. *Q. J. Mech. Appl. Math.*, **36**, 19–42. 134

Spruit, H.C. (2002). Dynamo action by differential rotation in a stably stratified stellar interior. *Astron. Astrophys.*, **381**, 923–932. 9

Squire, J. & Bhattacharjee, A. (2015). Statistical simulation of the magnetorotational dynamo. *Phys. Rev. Lett.*, **114**, 085002. 84

Srinivasan, K. & Young, W.R. (2012). Zonostrophic instability. *J. Atmos. Sci.*, **69**, 1633–1656. 85

Starchenko, S.V. (1997). Magnetohydrodynamics of a viscous spherical layer rotating in a strong potential field. *J. Exp. Theor. Phys.*, **85**, 1125–1137. 157

Stefani, F. & Kirillov, O.N. (2015). Destabilization of rotating flows with positive shear by azimuthal magnetic fields. *Phys. Rev. E*, **92**, 051001. 52

Stefani, F., Gundrum, T., Gerbeth, G., Rüdiger, G., Schultz, M., Szklarski, J. & Hollerbach, R. (2006). Experimental evidence for magnetorotational instability in a Taylor-Couette flow under the influence of a helical magnetic field. *Phys. Rev. Lett.*, **97**, 184502. 7, 8

Stefani, F., Gundrum, T., Gerbeth, G., Rüdiger, G., Szklarski, J. & Hollerbach, R. (2007). Experiments on the magnetorotational instability in helical magnetic fields. *New J. Phys.*, **9**, 295. 7

Stefani, F., Gerbeth, G., Gundrum, T., Szklarski, J., Rüdiger, G. & Hollerbach, R. (2008). Results of a modified PROMISE experiment. *Astron. Nachr.*, **329**, 652–658. 7, 8

Stefani, F., Gerbeth, G., Gundrum, T., Hollerbach, R., Priede, J., Rüdiger, G. & Szklarski, J. (2009). Helical magnetorotational instability in a Taylor-Couette flow with strongly reduced Ekman pumping. *Phys. Rev. E*, **80**, 066303. 7, 8

Stefani, F., Weier, T., Gundrum, T. & Gerbeth, G. (2011). How to circumvent the size limitation of liquid metal batteries due to the Tayler instability. *Energ. Convers. Manage.*, **52**, 2982 – 2986. 10

Suda, R. & Takami, M. (2002). A fast spherical harmonics transform algorithm. *Math. Comput.*, **71**, 703–715. 37

Suzuki, T.K. & Inutsuka, S.I. (2014). Magnetohydrodynamic simulations of global accretion disks with vertical magnetic fields. *Astrophys. J.*, **784**, 121. 5

Swarztrauber, P.N. (1982). Vectorizing the FFTs. *Parallel Comput.*, 51–83. 32

Tataronis, J.A. & Mond, M. (1987). Magnetohydrodynamic stability of plasmas with aligned mass flow. *Phys. Fluids*, **30**, 84–89. 64

Tayler, R.J. (1973). The adiabatic stability of stars containing magnetic fields-I: Toroidal fields. *Mon. Not. R. Astron. Soc.*, **161**, 365. 9, 67

Taylor, G.I. (1923). Stability of a viscous liquid contained between two rotating cylinders. *Phil. Trans. R. Soc. A*, **223**, 289–343. 2

Tobias, S.M. & Marston, J.B. (2013). Direct statistical simulation of out-of-equilibrium jets. *Phys. Rev. Lett.*, **110**, 104502. 85

Tobias, S.M. & Marston, J.B. (2017). Three-dimensional rotating Couette flow via the generalised quasilinear approximation. *J. Fluid Mech.*, **810**, 412–428. 86, 177

Tobias, S.M., Dagon, K. & Marston, J.B. (2011). Astrophysical fluid dynamics via direct statistical simulation. *Astrophys. J.*, **727**, 127. 84, 87

Turing, A.M. (1948). Rounding-off errors in matrix processes. *Q. J. Mech. Appl. Math.*, **1**, 287–308. 45

Vandakurov, Y.V. (1972). Theory for the stability of a star with a toroidal magnetic field. *Sov. Astron.*, **16**, 265. 9

Velikhov, E.P. (1959). Stability of an ideally conducting liquid flowing between rotating cylinders in a magnetic field. *Sov. Phys. JETP*, **36**, 995. 4

Verma, M.K., Roberts, D.A., Goldstein, M.L., Ghosh, S. & Stribling, W.T. (1996). A numerical study of the nonlinear cascade of energy in magnetohydrodynamic turbulence. *J. Geophys. Res-Space*, **101**, 21619–21625. 113

Walton, I.C. (1978). The linear stability of the flow in a narrow spherical annulus. *J. Fluid Mech.*, **86**, 673–693. 134

Weber, N., Galindo, V., Stefani, F., Weier, T. & Wondrak, T. (2013). Numerical simulation of the Tayler instability in liquid metals. *New J. Phys.*, **15**, 043034. 10

Weber, N., Galindo, V., Stefani, F. & Weier, T. (2014). Current-driven flow instabilities in large-scale liquid metal batteries, and how to tame them. *J. Power Sources*, **265**, 166–173. 10

Wei, X. & Hollerbach, R. (2010). Magnetic spherical Couette flow in linear combinations of axial and dipolar fields. *Acta Mech.*, **215**, 1–8. 158, 159

Wei, X., Ji, H., Goodman, J., Ebrahimi, F., Gilson, E., Jenko, F. & Lackner, K. (2016). Numerical simulations of the princeton magnetorotational instability experiment with conducting axial boundaries. *Phys. Rev. E*, **94**, 063107. 16

Wimmer, M. (1976). Experiments on a viscous fluid flow between concentric rotating spheres. *J. Fluid Mech.*, **78**, 317–335. 12, 134

Wimmer, M. (1981). Experiments on the stability of viscous flow between two concentric rotating spheres. *J. Fluid Mech.*, **103**, 117–131. 12, 134

Yuan, L. (2004). Numerical study of multiple periodic flow states in spherical Couette flow. *Sci. China Ser. A*, **47**, 81–91. 137, 178

Zikanov, O.Y. (1995). Numerical simulation of instabilities and secondary regimes in spherical Couette flow. *Fluid Dyn.*, **30**, 1–10. 136

Zikanov, O.Y. (1996). Symmetry-breaking bifurcations in spherical Couette flow. *J. Fluid Mech.*, **310**, 293–324. 136